

REPORT DOCUMENTATION PAGE				Form Approved OMB NO. 0704-0188	
<p>The public reporting burden for this collection of information is estimated to average 1 hour per response, including the time for reviewing instructions, searching existing data sources, gathering and maintaining the data needed, and completing and reviewing the collection of information. Send comments regarding this burden estimate or any other aspect of this collection of information, including suggestions for reducing this burden, to Washington Headquarters Services, Directorate for Information Operations and Reports, 1215 Jefferson Davis Highway, Suite 1204, Arlington VA, 22202-4302. Respondents should be aware that notwithstanding any other provision of law, no person shall be subject to any penalty for failing to comply with a collection of information if it does not display a currently valid OMB control number.</p> <p>PLEASE DO NOT RETURN YOUR FORM TO THE ABOVE ADDRESS.</p>					
1. REPORT DATE (DD-MM-YYYY) 05-12-2012		2. REPORT TYPE Final Report		3. DATES COVERED (From - To) 1-Nov-2010 - 30-Jun-2012	
4. TITLE AND SUBTITLE FFATA: MACHINE AUGMENTED COMPOSITES FOR STRUCTURES WITH HIGH DAMPING WITH HIGH STIFFNESS				5a. CONTRACT NUMBER W911NF-11-1-0004	
				5b. GRANT NUMBER	
				5c. PROGRAM ELEMENT NUMBER 0620BJ	
6. AUTHORS Terry S. Creasy, Gary Hawkins, Ching-Yao (Tony) Tang, Brian W. Gore, Juliet N. Schurr, Aaron L. Cheung, Gene Cha				5d. PROJECT NUMBER	
				5e. TASK NUMBER	
				5f. WORK UNIT NUMBER	
7. PERFORMING ORGANIZATION NAMES AND ADDRESSES Texas Engineering Experiment Station 400 Harvey Mitchell Parkway Suite 300 College Station, TX 77845 -4375				8. PERFORMING ORGANIZATION REPORT NUMBER	
9. SPONSORING/MONITORING AGENCY NAME(S) AND ADDRESS(ES) U.S. Army Research Office P.O. Box 12211 Research Triangle Park, NC 27709-2211				10. SPONSOR/MONITOR'S ACRONYM(S) ARO	
				11. SPONSOR/MONITOR'S REPORT NUMBER(S) 58854-MS-DRP.1	
12. DISTRIBUTION AVAILABILITY STATEMENT Approved for Public Release; Distribution Unlimited					
13. SUPPLEMENTARY NOTES The views, opinions and/or findings contained in this report are those of the author(s) and should not be construed as an official Department of the Army position, policy or decision, unless so designated by other documentation.					
14. ABSTRACT The Material Logic program aims to create novel materials that exhibit high stiffness and high damping. The joint Texas A&M University (Texas Engineering Experiment Station or TEES)/The Aerospace Corporation (AERO) effort seeks to develop a new composite material by exploiting negative-stiffness, positive-stiffness, and damping elements to form a novel material system. Overall success is defined as developing a material that can achieve a 1.0 damping coefficient with a 100 GPa elastic modulus. The material system should also be optimized for 0.01 s					
15. SUBJECT TERMS high stiffness/high damping, negative stiffness materials					
16. SECURITY CLASSIFICATION OF:			17. LIMITATION OF ABSTRACT UU	15. NUMBER OF PAGES	19a. NAME OF RESPONSIBLE PERSON Terry Creasy
a. REPORT UU	b. ABSTRACT UU	c. THIS PAGE UU			19b. TELEPHONE NUMBER 979-458-0118

Report Title

FFATA: MACHINE AUGMENTED COMPOSITES FOR STRUCTURES WITH HIGH DAMPING WITH HIGH STIFFNESS

ABSTRACT

The Material Logic program aims to create novel materials that exhibit high stiffness and high damping. The joint Texas A&M University (Texas Engineering Experiment Station or TEES)/The Aerospace Corporation (AERO) effort seeks to develop a new composite material by exploiting negative-stiffness, positive-stiffness, and damping elements to form a novel material system. Overall success is defined as developing a material that can achieve a 1.0 damping coefficient with a 100 GPa elastic modulus. The material system should also be optimized for 0.01 s duration impulses and cyclic loadings in the 0.1 to 10 Hz regime and be adaptable to a wide load range.

The AERO team made a breakthrough in applying the negative spring by stabilizing the spring within a positive stiffness composite structure. Figure 1 shows one application concept: a composite structure that stabilizes the clover dome's negative stiffness régime with damping integrated into the mobile interface between positive and negative springs.

Further, a design from AERO, the WTG fluidic damping element, showed adaptive response when filled with shear thickening fluids.

Enter List of papers submitted or published that acknowledge ARO support from the start of the project to the date of this printing. List the papers, including journal references, in the following categories:

(a) Papers published in peer-reviewed journals (N/A for none)

Received

Paper

TOTAL:

Number of Papers published in peer-reviewed journals:

(b) Papers published in non-peer-reviewed journals (N/A for none)

Received

Paper

TOTAL:

Number of Papers published in non peer-reviewed journals:

(c) Presentations

Number of Presentations: 0.00

Non Peer-Reviewed Conference Proceeding publications (other than abstracts):

<u>Received</u>	<u>Paper</u>
1	1
2	2
3	3
4	4
5	5
6	6
7	7
8	8
9	9
10	10
11	11
12	12
13	13
14	14
15	15
16	16
17	17
18	18
19	19
20	20
21	21
22	22
23	23
24	24
25	25
26	26
27	27
28	28
29	29
30	30
31	31
32	32
33	33
34	34
35	35
36	36
37	37
38	38
39	39
40	40
41	41
42	42
43	43
44	44
45	45
46	46
47	47
48	48
49	49
50	50
51	51
52	52
53	53
54	54
55	55
56	56
57	57
58	58
59	59
60	60
61	61
62	62
63	63
64	64
65	65
66	66
67	67
68	68
69	69
70	70
71	71
72	72
73	73
74	74
75	75
76	76
77	77
78	78
79	79
80	80
81	81
82	82
83	83
84	84
85	85
86	86
87	87
88	88
89	89
90	90
91	91
92	92
93	93
94	94
95	95
96	96
97	97
98	98
99	99
100	100

TOTAL:

Number of Non Peer-Reviewed Conference Proceeding publications (other than abstracts):

Peer-Reviewed Conference Proceeding publications (other than abstracts):

<u>Received</u>	<u>Paper</u>
1	1
2	2
3	3
4	4
5	5
6	6
7	7
8	8
9	9
10	10
11	11
12	12
13	13
14	14
15	15
16	16
17	17
18	18
19	19
20	20
21	21
22	22
23	23
24	24
25	25
26	26
27	27
28	28
29	29
30	30
31	31
32	32
33	33
34	34
35	35
36	36
37	37
38	38
39	39
40	40
41	41
42	42
43	43
44	44
45	45
46	46
47	47
48	48
49	49
50	50
51	51
52	52
53	53
54	54
55	55
56	56
57	57
58	58
59	59
60	60
61	61
62	62
63	63
64	64
65	65
66	66
67	67
68	68
69	69
70	70
71	71
72	72
73	73
74	74
75	75
76	76
77	77
78	78
79	79
80	80
81	81
82	82
83	83
84	84
85	85
86	86
87	87
88	88
89	89
90	90
91	91
92	92
93	93
94	94
95	95
96	96
97	97
98	98
99	99
100	100

TOTAL:

Number of Peer-Reviewed Conference Proceeding publications (other than abstracts):

(d) Manuscripts

<u>Received</u>	<u>Paper</u>
1	1
2	2
3	3
4	4
5	5
6	6
7	7
8	8
9	9
10	10
11	11
12	12
13	13
14	14
15	15
16	16
17	17
18	18
19	19
20	20
21	21
22	22
23	23
24	24
25	25
26	26
27	27
28	28
29	29
30	30
31	31
32	32
33	33
34	34
35	35
36	36
37	37
38	38
39	39
40	40
41	41
42	42
43	43
44	44
45	45
46	46
47	47
48	48
49	49
50	50
51	51
52	52
53	53
54	54
55	55
56	56
57	57
58	58
59	59
60	60
61	61
62	62
63	63
64	64
65	65
66	66
67	67
68	68
69	69
70	70
71	71
72	72
73	73
74	74
75	75
76	76
77	77
78	78
79	79
80	80
81	81
82	82
83	83
84	84
85	85
86	86
87	87
88	88
89	89
90	90
91	91
92	92
93	93
94	94
95	95
96	96
97	97
98	98
99	99
100	100

TOTAL:

Number of Manuscripts:

Books

<u>Received</u>	<u>Paper</u>
-----------------	--------------

TOTAL:

Patents Submitted

A High Stiffness, High Damping Composite Material

Patents Awarded

Awards

Graduate Students

<u>NAME</u>	<u>PERCENT SUPPORTED</u>	Discipline
Mr. Gene Cha	1.00	
FTE Equivalent:	1.00	
Total Number:	1	

Names of Post Doctorates

<u>NAME</u>	<u>PERCENT SUPPORTED</u>
FTE Equivalent:	
Total Number:	

Names of Faculty Supported

<u>NAME</u>	<u>PERCENT SUPPORTED</u>	National Academy Member
Terry S. Creasy	0.02	No
FTE Equivalent:	0.02	
Total Number:	1	

Names of Under Graduate students supported

<u>NAME</u>	<u>PERCENT SUPPORTED</u>
FTE Equivalent:	
Total Number:	

Student Metrics

This section only applies to graduating undergraduates supported by this agreement in this reporting period

The number of undergraduates funded by this agreement who graduated during this period: 0.00

The number of undergraduates funded by this agreement who graduated during this period with a degree in science, mathematics, engineering, or technology fields:..... 0.00

The number of undergraduates funded by your agreement who graduated during this period and will continue to pursue a graduate or Ph.D. degree in science, mathematics, engineering, or technology fields:..... 0.00

Number of graduating undergraduates who achieved a 3.5 GPA to 4.0 (4.0 max scale): 0.00

Number of graduating undergraduates funded by a DoD funded Center of Excellence grant for Education, Research and Engineering:..... 0.00

The number of undergraduates funded by your agreement who graduated during this period and intend to work for the Department of Defense 0.00

The number of undergraduates funded by your agreement who graduated during this period and will receive scholarships or fellowships for further studies in science, mathematics, engineering or technology fields: 0.00

Names of Personnel receiving masters degrees

NAME

Total Number:

Names of personnel receiving PHDs

NAME

Total Number:

Names of other research staff

NAME

PERCENT SUPPORTED

FTE Equivalent:

Total Number:

Sub Contractors (DD882)

1 a. The Aerospace Corporation

1 b. 2310 E. El Segundo Blvd.

El Segundo

CA

90245-4691

Sub Contractor Numbers (c):

Patent Clause Number (d-1):

Patent Date (d-2):

Work Description (e): Basic research, positive/negative stiffness materials

Sub Contract Award Date (f-1): 11/1/2010 12:00:00AM

Sub Contract Est Completion Date(f-2): 6/30/2012 12:00:00AM

Inventions (DD882)

Scientific Progress

The AERO team made a breakthrough in applying the negative spring by stabilizing the spring within a positive stiffness composite structure. Figure 1 shows one application concept: a composite structure that stabilizes the clover dome's negative stiffness régime with damping integrated into the mobile interface between positive and negative springs. Further, a design from AERO, the WTG fluidic damping element, showed adaptive response when filled with shear thickening fluids.

Technology Transfer

**FFATA: MACHINE AUGMENTED COMPOSITES FOR STRUCTURES WITH HIGH DAMPING WITH
HIGH STIFFNESS**

Grant Number W911NF-11-1-0004

Final Progress Report

Due Date: 30 September 2012

Delivery Date: 1 October 2012

PERIOD OF PERFORMANCE: 1 NOVEMBER 2010 TO 30 JUNE 2012

SUBMITTED TO

Dr. Aaron Lazarus, (Aaron.Lazarus@darpa.mil)

DARPA

Dr. David Stepp, (david.m.stepp@us.army.mil)

US Army Engineer Research and Development Center

AUTHORS

Terry S. Creasy, Gary Hawkins, Ching-Yao (Tony) Tang, Brian W. Gore, Juliet N. Schurr, Aaron L. Cheung, Gene Cha

Contents

EXECUTIVE SUMMARY	1
INTRODUCTION.....	3
TASK 1 DEVELOP LIBRARY OF CONSTITUENTS / PROOF OF CONCEPT.....	3
TASK 1-1 NEGATIVE STIFFNESS MATERIAL (AERO)	3
<i>NEGATIVE-STIFFNESS ELEMENT (CLOVER DOMES)</i>	3
Mechanical Response of Clover Domes (Experimental).....	4
Bi-stable Assembly with Clover Domes	7
<i>PARAMETRIC STUDY AND DESIGN OF CLOVER DOMES</i>	9
Varying Web Thickness.....	12
Varying Number of Stress Cutouts	13
Varying the Outer Stress Cutout Angle (SCA)	15
Varying Height Angle (HA)	16
Improved Designs of Clover Domes	17
Comparing the Improved Models	20
Influence of Material	21
Influence of Support Base Inner Diameter (Size of Opening).....	22
<i>DESIGN AND FABRICATION OF CLOVER DOMES</i>	22
Improved Clover Dome Designs	22
Fabrication of Original Clover Domes.....	23
TASK 1-2 DAMPING ELEMENT (TEES)	27
<i>Design and Analyze Damping Element</i>	27
Physical experiment with the damping material.....	28
LHG machine compressive cyclic test.....	38
Element 1 – Simple Fluid	49
Element 2—Shear Thinning Fluid Computational research of HG with shear thinning fluids	59
Element 3 – Shear Thickening Fluid.....	69
<i>Combine Two Elements</i>	70
Stacked panel performance	72
<i>Size Reduction</i>	74
<i>Design and Analyze Damping Element</i>	76
Shape studies	84
Stiffness Study	89
Reducing spring constant in TEES damping panels	92
Effect of new reservoir method	97
Alternate fabrication with tubes and plates.....	98
Reducing spring constant in TEES damping panels	100
Computational analysis for design and evaluate Machine augmented composite materials	106
<i>Modeling of Hourglass Damping Elements with Fluid-Solid Interactions</i>	111
Software Implementation	111
Improving Modeling Implementation	114
Validation with Existing Experimental Data	116
Geometric studies	117
WTG Simulations	121
Shear-Thinning Fluid.....	122
Shear Thickening	123
Modeling Conclusions and Future Work	125

TASK 2 INTEGRATION	126
TASK 2-1 MODELING (AERO).....	126
<i>System Stability Analyses (LMS DADS).....</i>	<i>126</i>
<i>An Unstable System Displaying High Stiffness and High Damping</i>	<i>127</i>
<i>A Stable System Displaying Low Stiffness and High Damping</i>	<i>129</i>
<i>Increased Damping Due to Presence of a Negative Spring</i>	<i>130</i>
<i>A Stable System Displaying High Stiffness and High Damping</i>	<i>131</i>
<i>Verification Of Motion Amplification (Proving The Concept Of Combining Positive And Negative Springs)</i>	<i>133</i>
<i>Assembly Fabrication And Component Response Characterization.....</i>	<i>137</i>
Concept for a Material System Displaying High Stiffness and High Damping.....	137
Constitutive Properties and Mechanical Advantage of 5-Degree Composite Beams.....	139
ASSEMBLY MODELING	140
Multi-body Dynamics Modeling (Updated Results).....	140
Correlating Damping Coefficient and $\tan \delta$	141
Multi-Body Dynamics Analysis (10x Motion Amplification)	142
Parametric Study via Modeling.....	143
Influence of $k_{eff}/k_{lateral}$ on System Performance.....	145
EXPERIMENTS AND PERFORMANCE CHARACTERIZATION OF INTEGRATED MATERIAL SYSTEM.....	146
Integrated Material System (5-Degree Composite Beam)	146
Integrated Material System with Die Spring (5-Degree Composite Beam)	147
Integrated Material System with Butyl Rubber (5-Degree Composite Beam)	148
Integrated Material System with Silicone O-Rings (5-Degree Composite Beam)	149
Integrated Material System with Silicone Rubber (5-Degree Composite Beam)	150
Integrated Material System with Die Spring (2-Degree Composite Beam)	151
Integrated Material System with Silicone Rubber (2-Degree Composite Beam)	154
Impact Testing of High Stiffness, High Damping Material	154
Fatigue Testing of High Stiffness, High Damping Material.....	155
Best Performance To-Date of a High Stiffness, High Damping Material	155
APPLICATIONS	156
Conventional Structures.....	156
Structural Skin or Shell (Applied Bending).....	157
Material System as Stiffening Ribs	158
Material System as Struts.....	160
Material System as Building Structural Systems	160
CONCLUSIONS.....	162
APPENDIX	163
PARAMETER VALUES FOR EACH VARIATION MODEL	163
FINITE-ELEMENT MODEL (ABAQUS)	164
MESH REFINEMENT AND UTILIZING A HALF MODEL	165

EXECUTIVE SUMMARY

The Material Logic program aims to create novel materials that exhibit high stiffness and high damping. The joint effort by Texas A&M University (Texas Engineering Experiment Station or TEES) and The Aerospace Corporation (AERO) seeks to develop a new class of composite material by exploiting the unique properties when negative-stiffness, positive-stiffness, and damping elements combine to form a novel material system. Overall success is defined as developing a composite material system that can achieve a damping coefficient of 1.0 with an elastic modulus of 100 GPa. The material system should also be optimized for impulses of 0.01 s of duration and cyclic loadings in the 0.1 to 10 Hz regime and be adaptable to a wide range of loads.

The AERO team made a breakthrough in applying the negative spring by stabilizing the spring within a positive stiffness composite structure. Figure 1 shows one application concept: a composite structure that stabilizes the negative stiffness régime of the clove dome with damping integrated into the mobile interface between positive and negative springs.

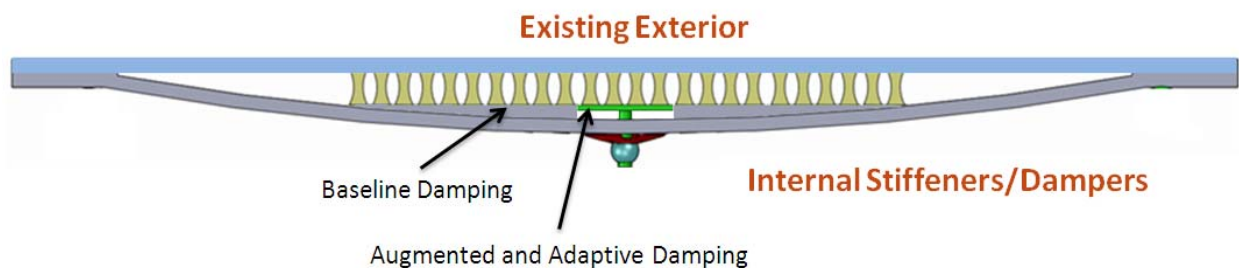


Figure 1. The negative spring element—a clove dome device—is stabilized in the structure build from positive stiffness material.

Further, a design from AERO, the WTG fluidic damping element, showed adaptive response when filled with shear thickening fluids. Figure 2 shows the 64 mm tall model structure and Figure 3 shows the nearly consistent response of this element to driving frequencies from 0.1 to 10 Hz.

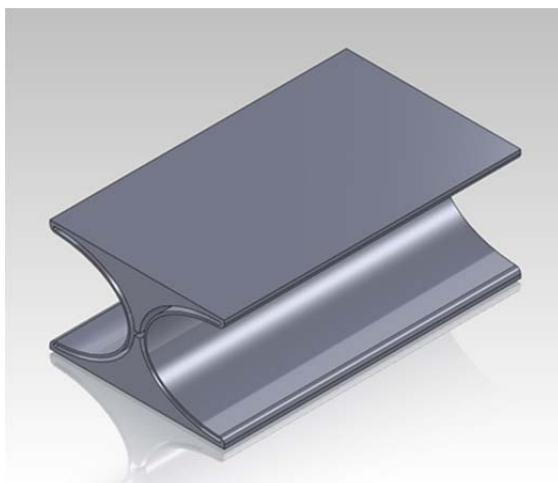


Figure 2. The WTG element pumped fluids with a low-stiffness structure that contained shear thickening fluids for adaptive response.

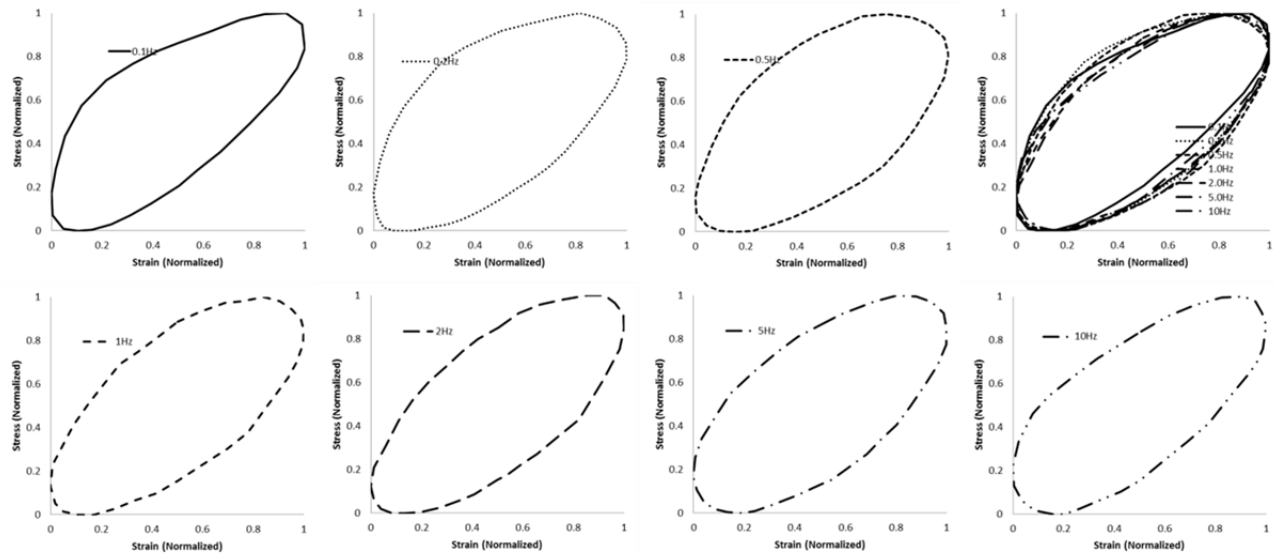


Figure 3. Loop plots for $\frac{1}{2}$ C/T test of 64mm tall WTG with the shear thickening fluid show that response adapts to the range of input frequencies by adjusting the viscosity of the damping fluid passively.

INTRODUCTION

The Material Logic program aims to create a novel material that exhibits both high stiffness and high damping. The joint effort by Texas A&M University (Texas Engineering Experiment Station) and The Aerospace Corporation seeks to develop a new class of composite material that can adapt to varying environmental and tactical loads while simultaneously exhibit high stiffness and high damping. The concept involves exploiting the unique properties when negative-stiffness, positive-stiffness, and damping elements are combined to form a novel material system.

The overall success is defined as developing a composite material system that can achieve a damping coefficient of 1.0 with an elastic modulus of 100 GPa. The material system should also be optimized for impulses of 0.01 s of duration and cyclic loadings in the 0.1 to 10 Hz regime and be adaptable to a wide range of loads.

The approach to the project is to complete modeling and analysis at the component level and system level separately, and then bringing everything together. This is a highly iterative process because information is needed at the component level to serve as input to predict performance at the system level, and requirements at the system level are needed to design improved components.

In the first 8 months of this program, a great deal of modeling and experiments were conducted to understand the negative-stiffness element, specifically Clover Domes. In addition, computational multi-body dynamics was utilized to predict overall system (combination of negative spring, positive spring, and dashpot) response. This section of the report focuses on the characterization and design of Clover Domes (negative-stiffness element), system stability analyses, and a design of a high stiffness, high damping material through modeling.

Task 1 Develop Library of Constituents / Proof of Concept

Task 1-1 Negative Stiffness Material (AERO)

NEGATIVE-STIFFNESS ELEMENT (CLOVER DOMES)

One significant challenge for our concept in the Material Logic program is the incorporation of a negative stiffness constituent into the material design. Clover Domes, which are similar to Belleville washers, were chosen as the negative stiffness constituent in the overall design. Clover Domes exhibit the negative stiffness property in a limited range of its deflection when compressed. The main goal was to improve the designs for the Clover Dome that would increase negative stiffness and negative-stiffness range. Because of the high cost of fabricating and testing Clover Domes of various sizes and geometries, the designs were conducted using finite element analysis (FEA) with ABAQUS. The original CAD model of a Clover Dome was obtained from the manufacturer (Associated Spring, Maumee, OH) and the design changes were made to the model in Solidworks before they were imported into ABAQUS. The force-versus-displacement profiles, which show the stiffness and negative-stiffness range, were determined for each Clover Dome variation in ABAQUS.

After completing the parametric study, the desired characteristics were incorporated into improved Clover Dome models. These new models were created in Solidworks and then analyzed in FEA to verify results. Out of all the various models created and analyzed, only a few were chosen to be fabricated and tested in the lab.

Several Clover Domes (Figure 4) were procured from Associated Spring to obtain the baseline response, and to assist in the validation the FEA model. These springs come in various diameters and thicknesses, which dictate the effective stiffness of the springs. The Clover Domes are mono-stable, meaning once they are compressed through center, the springs snap back to their original position instead of popping through. The advantage of the mono-stable Clover Dome is that the negative-stiffness property can be realized with purely a compressive force.



Figure 4. An example of a material that exhibits negative stiffness (Clover Domes).

Mechanical Response of Clover Domes (Experimental)

The test fixture shown in Figure 5 was fabricated to allow testing of Clover Domes in an Instron material testing system. The machine drawing of the fixture is provided in Figure 6. The Clover Dome sits inside the pocket while being loaded in compression from above via a silicon-nitride ball attached to the crosshead of the test frame. A 1/2"-diameter silicon-nitride ball, which is much stiffer than the stainless steel Clover Dome, makes contact with and compress the Clover Dome in the center until the Clover Dome has gone beyond its flat position. As the Clover Dome is compressed, it naturally wants to expand radially. When compressed beyond a critical strain, the Clover Domes display unique load-deflection properties, as shown in Figure 7. The negative-stiffness regime is the region of interest because this portion of the Clover Dome serves as the negative spring in our concept. The test was stopped once the load limit was reached for the test system, generally beyond the useful negative-stiffness regime of the Clover Domes.



Figure 5. Test fixture with a Clover Dome.

The Clover Domes can be stacked in series, parallel, or a combination of both. In parallel stacking, the Clover Domes are stacked in the same orientation, and for series stacking, the Clover Domes are oriented in opposite directions (Figure 8).

Mechanical testing was completed for several configurations, which are shown in Figure 9 : 1) a single Clover Dome, 2) two Clover Domes in parallel, 3) three Clover Domes in parallel, 4) three Clover Domes in series, 5) four Clover Domes stacked down-down-up-down, 6) four Clover Domes stacked down-up-up-down, and 7) four Clover Domes stacked down-up-down-down. A preload of 10 N was initially applied, and the Clover Dome was compressed using a displacement rate of 1 mm/min. Three tests were performed for each arrangement, and the results, though not all shown in Figure 9 , were repeatable.

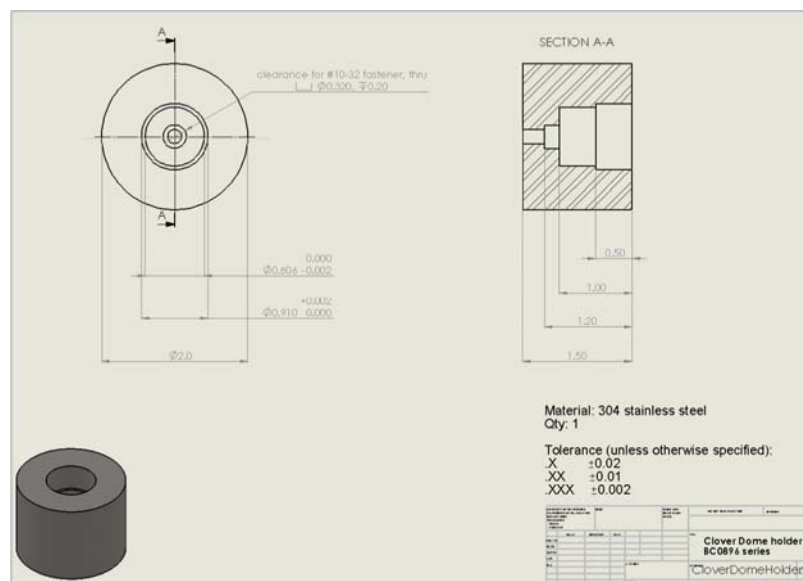


Figure 6. Machine drawing for a Clover Dome holder.

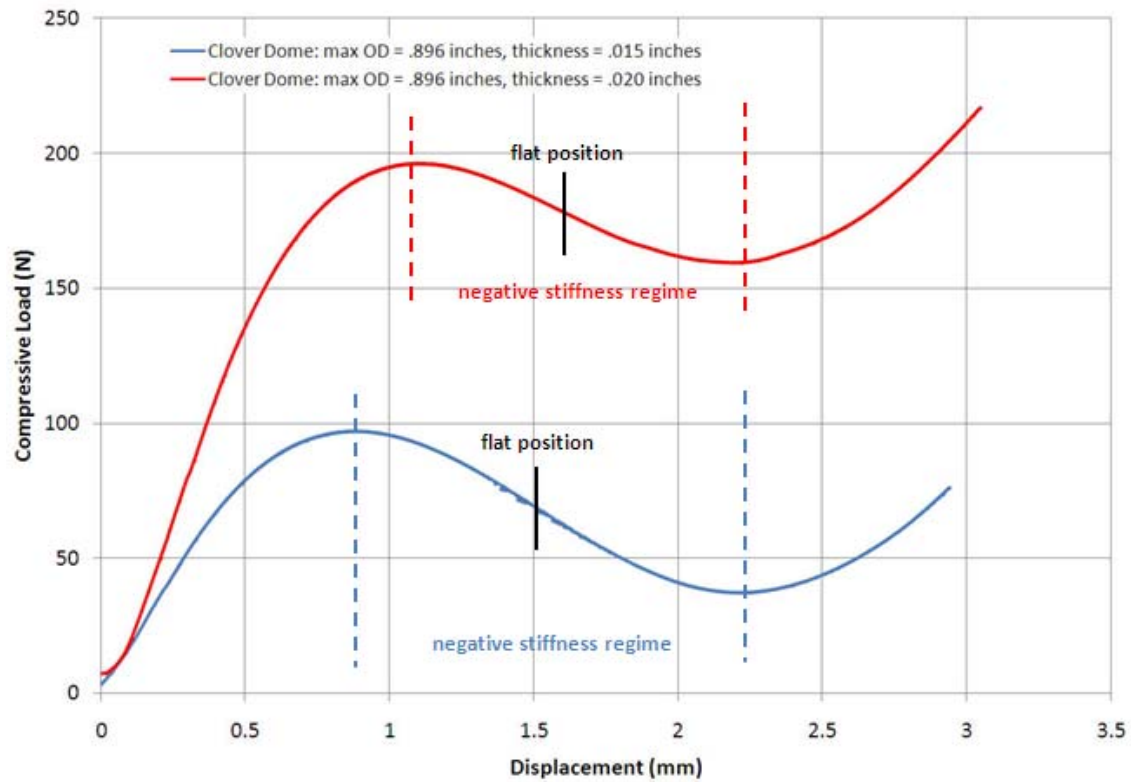


Figure 7. Experimental data showing typical behavior of Clover Domes under compression.



Figure 8. Parallel stacking (left) and series stacking (right) of Clover Domes. Images obtained from Associated Spring (<http://www.asbg.com/en/spring-washers/disc-springs/technical-data>).

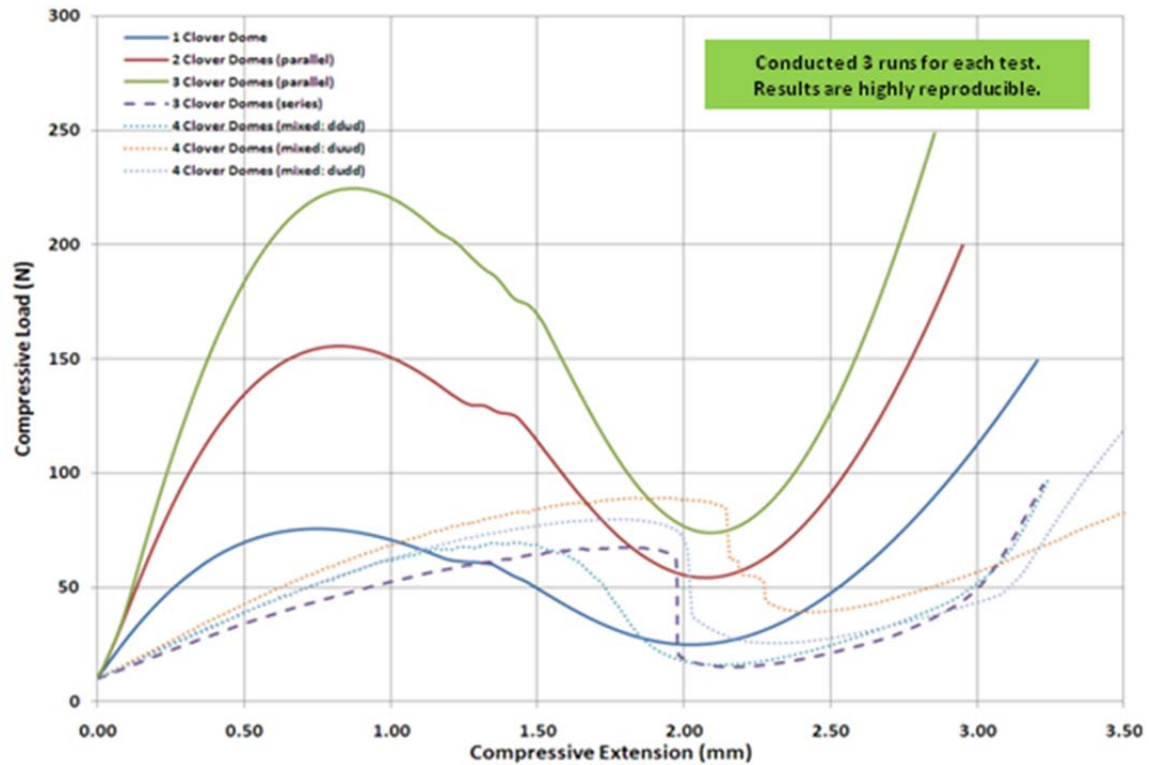


Figure 9. Load-displacement response of various Clover Dome arrangements.

Parallel stacking of the Clover Domes exhibited response that was expected – the greater the number of Clover Domes, the stiffer the material becomes (in positive and negative regions). Theoretically, the increase in stiffness (or the maximum load achieved before entering negative-stiffness regime) should be linear. Due to minor differences in each Clover Dome from manufacturing, the measured response was not exactly linear. With parallel stacking, any magnitude of negative stiffness can be achieved.

Series stacking and mixed stacking of more than 3 Clover Domes showed behavior where one of the Clover Domes (weakest one) took up the entire load. Any misalignment in the set-up would also cause this to occur. If the test was allowed to continue for the arrangements with 4 Clover Domes, one will see a second negative-stiffness response at a much higher load when the other Clover Domes finally react to the applied load.

Bi-stable Assembly with Clover Domes

An individual Clover Dome is mono-stable, i.e., the Clover Dome would want to revert to its initial state when compressed. An assembly technique was discovered that allows the Clover Domes to be bi-stable, i.e., the Clover Dome would want to snap through under compression beyond a certain applied strain.

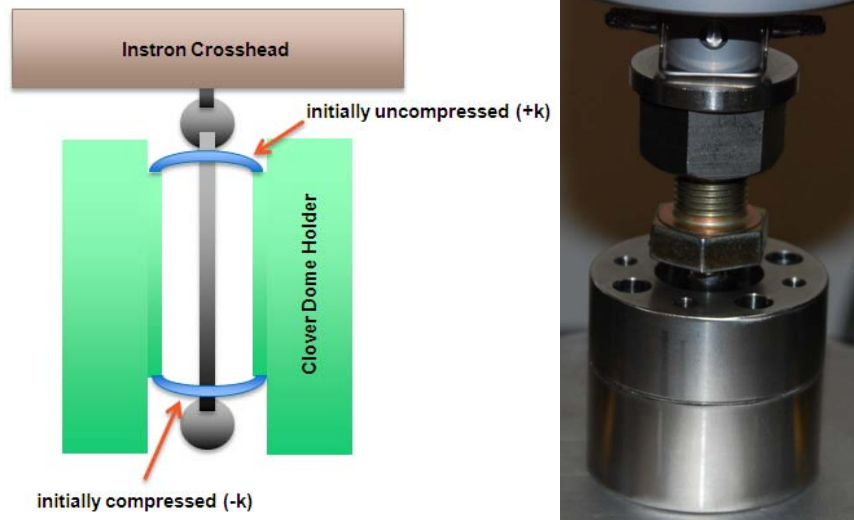


Figure 10. Sketch of a bi-stable assembly (left) and the assembly under an Instron (right).

Figure 10 shows the configuration of a bi-stable assembly. The two Clover Domes resting on opposite ends of a hollow cylinder were attached in series using a threaded rod and ball assembly. The balls were tapped so that they compressed the Clover Domes when tightened. The Clover Dome on top was initially uncompressed, and the Clover Dome at the bottom was initially compressed. Because the bottom Clover Dome was under compression, it wants to revert to its original uncompressed state. The spring-back force was counteracted by the stiffness of the Clover Dome on top (positive spring).

When the top ball was compressed, the load increased, then decreased in the negative-stiffness regime, and snap-through occurred. After snap through, the Instron sensed tensile load because of the presence of another stable position. Figure 11 shows the load-displacement response for bi-stable assembly consisting of Clover Domes in three different arrangements: a) 1 top Clover Dome and 1 bottom Clover Dome, b) 2 top Clover Domes and 1 bottom Clover Dome, and c) 1 top Clover Dome and 2 bottom Clover Domes.

For the “1 Top 1 Bottom” arrangement, the load-displacement profile is symmetric about the snap-through location (shown by a sudden dip in load when the compressive load is nearly zero in the negative-stiffness regions). The effect of adding an additional Clover Dome on the top or the bottom shifts the snap-through position from the midpoint of the curve to the left (displacement ≈ 0.7 mm) or the right (displacement ≈ 1.8 mm), respectively. In addition, the magnitude of the positive-stiffness region was greater for the “2 Top 1 Bottom” configuration than the “1 Top 2 Bottom” case.

This assembly demonstrates flexibility in the response of the negative-stiffness element, which could prove beneficial during the integration portion of this program.

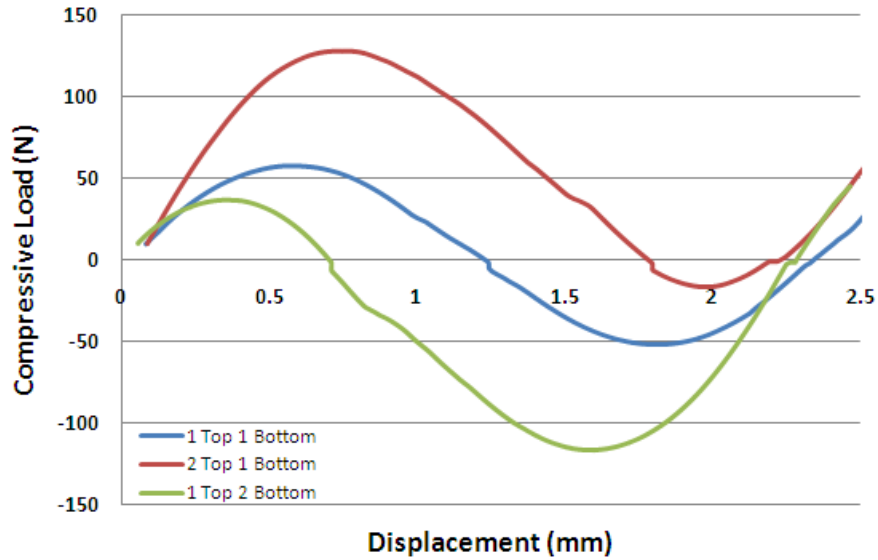


Figure 11. Load-displacement responses of different bi-stable assembly configurations.

PARAMETRIC STUDY AND DESIGN OF CLOVER DOMES

Using the BC0896015S series Clover Dome from Associated Spring as the base model, various changes were made to the geometry of the Clover Dome with the goal of increasing the overall stiffness and, more importantly, extend the negative-stiffness range of the Clover Dome. The base model Clover Dome is made out of 17-7-PH stainless steel and has an outer diameter of 0.896 inches and a thickness of 0.015 inches. Because different outer diameters and thicknesses can be obtained through the manufacturer and physically tested, changes in these two parameters were not considered in the design. Parameters that were altered in the CAD model are identified as the following: height angle (HA), inner circle radius (ICR), center circle radius (CCR), center circle angle (CCA), and stress cutout angle (SCA). The diagram of these parameters can be seen in Figure 12 and Figure 13. For the parametric study these parameters will be adjusted and their effect on the overall stiffness and negative-stiffness range was analyzed. Detailed information regarding the values of the parameters can be found in Appendix 6.1.

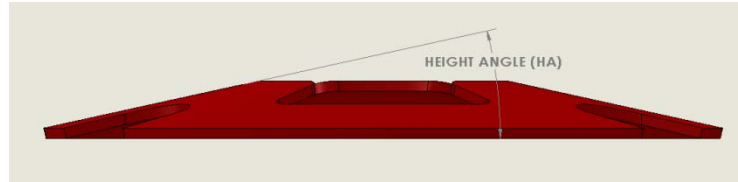


Figure 12. Side view of a Clover Dome.

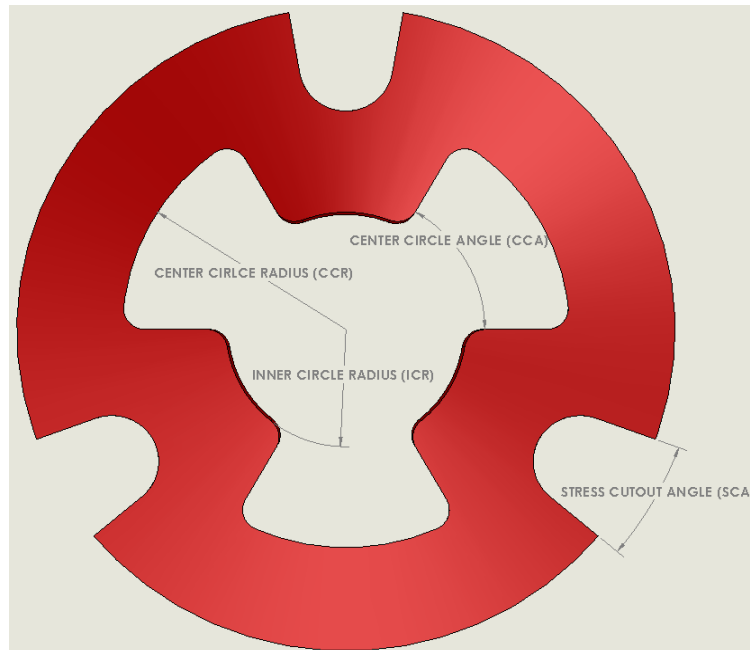


Figure 13. Top view of a Clover Dome.

After creating the variation models in Solidworks, the Clover Domes were imported in ABAQUS for FEA. The analysis consisted of placing the clover on top of a circular base and then compressing the clover with a sphere at the center (Figure 14). The force applied on the base as well as the displacement of the top of Clover Dome plotted to determine its stiffness profile over the range of the applied displacement. More information about the ABAQUS model can be found in Appendix 6.2 and 6.3.

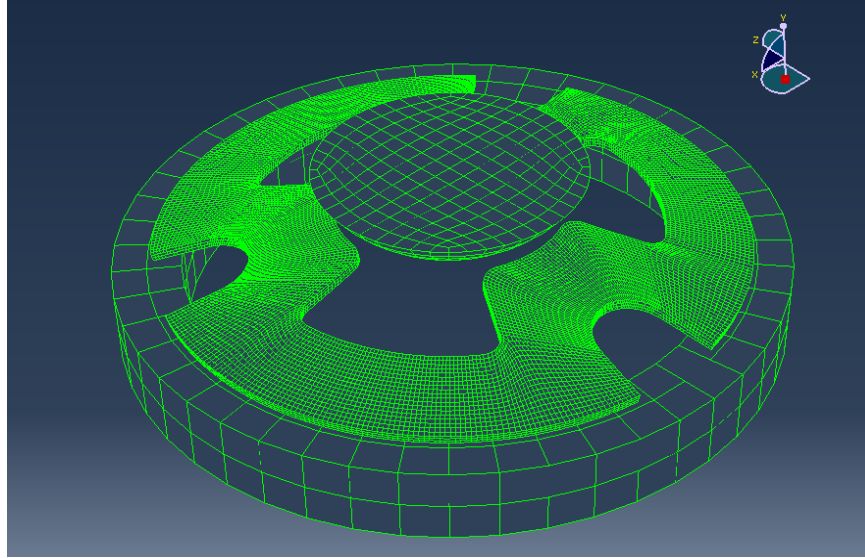


Figure 14. ABAQUS model for characterizing Clover Dome behavior.

The compression test of the original model generated a load versus displacement profile as seen in Figure 15. The displacement value corresponds to the displacement (in the negative y-direction) of the sphere upon making contact with the Clover Dome, and the load corresponds to the resulting force on the Clover Dome. The positive-stiffness region is represented by the positive slope of the curve and the negative-stiffness region is represented by the negative slope region of the curve. From Hooke's Law (Eq. 1), the slope of the load (F) – deflection (x) curve represents the stiffness (spring constant = k) of the Clover Dome.

$$F = kx \quad (1)$$

As seen in the Figure 15, the Clover Dome exhibited negative stiffness only in a small range of about 0.8 mm from a deflection of 0.9 mm to 1.7mm. The linear positively-sloped section after 1.7 mm of deflection represents when the Clover Dome had fully flipped over and was simply acting like a normal positively-stiff material.

In terms of the stiffness curve, the desired profile would have a wider deflection range of negative stiffness and a steeper negative-stiffness slope.

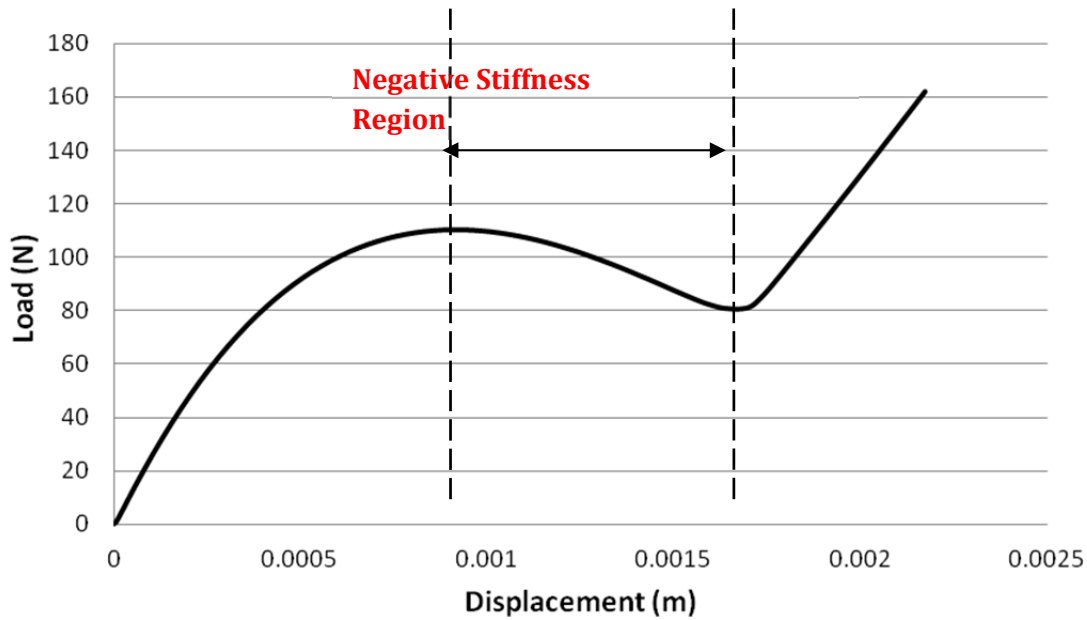


Figure 15. Stiffness profile of an original Clover Dome (BC0896015S series).

Varying Web Thickness

In the first set of variations, three different parameters of the Clover Dome were grouped together to form the web thickness parameter. The web thickness was identified by finding the difference in the outer circle radius (OCR) and the center circle radius (CCR). This value became the reference length for the space between the inner circle radius (ICR) and the outer stress cutouts (SCA) as well as the width between the center circle angle (CCA) and the outer stress cutouts. The web thickness was altered by percentages ranging from 50 percent to 120 percent of the original (Table 1). Figure 16 provides a few models of the Clover Domes with different web thicknesses.

Table 1. Web thickness values by percentage of original.

	Web Thickness (in.)
Original	0.144
50% Original Thickness	0.072
80% Original Thickness	0.115
90% Original Thickness	0.130
110% Original Thickness	0.158
120% Original Thickness	0.173

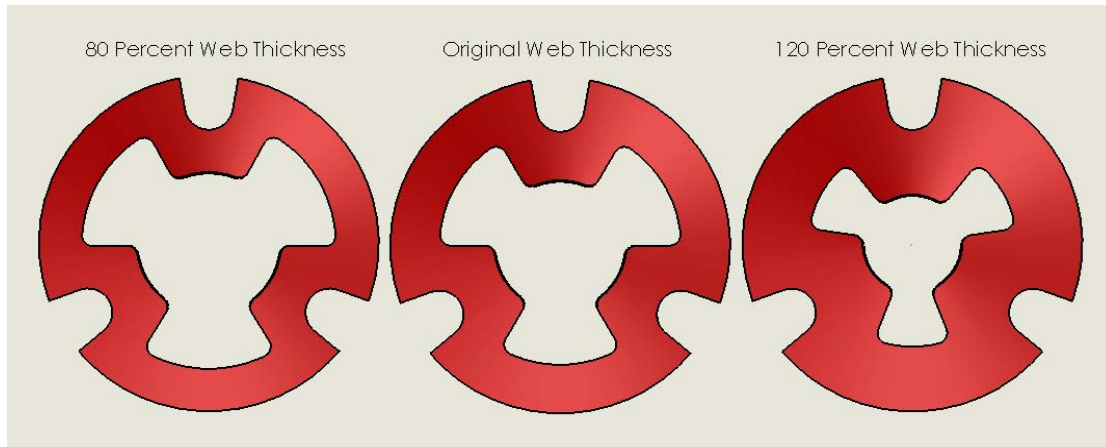


Figure 16. Clover Dome models with various web thicknesses.

As the web thicknesses increases, it is clear that the stiffness of the Clover Dome would increase because more material is added to the Clover Dome. Based on the results shown in Figure 17, the extra material increases the overall stiffness of the Clover Dome. Thus, for the optimized Clover Domes, a larger web thickness would be preferred.

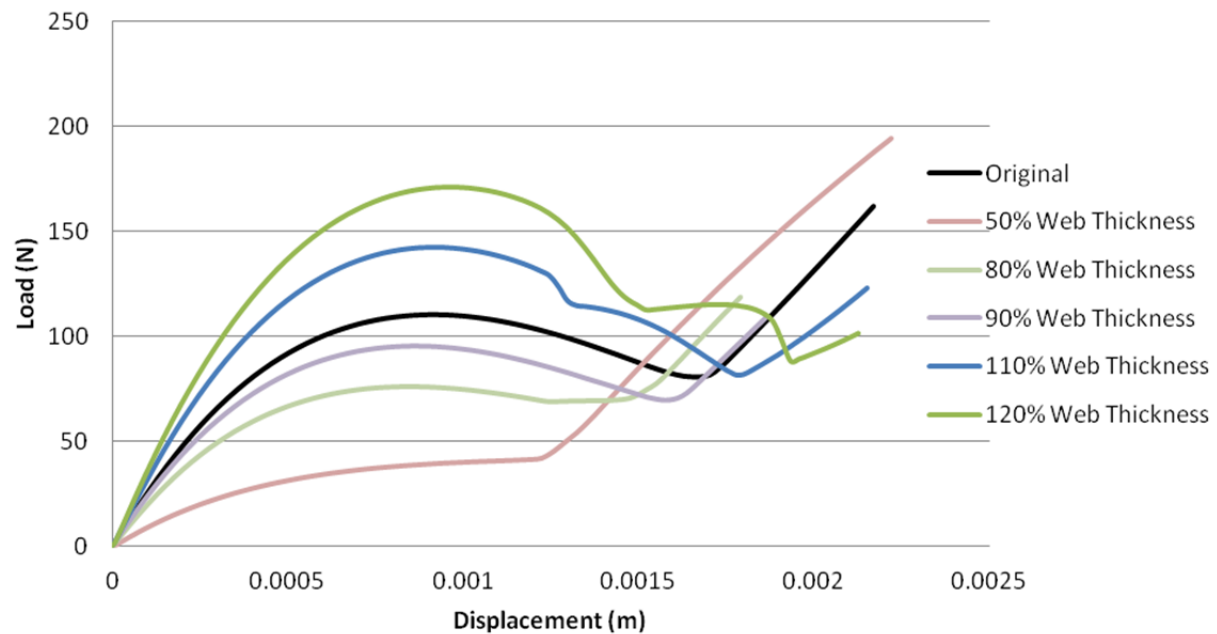


Figure 17. Clover Dome stiffness profile with different web thicknesses.

Varying Number of Stress Cutouts

The second set of changes came from adding the number of inner and outer stress cutouts. The additional cutouts were placed equally around the circumference of the Clover Dome, i.e., the 3 cutouts had 120-degree span between them, the 4 cutouts had 90-degree span between them, etc. (Figure 18). The ICAs were also changed to match the symmetry of the Clover Domes, but the SCAs were kept the same. A summary of these designs are presented in Table 2.

Table 2. Clover Dome specifications with various cutouts.

	Angle between cutouts (deg)	ICA (degrees)	SCA (deg)
Original (3 Cutouts)	120	60	20
4 Cutouts	90	45	20
5 Cutouts	72	36	20

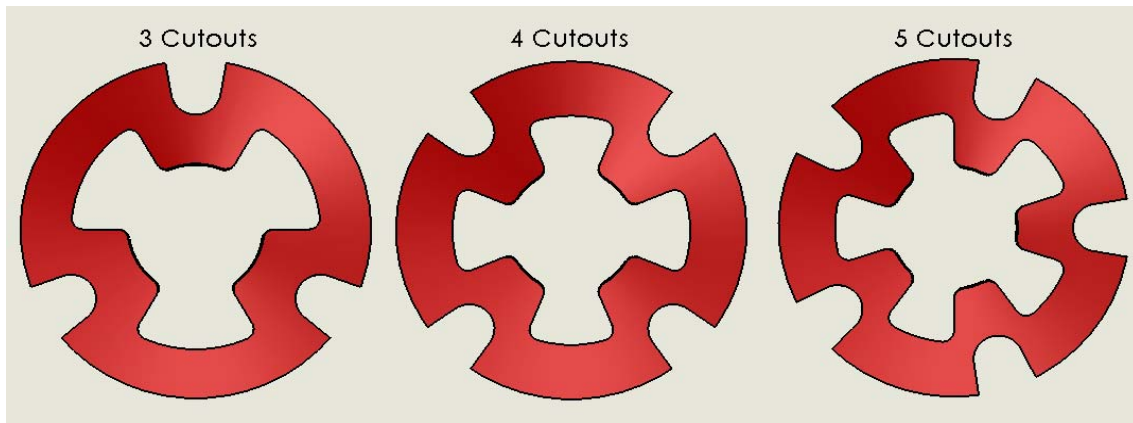


Figure 18. Clover Dome models with varying number of stress cutouts.

Figure 19 shows that the Clover Dome became less stiff with more cutouts. With 5 cutouts, the negative-stiffness region disappeared altogether. Therefore, it was concluded that the original number of cutouts was the optimal design.

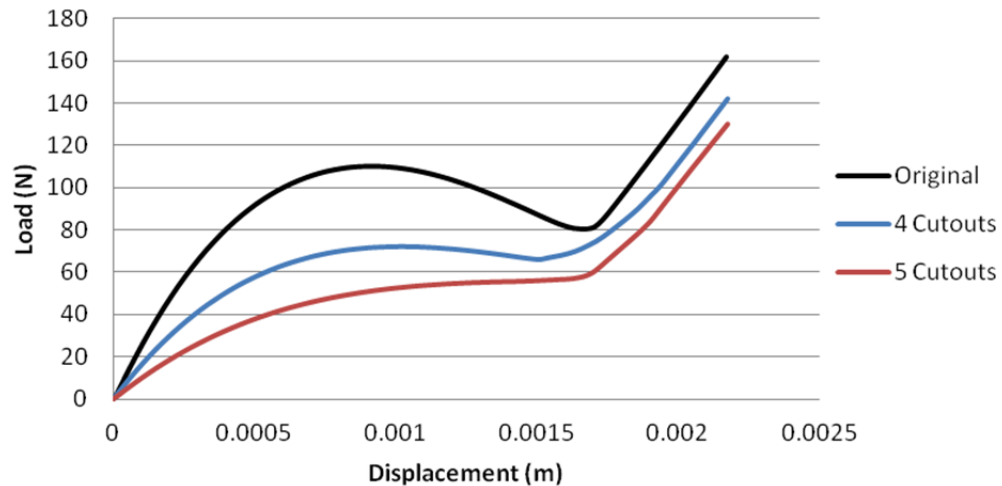


Figure 19. Clover Dome stiffness profile with different number of stress cutouts.

Varying the Outer Stress Cutout Angle (SCA)

The stress cutouts are designed to relieve high stress concentrations at the outer edge of the Clover Domes due to high deformations. Altering these cutouts may potentially significantly increase the stress on the edge of the Clover Dome.

The angle identifying the size of the cutouts (Figure 20) come from the angle that the two sides of the cutout make because those lines intersect at the center of the Clover Dome. The original cutout angle was 20 degrees and the two variations tested were 14 degrees and 26 degrees, as shown in Figure 21. The semi-circle radius was enlarged such that it was coincident with the two sides of the cutout. The center of the circle remained at the same location.

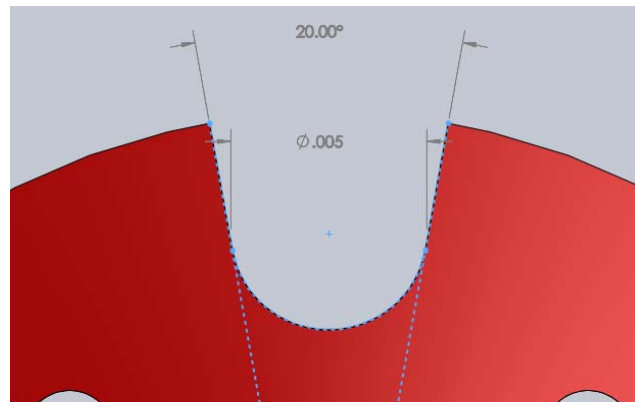


Figure 20. A schematic identifying the stress cutout angle (SCA).

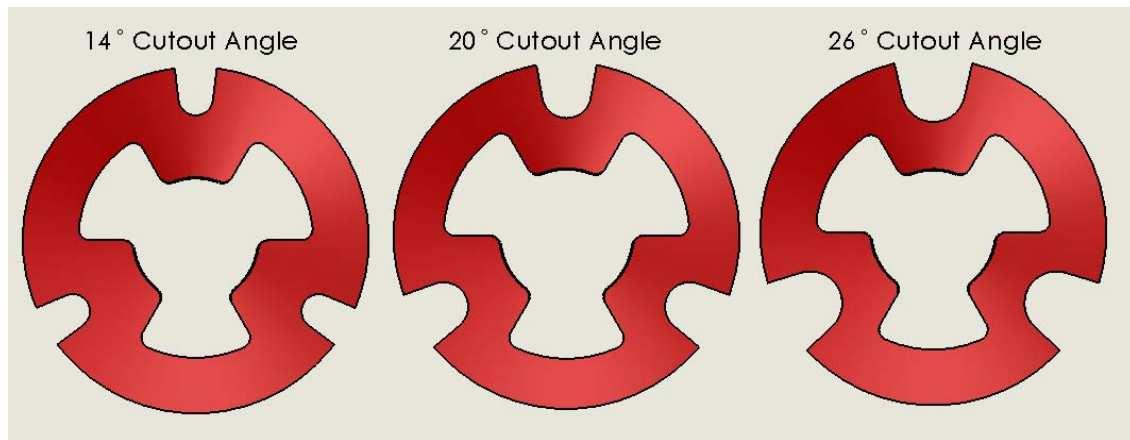


Figure 21. Clover Dome models with various stress cutout angles.

Shrinking the size of the stress cutouts did not extend the negative-stiffness range, but increased the stiffness of the Clover Dome slightly. In designing an optimized Clover Dome, the increase in stress must be considered. Decreasing the cutout angle from 20 degrees to 14 degrees increased the maximum stress by 12.5%, which is shown in Table 3.

Table 3. Clover Dome specifications with different stress cutout angles.

Stress Cutout Angle	SCA (degrees)	Maximum von Mises Stress
14 Degrees	14	4.083 GPa
Original 20 Degrees	20	3.632 GPa
26 Degrees	26	2.922 GPa

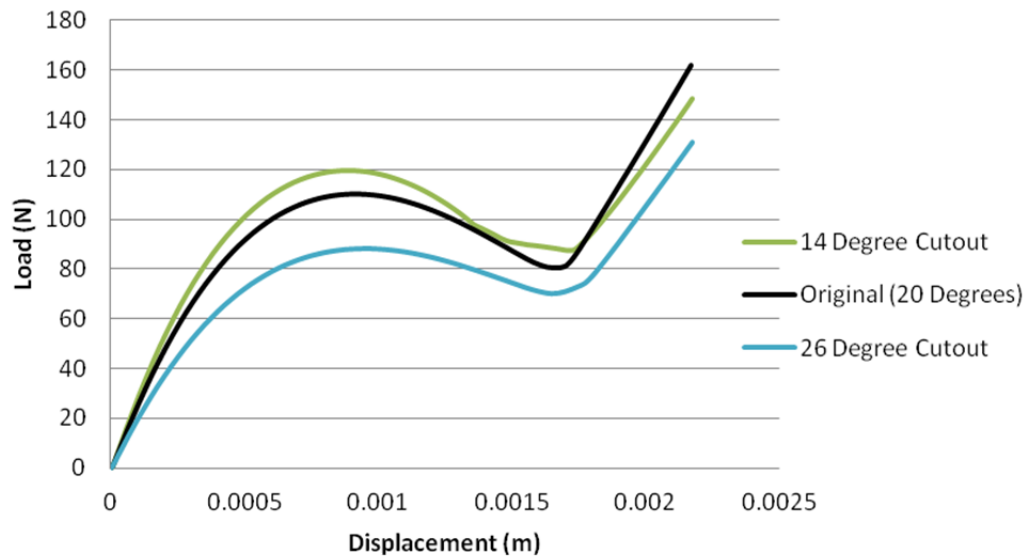


Figure 22. Clover Dome stiffness profile with different outer stress cutout angles.

Varying Height Angle (HA)

The last variation parameter analyzed was the height (or cone) angle (HA). The height angle is the angle that the sides make with the base of the Clover Dome. The original Clover Dome had a height of 13 degrees, and the angles used in the parametric study were 10, 16, and 20 degrees (Figure 23). The outer diameter was kept constant at 0.896 inches.



Figure 23. Side view of Clover Dome models with different height angles.

Since increasing the height angle increased the total deflection of the Clover Dome, a greater height angle was also expected to increase the negative-stiffness region of the Clover Domes. As seen in Figure 24, the key benefit to increasing the height angle was the expansion of the negative-stiffness region. So far, none of the other parameters gave such a distinct improvement in the negative-stiffness region.

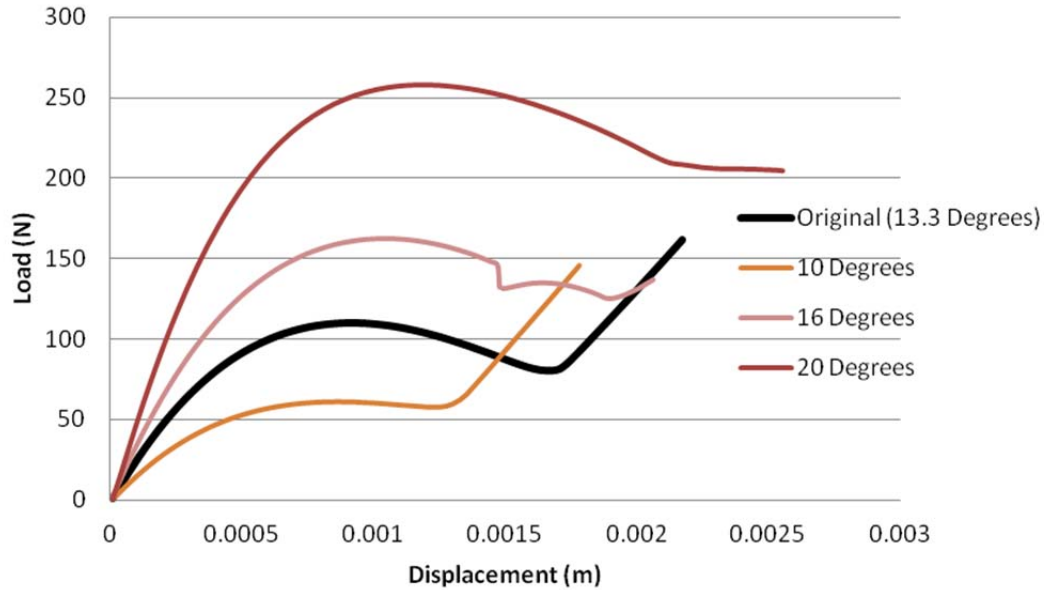


Figure 24. Clover Dome stiffness profile with different height angles.

Improved Designs of Clover Domes

The parametric study of the Clover Domes provided a clearer understanding of how each parameter altered the stiffness profile of the Clover Domes. The new knowledge was used to create improved models. As previously stated, the intention of the study was to create a Clover Dome that would maximize the negative-stiffness region and the overall stiffness. From the parametric study, it can be concluded that an improved model should possess smaller ICR, CCR, CCA and SCA, as well as a larger HA. Taking into account the material limitations of the Clover Domes, a few models were designed to determine the desirable combinations of parameters for the Clover Domes.

Model A

Model A was an attempt to maximize all the parameters regardless of the tolerance levels to see the limitations of the best possible model. The height angle was increased to 20 degrees to increase the negative-stiffness region while the other parameters were decreased to increase overall stiffness of the Clover Dome (Table 5).

Table 4. Model A specifications.

Parameter	Change from Original	Actual Value
HA	+7°	20°
CCA	-30°	30°
CCR	-20%	0.24323
SCA	-6°	14°
ICR	-20%	0.13065

Model A showed a tremendous increase of stiffness and negative-stiffness range in the analytical model. However, an area of concern is the fact that the maximum stress had increased to over 10 GPa and that the ABAQUS run did not run to completion. It is likely that Model A had exceeded the limits of the material and the Clover Dome might have plastically deformed.

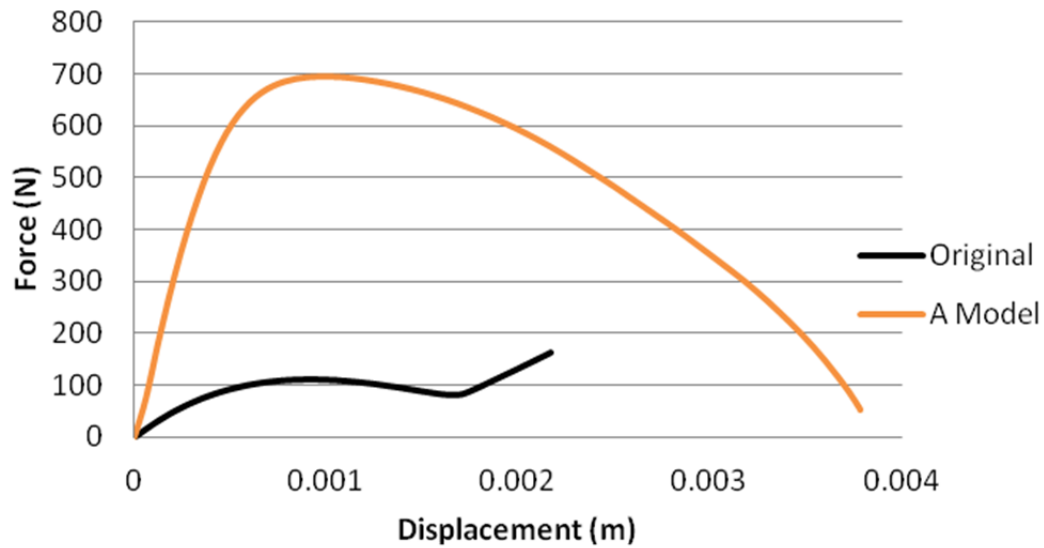


Figure 25. Model A stiffness profile and drawing.

Model B

Model B was similar to Model A except for the height angle. The height angle was reduced to 16 degrees (from 20 degrees), but was still higher than the original 13 degrees (Table 3.5). Unlike Model A, the ABAQUS run for Model B ran to completion. The negative-stiffness region had more than doubled the original Clover Dome's deflection in the negative-stiffness region.

Table 5. Model B specifications.

Parameter	Change from Original	Actual Value
HA	+3°	16°
CCA	-30°	30°
CCR	-20%	0.24323
SCA	-6°	14°
ICR	-20%	0.13065

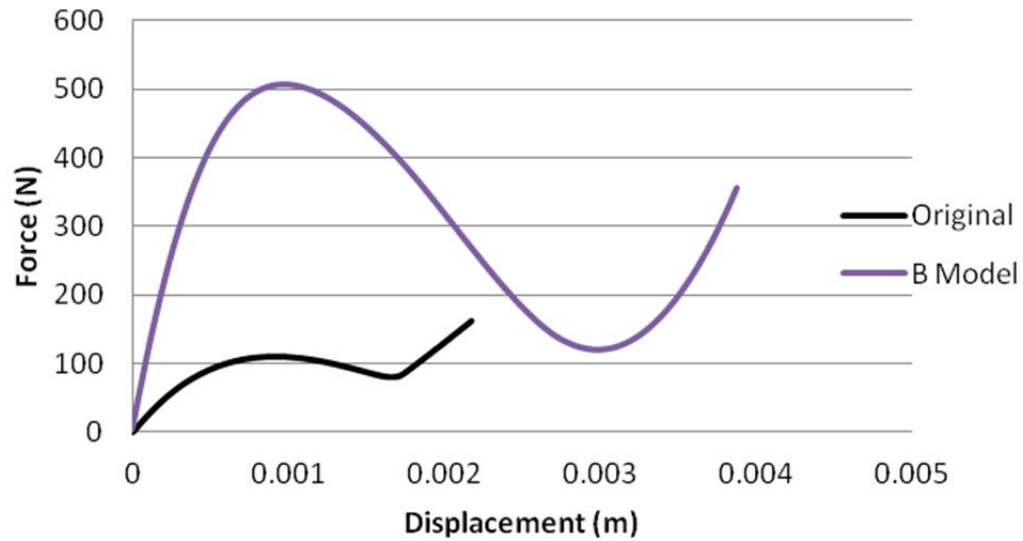


Figure 26. Model B stiffness profile and drawing.

Model C

Model C was similar to Model B, but with a smaller change in the center circle angle (CCA). The CCA for Model C was lowered to 45 degrees (Table 3.6). The load-displacement response of Model C was similar to that of Model B with a lower stiffness (Figure 27).

Table 6. Model C specifications.

Parameter	Change from Original	Actual Value
HA	+3°	16°
CCA	-15°	45°
CCR	-20%	0.24323
SCA	-6°	14°
ICR	-20%	0.13065

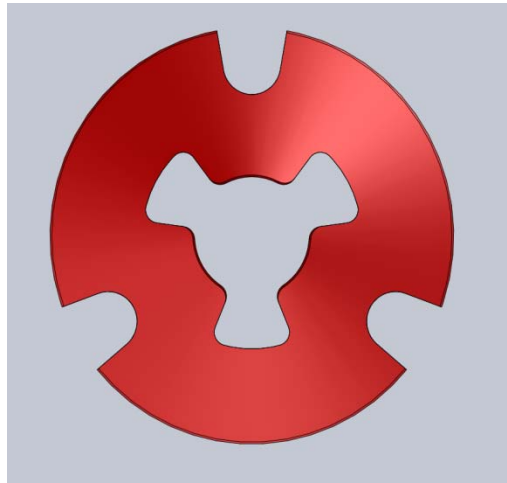
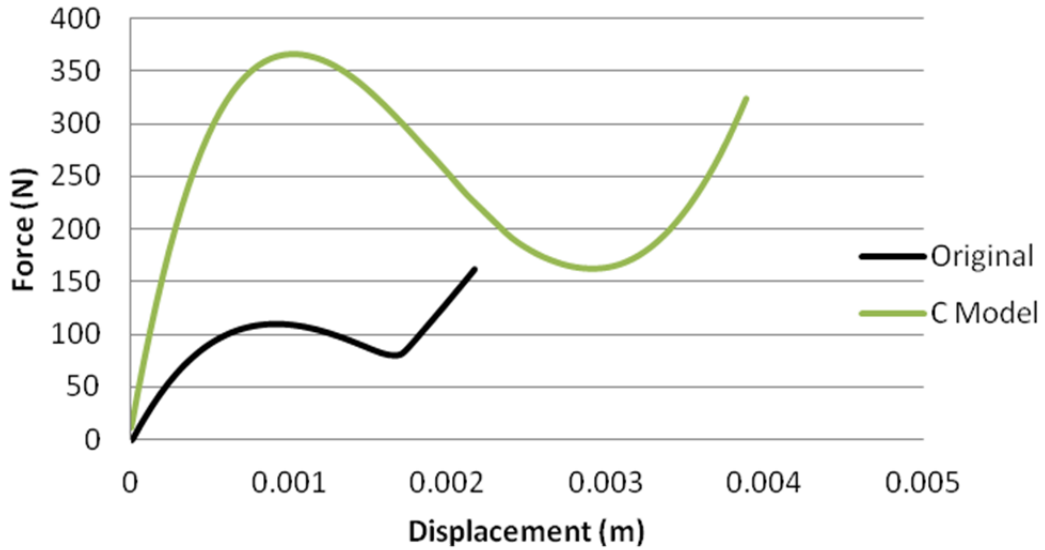


Figure 27. Model C stiffness profile and drawing.

Comparing the Improved Models

All the improved Clover Dome models exhibited a desired increase in stiffness and negative-stiffness range. Looking at Figure 28, the negative-stiffness range is expected to be the longest for Model A, and then B, and then C. The stiffness slope of Model A and B appeared to be similar, while Model C has a less steep curve. The next step of the program would be to build a few of the improved models to validate the computational results in this study. In addition, more analysis will be needed to determine whether these models exceed the material property limits.

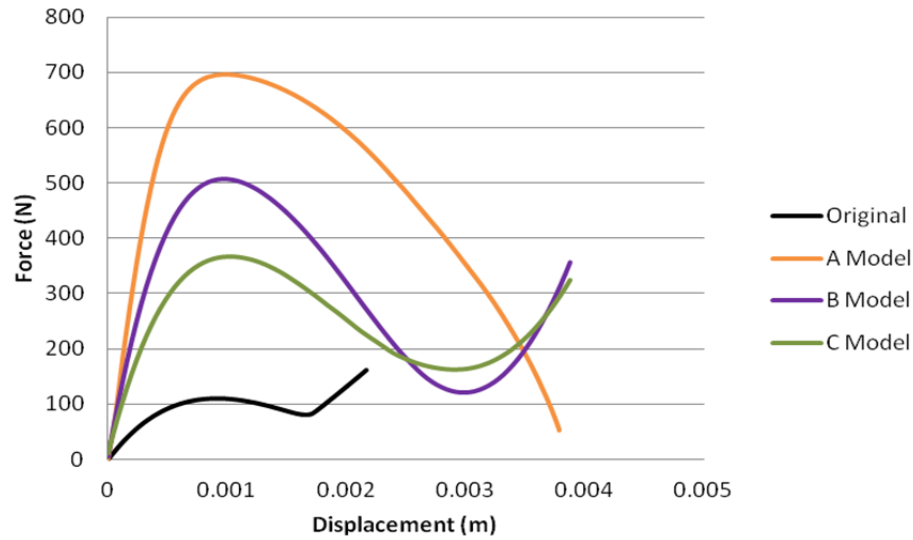


Figure 28. Stiffness profile of improved models (Models A, B, and C).

Influence of Material

The influence of material on the stiffness profile of the Clover Dome was also studied. The result of a Clover Dome made from 6061-T6 aluminum was compared with the original material (17-7-PH stainless steel). As expected, the aluminum Clover Dome showed a softer response (Figure 29), which could be achieved by using a stainless steel Clover Dome with a smaller thickness. The behavior predicted by ABAQUS showed a stiffer response than what was measured experimentally, although it is still within the range of the manufacturer's quoted value.

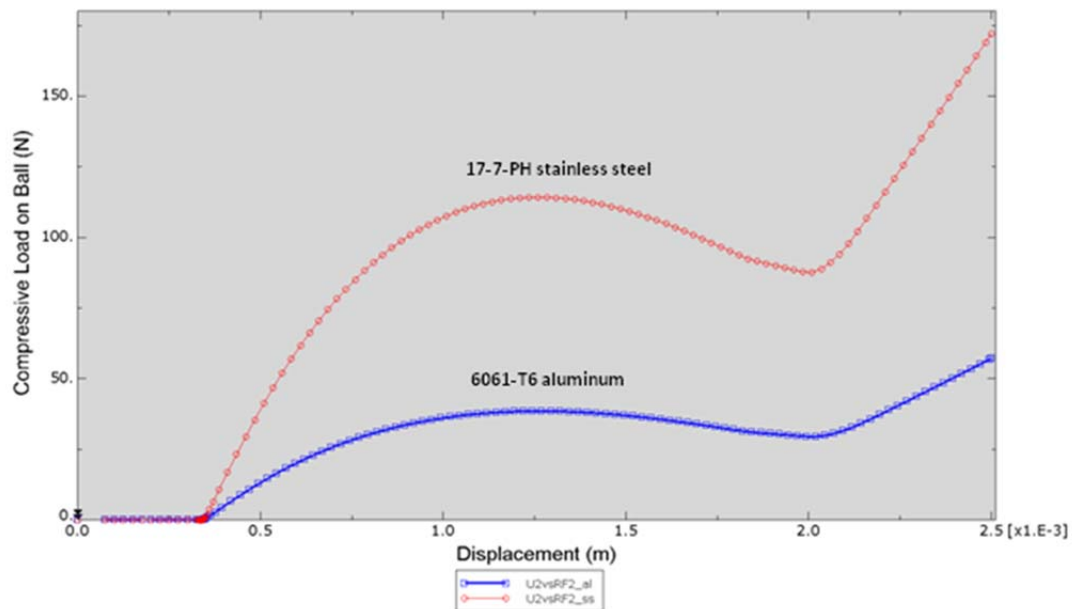


Figure 29. Load-displacement response of a single Clover Dome made from 17-7-PH and 6061-T6 aluminum.

Influence of Support Base Inner Diameter (Size of Opening)

The influence of the base inner diameter (size of the opening) on Clover Dome behavior was investigated. Results (Figure 30) showed that the functional regime of the negative-stiffness region can be adjusted by simply increasing or decreasing the size of the opening in the substrate. If the base ID was decreased by 10%, the negative-stiffness regime decreased by approximately 33%. This information could be useful during the integration phase to allow adaptability in the composite by limiting total strain (i.e., a hard stop).

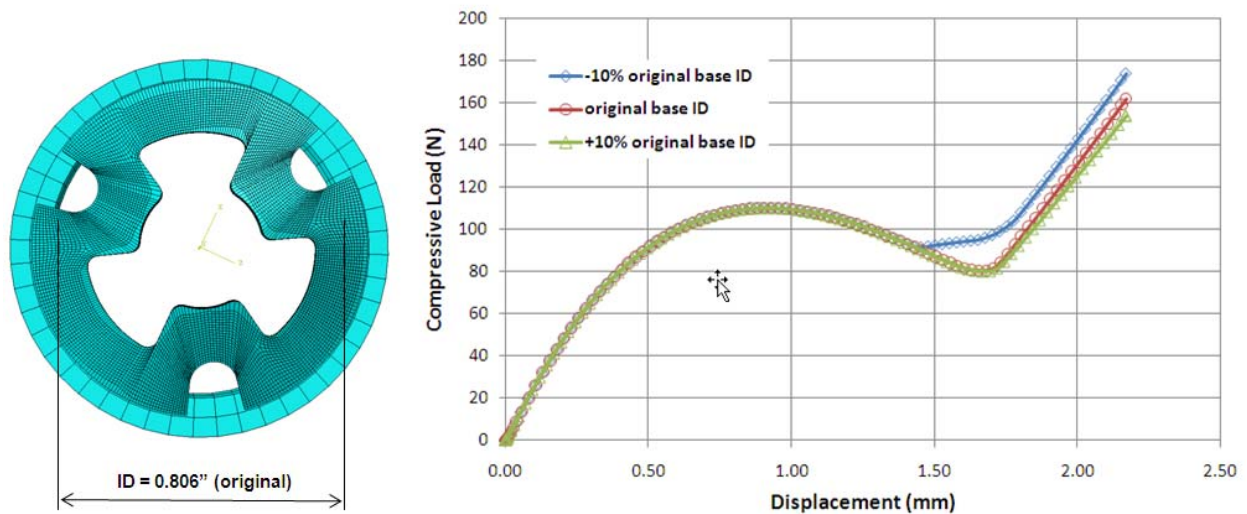


Figure 30. Influence of ID dimension of base on negative-stiffness response.

DESIGN AND FABRICATION OF CLOVER DOMES

Improved Clover Dome Designs

A parametric study was conducted on the Clover Dome to understand the effect on the load-displacement profile by changing various geometries and dimensions of the Clover Dome. This study would enable us to design a new Clover Dome that would maximize the responses that best suits our application, specifically higher stiffness and greater range of negative-stiffness displacement. Figure 31 shows the various parts of a Clover Dome that we varied in our study.

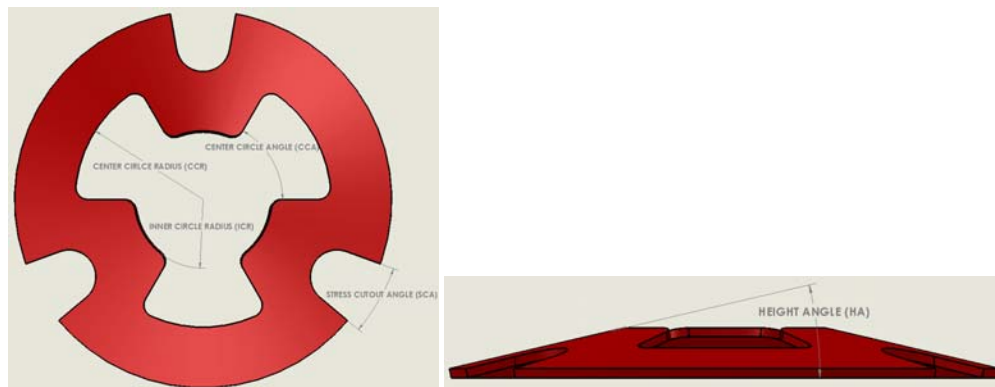


Figure 31. Schematic of a Clover Dome with labels identifying the geometries of the part.

Table 1 summarizes the effect of changing the geometries on the stiffness and the negative-stiffness range. Increasing HA and decreasing ICR had the greatest impact on increasing the range of negative-stiffness. The information learned from this study would allow us to design and fabricate a new Clover Dome with enhanced properties, as demonstrated by examples in Figure 32. The specifications of Model D and Model E are listed, and the resulting responses show a dramatic increase in stiffness as well as the range of the negative-stiffness regime.

Clover Dome Geometry		Stiffness	Negative-Stiffness Range
Number of "Clovers"	↓	Increases	No effect
Stress Cutout Angle (SCA)	↓	Increases	No effect
Center Circle Radius (CCR)	↓	Increases	Increases
Inner Circle Radius (ICR)	↓	Increases	Increases
Web Thickness (constant CCR/ICR)	↑	Increases	Increases
Height Angle (HA)	↑	Increases	Increases

Table 7. Influence of geometric changes on the load-displacement profile of a Clover Dome. The arrows signify an increase (pointed up) or a decrease (pointed down) of the geometric feature.

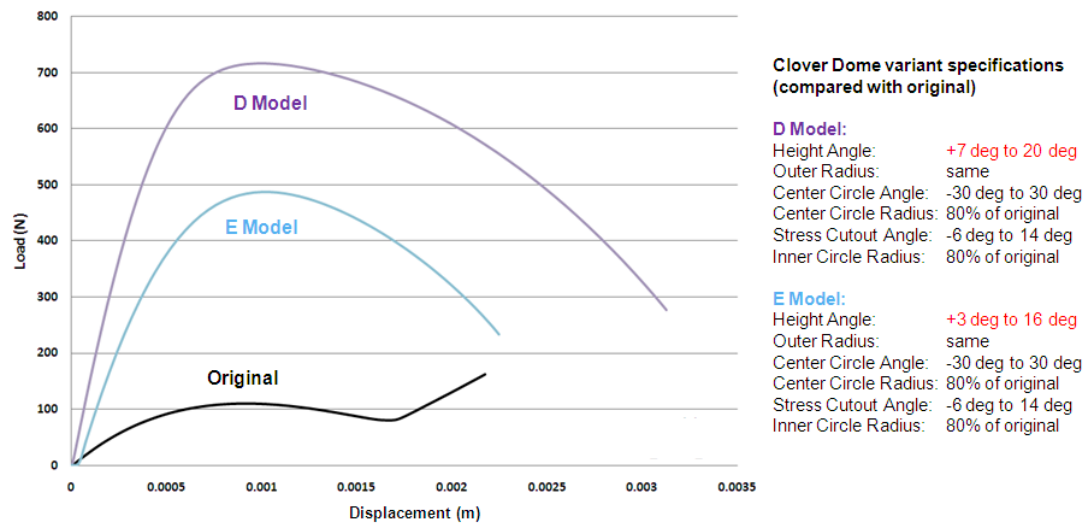


Figure 32. Load-displacement profile from FEA of improved Clover Dome models.

Fabrication of Original Clover Domes

A couple original Clover Domes were replicated using investment casting of 17-4 stainless steel by ProtoCAM (Northampton, PA). These investment-casted Clover Domes were different from the Clover Domes that were originally procured from Associated Spring, which were made out of 17-7-PH stainless steel (Figure 33). The investment casted sample had to be heat treated, which was conducted by subjecting the samples to a temperature of 900 F for 1 hour (a standard heat treating schedule for 17-4 stainless steel).

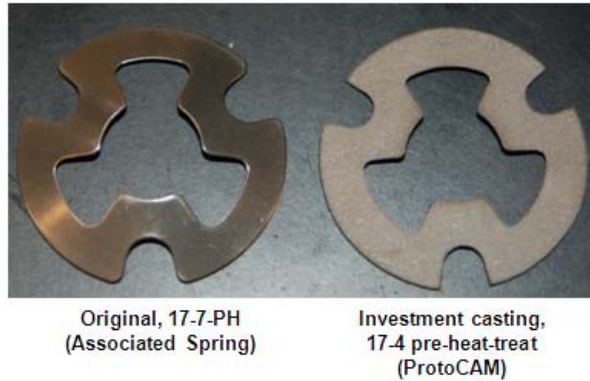


Figure 33. Comparison of Clover Domes.

Aerospace fabricated several Clover Domes variants (as designed from finite-element modeling) in-house that would provide enhanced stiffness and extended negative-stiffness regime. Aerospace successfully re-created the original Clover Dome that was purchased from Associated Spring. Figure 34 shows the dye that was designed and fabricated by Aerospace, which was needed to fabricate the Clover Domes. The process for making the Clover Dome was as follows: 1) anneal a 17-7-PH flat stock so that the material can be formed and machined, 2) cut the stock to size (in the shape of a washer) so that the material fits inside the dye, 3) the flat washer was pressed inside the dye to form the conical shape and the stress cut-out features are carefully created using fine end mills, and 4) the completed Clover Dome was heat treated at 900 F for 1 hour.



Figure 34. Dye components fabricated by Aerospace used for making Clover Domes.

Figure 35 shows the load-displacement response (stiffness profile) of the Aerospace-fabricated Clover Dome compared to the original one procured from Associated Spring and one made from investment casting by ProtoCAM. The plot shows that the stiffness (peak load) and the negative-stiffness regime of the Aerospace Clover Dome are comparable to the original Clover Dome and the one made by investment casting of 17-4 did not meet the desired behavior due to difference in material.

Fabrication of Clover Dome Variants

Aerospace successfully demonstrated the ability to reproduce the original Clover Dome (BC0896015S series) that was purchased from Associated Spring. This success provided us with the confidence to proceed with the fabrication of various Clover Domes that were designed via FEA. The goals of designing the Clover Dome variants were to increase their stiffness and expand the negative stiffness regime, which would add to our library of positive and negative stiffness materials. Furthermore, a wide selection of materials would enable us to better match the stiffness of the positive spring and the negative spring to achieve greater motion amplification.

Figure 36 and Figure 37 show the stiffness profiles (experimental and modeling) of the CC80 and IC80 Clover Dome variants, respectively. The stiffness profile of the original Clover Dome (fabricated by Aerospace) was also plotted to elucidate the improvement from each variant.

For the CC80 variant, the center circle cut was 80% of the original, which increases the overall stiffness when compared to the original. The actual part matched well with FEA in the positive stiffness regime, but due to plasticity (FEA assumes linear elastic), the actual part exhibited greater negative slope, which was actually a good outcome.

The goal of the IC80 variant (inner circle cut was 80% of original) was to expand the negative stiffness regime. Although there were differences quantitatively in the range of negative stiffness between experiment and FEA, the trend was captured quite well. FEA predicted, and the experimental data showed, an increase of 14% in the negative stiffness range of the IC80 variant compared to the original Clover Dome.

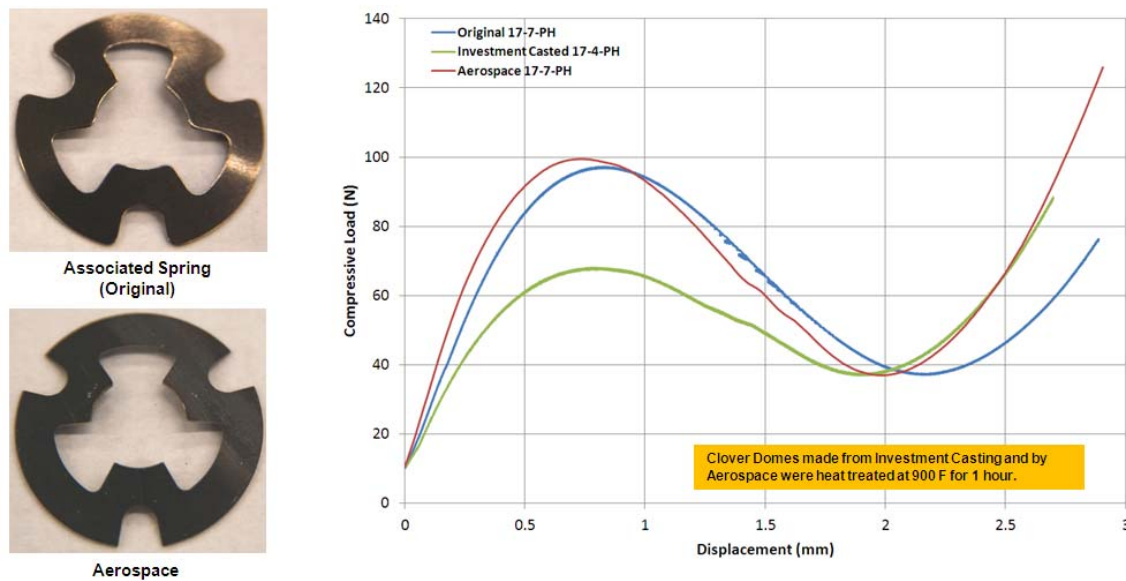


Figure 35. Stiffness profiles for various Clover Domes (original one procured from Associated Spring vs. Aerospace-fabricated Clover Dome vs. ProtoCAM investment casting).

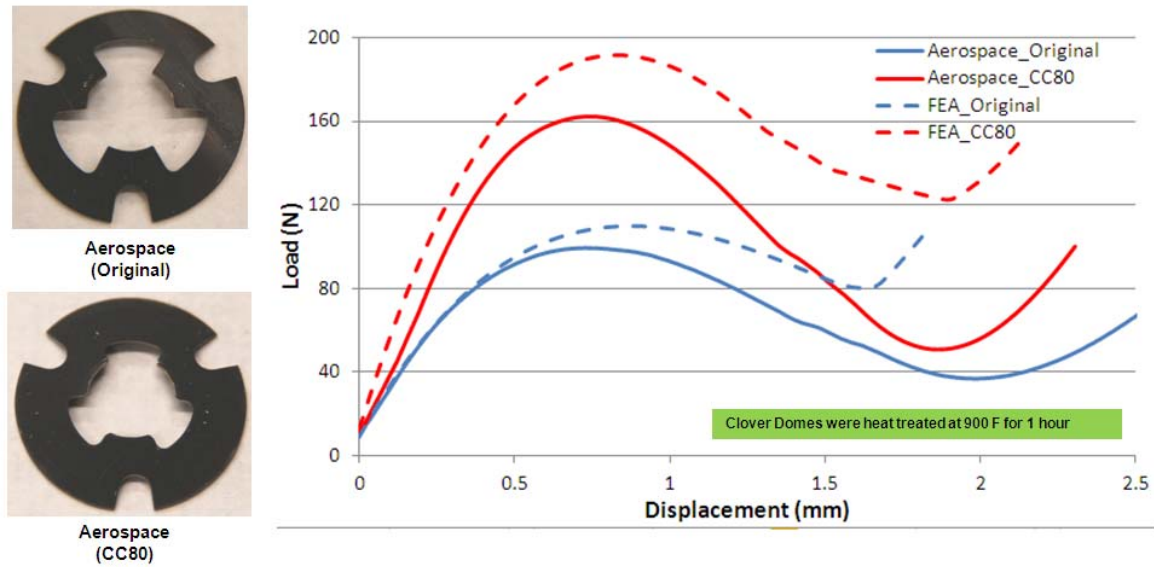


Figure 36. Stiffness profile for the CC80 variant (experiment and FEA) plotted with the stiffness profile of the Aerospace-fabricated original Clover Dome.

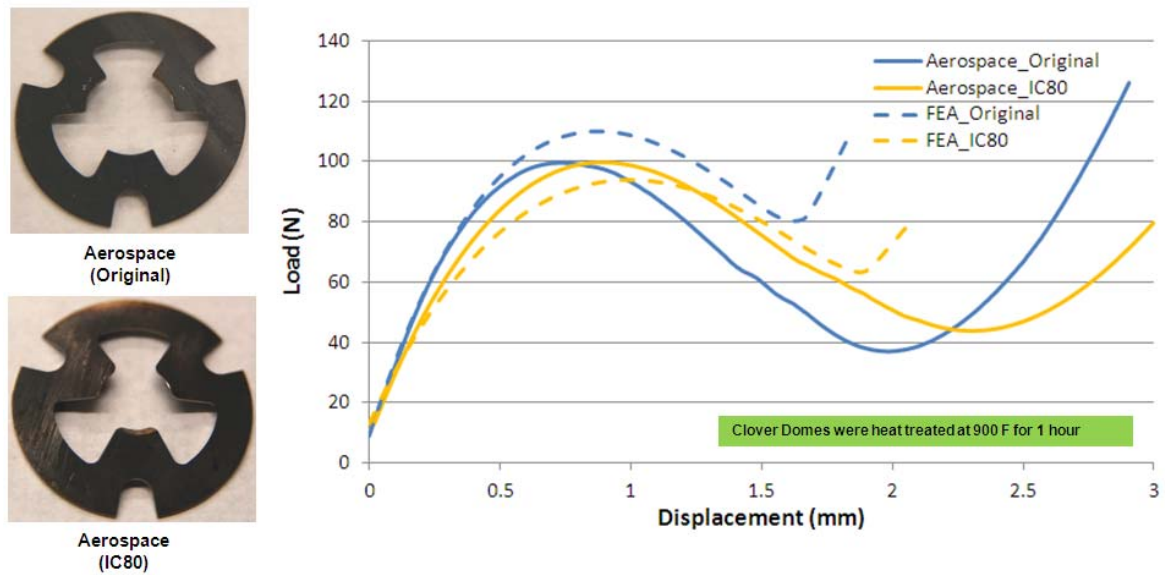


Figure 37. Stiffness profile for the IC80 variant (experiment and FEA) plotted with the stiffness profile of the Aerospace-fabricated original Clover Dome.

Task 1-2 Damping Element (TEES)

TEES performed two subtasks during the period of performance. First, with physical experiments TEES explored low hydraulic-radius hourglass element's (LHG's) damping properties, and second, TEES simulated the LHG dampers with Solidworks and Ansys.

DESIGN AND ANALYZE DAMPING ELEMENT

During the period of performance TEES designed and built damping elements, LHGs, using rapid prototyping machines at Texas A&M University and at Fineline Prototyping of Raleigh, NC.

The damping elements studied here produce passive damping from vibration and displacement provided by the structural material that contains them. Figure 38 shows the initial HG shape and the revised LHG shapes studied here. Figure 39 shows a physical model and its constituents. First, TEES had to characterize the constituent polymers used to build the LHG to assure that they were suited to functional models.

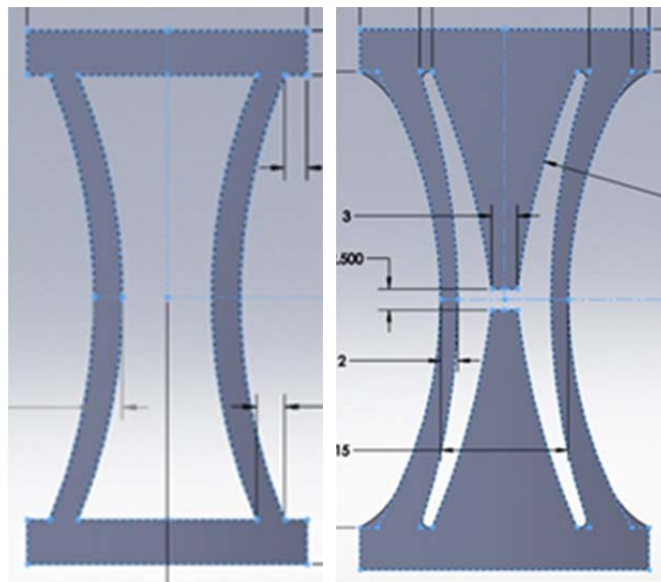


Figure 38. The left image shows the initial baseline form for the hourglass (HG) damping element. The right image shows a high pumping efficiency, low hydraulic radius (LHG) element designed during the project.



Figure 39. The 170 x 80 x 16 mm sandwich panel shown at the left damps vibration through three actions: an elastomer filling (which is the white material between LHGs in the right image), geometrically nonlinear deformation of the polymer that forms the LHG, and viscous dissipation in a fluid that the LHG pumps during vibration.

Physical experiment with the damping material

Rapid Prototyping Material property study

Stratasys Incorporated, who manufacture the Dimension RP, provide the P400 acrylonitrile butadiene styrene (ABS) material properties presented in Table 8. These properties, might not be available in the components built by the RP machine. The materials will not fuse together completely and show directional effect depending on the machine's tool path. Figure 40 shows RP machine operating software, Catalyst and its tool path. Like fibrous composite materials, orthotropic behavior presents depending on the direction of tool path. To obtain baseline properties TEES performed tensile tests that followed ASTM D0638. Figure 41 shows specimen shape and size in a Solidworks model and Figure 42 shows the specimen built by the RP machine.

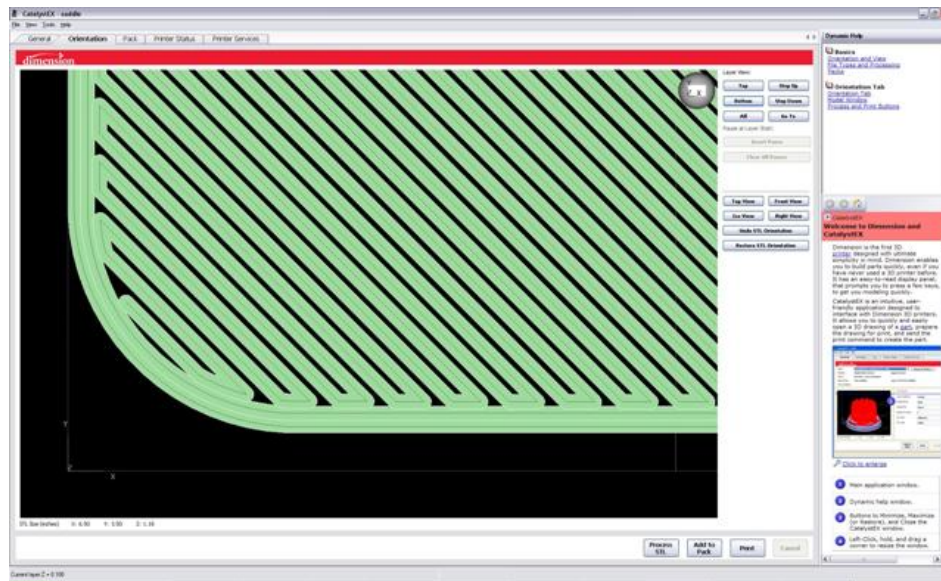


Figure 40. RP operating software, Catalyst, demonstrate its tool path.

Table 8 Stratasys provides material properties of P400 ABS for the RP.

MECHANICAL PROPERTIES¹

	Test Method	Imperial	Metric
Tensile Strength, Type 1, 2 in/min (51 mm/min) 0.125	ASTM D638	3,200 psi	22 MPa
Tensile Modulus, Type 1, 2 in/min (51 mm/min) 0.125	ASTM D638	236,000 psi	1,627 MPa
Tensile Elongation, Type 1, 2 in/min (51 mm/min) 0.125	ASTM D638	6%	6%
Flexural Delamination	ASTM D790	2,000 psi	14 MPa
Flexural Strength	ASTM D790	6,000 psi	41 MPa
Flexural Modulus	ASTM D790	266,000 psi	1,834 MPa
IZOD Impact, notched, (Method A, 73° (23° C))	ASTM D256	2.0 ft-lb/in	106 J/m

THERMAL PROPERTIES²

	Test Method	Imperial	Metric
Heat Deflection (HDT) @ 66 psi (0.5 MPa)	ASTM D648	195° F	90° C
Heat Deflection (HDT) @ 264 psi (1.8 MPa)	ASTM D648	169° F	76° C
Glass Transition (TG)	DMA (SSYS)	219° F	104° C
Melt Point		(NA) ³	(NA) ³

OTHER³

	Test Method	Value
Specific Gravity	ASTM D792	1.05
Vertical Burning Test	UL94	HB
Coefficient of Thermal Expansion	ASTM E831	5.60E-05 in/in/F
Dielectric Strength (kV / mm)	IEC 60112	32.0

¹ Build orientation is on side edge except for flexural delamination which is upright.

² Not applicable (NA) due to amorphous nature. Material does not display a melting point.

³ Literature value unless otherwise noted.

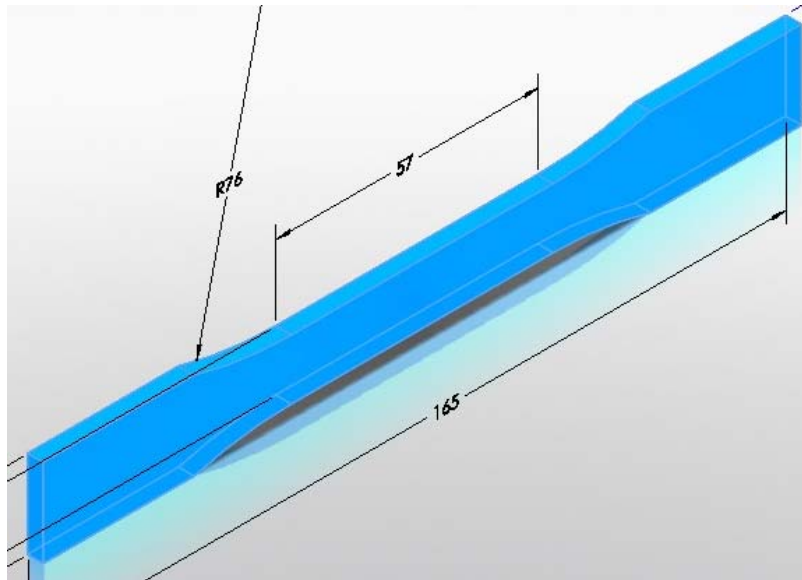


Figure 41. Solidworks design with ASTM D0638 dimensions.

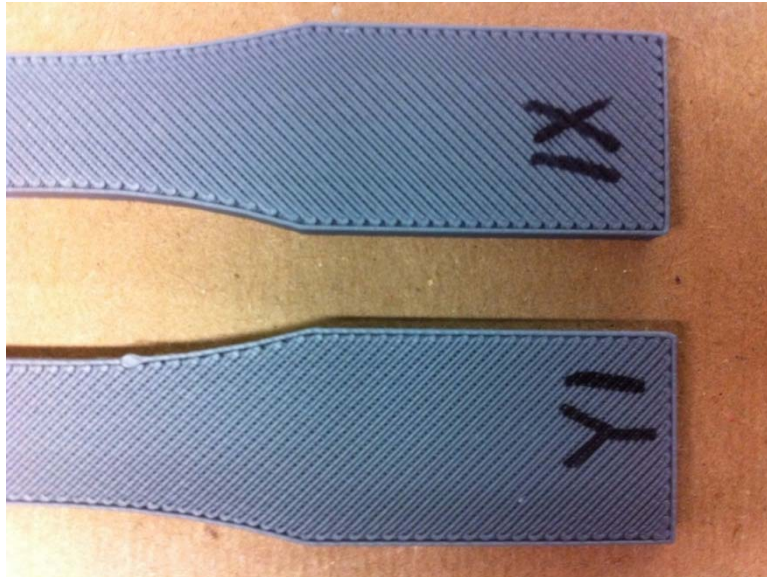


Figure 42. By using Dimension 3D Printer, TEES built ASTM D0638 specimens. It shows obvious fiber directions because the ABS material is not completely fused.

Each specimen has 14 plies, with either $(0, 90)_7$ or $(\pm 45)_7$ build directions. TEES tested 3 specimens in both build directions using red and gray material. An additional set of gray specimens let us check whether there is any significance to building ± 45 specimens with the machine's x or y axis matching the specimens long axis.

Table 9. Tensile test results of P400 ABS material manufactured by Dimension RP machine.

		Elastic Modulus (Mpa)	Yield Strength (Mpa)
Red	$(0, 90)_7$	587.68	18.03
	$(+45, -45)_7$	513.94	15.31
Gray	$(0, 90)_7$	580.98	18.21
	x(+45, -45) ₇	484.05	13.96
	y(+45, -45) ₇	467.71	14.83

HG and LHG Experiments

Static Experiments

We built 3 large HG machines. Two have 3.4mm sidewall thickness with 50mm long and the other has a 1.7mm thick sidewall running 34mm long. Figure 43 and Figure 44 show these HGs. Each ply has specific tool path direction. The first HG has 0, 90 degree plies, and the second and third have ± 45 degrees of plies as shown in Figure 44. Table 10 shows each HG machine's test results.

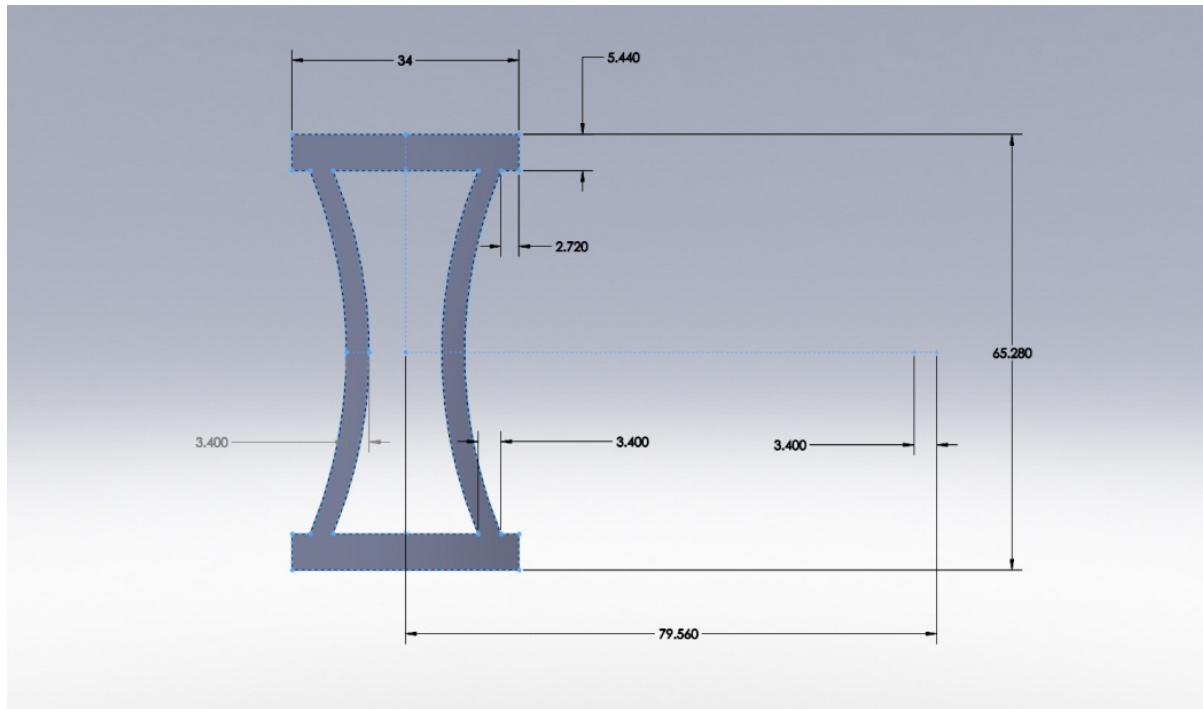


Figure 43. Dimension of 3.4 mm sidewall thickness HG machine that is 50 mm long. The 1.7mm sidewall thickness HG machine is otherwise identical.

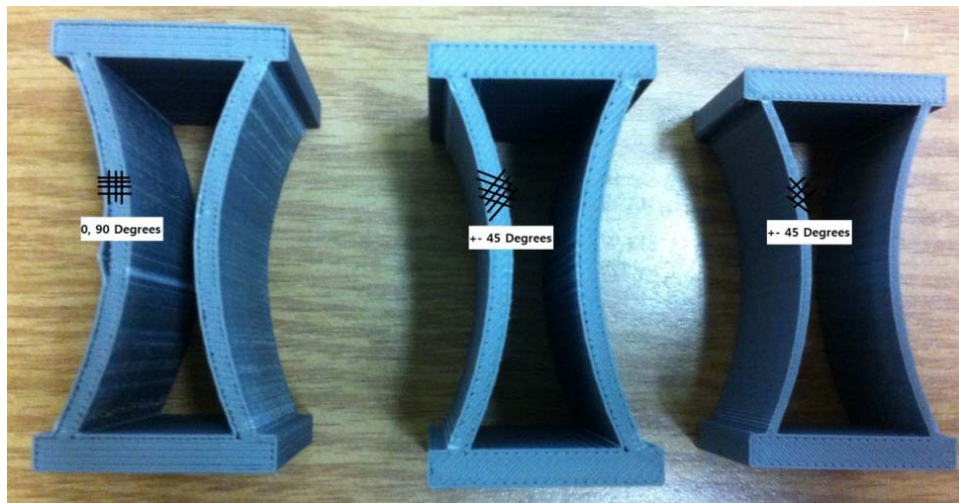


Figure 44. First two HG machines have 3.4 mm thick sidewalls and the last one is one-half as thick.

Table 10. HG machine's compressive test results show the effective stiffness for the HG. A forth order thickness effect is evident.

		Stiffness (MN/m)			Load for Side wall closing (kN)
		1st	2nd	3rd & 4th	3rd & 4th
3.4mm thick	0, 90 degree	1.17	0.41	0.31	1.04
	± 45 degree	1.42	0.55	0.40	1.56
1.7mm thick	± 45 degree	0.14	0.06	0.05	0.28

The structure needs fillets to avoid stress concentration as shown in the circle on Figure 45. When deformed for greatest pumping, the HG shown in Figure 46 underwent outer surface buckling. By redesigning the HG, we can reduce the distance of travel and increase the pumping efficiency.

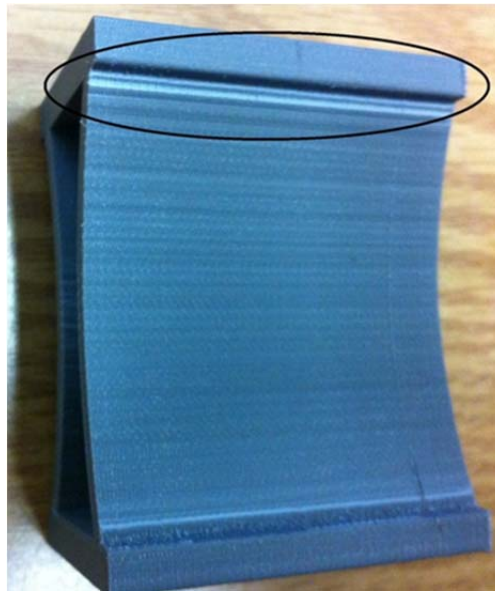


Figure 45. Stress concentration occurred at outer surface of the corner.

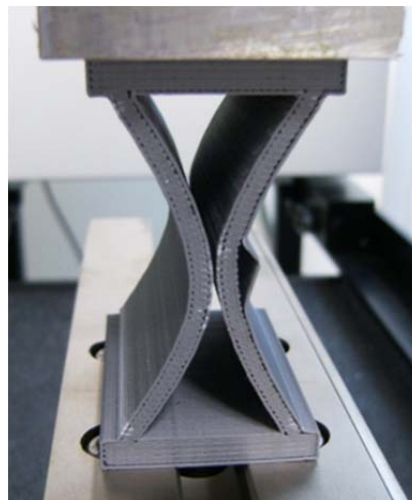


Figure 46. HG machine closed side wall by compression.

TEES designed a new HG after a design parameter study. Figure 47 shows the shape and dimension of a low hydraulic radius hourglass or LHG. The upper and lower triangle shape provides a geometric constraint. When compression works the LHG, fluid is pumped between the outer sidewall and the constraints.. A 1.25mm displacement on the top surface makes the inner channel gap distance equal throughout the LHG. Figure 48 shows this effect.

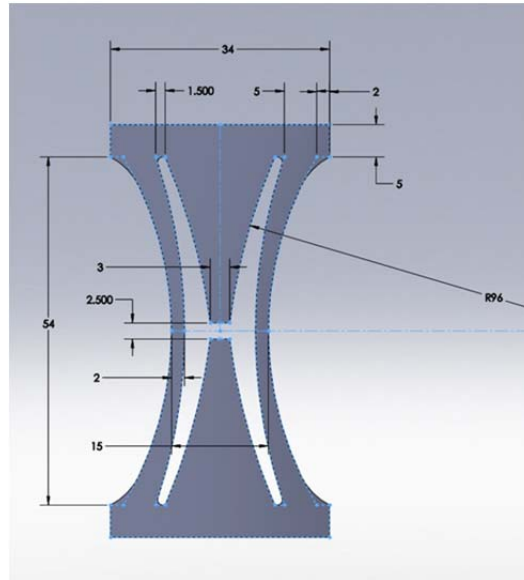


Figure 47. Solidworks part feature presents LHG specimen dimensions.



Figure 48. When compression applied, the inner channel will be the same width.

The best LHG machines have the Z axis vertical in the Dimension RP machine Figure 49 presents the coordinate system. A horizontal Z axis LHG is brittle because plies laminate in XZ plane. The team also did simple compressive test to show LHG's stiffness that showed $0.87 \pm 0.01 \text{ MN/m}$ excluding the first deformation because created permanent deformation as the specimen was conditioned for cyclic performance.

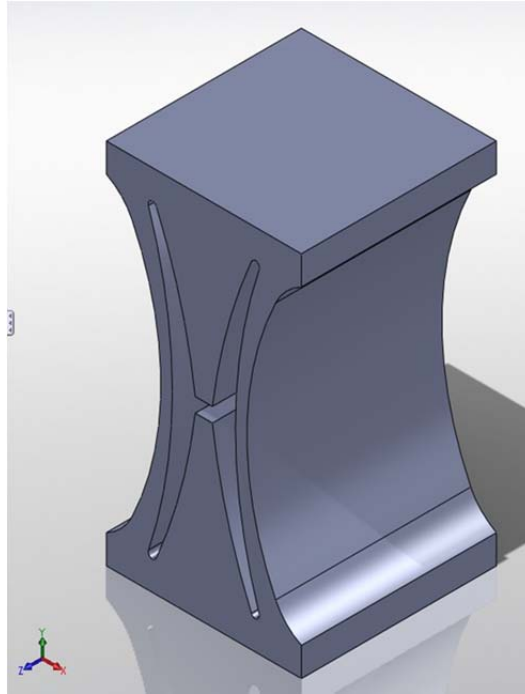


Figure 49. LHG has 34mm of length for testing. The long direction follows the RP machine's Z axis.

Low Frequency Cyclic Experiments

LHG specimens are polymer structures; therefore, they will have their own damping characteristics and cyclic tests must determine this damping ability and the polymer model suitability for moderate life demonstrations of damping. An Instron5567 screw controlled machine is suited to experiments up to 0.2Hz and a bit higher if operators are careful. These experiments applied displacement from minimum 0.1mm to maximum 1.25mm. The first sample, LHG_1, made from ABS P400, at 0.1, 0.2, 0.5, and 1Hz with 10 cycles, and at 0.1 and 0.2Hz as a fatigue test for 15 hours. Figure 50 is the 10 cycle test results that show damping increased by frequencies. Although damping increases as the frequency rises from 0.1 to 10 Hz, this ABS material has low damping in an LHG structure. Therefore, we expect experiments with this material to show the effects of the filler elastomer and fluid pumping strongly.

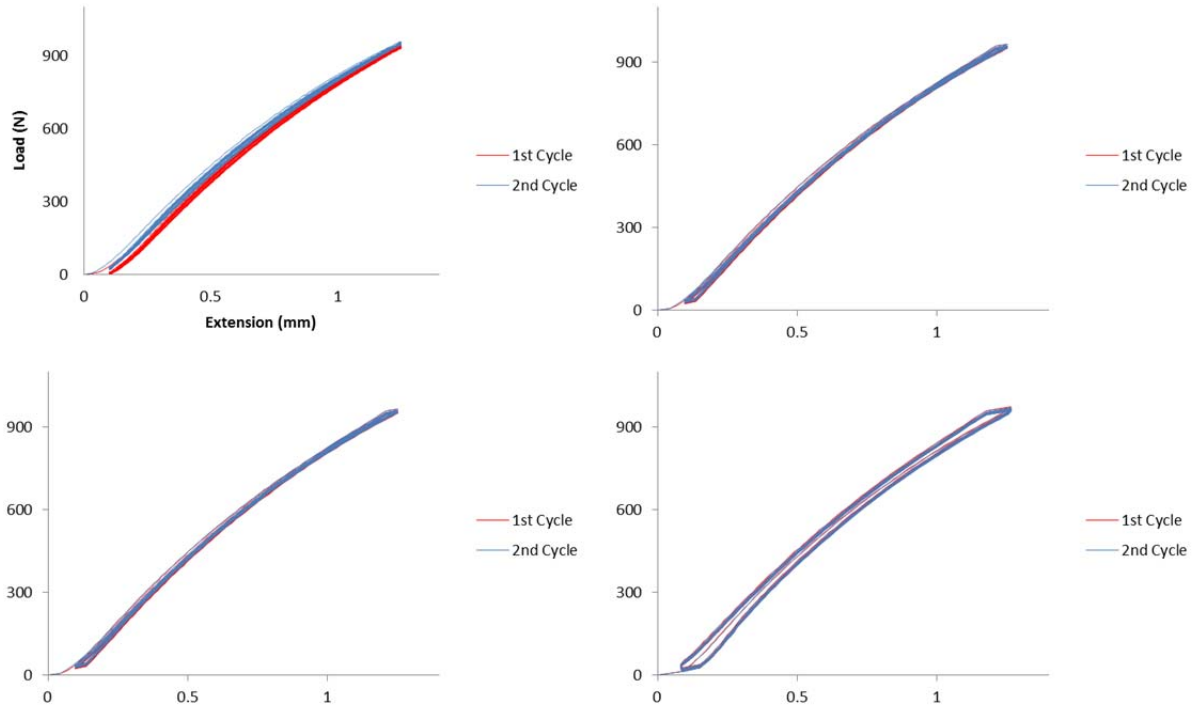


Figure 50. The inherent damping in an ABS LHG is low; therefore, the experiments should clearly show the effect of fluid damping on dissipation. Upper left: 10 cyclic test twice at 0.1Hz. Upper right: 10 cyclic test twice at 0.2Hz. Lower left: 10 cyclic test twice at 0.5Hz. Lower right: 10 cyclic test twice at 1Hz.

Ten hour fatigue test result shows the specimen fails at 5 hours, 3600 cycles shown in Figure 51. Our current target, more than 1000 cycles in a model material, is satisfied.

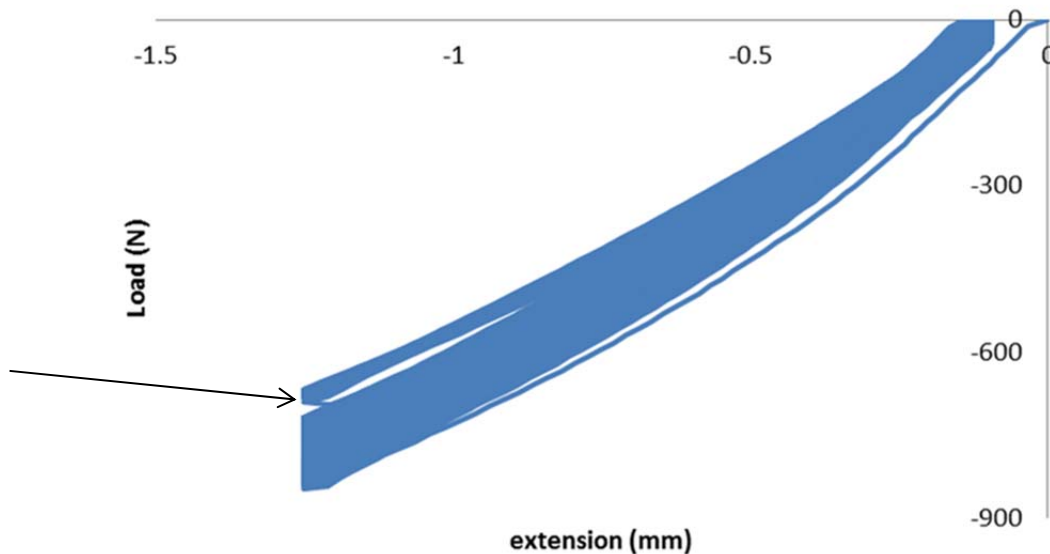


Figure 51. About 5 hour point, the load dropped suddenly during fatigue test.

Figure 52 presents LHGs manufactured from FineLine Prototyping, Raleigh, NC. The left white one's material property is P.P. like, and the right dark blue one shows P.E. like properties. The detail material property data is shown in Table 11. These materials are available for small scale LHGs that represent the damping material that will go into the Materials Logic structure.



Figure 52. LHGs made by FineLine Corp.

Table 11. RP material properties. The Somos and VisiJet make excellent models because their elongation is much larger than the other options.

Material Name	P400 ABS	P400 ABS	Somos 9120 Epoxy Photopolymer	VisiJet HR200
Specimen Color	Red	Yellow	White	Dark Blue
Tensile Strength	22 MPa	34 MPa	30 - 32 MPa	32 MPa
Tensile Modulus	1.63 GPa	2.48 GPa	1.23–1.46 GPa	1.72 GPa
Tensile Elongation	6 %	5 %	15 - 25 %	12.3 %
Notes			PP like	PE like

TEES applied compressive strain from 0.16% to 1.95% and 0.1 or 0.2Hz of cross head speed. Specimens with significant damping at 0.2 Hz were tested at 0.1Hz. Figure 53 is the single cyclic test plot of red P400 ABS LHG specimen. The five experiments show these LHG structure does not contribute to damping. Figure 54 is the Somos LHG single cyclic plot. Both x and y axes were normalized and calculated inner loop area, which is proportional to the energy dissipation, is 10.52% for Somos 9120 epoxy and 12.69% for VisiJet HR200.

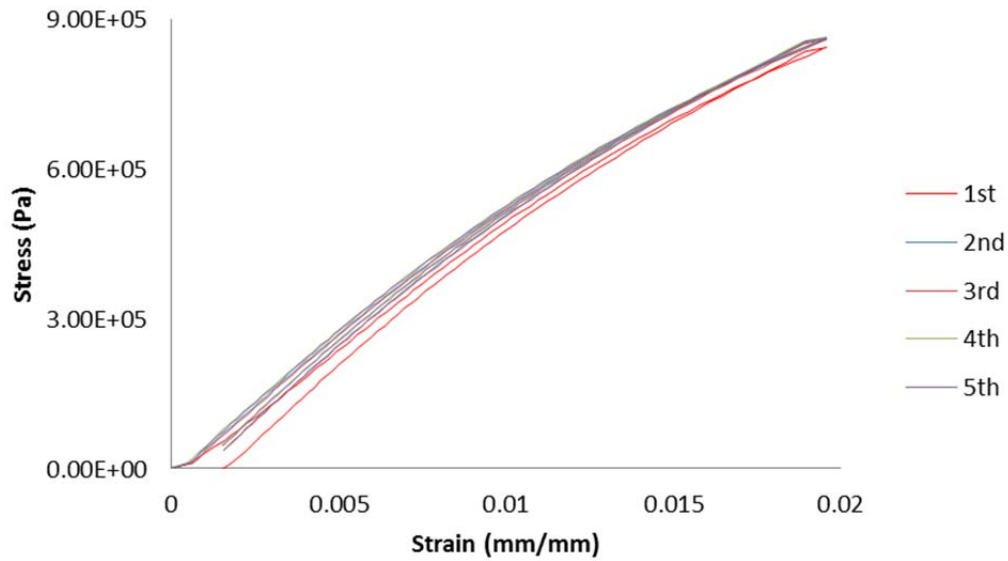


Figure 53. Single cyclic test result plot for red P400 ABS LHG specimen did not present meaningful damping effect.

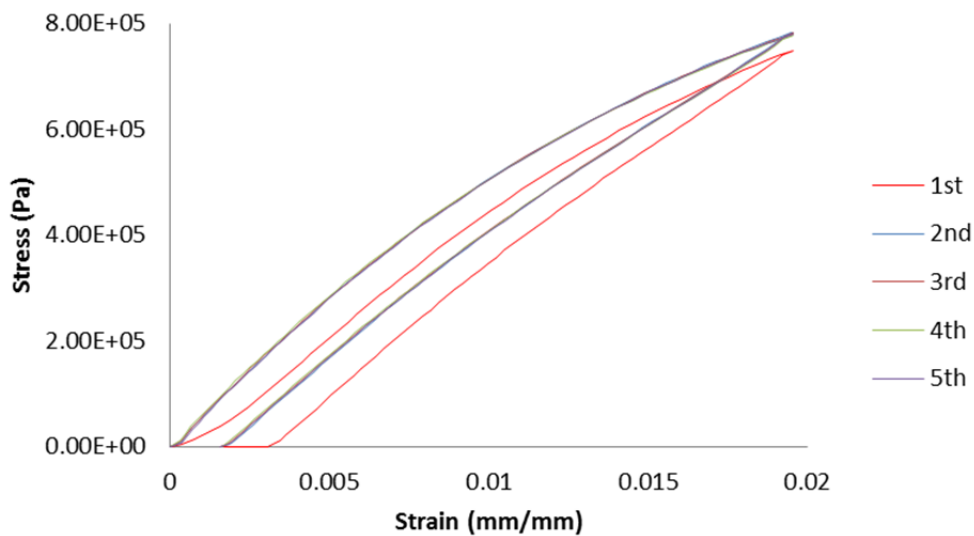


Figure 54. The white Fineline corp's LHG's single cyclic test result plots show this material base specimen has relatively high damping effect than ABS base LHG.

Table 12 shows LHG's performance depending on materials and frequency. Yellow P400 ABS specimen failed fatigue test at 0.2Hz, but it passed after adjusting it by 0.1Hz. FineLine LHGs had large difference between loading and unloading cycle and loading cycle showed non linearity. Thus, TEES measured the stiffness at unloading condition that showed linearity. In addition, those specimens showed large, first cycle, "permanent" deformations but they recovered after several seconds. In terms of cyclic testing, the deformations are permanent while the cyclic displacement is ongoing.

Table 12. LHG performance comparison in single cyclic test

Material Name	P400 ABS	P400 ABS	Somos 9120 Epoxy	VisiJet HR200
Specimen Color	Red	Yellow	White	Dark Blue
Frequency (Hz)	0.2	0.1	0.1	0.1
Stiffness (MPa)	45.93	53.25	43.35*	48.85*
Fatigue Test	>1000	>1000	>1000	>1000
Permanent Deformation**	0.0469	0.1406	0.1100	0.0742

* Stiffness measured when unloading. ** Permanent deformation measured after 1st cycle.

LHG machine compressive cyclic test

Large LHG models

TEES's own RP machine, Dimension BST, was used to make the first large LHG for fluid pumping experiments. The 64mm tall LHG was tested dry and wet—that is, filled with 104Kcps fluid. Figure 55 and Figure 56 presents the shape and test set up of the 64mm tall LHG machine.

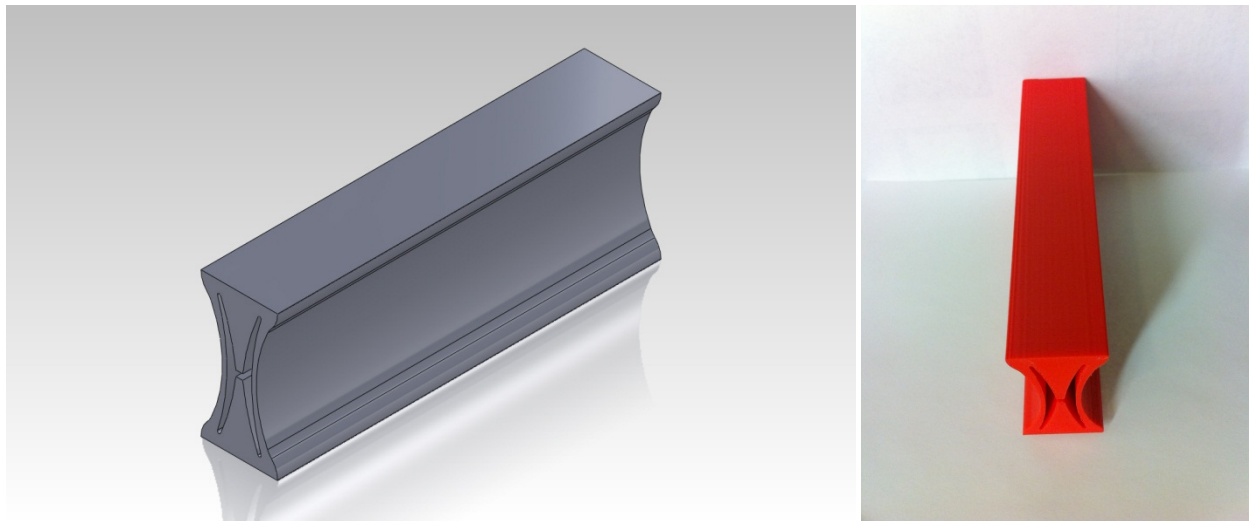


Figure 55. Shape of 64mm tall 170mm long LHG

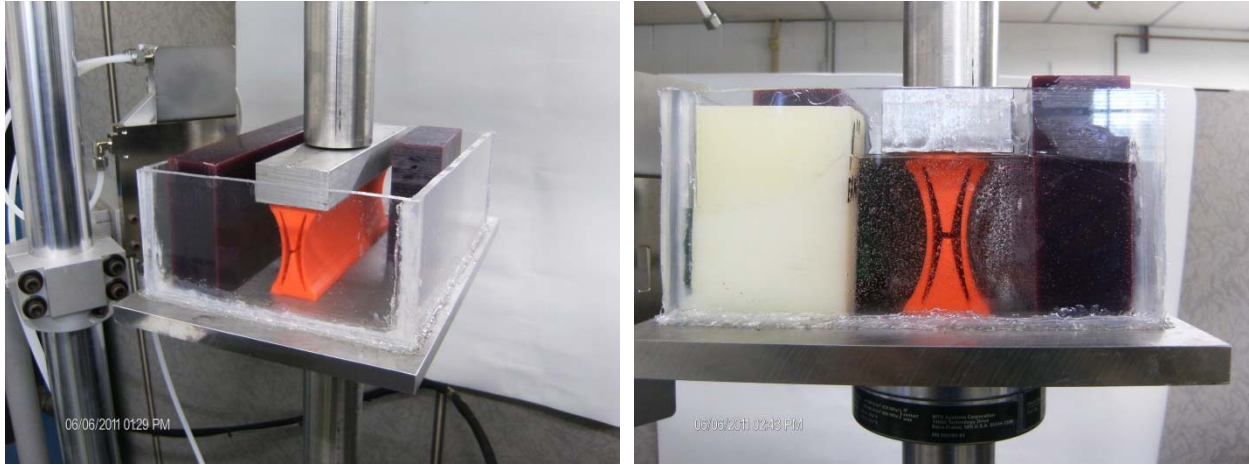


Figure 56. The test set up of 64mm tall LHG machine in dry and wet condition.

Figure 57 presents the damping performance comparison by wetting. The fluid's viscosity is 104Kcps that produce peak damping near 0.2Hz as shown in Figure 58. Additional tests near the peak point will help verify the peak value.

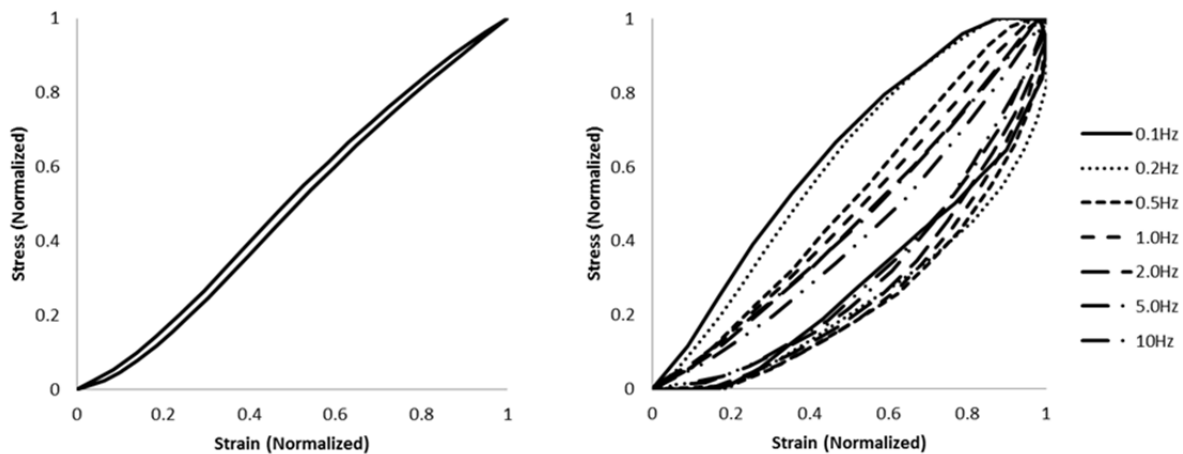


Figure 57. Left plot is 64mm tall LHG's dry test results—is does not show significant damping at any frequency between 0.1 and 10 Hz. Right plot presents the wet condition damping performance by the LHG containing 104Kcps fluid.

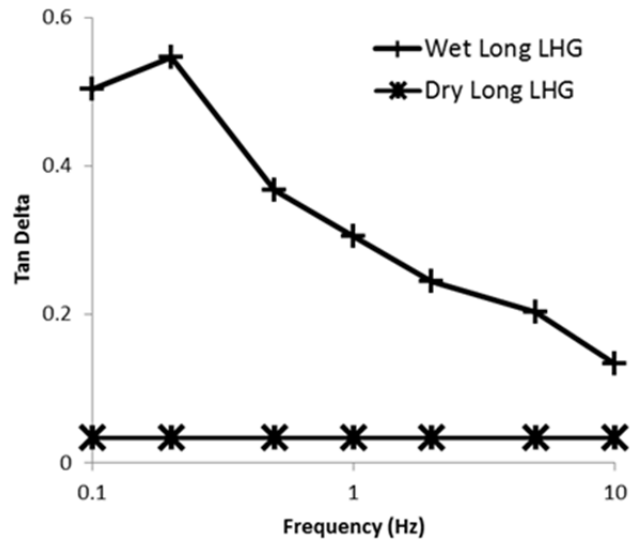


Figure 58. The 64mm tall LHG shows peak damping near 0.2Hz when a 102 Kcps fluid fills the element.

Quarter scale LHG models

LHG will be scaled down to make the high stiffness/high damping material. As the first step on that path, TEES order one-quarter height LHGs from Fineline Prototyping. Its length is the same as 170mm but 16mm tall, and arrayed with 5 damping cells as shown in Figure 59.

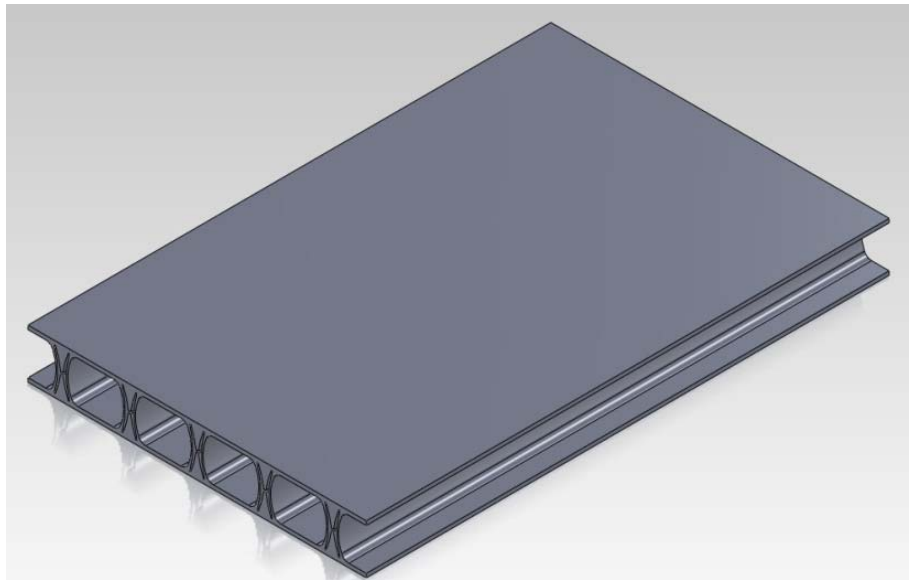


Figure 59. TEES ordered quarter size LHG arrays from Fineline Prototyping.

The initial candidate elastomer material for filling between hour glass cells were POR-A-Mold S111 and Freeman 1040. TEES cast specimens in both material as shown as Figure 60, and sent those to AERO for tangent delta measurements. Both materials are high elongation elastomers; S111 reached 500% and 1040 reaches 410% elongation at failure.



Figure 60. S111 and 1040 specimens for compression/compression damping experiments.

S-111 provides increased damping with frequency rise: however, there is no peak damping in our target range from 0.1Hz to 10Hz as Figure 61 shows.

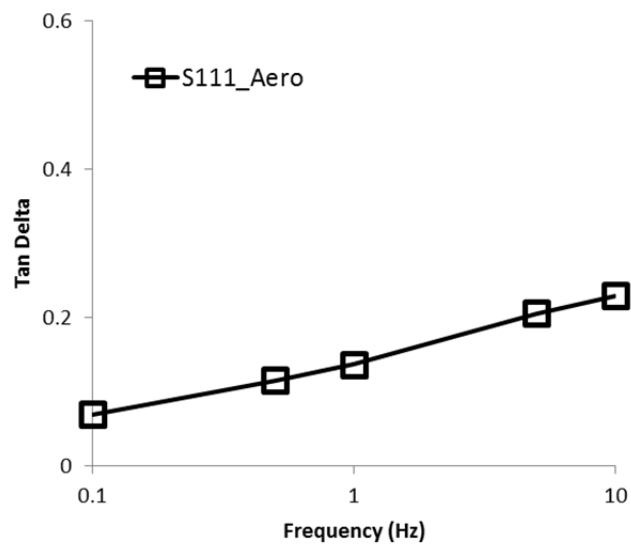


Figure 61. S111 elastomer cyclic test results show improved damping with increasing frequency.

We also tested “high damping” PlatSill 00 and SS6060, SS6080, but the damping performances are not better than S111, so S-111 will be the baseline elastomer for Task 1.

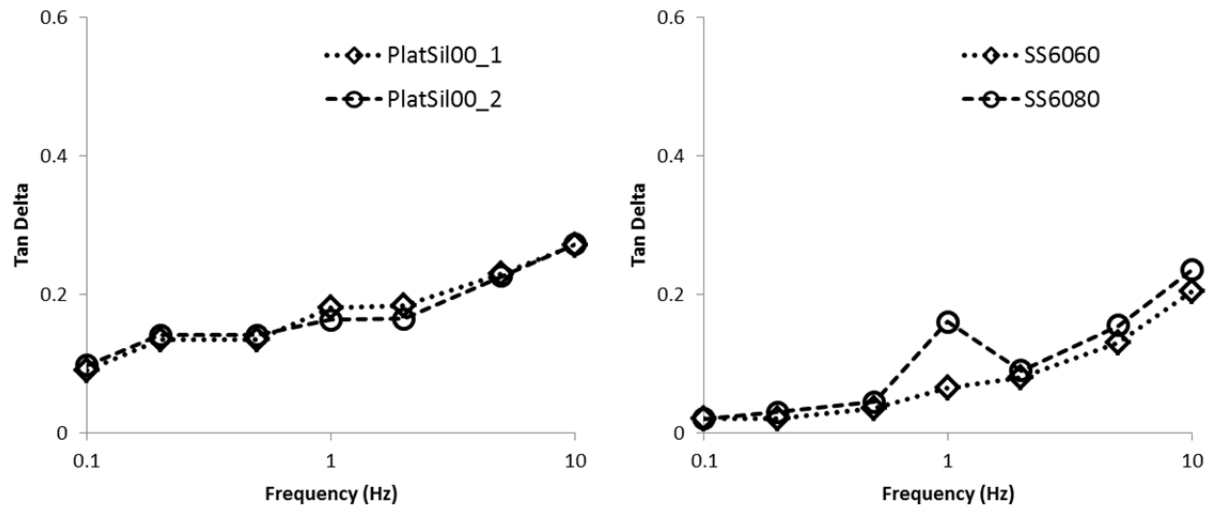


Figure 62. The cyclic test results of PlatSil 00 and SS6060, 6080 do not excel S111's one.

Prior work showed that elastomer added between HGs showed improved damping over elastomer alone even though the HGs increased panel stiffness. Figure 63 shows that, for elastomer alone, the maximum damping occurs at the sides of the block where the shear deformation is greatest. The elastomer near the center is ineffective because the shear deformation is low. On the other hand, elastomer filled HG arrays put an elastomer into high shear deformation at every HG element wall.

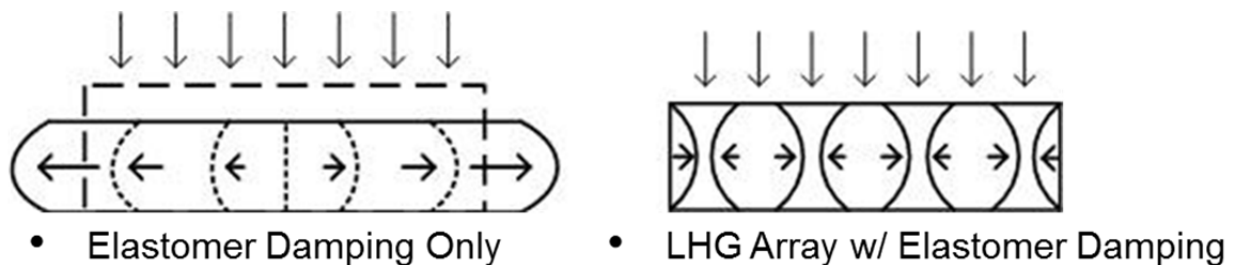


Figure 63. Damping performance compared between elastomer alone and an HG array filled with elastomer. Unlike neat elastomer, the array's damping occurs near every the machine's side wall.

A Visijet LHG array is shown in Figure 64, and Figure 65 shows the array with the S111 elastomer filling in between the cells. Because top and bottom skins warped in the RP machine, we cast an epoxy layer on the top and bottom surfaces to make them flat. That treatment made the specimen thicker by 2mm. TEES's first cyclic tests used the array dry without elastomer and wet with elastomer cases; this array was not tested dry after the elastomer was added.

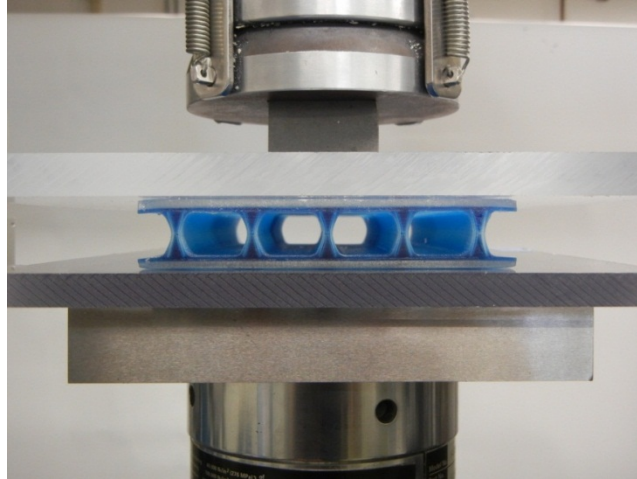


Figure 64. The shape and test set up for the 16mm tall Visijet HR200 array without elastomer.

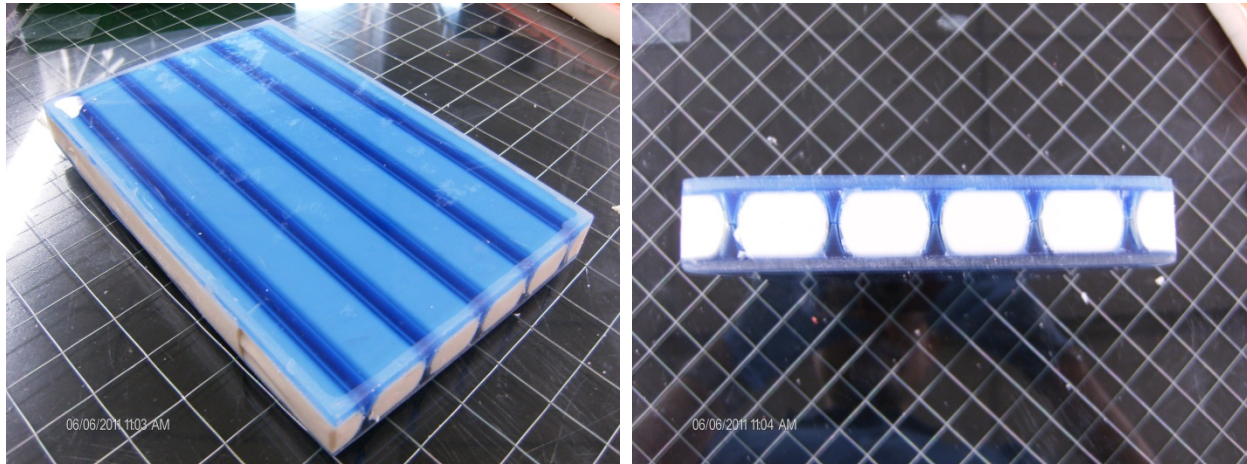


Figure 65. S111 elastomer filler is between the LHG cells.

The fluid will splash out right after the first cycle, so we attached short reservoir as shown in Figure 66. However, the reservoir did not contain the fluid fully and did not keep the channel wet perfectly.

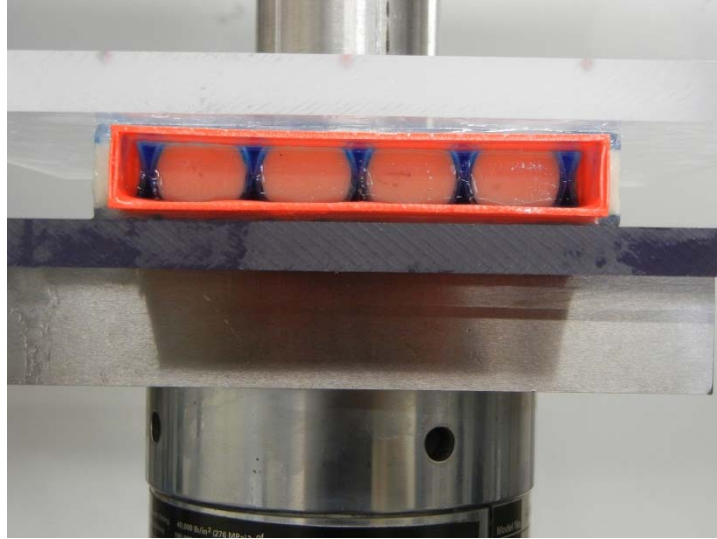


Figure 66. The red external ABS reservoir helped keep fluid and prevent splash out.

Figure 67 and shows the array tested dry without elastomer (left graph) and as a complete damping panel with LHGs, elastomer filling, and 12 kcps fluid in the LHGs. Without elastomer, the shear stiffness in the panel is low and we believe that contributed to the shape of the hysteresis curve; that is, the LHGs were not uniformly opening and closing during the experiment.

First, note that the left graph shows that Visijet material provides significant damping when acting alone. However, the right graph shows that the fluid and elastomer increase the damping. In addition, the fluid/solid interaction between the fluid

Figure 68 compares damping by elastomer alone, by the LHG array dry and unfilled, and by the LHG array with elastomer and 12 kcps fluid. The LHG/elastomer/fluid response shows a synergistic effect with the combined system outperforming the elastomer and LHG constituents at each frequency.

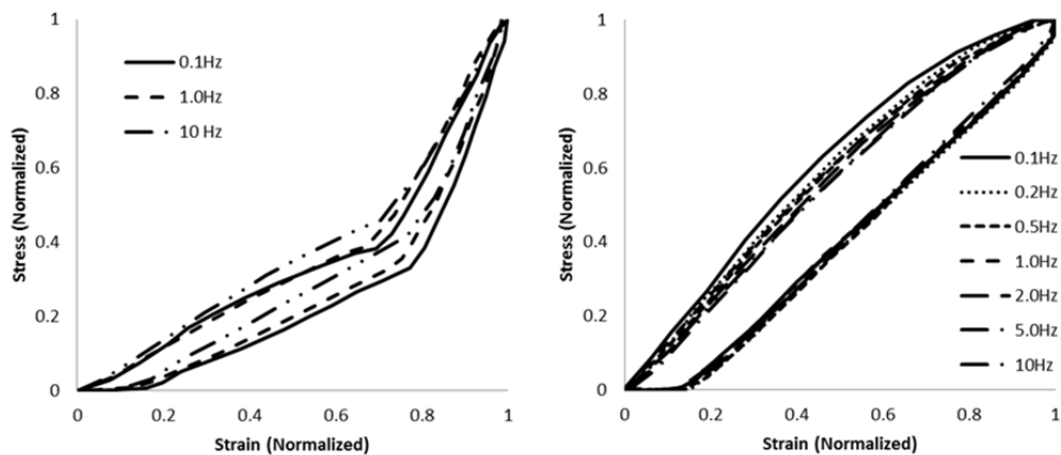


Figure 67. TEES performed the cyclic test on the Visijet array in dry condition without elastomer filling (Left) and with elastomer and fluid (Right).

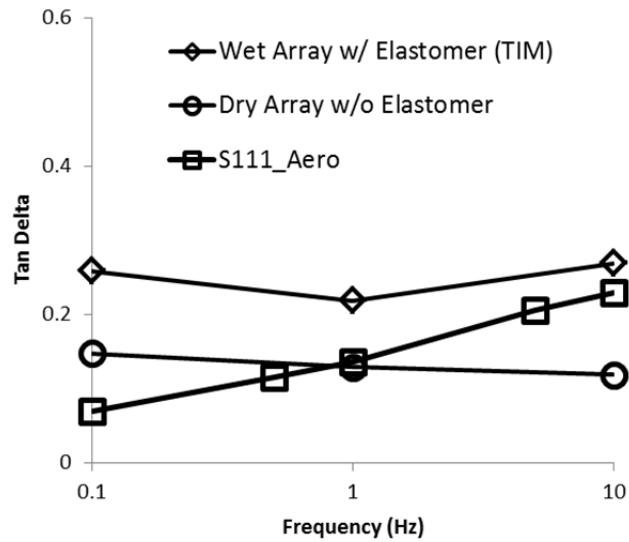


Figure 68. The elastomer filling and wetting helped increase damping performance.

After the technical interchange meeting, June 2011, TEES tested the LHG panel again through the frequencies, 0.1, 0.2, 0.5, 1.0, 2.0, 5.0, and 10Hz. To keep the panel filled with fluid all times, we attached large manifolds at both ends to contain fluids as shown in Figure 69. However, this large overhang may affect the test results by fluttering and increasing pumping resistance. In addition, we could see whether the channels were properly closing.

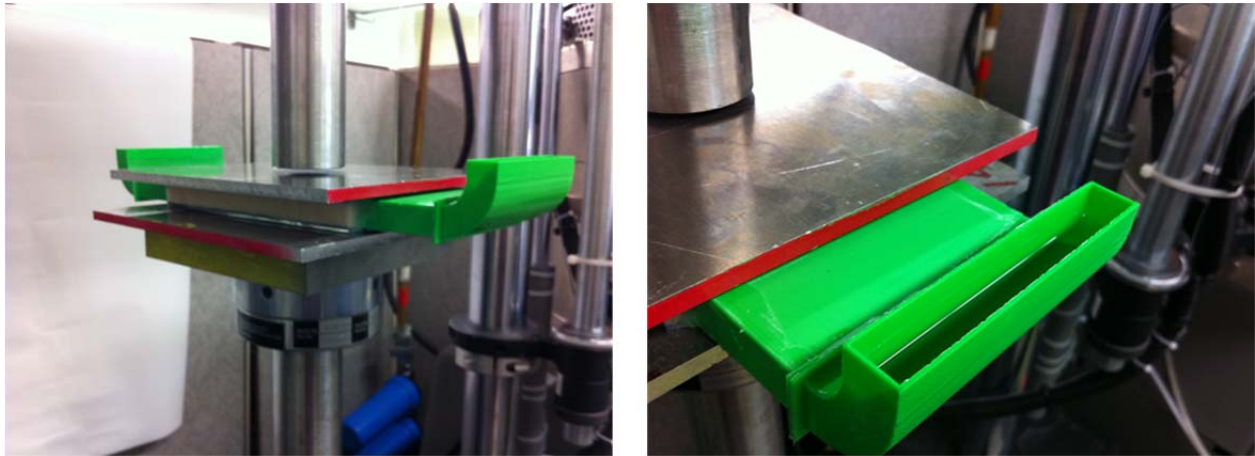


Figure 69. The green U shape is the manifold to contain fluid in the LHG channel.

Figure 70 still shows some synergistic effect—combination damps better than the components at most frequencies; however, by 5 Hz the combination has the same, and at 10 Hz, slightly lower performance than elastomer alone.

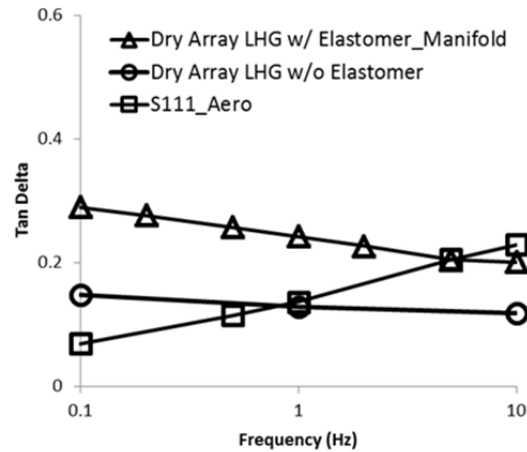


Figure 70. A more detailed series of tests with large, overhanging manifolds change the LHG panel response.

TEES eliminated the manifolds and tested again filled triangle with dashed line in Figure 71. The response is flatter across the frequency range.

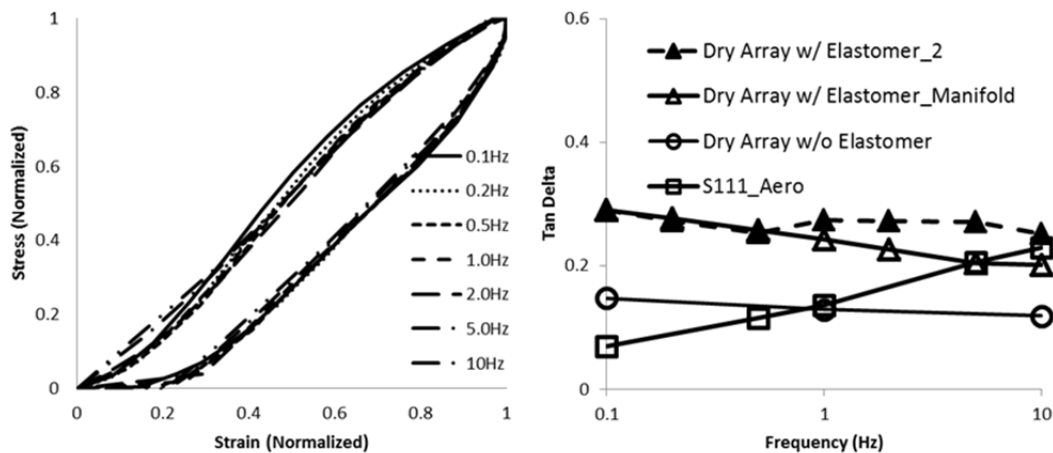


Figure 71. The retest result without the overhanging manifold array is flatter across the frequency range.

TEES eliminated the manifolds and used transparent plastic wrap to contain the fluid. However, the specimen was worn out by longer than expected cyclic test program. We needed to build a new panel to do the cyclic test.

We changed from VisiJet to Somos RP material because the Fineline stopped producing VisiJet products. In our early tests, the Somos 9120 shows almost the same performance as VisiJet, so we ordered five LHGs without a skin because the skins can cause the LHGs to warp. For this case, aluminum skins and solo LHGs compose the panel. The 16mm tall, 170mm long LHG array tested in dry without elastomer filling first as shown in Figure 70 first. The material, Somos 9120, produced some damping. Figure 69 shows the array's damping performance. Even if this case is dry without

elastomer filling, the structure presents about 0.2 of tangent delta value but not changing with frequencies.

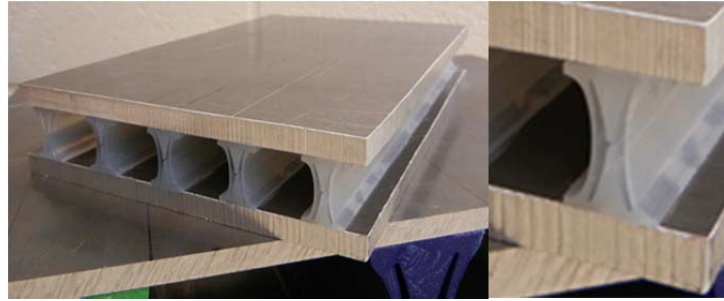


Figure 72. The 16mm tall LHG cells manufactured in Fineline Corp are arrayed with 6mm thick Al6061 skins.

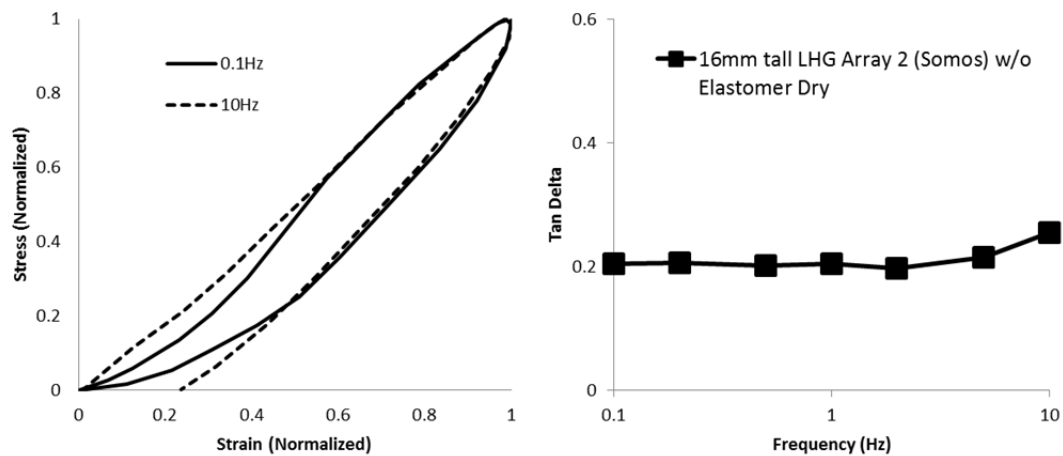


Figure 73. The damping did not change from 0.1 to 5Hz but increase a little in 10Hz in 16mm tall LHG array without elastomer in dry case.

Adding S111 elastomer in the 5 cells array of 16mm tall LHG increases damping about 20% as shown in Figure 74. However, the damping performance did not change by frequency. As we can see the left chart, all plots almost overlapped.

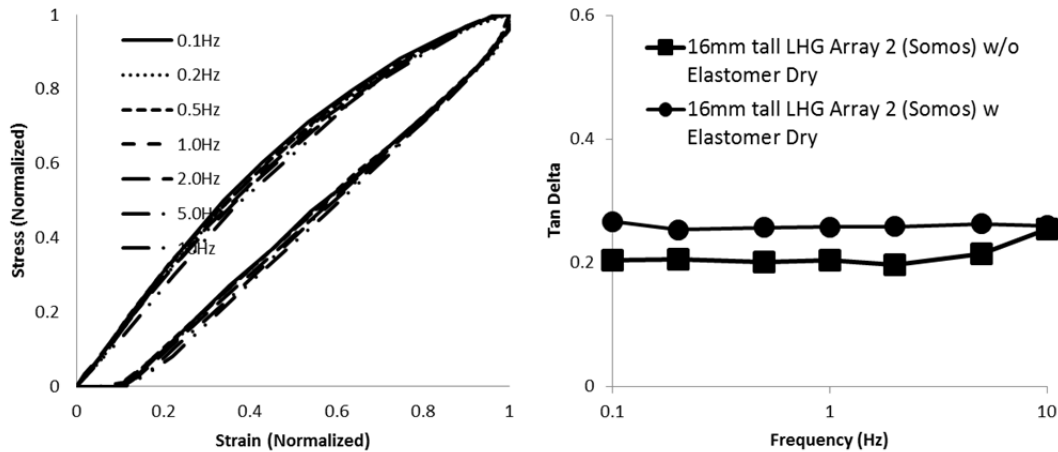


Figure 74. The cyclic test results of 16mm tall LHG array with S111 elastomer filling in dry .

For wet condition test, TEES designed short manifolds and attached them on the array. To make sure the channel properly closes, we also made windows—from thin, flexible, transparent sheet—and visually checked closing. Reynolds number analysis showed the proper viscosity for 16mm tall LHG is 25kcps.



Figure 75. TEES designed and attached short window manifolds on the array. 25K cps silicon oil fluid was used for cyclic test.

The test results, shown in Figure 76, illustrate the damping was good at low frequencies. Above 1Hz, the damping is decreases, which is what we expect from the results shown in Figure 58. In that experiment, the fluid was too viscous to allow the LHG sidewalls to pump. Therefore, the material is effectively stiffer and damping drops. This indicates that adaptive viscosity would be beneficial.

At low Hz the damping was so effective that the panel did not spring back immediately at unloading and maintain contact with the crosshead. Future experiments in load control mode will address this behavior.

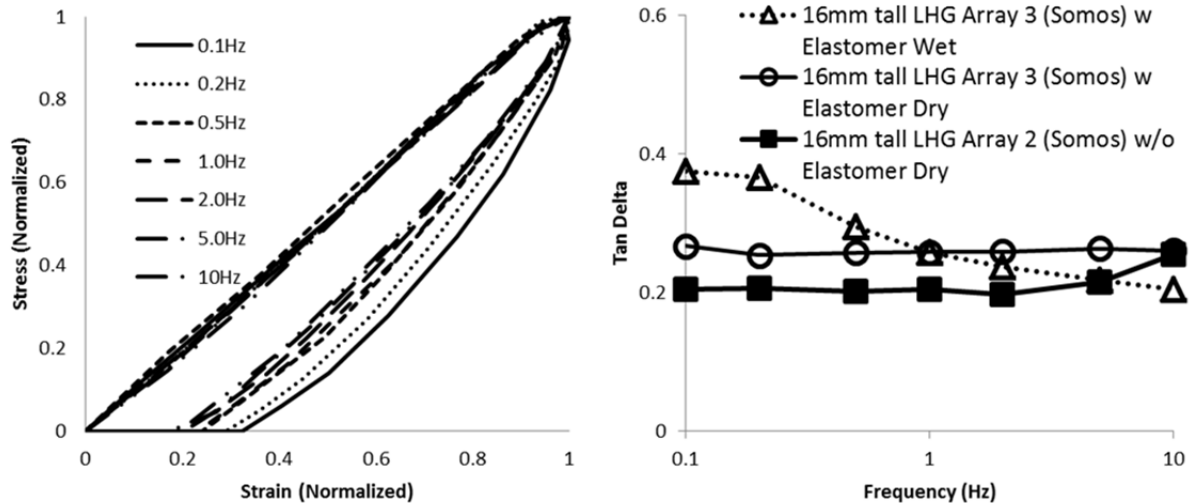


Figure 76. Somos LHG array with S111 with 15K cps fluid damping performances are good at low frequencies and, as expected, reduced at 10 Hz.

TEES also will build new 64mm tall LHG, and test without elastomer and dry and wet conditions. Specially designed short manifolds will be attached on the 64mm tall LHG case.

Element 1 – Simple Fluid

TEES performed wet cyclic tests for 64mm tall LHG filled with 102Kcps silicone oil by 4 methods: large and small chambers, short and long manifolds. Chambers require large amounts of fluids. Manifolds hold the right amount of fluid in the channel, are easy to align, and eliminate lubricated slipping between the specimen and the compression fixture; however, the thin wall manifolds, which bond to the edges of the specimen, might affect specimen's stiffness.

Figure 77 shows tank and manifold sizes. The large chamber held less fluid than the small chamber case because we put large wax blocks chamber to reduce the empty volume.

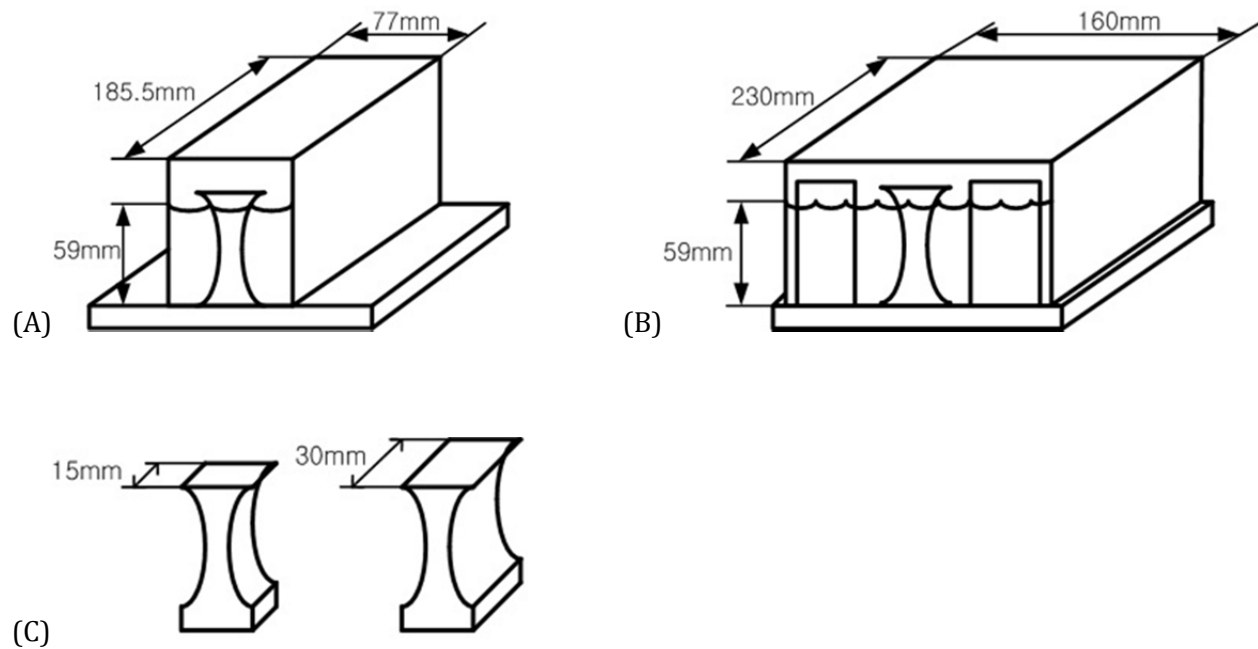


Figure 77. Several containment methods were used for wet cyclic tests. Fluid required for each case is (A) small chamber: 683cm³, (B) large chamber: 196cm³, (C) small and extended manifolds: 440 and 880cm³ respectively.

Chamber Experiments

Figure 78 presents results obtained from tests in both chambers. Even though the large chamber used less fluid, the damping performance was highest. As the LHG pumps the oil, it moves oil toward the chamber walls that face the LHG's channel openings. The distance between the chamber walls and the channel exits was greater in the large chamber than the distance provided by the small chamber. At this point, it appears that the longer distance increases damping performance. Both chambers provide similar flow and space between the small chamber's long walls and the wax blocks placed parallel to the LHG's long axis. Therefore, it seems probable that placing the chamber wall too close to the exit flow inhibits the flow and therefore, reduces the energy dissipation.

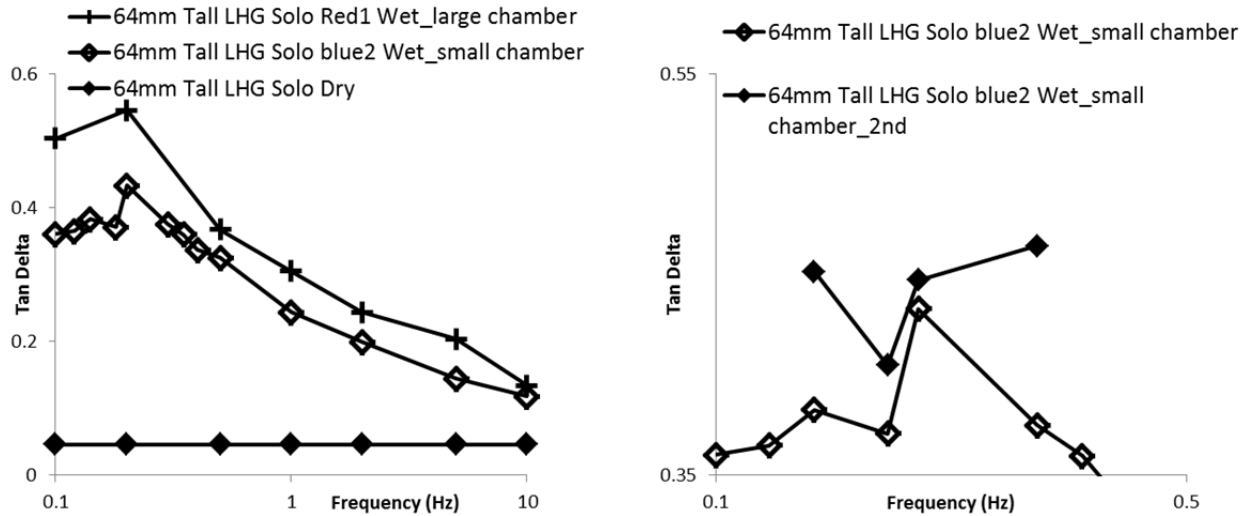


Figure 78. The 64mm tall LHG cyclic test result compares between large and small chamber in the left. TEES tested it again near peak region to show a range of experimental errors.

The right graph in Figure 78 shows that the small chamber experiment shows irregular performance near peak damping. This may be a combination of restricted flow and our current method of compression/compression experiments. We plan to expand our testing to compression/extension and that should clarify the effect.

Manifold Experiments

TEES built manifolds that are 15mm and 30mm long. These manifolds attached at the ends of a 64mm tall LHG, and contained right amount of fluid. To check proper channel closing, we attached a transparent plastic window at the edge. Figure 79 shows damping performance with long and short manifolds. The extended manifolds present larger damping performance than the short ones. In both, the fluid level rises as fluid leaves the LHG; this work against gravity is about the same for both manifolds. Therefore, we expect the extra space in the long manifold is providing an easier exit for the fluid. Near the peak damping region in compression/compression testing, we can lose contact with the specimen. We will use compression/tension tests with new fixtures to eliminate this effect and to understand better the issues at peak damping.

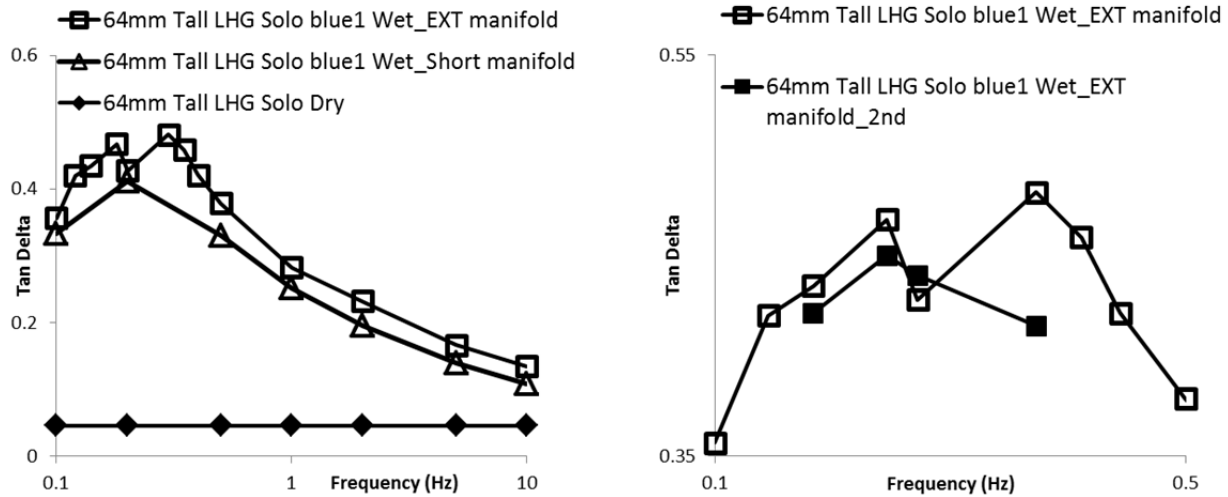


Figure 79. The 64mm tall LHG with short and extended (EXT) manifolds shows different amount of damping. The longer distance from the channel opening to the end of the manifolds affects increasing damping performance.

Load Control Experiments in Chambers

To determine and minimize experimental error, TEES switched to a smaller, 2.5Klb, load cell, switched to load control testing, and repeated the cyclic tests. The lubricated surface between the chamber floor and the specimen let the specimens go into shear deformation that kept them from pumping the fluid. New compression/tension fixtures will eliminate this problem and allow us to test the panels in October.

To determine whether load control would solve the problems with tests at high damping, we built a new LHG and attached a sand paper as shown in Figure 80. TEES dialed the amount load in the MTS machine to achieve the specific amount of displacements across the frequencies. The machine cannot reach the minimum displacement in high frequencies; therefore we will return to displacement control with new fixtures.

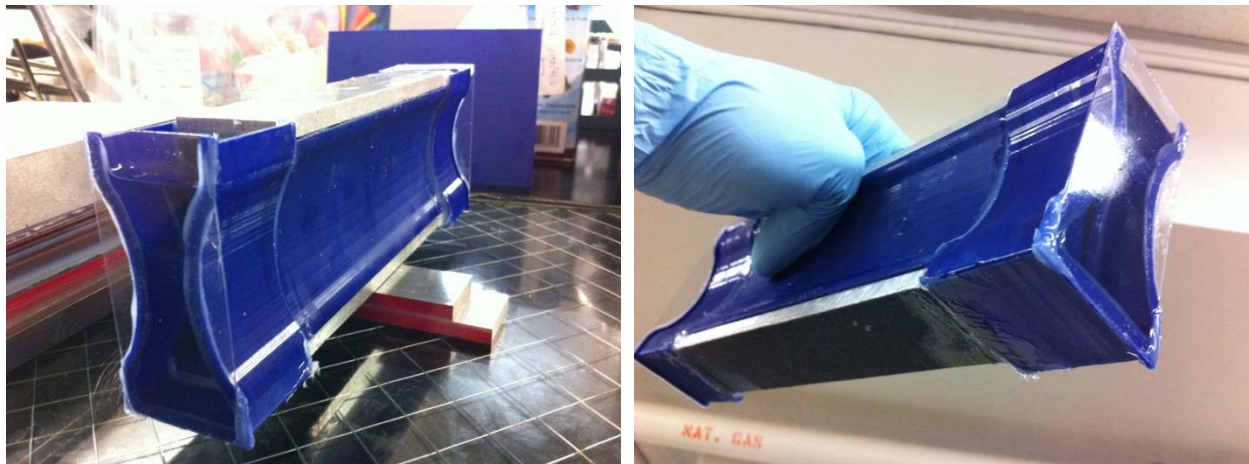


Figure 80. Newly built 64mm tall LHG with an anti-sliding bottom surface is shown.

The damping performance of 64mm tall LHG with 102Kcps fluid in the extended manifolds with force control mode appears in Figure 81. It also exhibit highest damping near 0.2Hz.

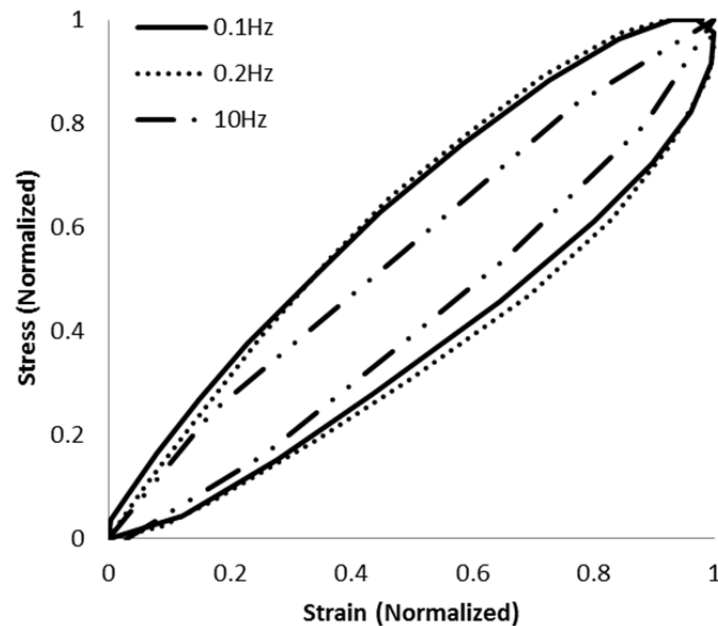


Figure 81. The force control mode operated cyclic test of 64mm tall LHG with 102Kcps extended manifold wet method.

Based on Aerospace Corp.'s design, the damping structure requires push and pull, but TEES has tested with compression-compression case. Figure 82 exhibits new clamp design that helps compression-tension. The six purple columns helps remove shearing, but this clamp attached the MTS machine by screws. We will remove those for manufacturing.

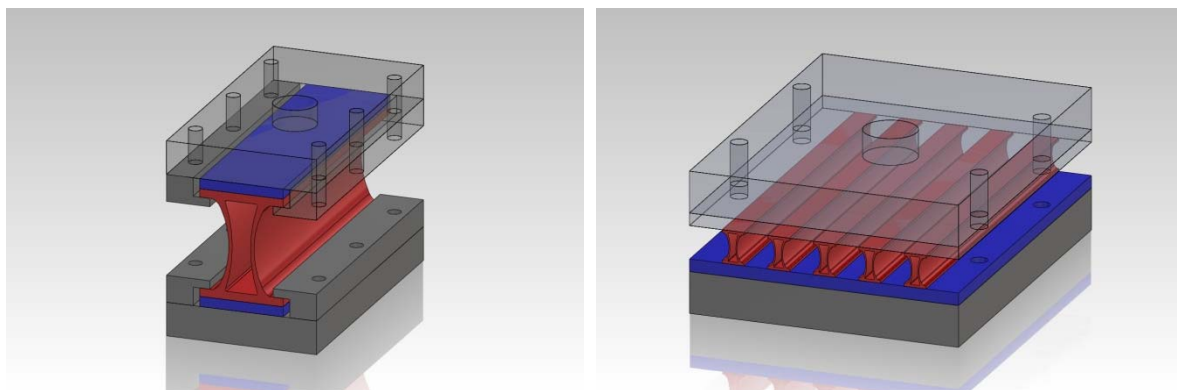


Figure 82. New clamp design helps operates compression-tension test.

Prior fixtures allowed separation between specimen's top surface and crosshead as highlighted in left chart in Figure 83. The new fixture eliminates separation; therefore, it produces a small positive load, which appears as a negative load in our compression graph, because displacements are constrained to the test machine's displacements.

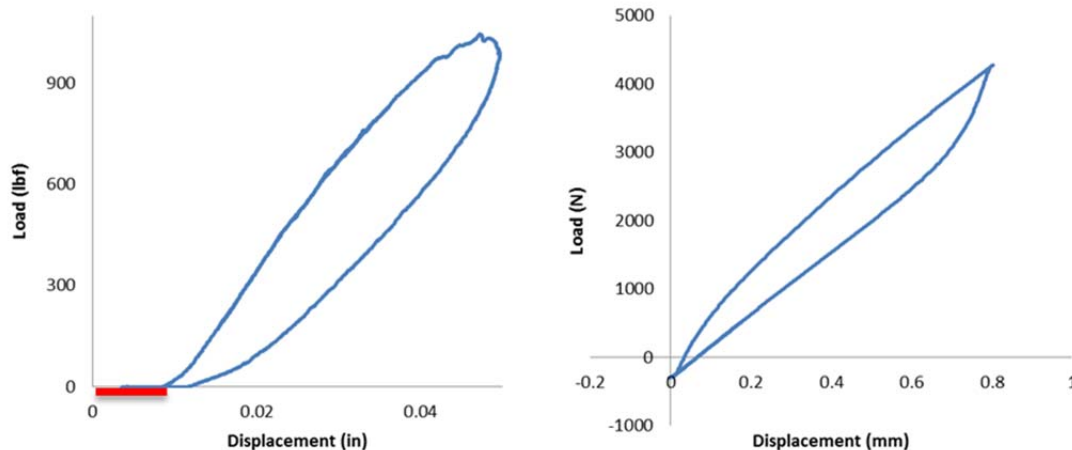


Figure 83. Old grip generated separation (left), but new constrain grip removed it (right).

The first test was compression/compression test from 0 to 0.8mm displacement. The tangent delta value was only 0.163, which is highlighted as a red dot in Figure 84. The normal 1.25mm displacement will produce larger tangent delta—more fluid will be pumped—when we use the hydraulic MTS machine.

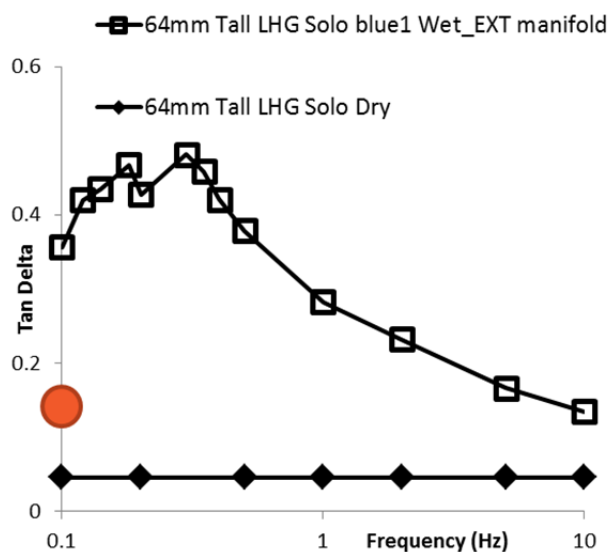


Figure 84. Compression/compression test from 0 to 0.8mm of displacement produced only 0.163 of tangent delta as highlighted as red dot while the plot was made by 1.25mm of displacement compression cyclic load using the old fixture with the MTS machine.

The second test was compression/tension test, $\pm 0.8\text{mm}$ of displacement. Figure 85 presents the test result plots. The upper section is compression part (middle chart), and the lower section is tension part (right chart). The tangent delta values of compression and tension parts are 0.206 and 0.123, respectively. The tension performance is lower than the compression because the LHG's are more effective in compression.

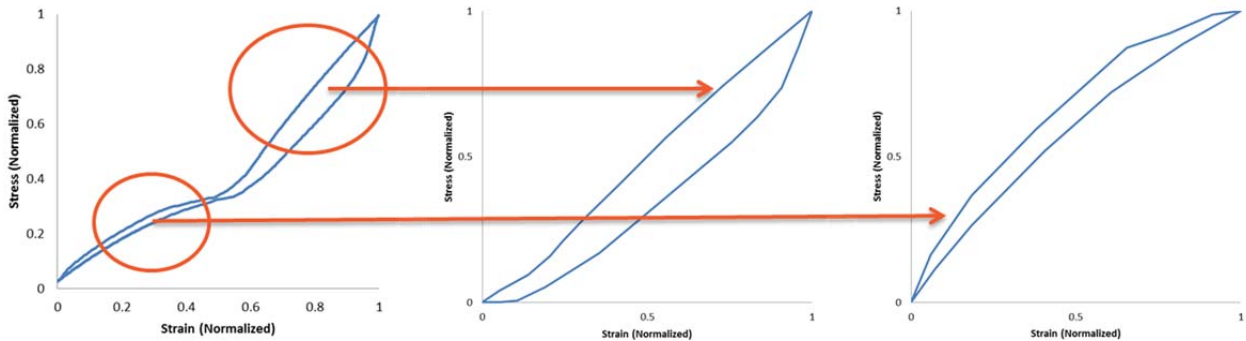


Figure 85. The upper section is compression part, and the lower section is tension part in the $\pm 0.8\text{mm}$ of compression/tension test result.

A new design of LHG array might increase damping during tension as shown in Figure 86. These parallel arrayed LHGs have a void area in between the cells. While the sidewall compresses and squeezing fluid, the void area is opening and accepts fluid. During tension displacements, the center region can pump fluid back into the LHG.

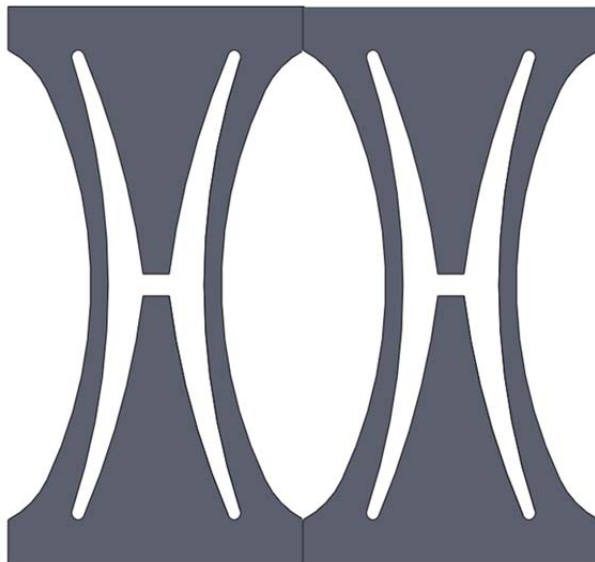


Figure 86. The array of LHGs will help increase damping in tension cycle.

A 60 kcps silicon oil was used to study damping and produce data for AERO's FEA work. Left picture in Figure 87 shows the sidewall marks TEES used to check that the wall closes uniformly along the length. Unlike 102 kcps fluid case, the 60 kcps fluid might splash at 10Hz; therefore, we extended the manifold height. Figure 88 shows loop area plots. The largest area occurs at 0.5Hz.

Previous experiments with 102 kcps fluid—using the old, non-constraining fixtures—exhibited a peak at 0.2 Hz. As expected, the lower viscosity, 60 kcps fluid allowed the peak frequency to move higher. In addition, the damping effect was broader. Figure 89 shows tangent delta values across the frequencies. As expected, the highest peak shifted up to 0.5Hz.

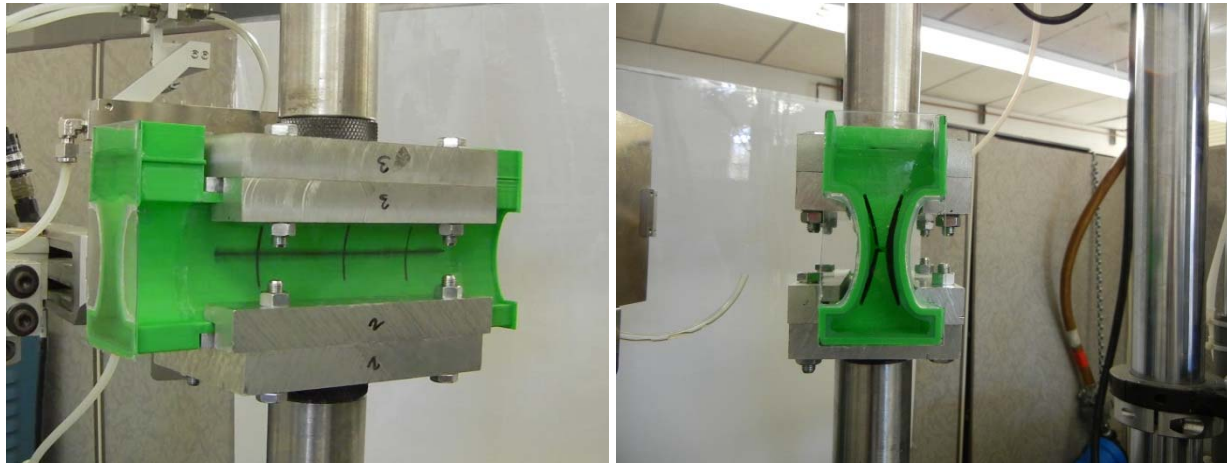


Figure 87. Marks on the side wall in the left figure help TEES confirm that the wall closed uniformly along the LHG's length. This LHG contains 60 kcps silicone oil.

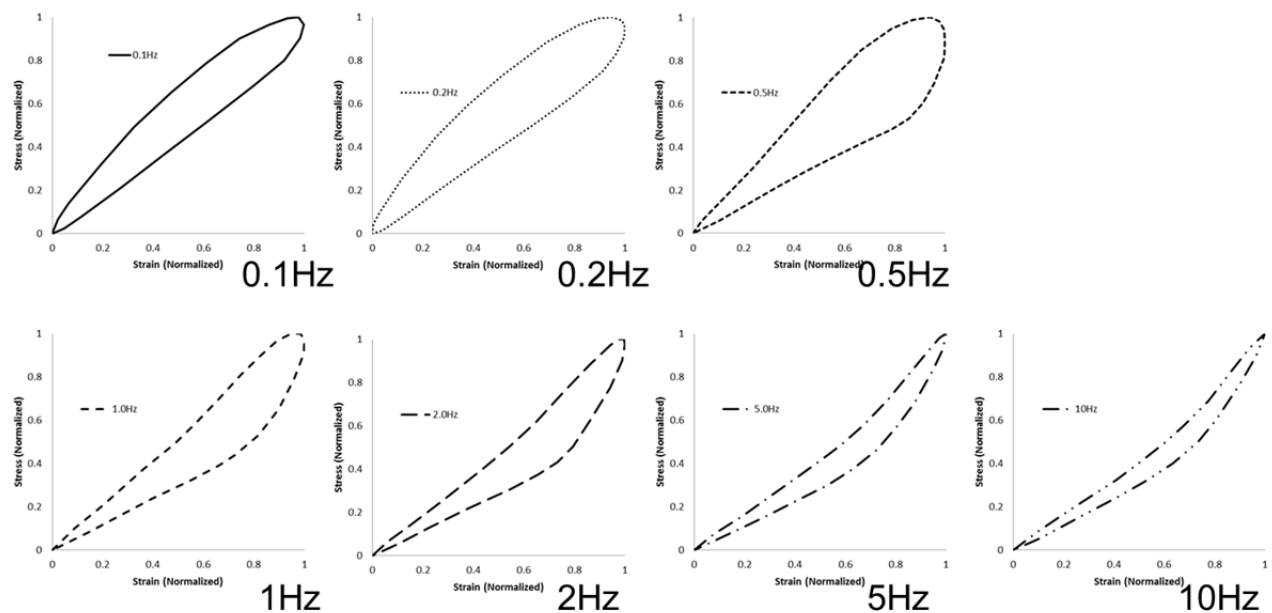


Figure 88. The 60 kcps fluid lets the LHG damp best at 0.5Hz.

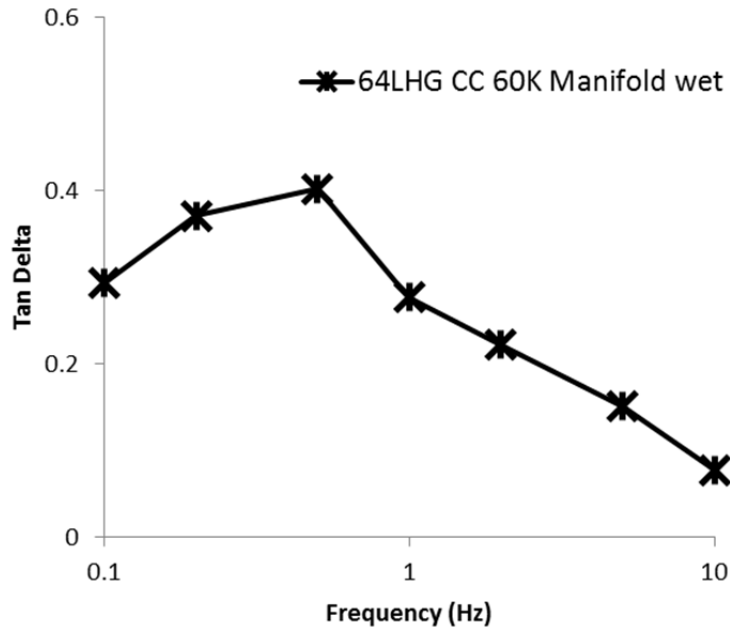


Figure 89. The 60 kcps wet cyclic test results for 64mm LHGs peaks at 0.5Hz.

TEES performed cyclic tests of 64mm tall LHG with three fluids, 102K, 60K, and 30Kcps silicon oils. The fixture clamped the specimen and drove it in both loading and unloading. The applied displacement was from 0.1mm to 1.25mm of compression/compression(C/C). Figure 90 shows the damping performance across the frequency range. The peak damping was at 0.2Hz with 102K and decreasing viscosity shifted the peak to higher frequency as we expected.

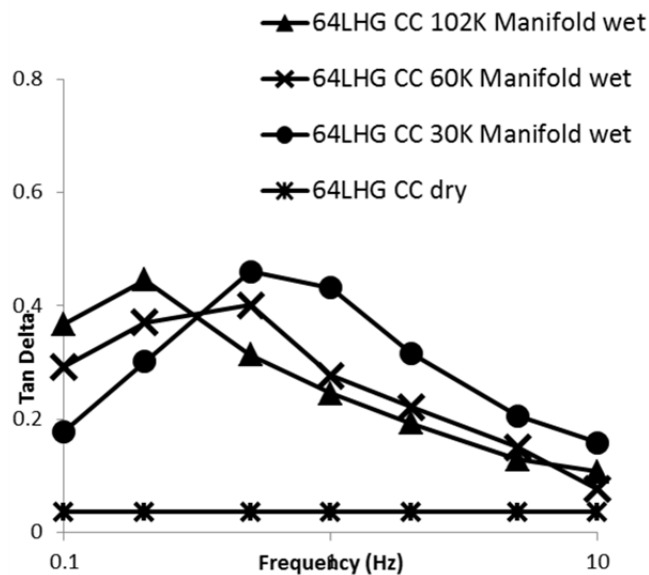


Figure 90. The applied displacement was 0.1mm to 1.25mm for compression/compression cyclic test on 64mm tall LHG. The 102K, 60K, 30Kcps silicon oils helped increasing damping.

TEES also performed $\pm 1.25\text{mm}$ displacement of compression/ tension cyclic tests on 64LHG with the constrained grip. Figure 91 shows the results for each viscosity. CT-C and CT-T are the compression and tension side the cycle, respectively. Top left and right plots are for 102K and 60Kcps cases, and bottom left is for 30Kcps case. Like the C/C case, peak damping shifts to higher frequency as viscosity decreases. The bottom right plot shows compression side damping performance for all three fluids. The damping performance of CT-C is about 40% higher than CC because the tension regime opens the channel wider, so it increases damping performance in the following compression regime. Figure 92 presents the fluid level changes during C/C and C/T tests. The C/T case in the right figure shows larger fluid level change than the C/C case in the left figure.

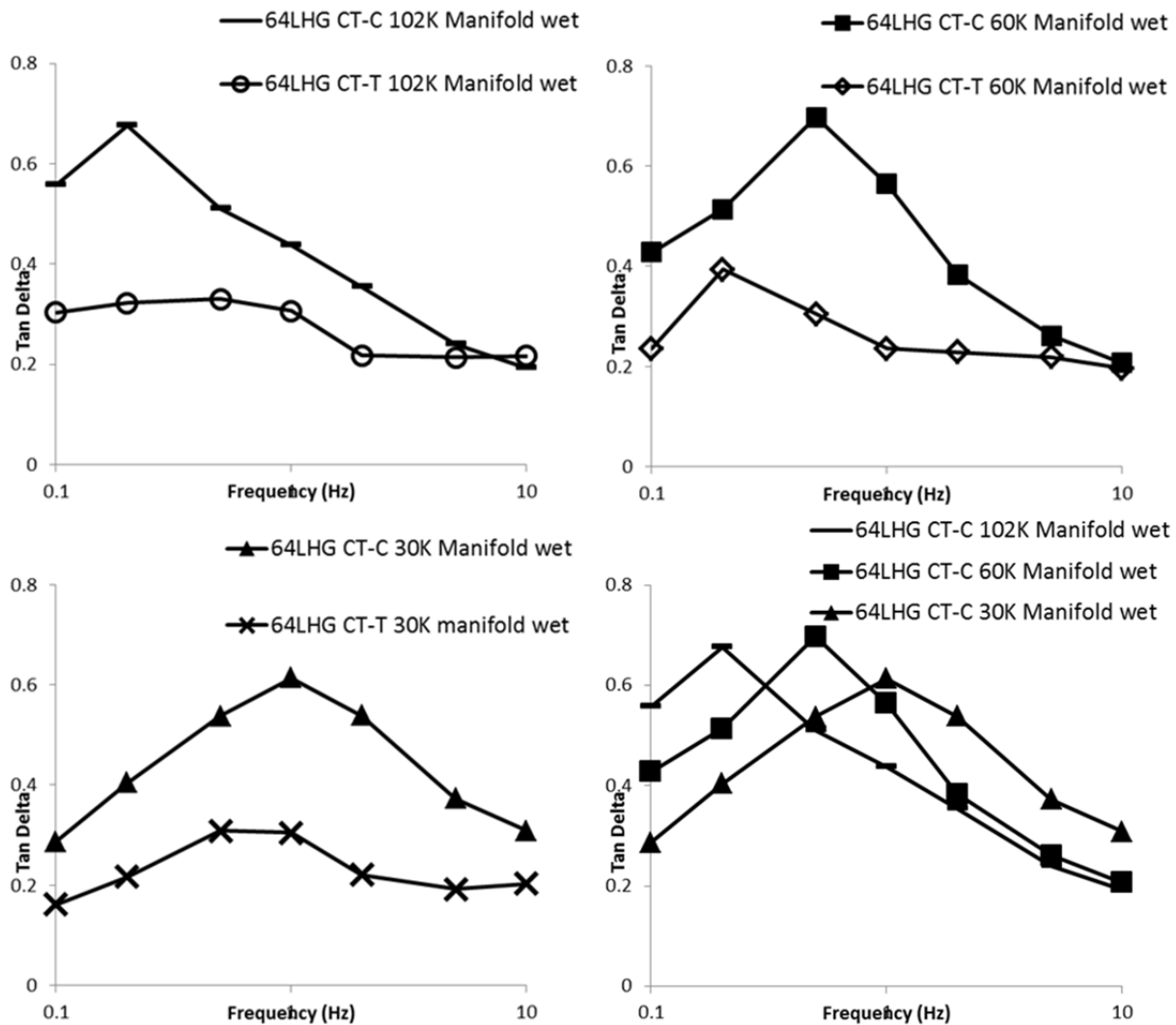
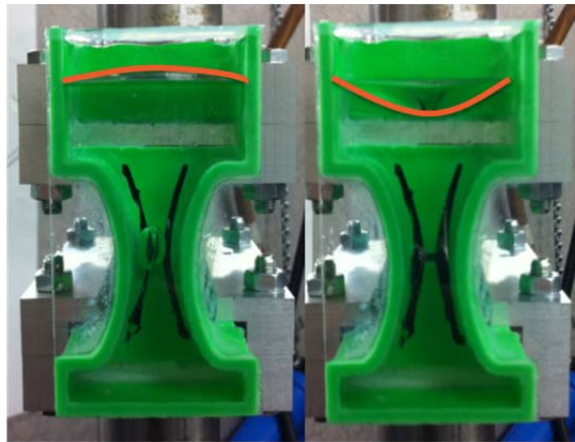
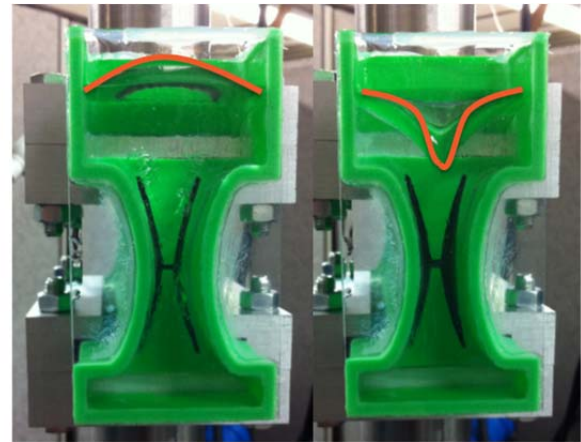


Figure 91. Top left plot is for 102Kcps wet compression/tension cyclic test result. CT-C is the compression side performance, and CT-T is the tension side one. Top right is for 60Kcps case, and bottom left is for 30Kcps case. The peak of the damping shifts to higher frequency with lowering fluid viscosity as shown in bottom right.



Fluid level of C/C test



Fluid level of C/T test

Figure 92. Left figure exhibits fluid level changes during C/C test that shows smaller than C/T test case in the right figure.

Element 2—Shear Thinning Fluid Computational research of HG with shear thinning fluids

TEES is designing an hourglass for shear thinning fluids. Removing the internal geometrical constraints increases the channel cross sectional area and reduces the shear strain rate at the walls. Solidworks simulation results show the displacement for the 0.1Hz case in Figure 93. The maximum displacement of this HG is 3mm before the vertical walls touch each other.

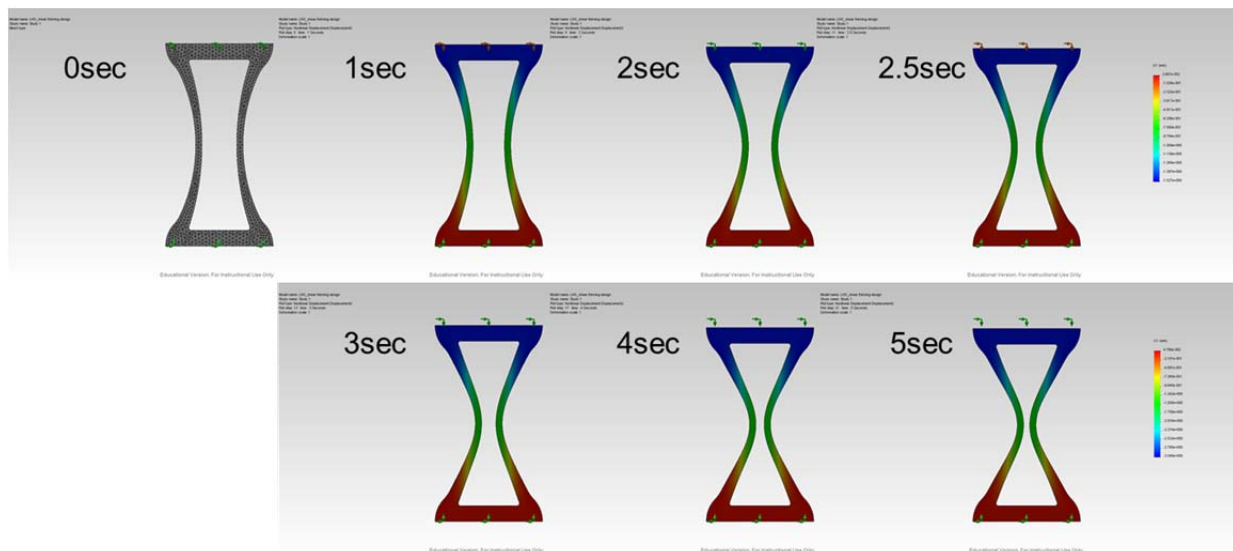


Figure 93. Solidworks simulation results show the displacement by the time at 0.1Hz. The maximum displacement is 3mm at 5 seconds.

We digitized the channel area at each time step, and fit a smooth, cyclic curve as shown in the left image of Figure 94. The region shown is the closing $\frac{1}{2}$ of the cycle. The volumetric flow rate, Q , is the first time derivative of the volume history. The right image in Figure 94 presents the Q , and maximum occurs near 2.5 sec. We built a model with a channel area that is the compression state at 2.5 seconds as shown in Figure 95.

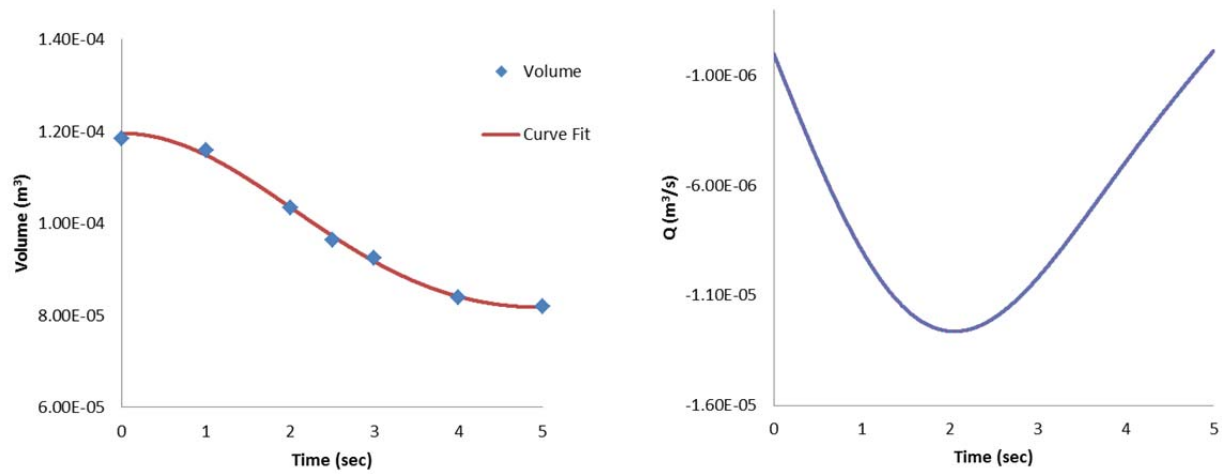


Figure 94. Volume changes at 0.1Hz lead to the Q rates shown in the right image.

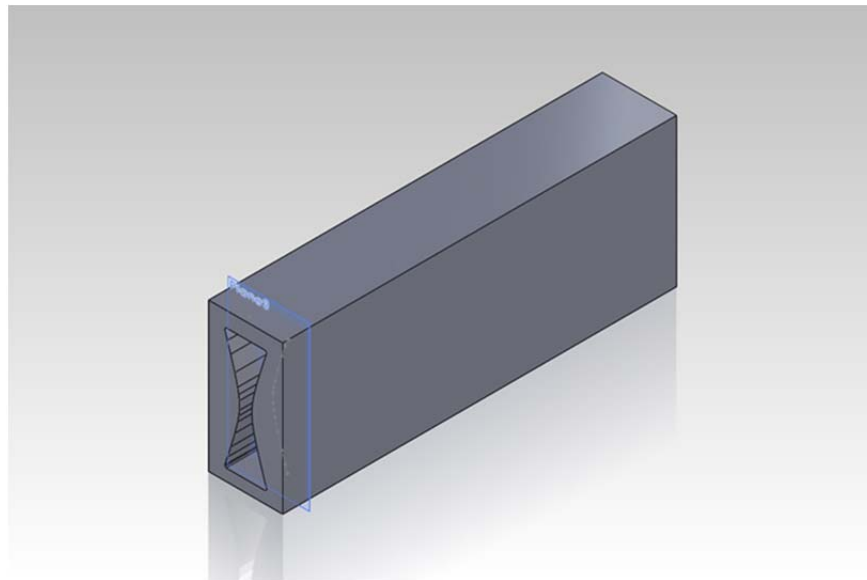


Figure 95. The maximum Q value measured in Figure 74 input in the 2.5 second compressed Solidworks model. The velocity profile plot at the plane, 10mm inside from the exit end.

We plot the velocity at the plane that is 10mm inside from the opening end. In the plane, velocity measured along the top and sidewall at 1mm away from the surfaces as shown in Figure 96. Figure 97 exhibits the gamma dot values obtained from the velocity profiles.

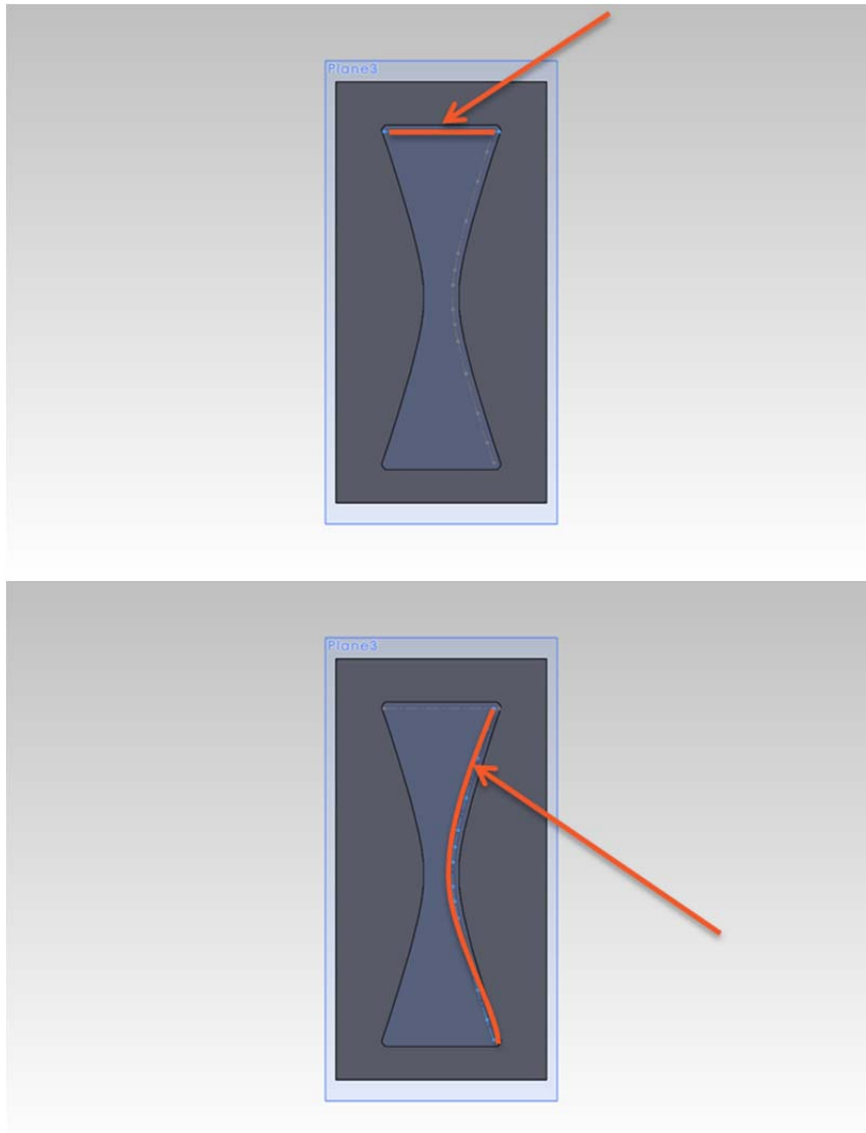


Figure 96. Velocity is measured along the top and sidewall at 1mm away from the surfaces.

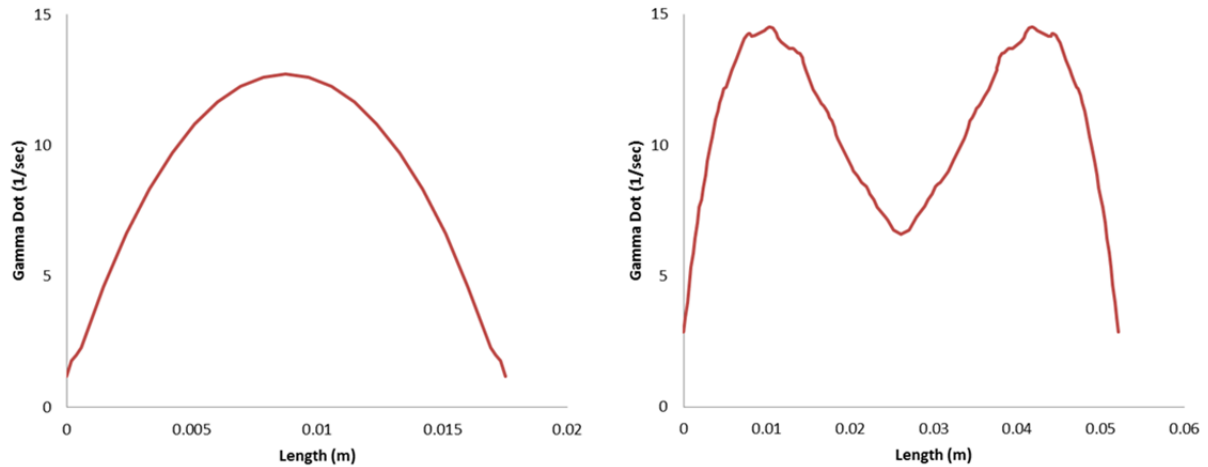


Figure 97. The gamma dot value along the top (right) and sidewall (left) 1mm away from the surface are shown.

To show reliability of the above measurement method, we studied simple circular case as shown in Figure 98. The Solidworks simulation results show 6.234 of gamma dot. According to Kundu*, the relation between gamma dot and Q is in Equation 1. Parameter a is radial direction distance of the tube. At the maximum radius, $a = r$, the analytic calculation shows 6.319 of gamma dot. If we adjust the location of measurement plane, we can obtain even closer results.

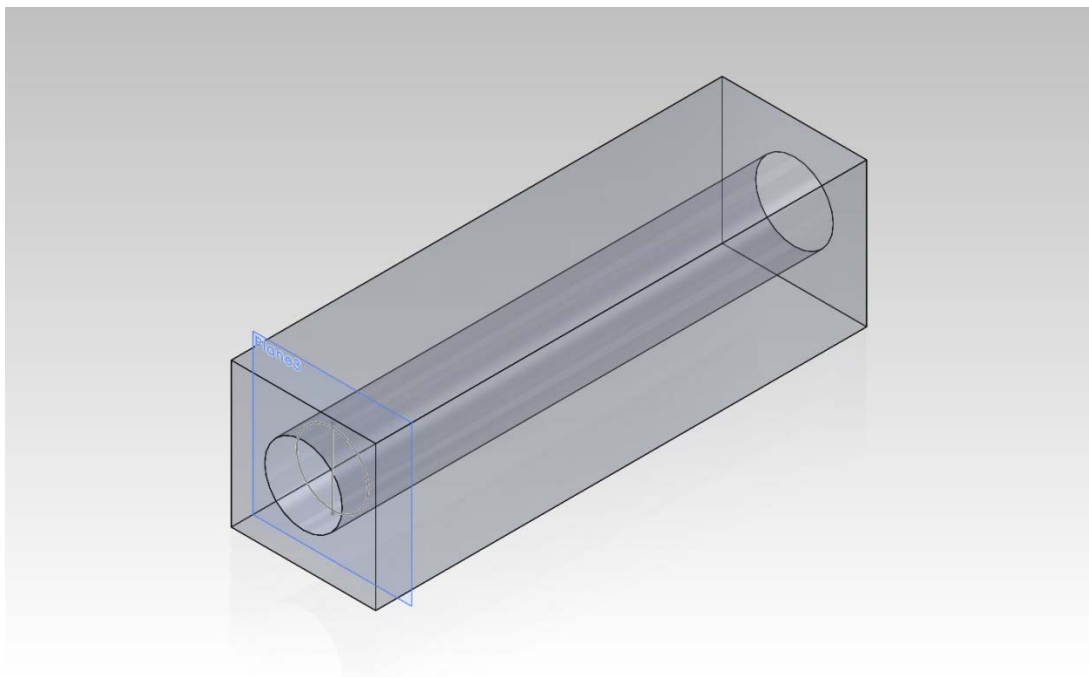


Figure 98. Simple circular shape study shows the reliability of the measuring methods in Figure 97.

$$Q = \frac{\pi a^3}{4} \dot{\gamma}$$

Equation 1

We have a known shear thinning data from Bird, Armstrong, and Hassager** as exhibited in Figure 99. The $\dot{\gamma}$, 15s^{-1} from Figure 97 does not match at viscosity of 102Kcps.

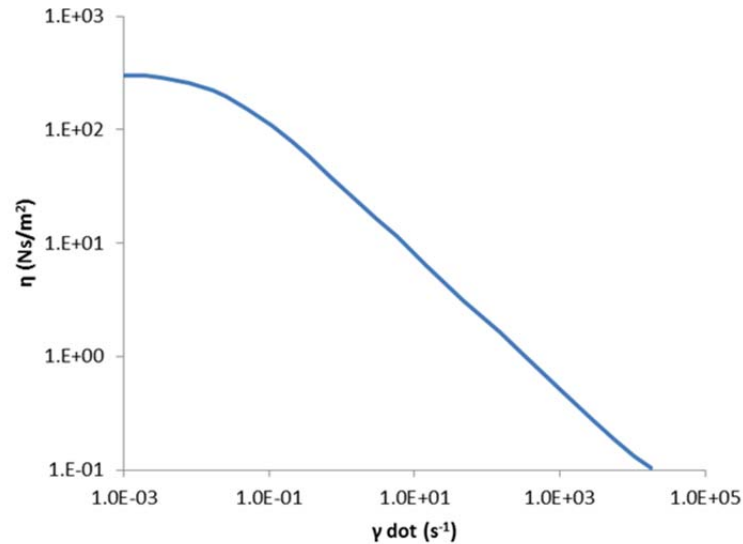


Figure 99. A 1.5% polyacrylamide (Separan AP 30) in a 50/50 mixture by weight of water and glycerin presents viscosity dropping with increasing gamma dot.**

We extended the HG to increase channel area and drop the gamma dot as shown in Figure 100. However, the gamma does not reach our target value of 0.1 even in 100mm extension plotted in Figure 101.

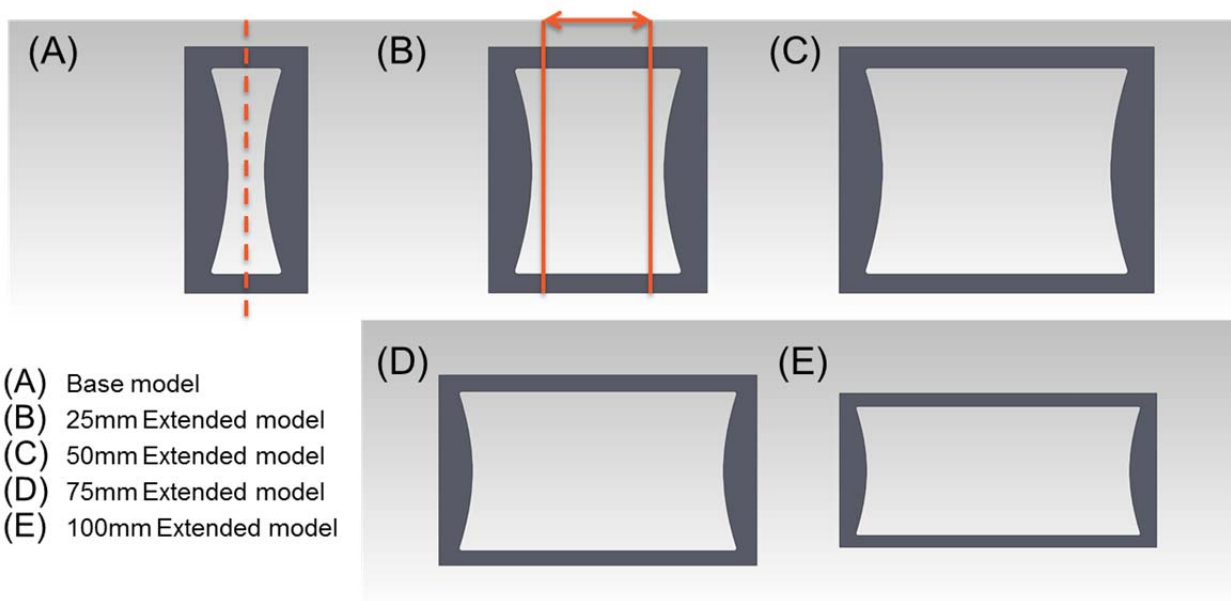


Figure 100. TEES analyze extended HG model to drop gamma dot from (A) 0mm to (E) 100mm.

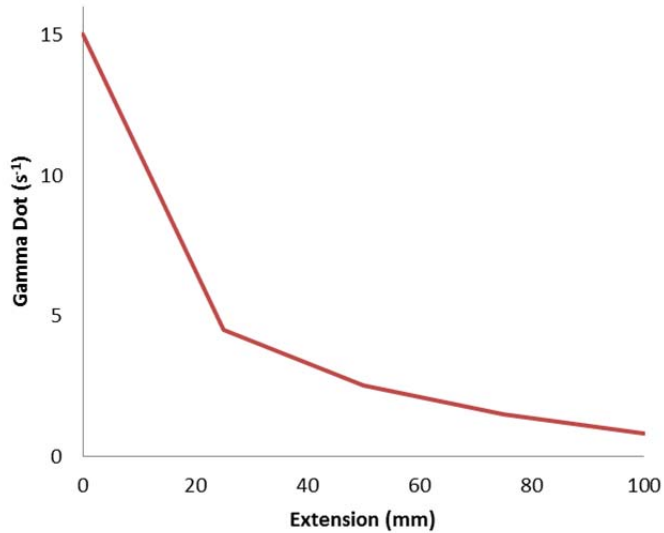


Figure 101. The gamma dot value drops by extension of channel area.

TEES will change the HG design for shear thinning fluid, and manipulate the shear thinning effect by adjusting the amount of polyacrylamide in the mixture.

TEES will test the 64mm tall LHGs with simple 102Kcps simple viscous fluid and shear thinning fluid with 0-1.25mm, and ± 1.25 mm of displacement. Figure 102 presents the grip for MTS machine and specimens. Right one with green manifold will hold shear thinning fluid, and left one held 102Kcps simple viscous fluid.

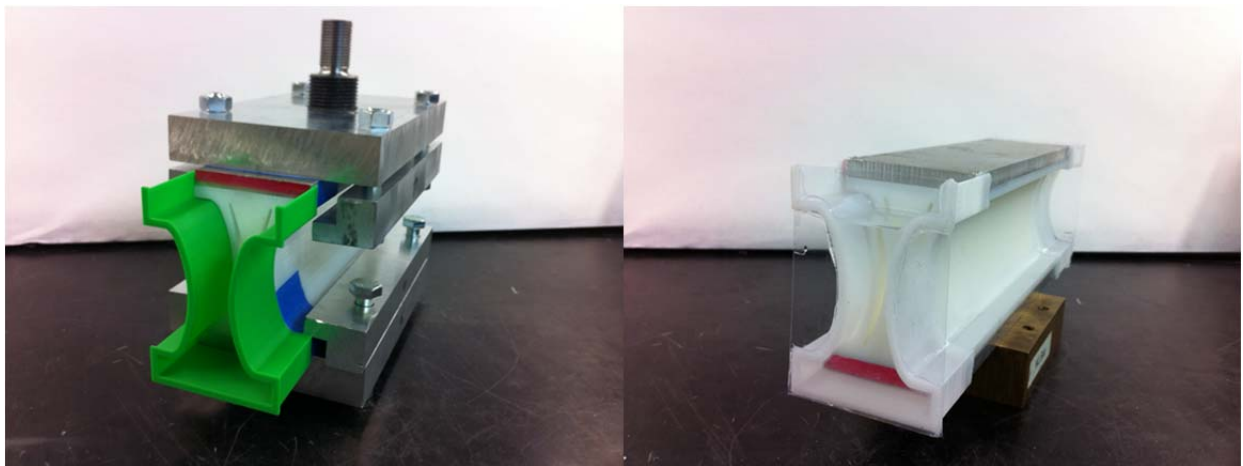


Figure 102. Two specimens that contain shear thinning fluid (left) and simple viscous fluid (right) will be performed two cyclic tests from 0-1.25mm and ± 1.25 mm.

TEES produced a shear thinning fluid with water-soluble polyacrylamide (PAM). The mixture contains 95% deionized water and 5% of the PAM and mixing for 104 hours in a tumbler system helps increase solubility.

Figure 103 presents viscosity by weight percentage PAM in water. It took 104 hours of roller tumbling to blend a 5% solution. Occasional, gentle stirring between tumbling sessions made the solution homogeneous. An air pressured injector was used to put the solution in the 64mm tall LHG. Figure 104 shows the shear thinning fluid in the 64LHG. TEES tested the 64LHG/PAM in compression/compression and compression/tension with displacement control from 0.1mm to 1.25mm for C/C and ± 1.25 mm for C/T. Figure 105 presents C/C result plots that show consistent damping across the frequencies, which is our objective for shear thinning fluids.

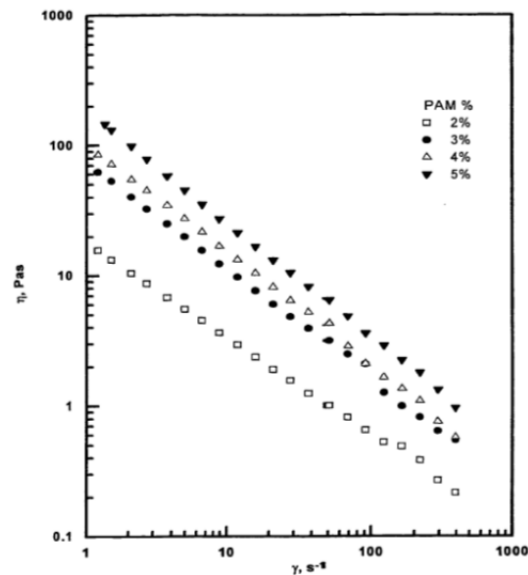


Figure 103. The shear thinning viscosity of PAM solutions shows uniform shear thinning with rising viscosity as PAM concentration increases. - Ali Kreiba, The Rheological Properties of Aqueous Polyacrylamide Solutions

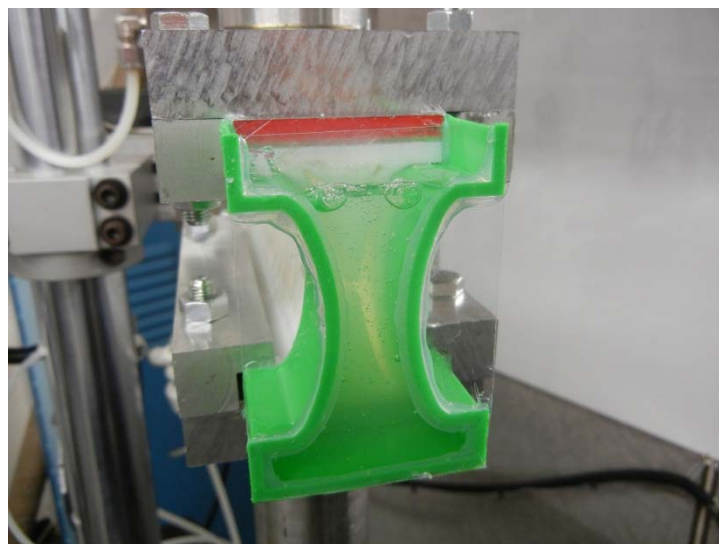


Figure 104. The 5 wt% PAM solution was injected in 64mm tall LHG channel, and installed in the constrained fixtures for cyclic testing.

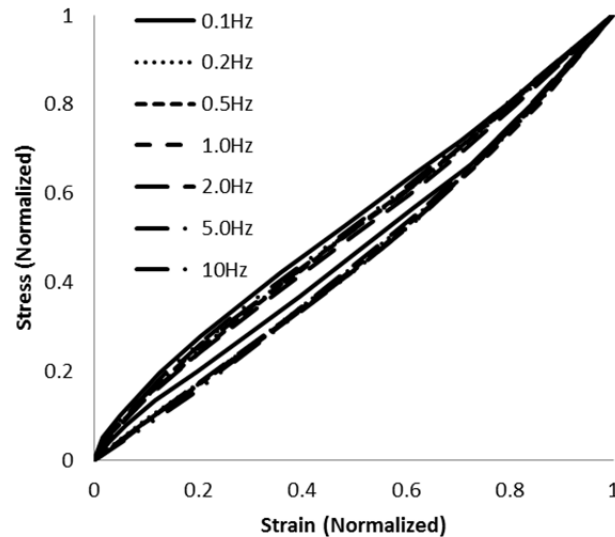


Figure 105. Compression/compression test results for 64LHG with shear thinning fluid shows consistent damping across frequencies.

In compression/tension tests, compression requires less force than tension because the LHG is a pre buckled structure that is easy to compress. Figure 106 presents test result plots. Right chart is compression and left one is tension. Figure 107 presents tangent delta values across the frequencies for C/C and C/T tests. C indicates the compression region and T denotes the tension region. Within experimental error, 5 % PAM/LHG shows consistent damping performance from 0.1 to 10 Hz.

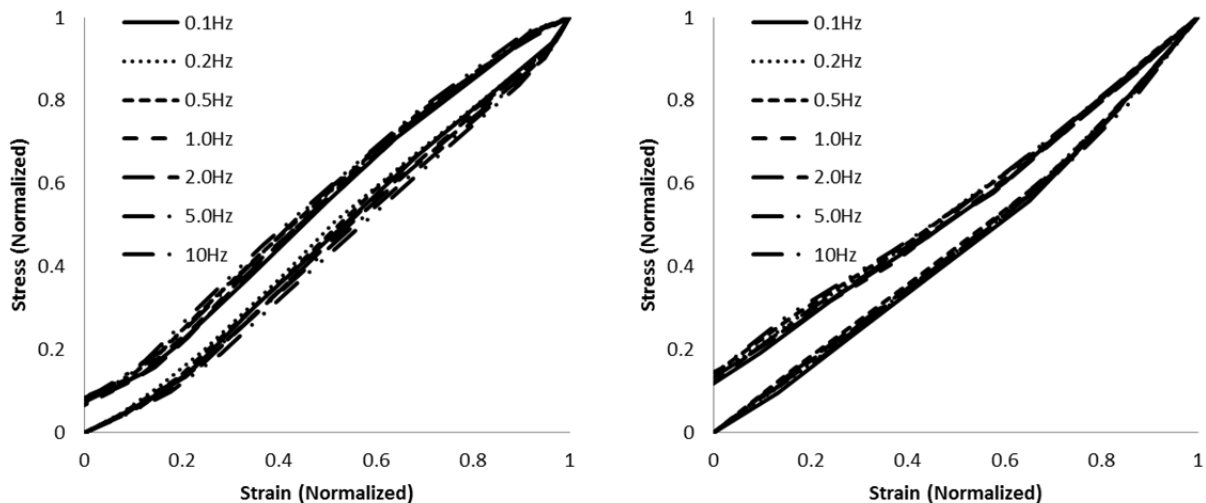


Figure 106. Right chart is compression part of Compression/Tension test results for 64LHG with shear thinning fluid, and left one is tension part. Both charts exhibit no big changes across the frequencies.

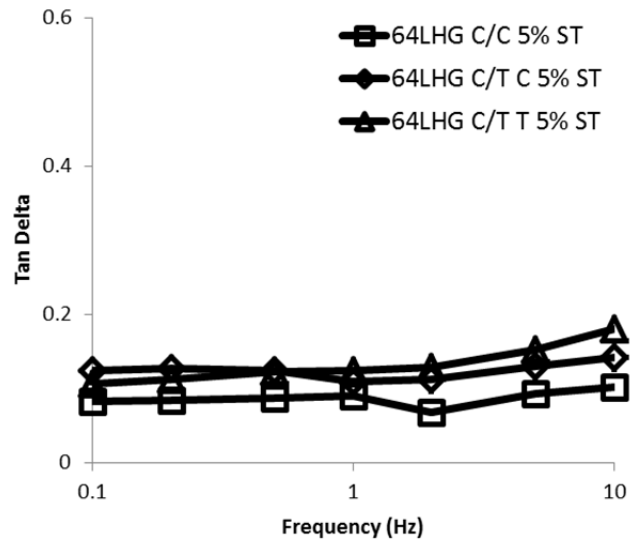


Figure 107. Tangent delta values did not shows big changing and consistent damping performance across our target frequencies.

The 5% PAM solution does not produce enough tan delta, but it shows that shear thinning allows the LHG to have the same effect at all frequencies. The viscosity is too low to produce the best performance. TEES tried to increase the viscosity for the 5% PAM solution by adding 5% PAM to a 50% by weight glycerin/water mixture; however, the glycerin appeared to crosslink the PAM so that it became a rubbery solid rather than a shear thinning liquid. TEES is mixing 7 and 10 weight percent PAM solutions to produce higher viscosity without glycerin.

A second approach that TEES will follow is to put the 5% PAM solution in a 16mm tall LHG array. Previous experiments showed that viscosity scales directly with LHG size; that is, if 102 kcps fluid is effective in 64 mm LHGs, then a 25 kcps viscosity fluid will damp in a 16 mm tall LHG. Therefore, using the same 5% PAM solution in 16LHG provides an effective viscosity 4 times higher.

To produce constant tangent delta through frequencies, we used 5% PAM solution as shear thinning fluid in 64LHG. The results showed flat tangent delta values through the frequency range, but the damping performance was low and did not meet our target. TEES built 16mm tall LHG as a five element panel.

S111 elastomer filled in between the LHG cells and 5% PAM solution was injected in the channel. Compared with 64LHG case, 16LHG has smaller channel, so we can expect higher damping performance with the same fluid because the effective viscosity is 4 times larger. A short reservoir keeps the solution in the channel as shown in left in Figure 108. The constrained fixture clamped the specimen to prevent separation in tension regime.



Figure 108. 16LHG array panel has short reservoir to keep 5% PAM solution in the channel. The fixture clamped the specimen to remove separation between specimen and cross head.

Displacement from 0 to 0.3125mm and ± 0.3125 mm were applied for C/C and C/T respectively. Figure 109 presents the results of 5% PAM wet 16LHG array's cyclic test. Unlike 64LHG case, this array's damping was higher, but not flat across the frequencies and had a peak at 0.2Hz in C/C test. C/T case also showed various tangent delta values.

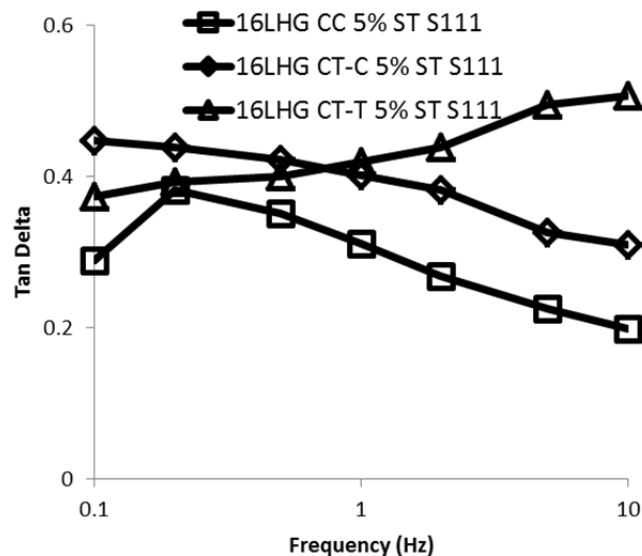


Figure 109. 5% PAM solution wet cyclic test of 16LHG array with S111 filling shows various tangent deltas.

According to Aerospace Corporation, butyl rubber exhibits high damping performance. TEES ordered a layer of butyl rubber from McMaster Carr and added beneath the 5% PAM wet 16LHG array as Figure 110 shows. Adding the butyl rubber layer helps to increase damping as shown in Figure 111. We did not bond the layer and this may cause separation during unloading.

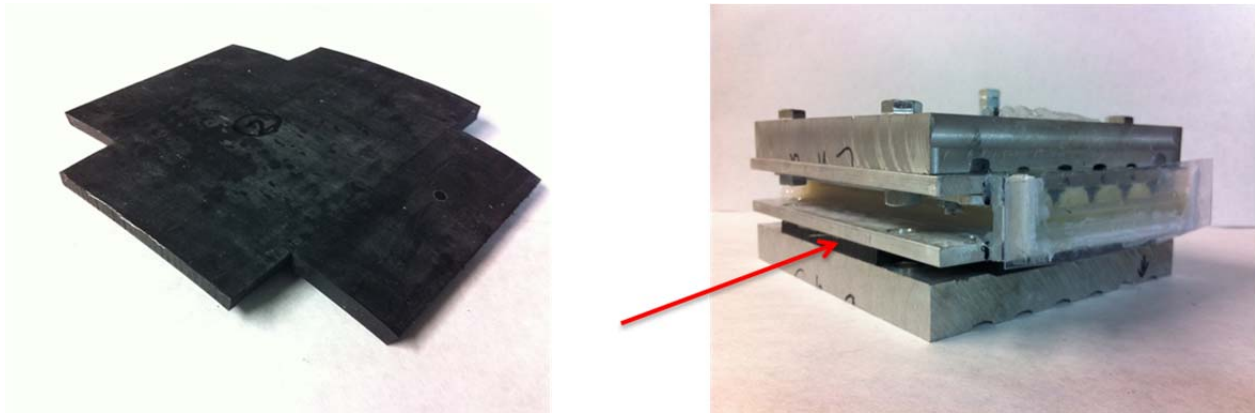


Figure 110. Left shows a layer of butyl rubber, and right figure presents installed state beneath the 5% PAM wet 16LHG array.

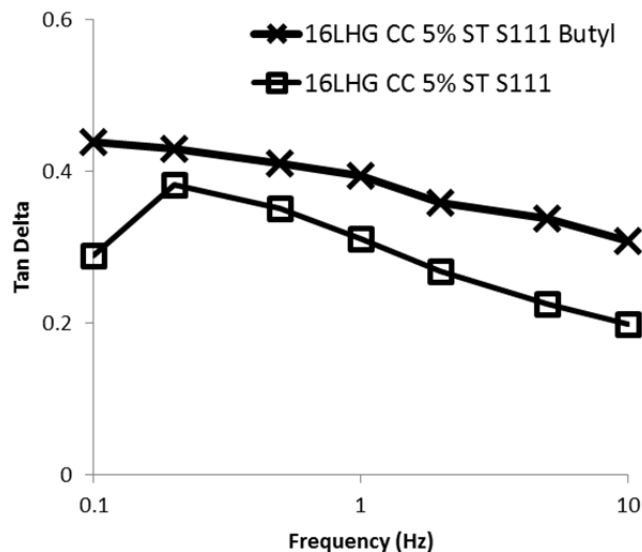


Figure 111. Adding butyl rubber layer increases damping, but the layer was tighten by bolt not bonded by glue that may cause noise at unloading cycle.

Element 3 – Shear Thickening Fluid

Issues with testing the simple fluid elements in chambers and manifolds delayed the model work for the shear thickening fluid element. This work will run in parallel with the shear thinning fluid work in October. The objective is to enhance adaptive damping by having a fluid that flows easily during the low Q sections of the cycle and damps with increased viscosity during the high Q flows.

TEES is reviewing candidate fluid systems for the shear thickening experiments.

The 500 nm spheres are due in early December and 200-mw polyethylene glycol (PEG) is in transit for our first shear thickening experiments.

TEES received 500 nm silica spheres for blending the shear thickening fluid in January.

COMBINE TWO ELEMENTS

TEES combined a 25Kcps silicon oil filled 16LHG/S111 tested previously with a butyl rubber layer and the 16 mm LHG shear thinning material. Figure 112 presents the simple viscous array (left) and installation under the 5% PAM wet 16LHG array and butyl rubber layer (right). Figure 113 shows the effect of adding 25K simple viscous layer. The result is hard to compare directly to the case without the 25K array because the grip separated in unloading condition. TEES will correct the fixtures in January.

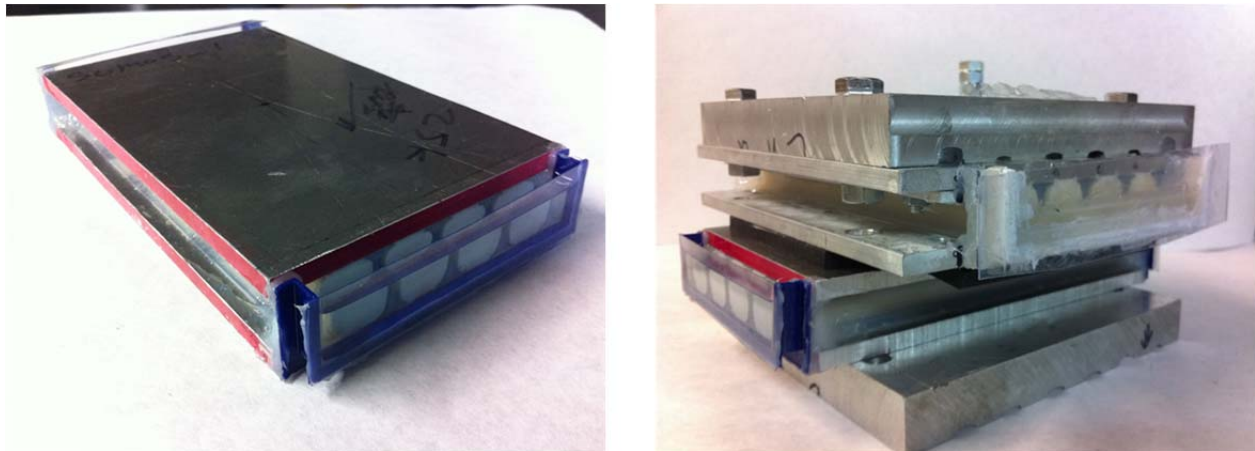


Figure 112. Left figure shows 25Kcps 16LHG array with S111 filling, and right one presents schematic of installation.

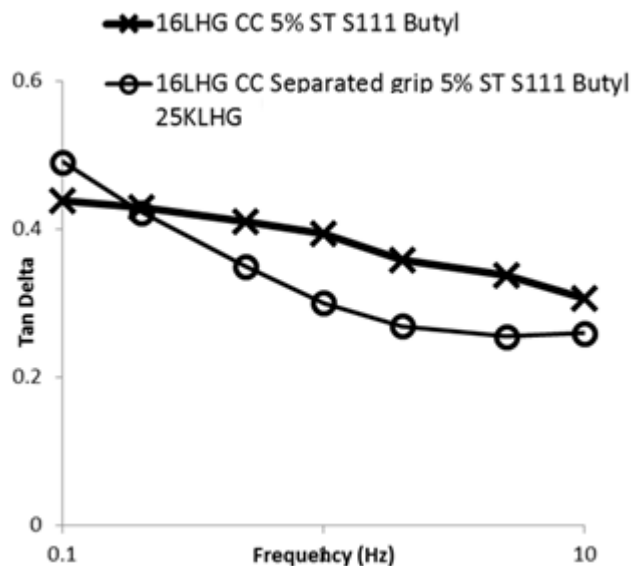


Figure 113. The adding simple viscous of 25Kcps array with S111 filling is shown as circle. Because of the fixture difference, it is hard to compare to without 25K array layer.

TEES built two 16mm tall LHG array panels filled with S111 elastomer between the LHGs. One panel contains 25 Kcps silicone oil, and the other has 7% PAM shear-thinning solution. These

two panels were glued together and tested across the target frequencies. Figure 114 shows the stacked panels in the constraint grip.

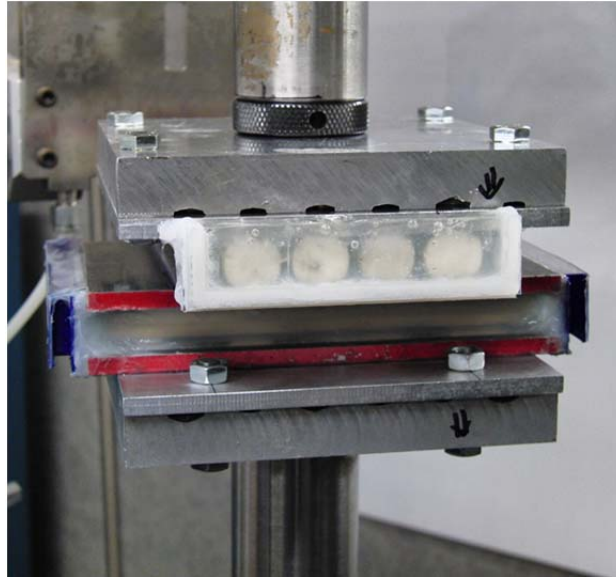


Figure 114. Top 16LHG array has 7% PAM solution, and bottom one has 25 Kcps silicon oil.

Figure 115 shows no advantages of stacking; however, the 7% PAM was difficult to inject and the LHGs contained air in a large void. Large air bubbles disrupt the flow and reduce dissipation. TEES must correct this and repeat this test. We will obtain or produce a longer needle, and inject fluids from the middle outward until fluid leaves the LHG at both ends. In addition, degassing 25 Kcps wet panel will remove dissolved air in the silicone oil.

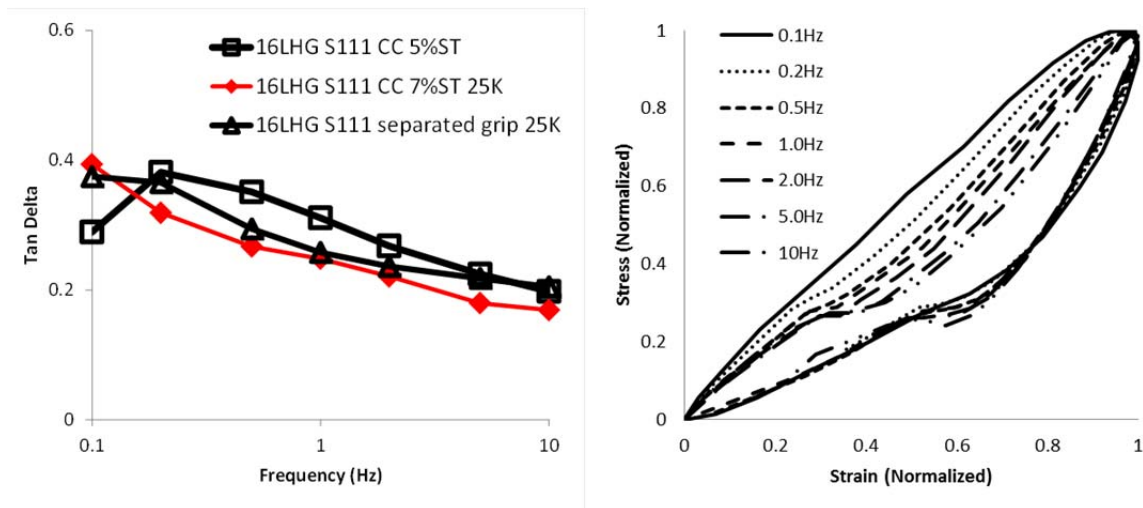


Figure 115. The results show no advantage to stacking panels; however, bubbles in the fluids interfered with the results.

To avoid delamination, we widened the LHG's top and bottom surfaces to increase the bonding area. Right picture in Figure 116 shows the arrayed LHGs on the aluminum skins that has extended skin and large bonding surfaces.

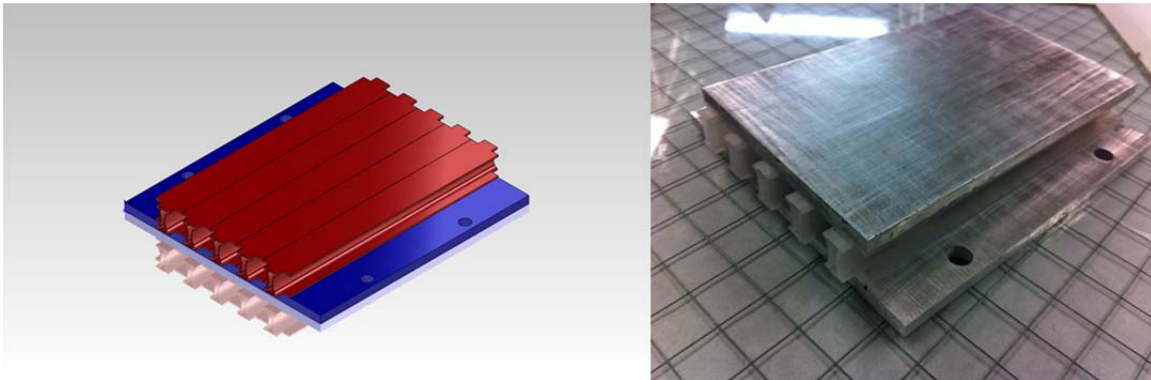


Figure 116. Extended top and bottom skin of 16LHG increases the bonding surface to avoid delamination.

Stacked panel performance

TEES tested a two-array, stacked structure in the cyclic test shown in Figure 117. Top array holds Somos 9120 16LHG with S111 filling and 7% of PAM solution for shear thinning effect. Bottom array is Somos 9120 16LHG with S111 and 25 kcps silicon oil.

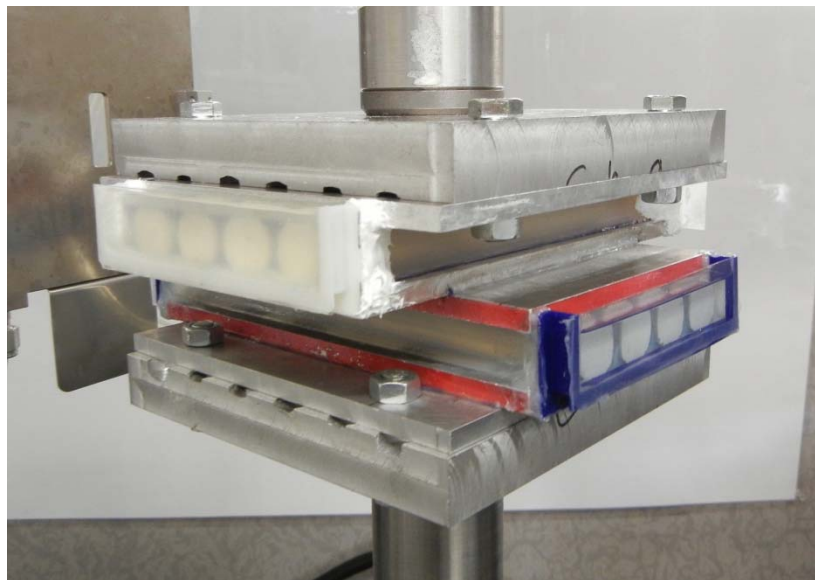


Figure 117. Containing 7%PAM solution in the top layer and 25 kcps oil in the bottom, the two array stacked system was cyclic tested.

Right plot in Figure 118 presents C/C damping. Eliminating bubbles by using 15 torr vacuum pump increases damping by reducing cavitation that limits viscous dissipation.

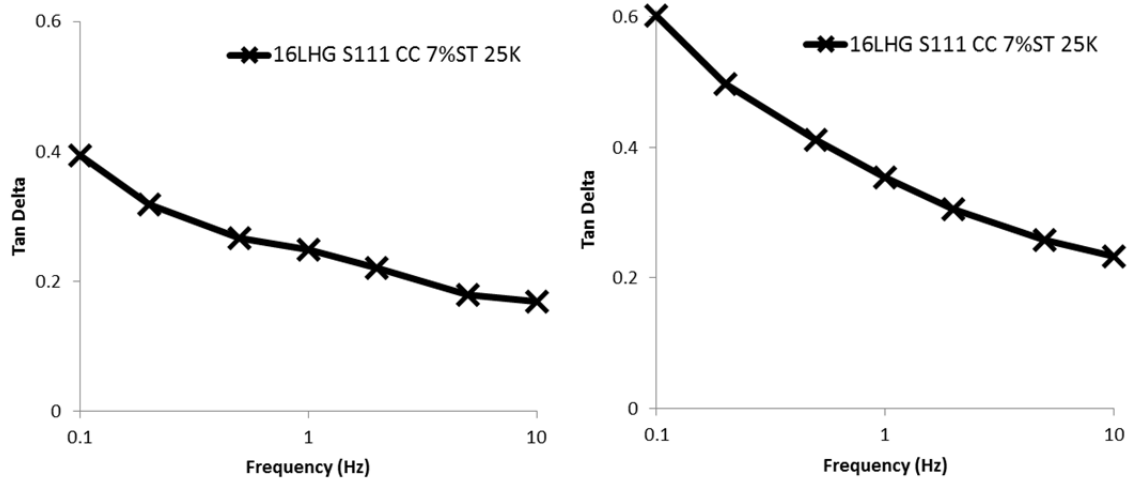


Figure 118. Left: double stacked system's damping before eliminating bubble / Right: after removing bubble by vacuum pump.

Figure 119 shows the case study of half C/T condition. The damping is a little lower in half C/T than C/C, but compression part of half C/T exhibits even higher than 1 at 0.1Hz.

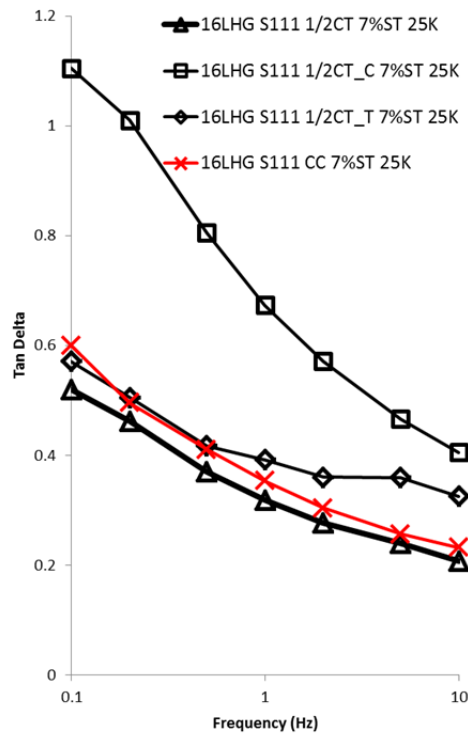


Figure 119. Half C/T case study of 7%PAM and 25 kcps stacked system shows tangent delta greater than 1 at 0.1Hz.

SIZE REDUCTION

This damping structure will be integrated with Aerospace Corp's negative spring constant structure. For following Aerospace's design limitation, we need to reduce the height of LHG array. To check possible size of LHG, TEES ordered up to 6mm tall short LHG to Fineline Corp as shown in left picture of Figure 120. Top one is Somos 9120 that is the same as current 16LHG, and bottom one is Watershed. Both materials show good opening channel in 6mm tall LHG cases. We performed compression/compression cyclic tests on both 16mm tall Somos and Watershed LHGs to show performance comparison. The displacement was the same as normal 16LHG array case, from 0 to 0.3125mm.

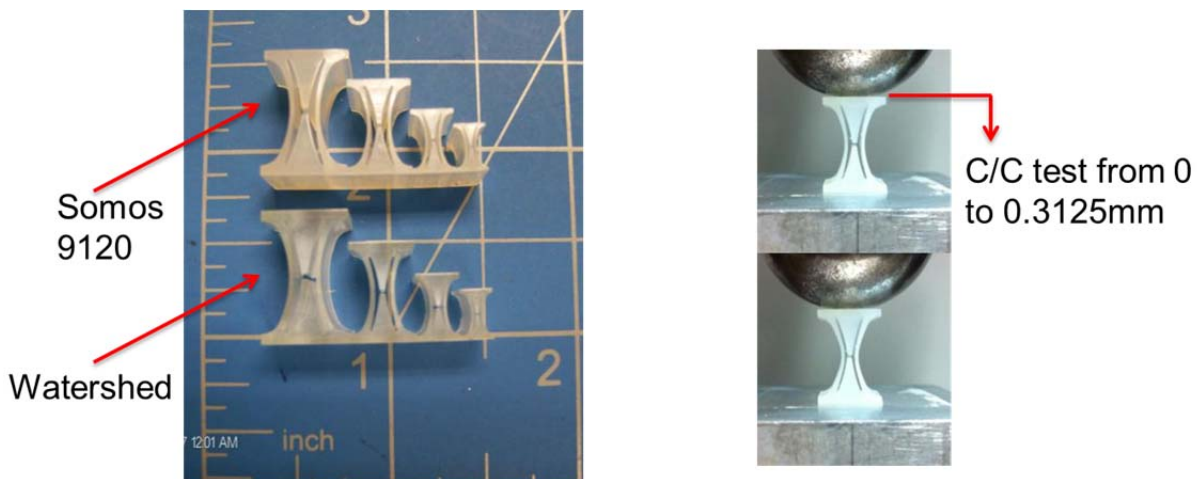


Figure 120. Fineline Corp provided Somos 9120 and Watershed LHGs(left). Both materials' 16LHG were tested in C/C(right).

Figure 121 exhibits the C/C test results. Somos 9120 is softer than Watershed. Both materials did not show large damping performance. The tangent delta for Somos 9120 is 0.098 and for Watershed is 0.043.

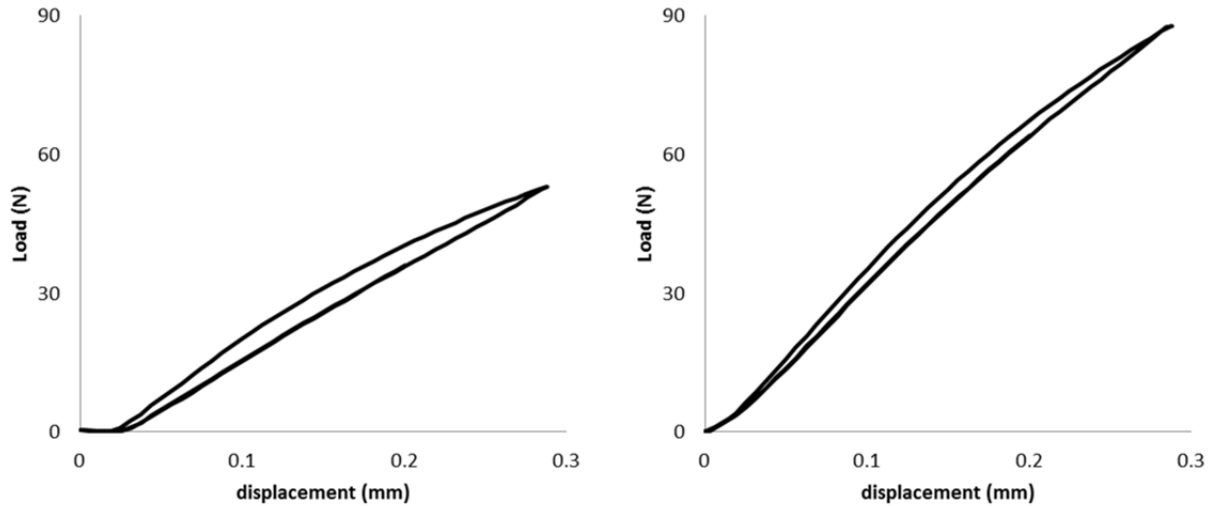


Figure 121. Somos 9120 is softer and higher damping performance. Tangent delta for somos 9120: 0.098 / Watershed: 0.043.

TEES built three types of 6 mm LHG panels for AERO. One was LHG only, another LHG with S111 elastomer, and a third LHG with S111 and 5 kcps silicone oil as shown in Figure 122. However, the specimens are too small to fit TEES' test machine, so we requested testing at AERO. These panels were our first small size panels at the scale that is compatible with AERO's rig.

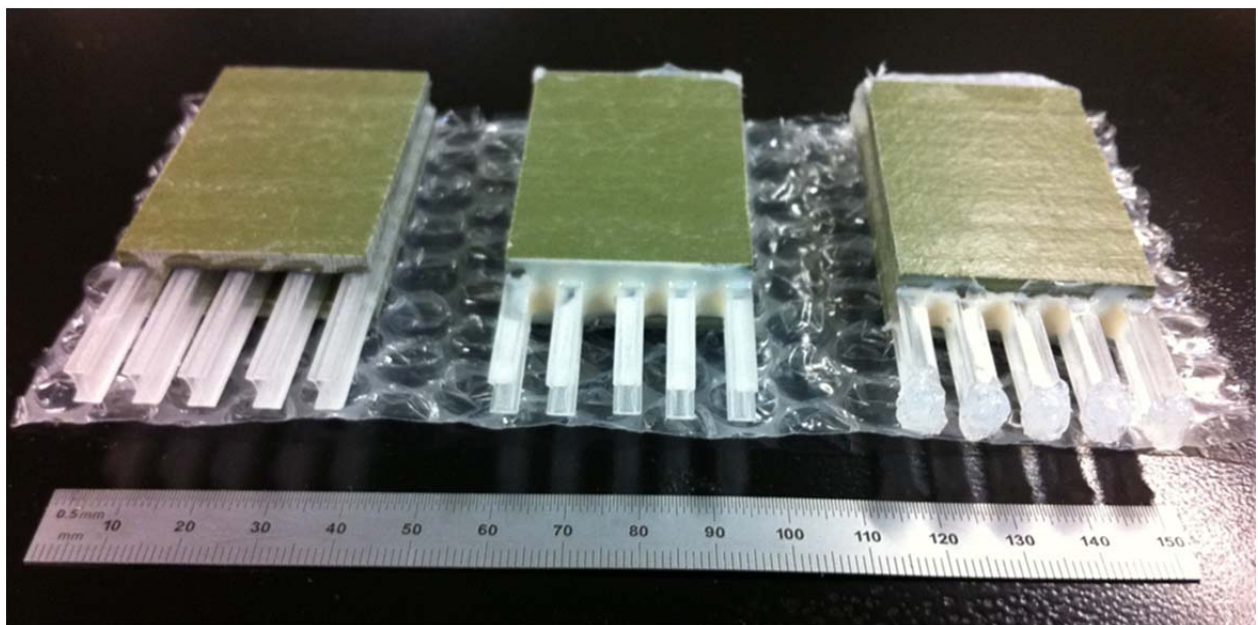


Figure 122. 6LHG array1(machine only), 6LHG array2(machine+elastomer), 6LHG array3(machine+elastomer+fluid) (from left to right).

Figure 123 shows panels built to fit the AERO positive/negative spring experiment. The 6LHG array has S111 filling and 5 kcps oil. The hole in the middle matches the size of AERO's rig.

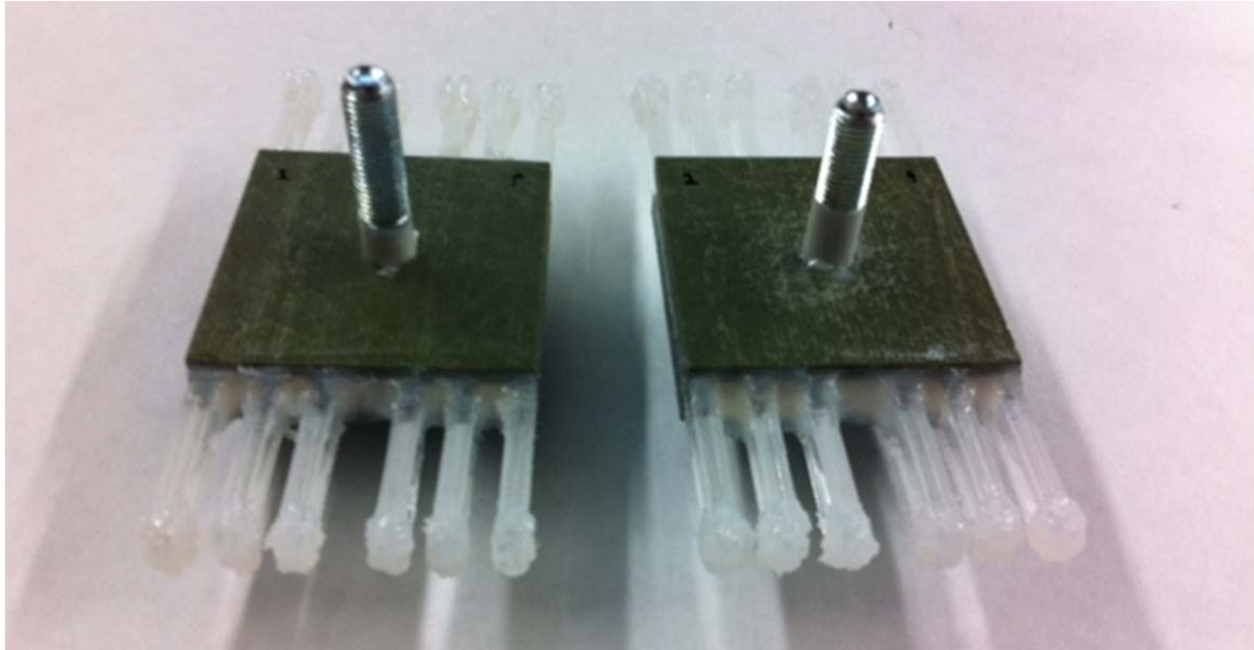


Figure 123. Left: 6LHG array4_full #1, right: 6LHG array 5_full #2.

DESIGN AND ANALYZE DAMPING ELEMENT

Initial program expectations were for damping layers to perform in compression/compression (C/C) alone; however, compression/tension modes might be beneficial to performance and C/C at high damping frequencies always results in tension in the specimen from the lag effect. To assure that the panels can support these tensile loads, TEES performed debonding tests. One determined the bonding strength of Loctite Ultra Control Super Glue between a 16mm tall Somos LHG and the 6061 aluminum skins, and the second determined the bond strength between S111 elastomer and 6061 aluminum. Figure 124 shows a quarter length, 42.5mm, Somos 16LHG and aluminum plates bonded with super glue. The glue requires 72 hours to be fully cured at room temperature. The surface of LHG and aluminum plates were cleaned first and sanded with 150 grit sandpaper in a ± 45 degree pattern to maximize bond strength.



Figure 124. The quarter length of LHG and aluminum plates was tested in Instron to estimate bonding strength of 16LHG array.

Figure 125 presents two experiments. The minimum failure load is 580 N. The specimen was quarter length and the array has 5 cells, so the load the structure can sustain is 11.6 kN as shown in Equation 2.

Equation 2. $580 \text{ N} \times 5 \text{ LHGs} \times 4 \text{ time longer} = 11.6 \text{ kN}$

A finished panel has S111 elastomer injected in-between LHG cells. We do not apply glue between the elastomer and aluminum plates because the elastomer is tacky, it cures in place, and it might bond to aluminum. Figure 126 shows the sandwich panel of aluminum 6061 plates and S111 elastomer. It is also quarter length specimen.

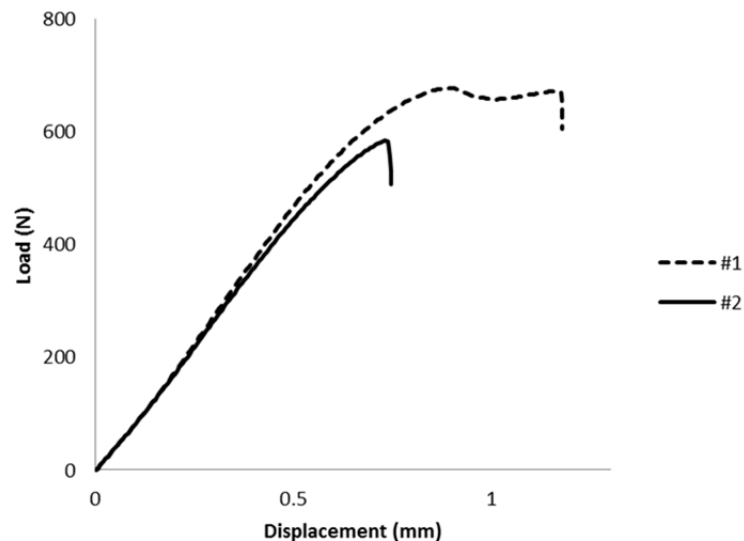


Figure 125. The average bonding strength of Loctite Ultra Control Super Glue between 16mm tall Somos LHG and aluminum 6061 plates is 630N.

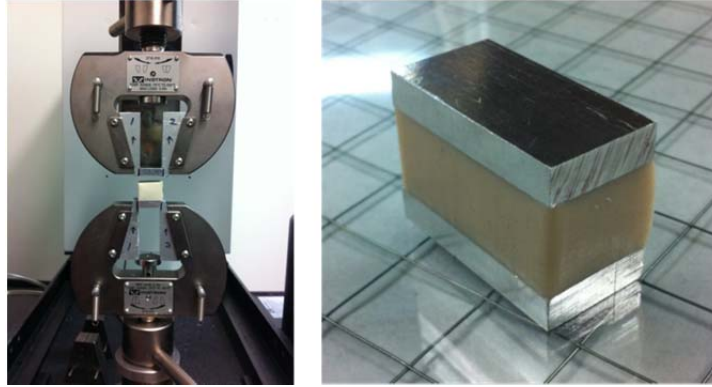


Figure 126. The S111 elastomer might bond to aluminum and support tensile loads, so TEES tested quarter size, sandwich specimen to measure debonding load.

The minimum bonding load is 35 N as shown in Figure 127. The 16LHG array has four times of S111 injection that is placed in between LHGs. Just like previous calculation, Equation 3 predicts 560 N bonding load in the array.

Equation 3. $35 \text{ N} \times 4 \text{ elastomer regions} \times 4 \text{ times longer} = 560 \text{ N}$

Minimum bond strength for a 16LHG array with S111 injection will be about 12.2 kN. Previous experiments showed maximum applied load during cyclic test of 16LHG and S111 panel in compression/tension condition with PAM solution wet case at 0.1Hz was 1.0 kN. The panel should not delaminate by test condition for the duration of the TEES experiments. Bondline strength could be an issue for long term durability.

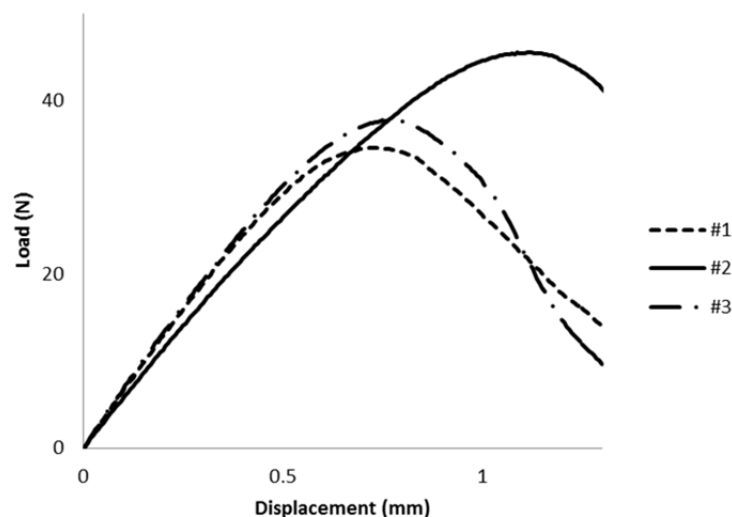


Figure 127. S111 elastomer/aluminum bonds are weaker than the Somos/ superglue/ aluminum bond.

Aerospace Corp's negative spring structure needs a scaled down LHG of 6mm. Figure 128 shows new 6LHG test fixture. Instead of the aluminum plates, we used fiber composite plates. Figure 129 exhibits 6mm tall LHG array made by Watershed LHG and composite plates.

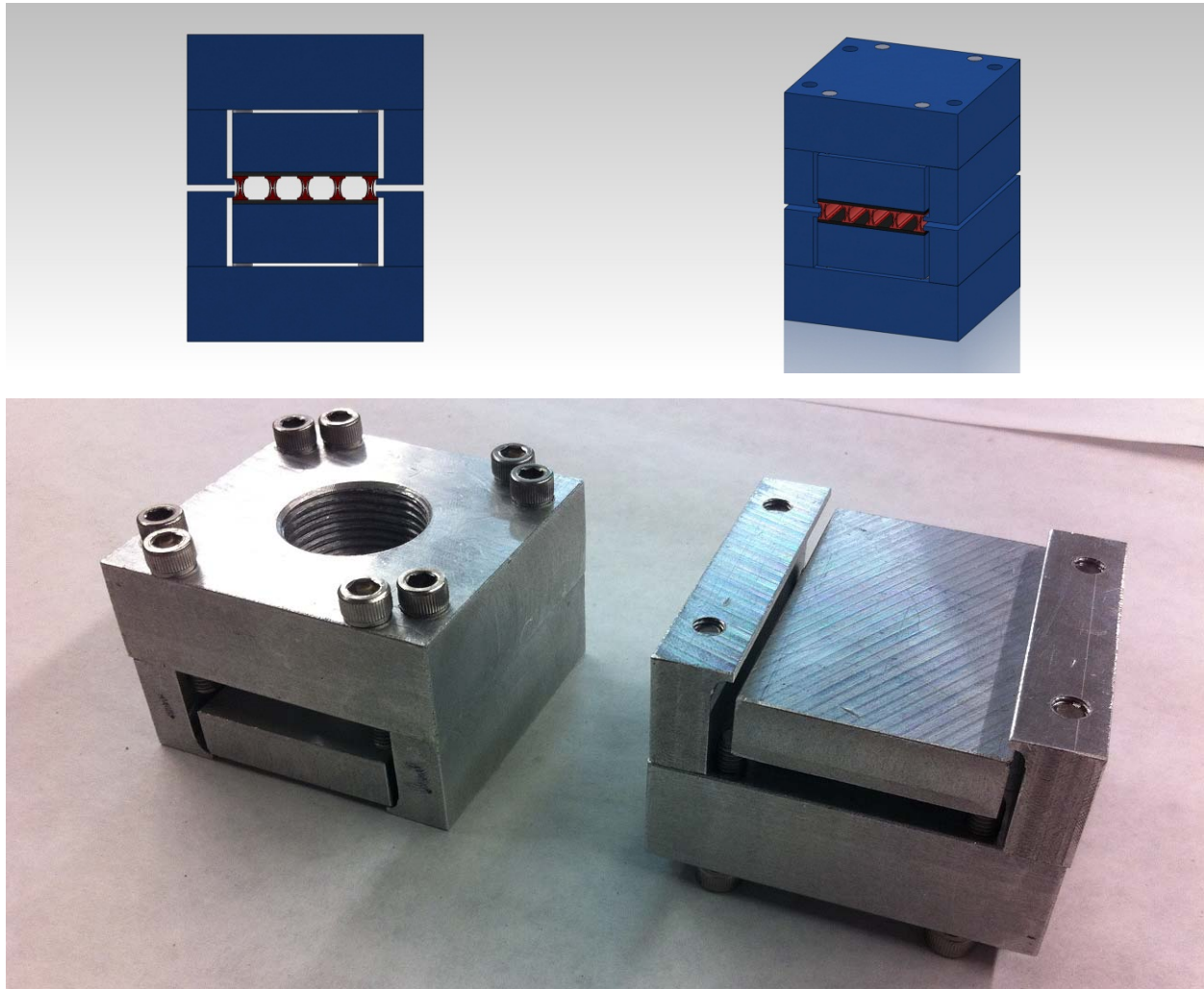


Figure 128. TEES newly designed and manufactured 6LHG array test fixture.

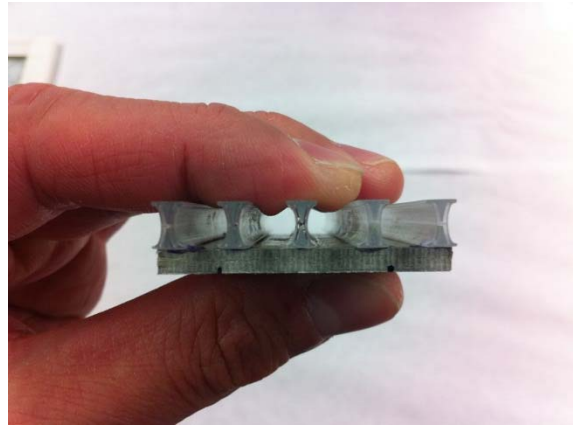
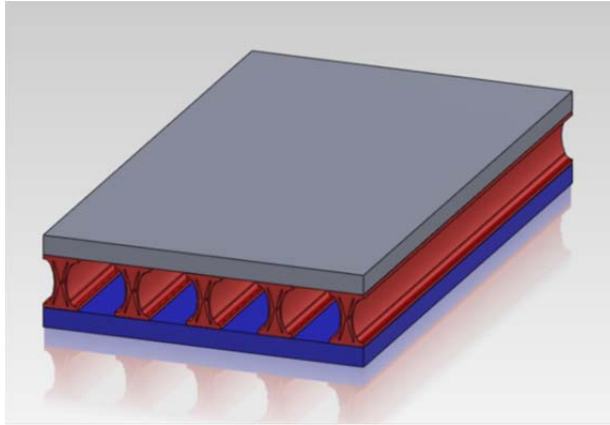


Figure 129. New 6LHG array was made from Watershed material LHGs and composite plates.

TEES designed an LHG with more pumping volume in the same LHG volume. Left figure in Figure 130 presents the normal LHG, and right one shows increased volume LHG. A preliminary 0.1Hz cyclic test will let us compare the performance between LHGs.

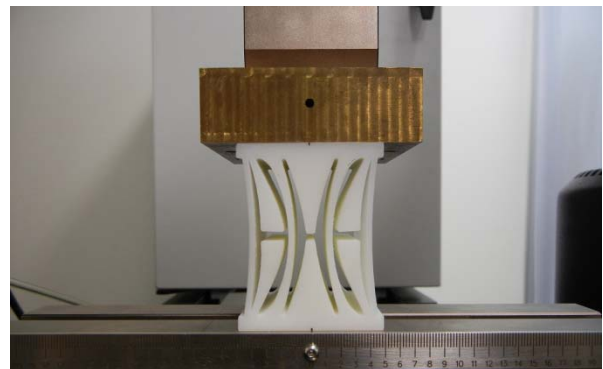
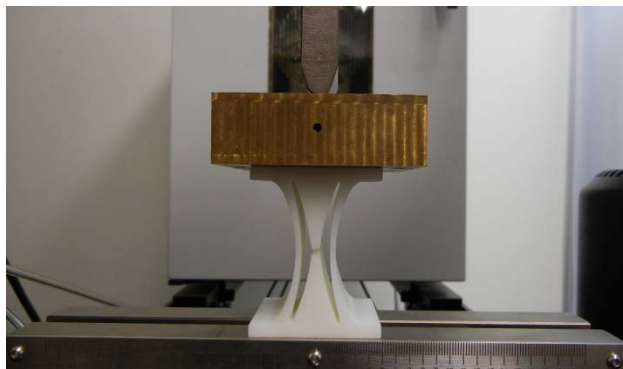


Figure 130. Left picture shows normal LHG, and right one shows an LHG with more pumping volume.

However, the outer shell of shear thickening LHG closed without not moving the inner structure—circled in Figure 131. TEES will update the design to add a web that will act as a hinge and force the gap filling lobes to move inward.

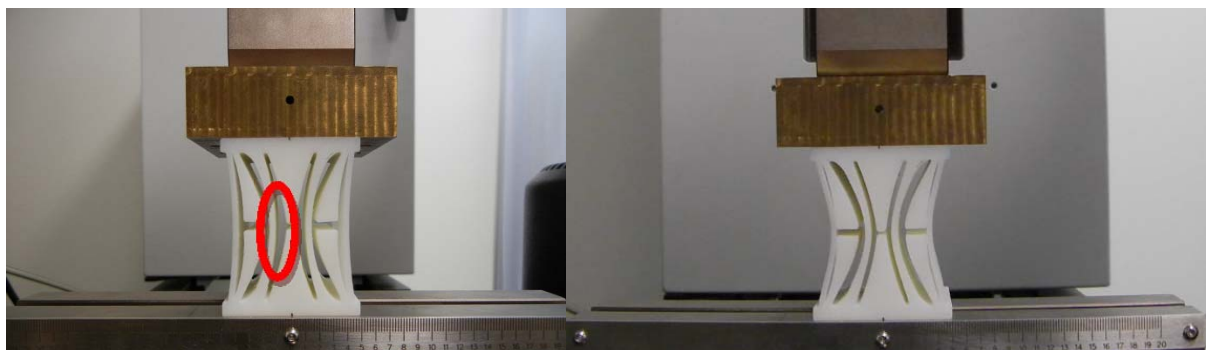


Figure 131. The inner structure—circled in the left image—did not close as expected.

Figure 132 presents the result of a 0dry .1Hz cyclic test. The additional structure stiffens the LHG, which might be a benefit if AERO uses this as part of the positive spring.

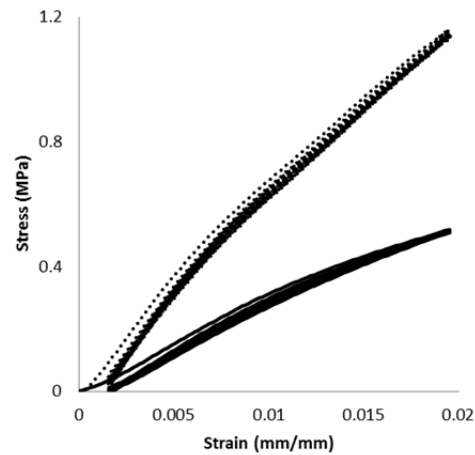


Figure 132. The preliminary cyclic test result at 0.1Hz shows the new LHG is stiffer.

While running the compression/tension test, TEES learned compression/tension shows larger damping performance in the compression region because, when in tension, the LHG structure opens wider and pumps more fluid in compression. When we lift the top surface up 1.25mm as shown in Figure 133, the side wall is straighter and the inner channel area increases.

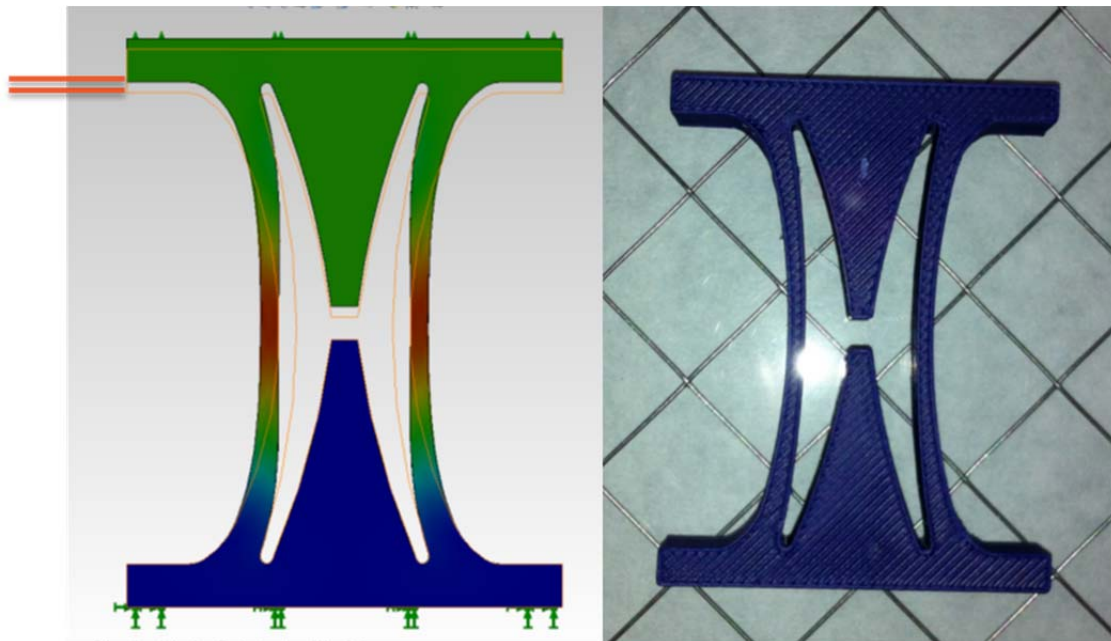


Figure 133. New LHG design has straighter sidewalls and larger inner channel area.

Figure 134 presents a concept ring 16LHG damping element. It matches the volume fraction for the linear LHGs. We will use an injection method that does not entrain air bubbles. This element will be installed vertically with the cone reservoirs facing upward.



Figure 134. Ring type 16LHG concept shown with reservoirs.

We built a new, 64mm tall LHG that has a narrower channel that we call the New Trial Geometry or NTG. Figure 135 shows the shape difference between the NTG, 65LHG, and 64LHG. The 65LHG shape matches a 64LHG drawn 1.25mm taller by tension forces. The 65LHG has a larger volume of fluid to pump. It allows only compression/compression performance. During our first experiment the interface between 65LHG and reservoir failed because of the increased side wall motion. We will fix this issue and complete the 65LHG C/C test.

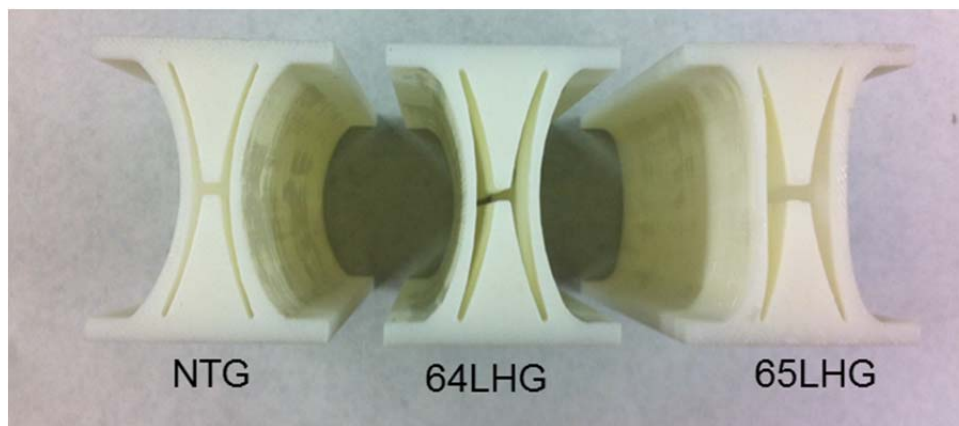


Figure 135. Left: New Trial Geometry has narrow channel / Middle: normal 64LHG / Right: 65LHG has straightener side walls and 1mm more height than 64LHG.

TEES filled the NTG with 100 kcps to compare the new shape with our 64LHG at 0.1 and 0.2 Hz. Figure 136 shows the performance is lower; however, we did not degas the fluid properly. In addition, AERO's analysis calls for 60 kcps fluid. We will correct the experiment with degassed 60 kcps fluid. Figure 137 exhibits 60 Kcps wet NTG that was degassed for 36hours.

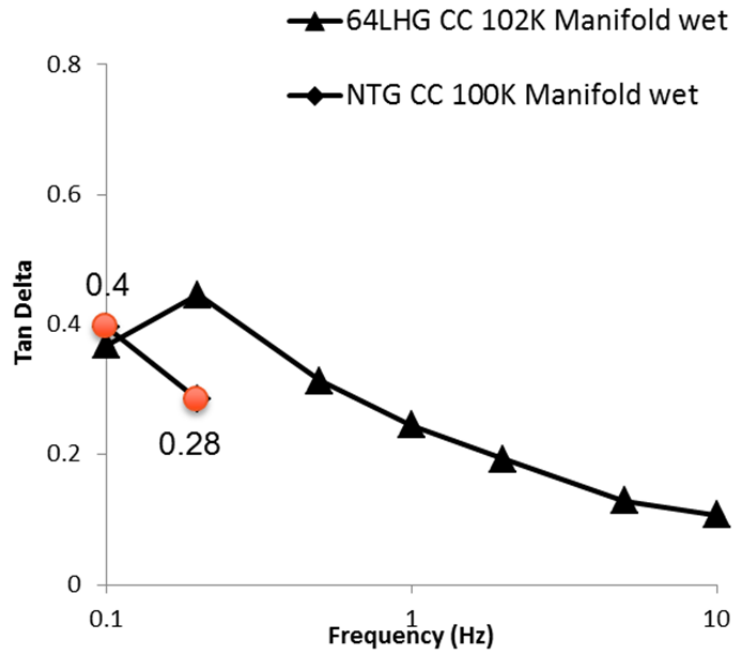


Figure 136. NTG shows less damping performance compared with normal 64LHG; however, bubbles interfered with the flow.



Figure 137. 60 Kcps wet NTG was prepared with 35 hours degassing.

TEES built the double LHG (DLHG) that has a larger pumping volume shown in Figure 138, and will test this element with the constraint fixture shown at right. Both 60 kcps and shear thickening fluids will be tested in this element.



Figure 138. Double LHG will be performed with shear thickening fluid and 60 kcps silicone oil.

According to Amanda S. Lim (2010), 54, 52, and 50% volume fraction silica particles in the suspending medium polyethylene glycol (PEG) shows shear thickening. Figure 139 shows the relation between shear stress and viscosity for these fluids. We baked the 500 nm diameter silica particles at 185C for 5 hours and hand mixing and rolling them into PEG for 72 hours.

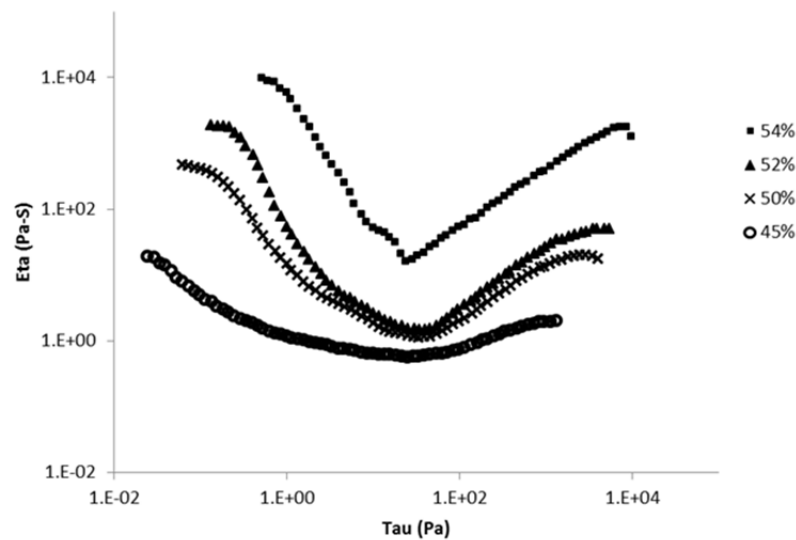


Figure 139. Behavior of shear thickening fluid(STF).

Shape studies

TEES built 4 types of hourglass (HG) elements. All HGs are 170mm long and 64mm high, but differ by channel shape as Figure 140 shows. LHG is the baseline shape we have used since the program started. NTG has a narrower channel and more curved side walls. The 65LHG shape comes from compression/tension experiments with the LHG; those experiments showed the compression

regime of the compression/tension tests provided better damping, which we expect comes from holding more fluid in the LHG as displacement reverses from tension to compression. Applying 1.25mm upward displacement to an LHG using finite element analysis provided the 65LHG shape, which has straighter side walls and larger internal volume. The double LHG (DLHG) increases the internal volume too; however, it adds straighter sidewalls, which increase elastic stiffness, to the structure.

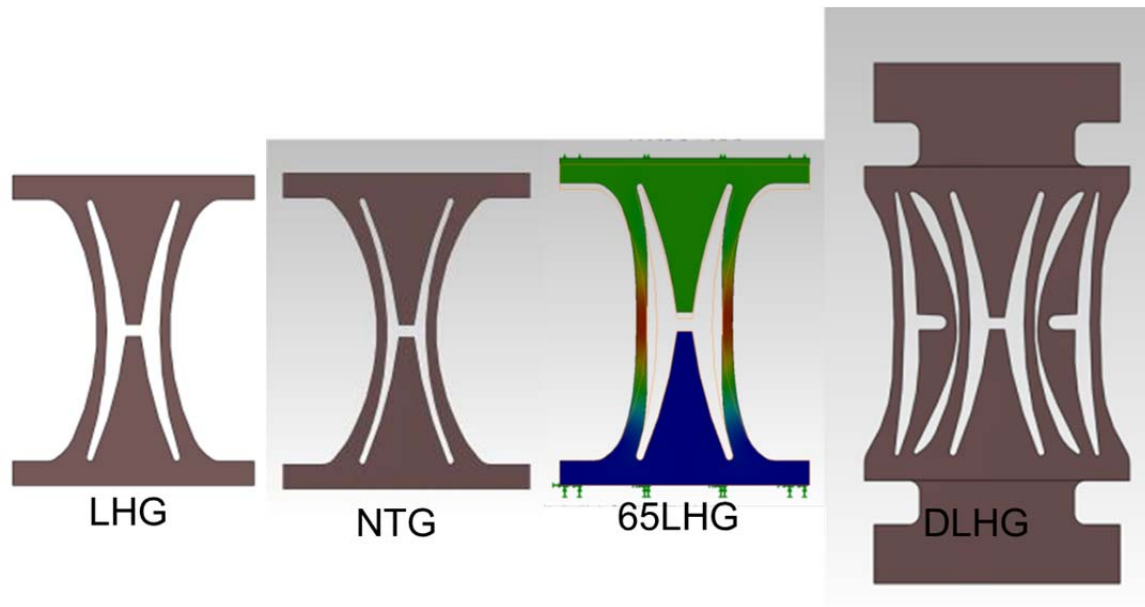


Figure 140. Four types of HGs have channel shapes that may affect damping performance.

To match AERO's FEA results, TEES used 60K fluid in all experiments. Figure 141 shows the NTG shape and the element in a fixture with 60 kcps silicone oil filling.



Figure 141. TEES built 64mm tall NTG holding 60 kcps silicon oil.

TEES performed 3 types of cyclic tests:

1. Compression/compression condition (C/C) is displacement from 0.1 to 1.25mm
2. Half compression/tension condition (0.5C/T) is displacement at ± 0.625 mm
3. Full compression/tension condition (C/T) is displacement at ± 1.25 mm.

The left plot in Figure 142 presents NTG's damping performance that can be compared with baseline 64LHG result in the right plot. Compression/compression test of NTG produced significantly larger damping at 0.1Hz than the baseline shape.

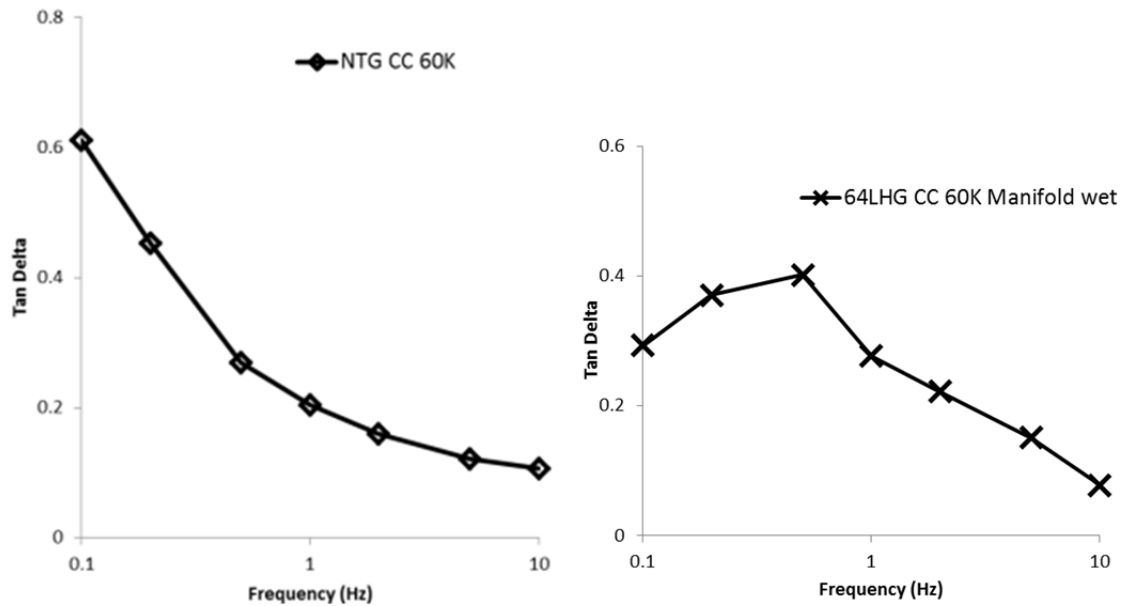


Figure 142. Left plot is the damping with an NTG. Right plot one is the baseline LHG result. Both results are from compression/compression condition.

For compression tension condition, we calculate the damping in two ways: whole cycle equivalent tan delta, and separate tension and compression regime equivalent tan deltas. Figure 143 (A) shows the whole cycle hysteresis loop. We split the circle at 0 displacement point as shown in (B) case, and calculate compression (C/T_C) and tension (C/T_T) tan deltas separately.

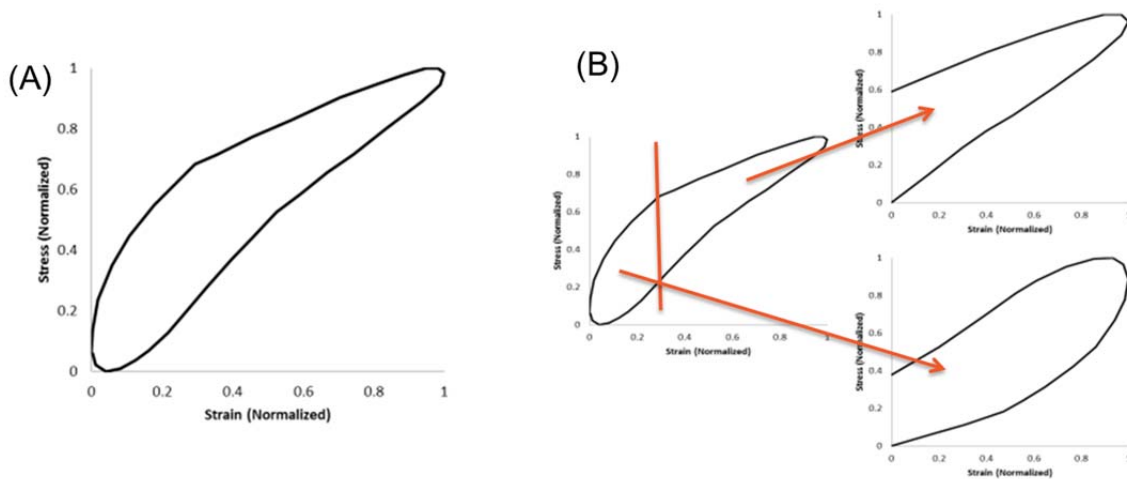


Figure 143. In compression/tension experiments we obtain whole cycle and separate regime values for equivalent tan delta.

NTG's compression/tension test results appear in Figure 144. Although half compression/tension condition pumps less fluid than an LHG, it has higher damping performance in all conditions. We hypothesize that the $\frac{1}{2}$ C-T mode improves overall pumping while minimizing the stiffness increase that occurs during the tension stroke.

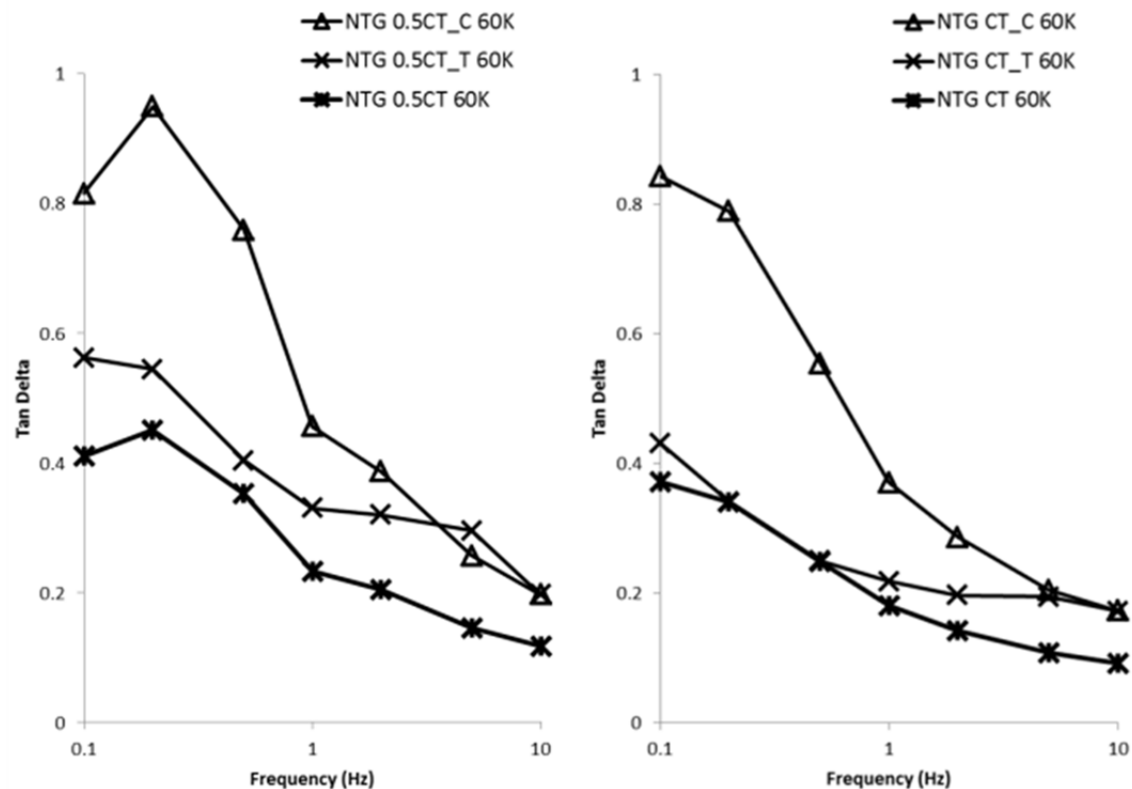


Figure 144. Half C/T cyclic test of NTG on the left shows higher damping than full C/T on the right in all C/T, C/T_C, and C/T_T cases.

We firstly expected that larger pumping volume to increase damping performance. Figure 145 shows a DLHG set up with 60 kcps oil and its poor damping result. DLHG only operates in C/C because outer side wall is too straight to take tension displacement. DLHG has less damping than LHG; the stiffness increased faster than pumping increased and this shape lost performance.

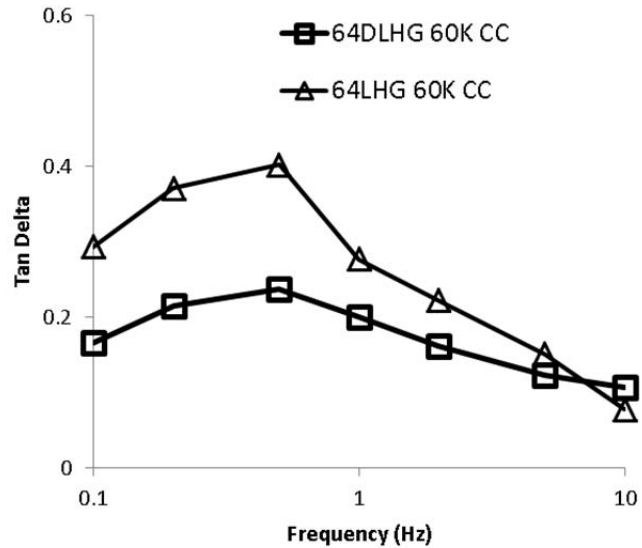
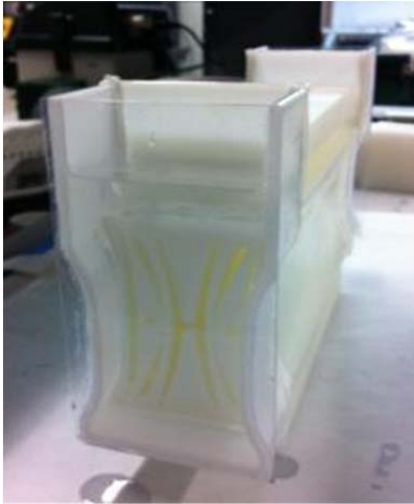


Figure 145. DLHG's damping performance is larger than normal LHG case at 60 kcps wet.

Shear thickening fluid, 54% volume fraction silica particles in the suspending medium PEG, was injected in DLHG, and tested with the same condition. This was a poor choice, given the low performance of the shape. The result in Figure 146 shows the shear thickening effect is increasing tan delta as frequency rises. The amount of damping is not high enough; so we will put this fluid in a smaller LHG/NTG to increase relative viscosity. No further experiments will use a DLHG.

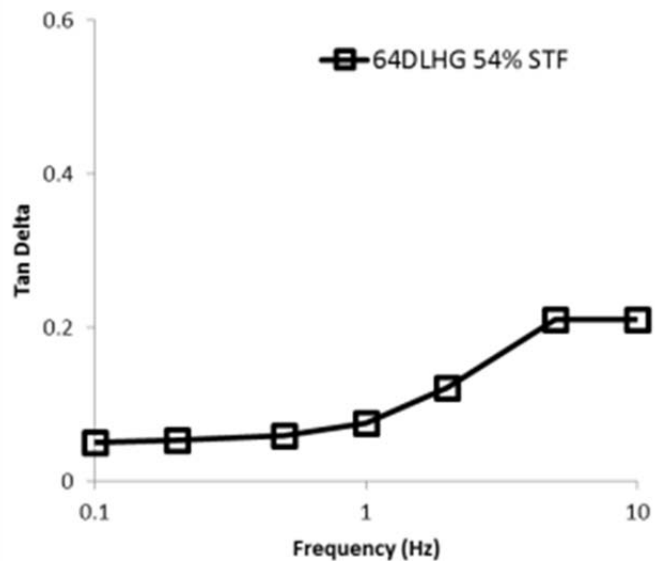


Figure 146. Shear thickening fluid, 54% volume fraction silica particles in the suspending medium PEG, was in DLHG. The result on the right plot shows the shear thickening effect.

One definition of tangent delta, loss modulus divided by storage modulus, shows that we can increase damping by decreasing structural stiffness while maintaining fluid pumping losses.

NTG has highly curved sidewalls at a smaller radius of curvature than the LHG. This reduces storage modulus.

Stiffness Study

As AERO nears testing of a complete high stiffness/high damping component, we now have design targets for damping element stiffness and displacement. Obtaining a 2 mm stroke in $\frac{1}{2}$ to 1 inch of thickness is not an issue for our shapes; however, AERO requires 53 N/mm as the panel's spring constant. The first panels shipped from TEES were too stiff at 1700 N/mm. Reducing the spring constant by a factor of 32 requires redesign—materials substitutions will only drop the stiffness by a factor of 2 to 3.

The first check was to measure the change in stiffness with scale for LHGs. TEES performed compressive cyclic tests on the specimens appearing in Figure 147. Both are 11mm long, Somos 9120 elements, but one is 12mm tall (on the left) and the other is 8mm tall.

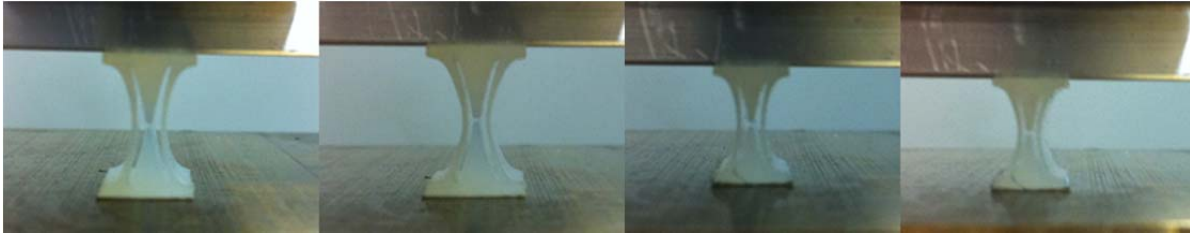


Figure 147. A 2% strain applied on 11mm long samples of 12 mm and 8 mm tall LHGs.

Figure 148 presents the tenth cycle stiffness and we added the 16LHG results for analysis. The structural stiffnesses are 198, 170, and 225N/mm for 16, 12, and 8LHG respectively. The results show the size does not affect stiffness. That is, although the sidewalls become thinner, which would lower stiffness, as we reduce the scale, the shorter sidewall height makes the stiffness approximately constant. Therefore, we must change the shape to drop the spring constant.

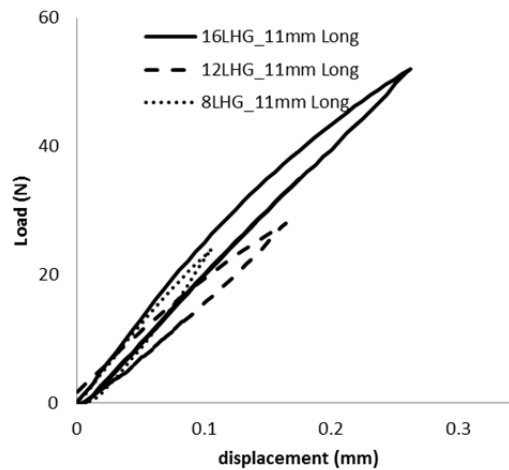


Figure 148. The structural stiffness is approximately constant (198, 170, and 225N/mm for 16, 12, and 8LHG respectively) as the LHGs get smaller.

Fortunately the new WTG (wide trial geometry) shape is much softer than the prior geometries. TEES built four 50mm long specimens shown in Figure 149. The bottom right picture shows Wide Trial Geometry, WTG that has thin side wall with an elliptical shape that decreases structural stiffness.

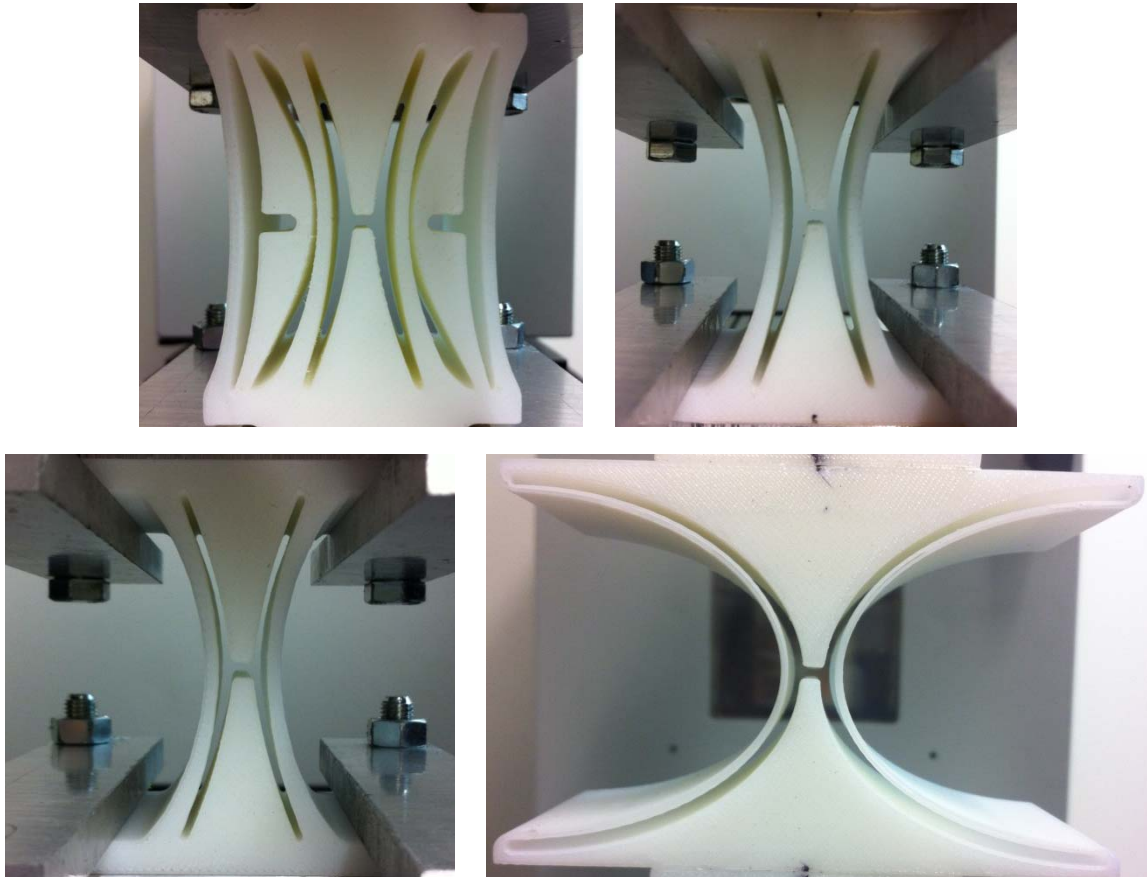


Figure 149. Top left is DLHG, top right is the baseline LHG, bottom left is NTG that has narrower channel and curved side wall, and bottom right is Wide Trial Geometry, WTG that is thin side wall and much more curved side wall than NTG.

Figure 150 presents the spring constants for DLHG, LHG, NTG, and WTG, which have 2746, 1127, 857, and 0.7N/mm respectively. All built in the same material at the same scale, WTG drops the spring constant by a factor of 1610, which will allow us to meet AERO's requirements. We will test a 170mm long 64WTG for damping performance.

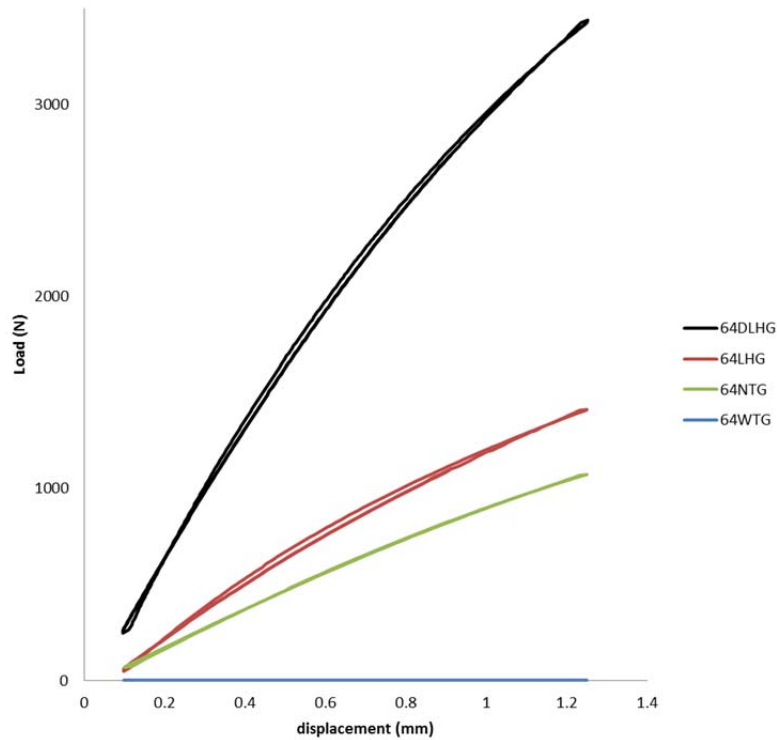


Figure 150. DLHG, LHG, NTG, and WTG show structural stiffness of 2746, 1127, 857, and 0.7N/mm respectively.

TEES is keeping alternate methods of lowering the spring constant as backup options if the miniaturized WTG presents a problem. One way to decrease structural stiffness is to make the panel from elastomer molded with a fluid pumping chamber void that does not contain a stiff polymer structure. TEES designed NTG channel shape mold tool as shown in Figure 151, Pouring S111 elastomer in a square casing, and removing the casing and mold tool after curing will create an elastomer panel with fluid pumping channels.

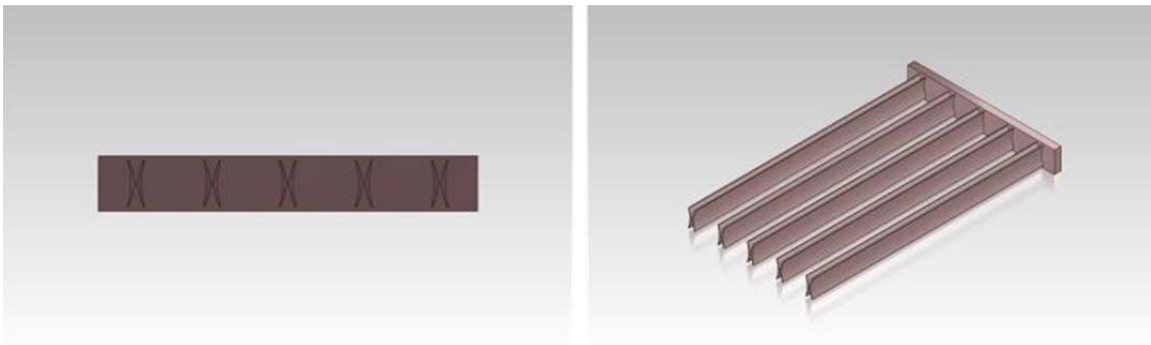


Figure 151. NTG channel shape comb can be used for mold tool that can make S111 panel without hourglass machine.

Another idea is to make LHG side wall from plastic tubes as shown in Figure 152. The geometric constraints within the pumping chambers would be machined into the skins or the skins would be made by rapid prototyping. Making elliptical tubes would form the WTG shape.

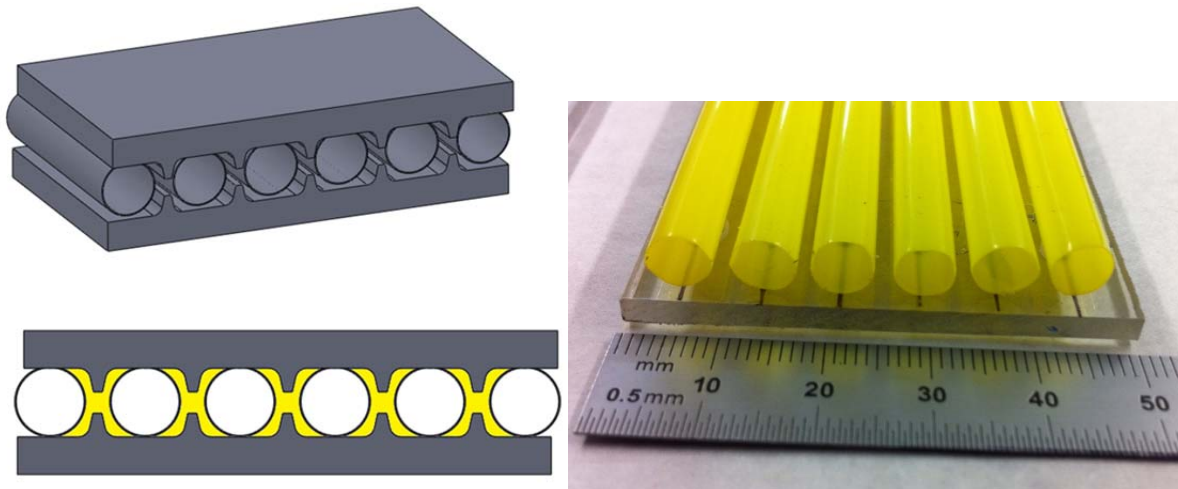


Figure 152. Making LHG's side walls with plastic tubes helps decrease stiffness.

Reducing spring constant in TEES damping panels

One calculation of tan delta is the loss modulus—dissipation behavior—divided by the storage modulus—elastic behavior. To increase damping performance, we can decrease storage modulus, increase loss modulus, or do both. The Wide Trial Geometry (WTG) proposed by Aerospace Corporation has thin, elliptical sidewalls shown in Figure 153. These features drop stiffness significantly. In the experiment, the reservoirs at both ends contain simple, 60 kcps fluid and they act as fixed end boundary conditions that add a little stiffness. The silicone oil was under vacuum for 72 hours at 1.5 Torr; that treatment removed enough dissolved air to avoid bubble creating during cyclic tests. Compression/compression cyclic test from 0.1 to 1.25 mm produced tan delta of 1.34 at 0.2 Hz, shown in Figure 154. This is more than triple the LHG 60 kcps tan delta.

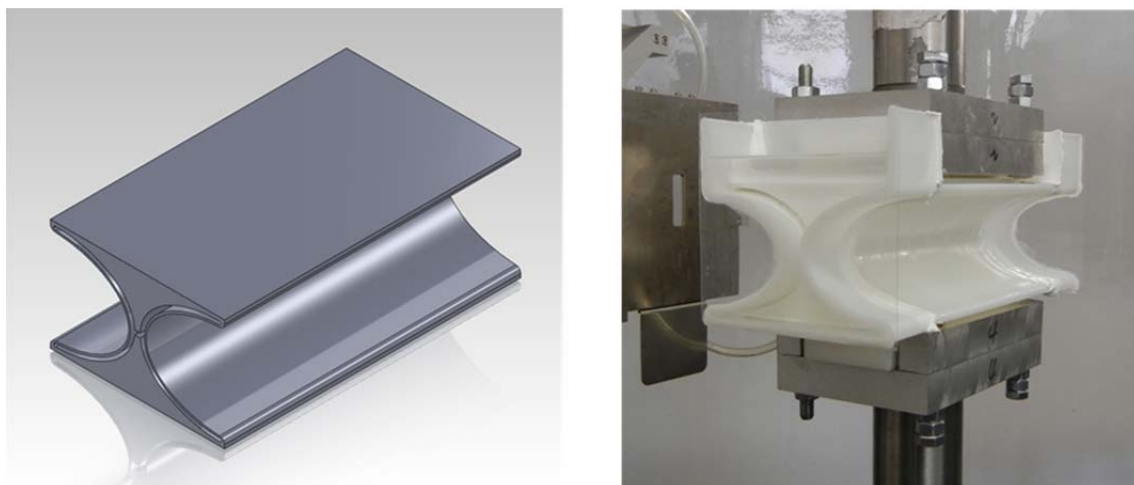


Figure 153. The 64mm tall WTG has thin, elliptical sidewalls that reduce structural stiffness. The reservoirs(right) add a little more stiffness.

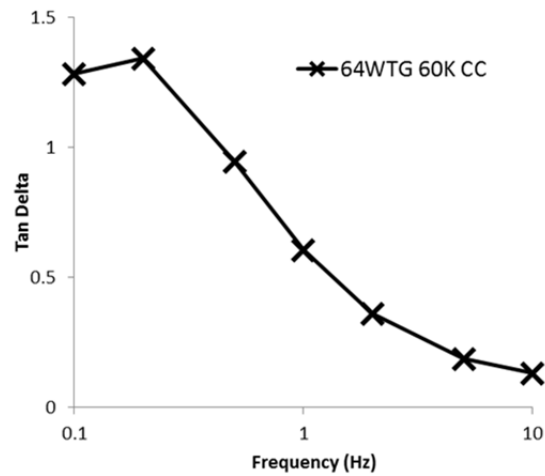


Figure 154. Compression/compression cyclic test produce tangent delta of 1.34 at 0.2Hz.

Figure 155 shows two compression/tension cyclic data sets. Left is $\frac{1}{2}$ compression/tension—displacement of ± 0.625 mm. The right image is full compression/tension with a ± 1.25 mm displacement.

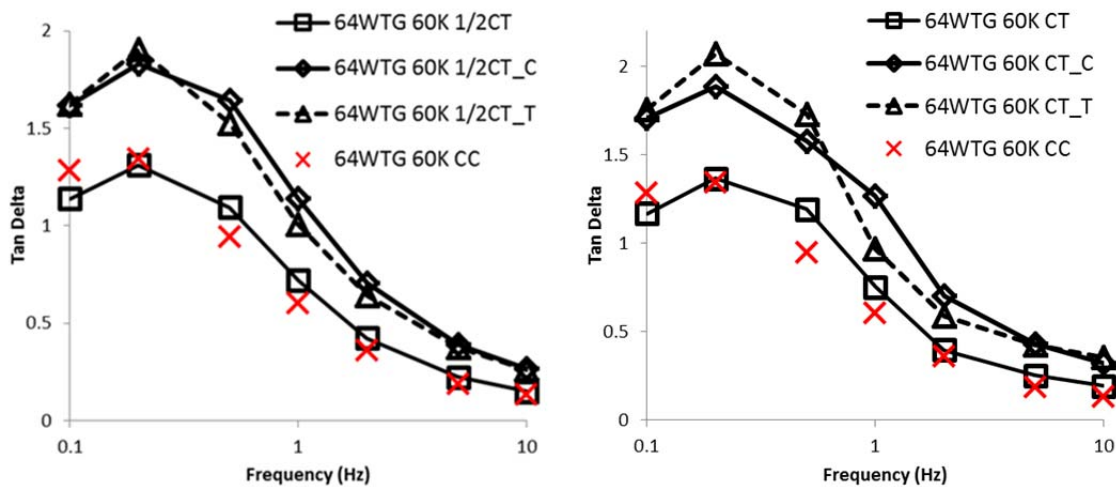


Figure 155. The 64WTG was tested in half and full compression/tension cyclic tests. TEES calculates the loop as one whole circle, and splits at the zero displacement point and calculates compression side and tension side separately.

TEES ordered 13mm tall WTG from Fineline Corp. that can function in Aerospace Corp's rig design. Figure 156 shows its size and shape at 13 mm tall, two inches long, with one inch long reservoirs on both ends. The total length is four inches long. When scaled down from AERO's design, the sidewalls were too thin for rapid prototyping; therefore, we increased sidewall thickness to 0.13 inch.

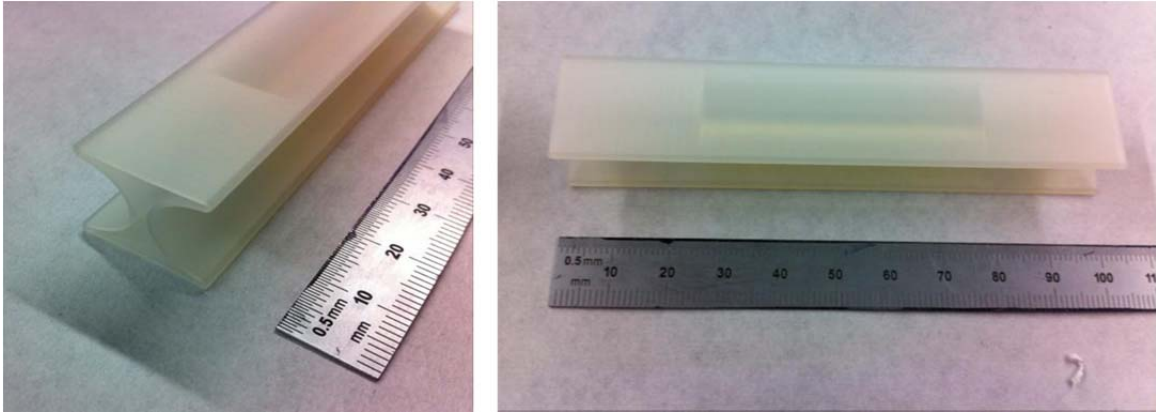


Figure 156. The 13mm tall WTG will fit in Aerospace's rig. This unit is originally two inch, and one inch long reservoir attached on both ends, total 4 inch long

TEES ordered the 13WTG made from two materials: Somos 9120 and Watershed. Figure 157 shows stiffness measured at 0.1Hz on 13WTGs in both materials. Somos 9120 WTG is 10.63 ± 0.47 N/mm and Watershed WTG is 14.50 ± 0.08 N/mm. Aerospace's stiffness requirement is from 54 N/mm to 60 N/mm for the two-machined panel.

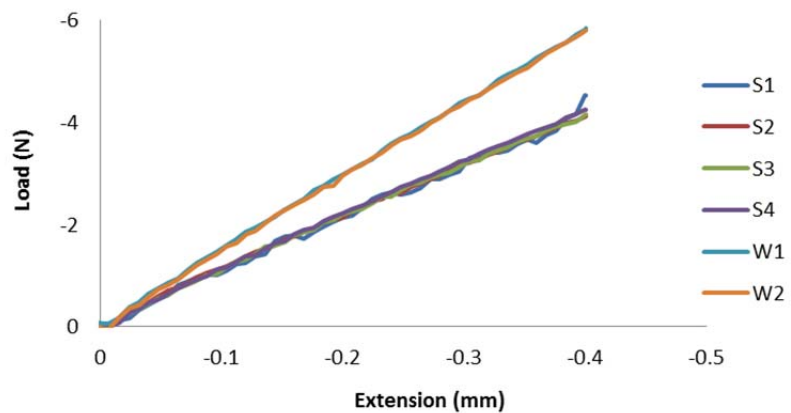
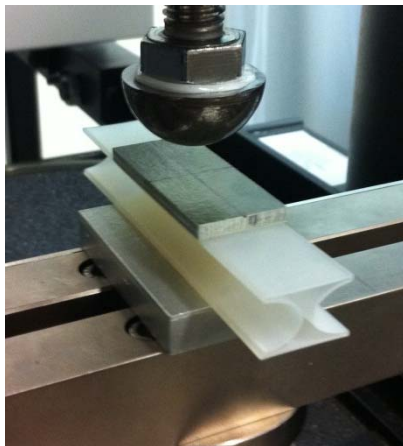


Figure 157. Stiffness measurement for WTGs. Somos 9120 produces 10.63 ± 0.47 N/mm; Watershed produces 14.50 ± 0.08 N/mm.

The RP parts did not match our numerical result, which predicted a 1 mm displacement range. TEES manually sanded the geometrical constraint in the Watershed RP material as shown in Figure 158 to make sure it provides 1 mm displacement.

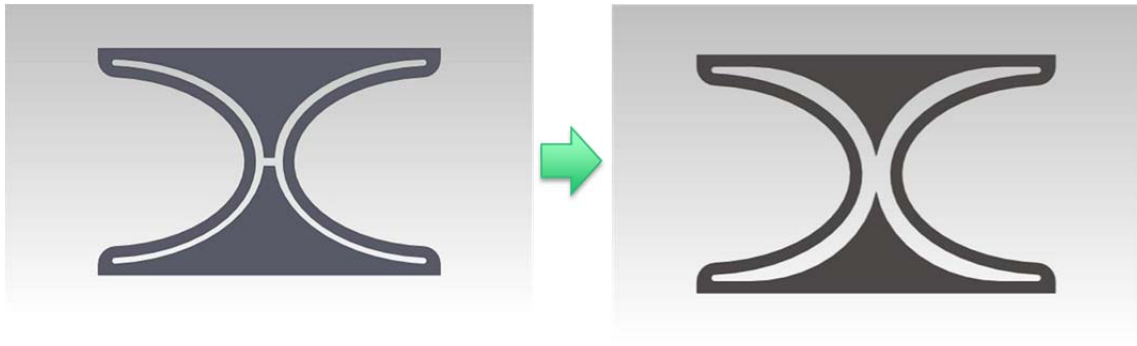


Figure 158. The 13WTG from Fineline did not produce 1mm of displacement (left). TEES manually sanded geometrical constraint of Watershed RP material to get right displacement (right).

Two Watershed WTGs arrayed on two inch square aluminum plates produced the panel shown in Figure 159. Both ends of reservoirs were sealed with plastic windows and filled with 5 kcps silicone oil. One end was fully filled, and the other end was half filled. Stiffness was too high at 150 N/mm, and we thought that the sealed reservoirs were acting as an air spring. We drilled holes to vent air during cycling. The left image in Figure 159 shows one vent hole. The reaches 110 N/mm, which is twice the target spring constant. With this stiffness we could not add an elastomer, which would help the machines pump the fluid. We needed a new means to contain the fluid.

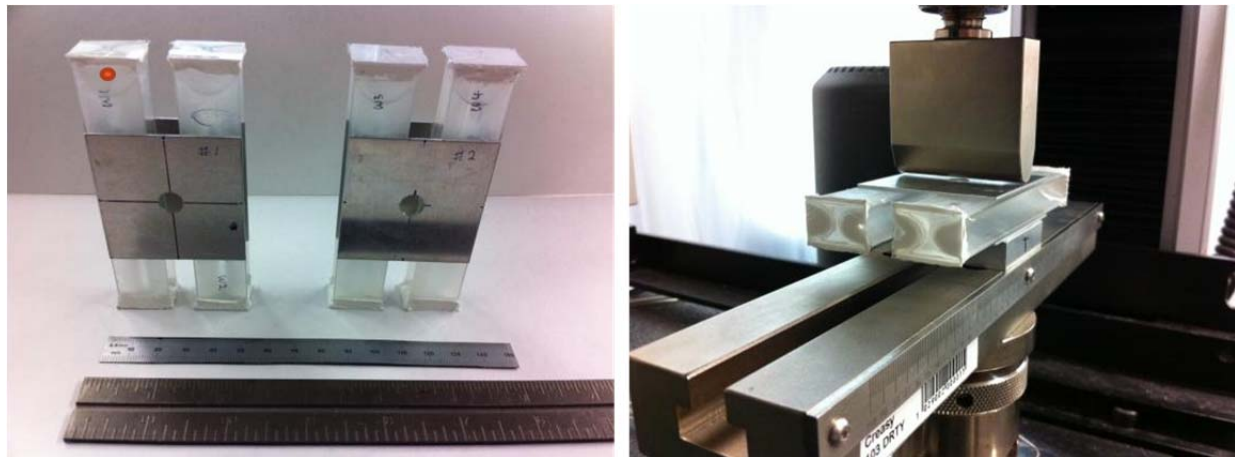


Figure 159. Two Watershed WTGs were sanded for 1mm of displacement and arrayed on two inch square aluminum plates to produce a panel. Each cell contained 5 kcps silicone oil, one end was fully filled, and the other end was half filled. Both reservoir ends sealed with plastic windows.

TEES ordered new 13WTGs with Somos 9120. These had no reservoirs and smaller geometrical constraints to provide 1mm displacement. We wrapped the cell with polyethylene film and filled the machine and the film with degassed fluid as shown in Figure 160.



Figure 160. New 13WTGs have no reservoirs and reduced geometrical constraint. Wrapping the cell with polymer film the contained fluids and helped the channel pump.

Figure 161 shows the panel TEES sent to Aerospace Corp. Both WTGs contained 13 kcps silicone oil, but now the stiffness (22 N/mm) was only $\frac{1}{2}$ the target value. To increase stiffness, we inserted several damping materials between the WTG cells. S-111 elastomer brought the panels to 42 N/mm, which is still lower than Aerospace's minimum requirement.



Figure 161. This panel contains two Somos WTGs, filled with 5 kcps silicone oil in bags, reached a 22 N/mm spring constant. Adding S111 elastomer blocks between the WTGs raised the spring constant to 42 N/mm.

Next, we added felt blanket in a mixed stack of "medium duty" and "heavy duty" grades with butyl rubber caulk. Figure 162 shows two stacks. The left stack has two layers of heavy duty felt and butyl rubber caulk. The right stack has one heavy-duty felt layer, two medium-duty felt layers, and butyl rubber caulk layers.



Figure 162. Two types of middle section dampers are demonstrated. Felt3-1(at left): 2 heavy duty felt + 2 butyl rubber caulk. Felt4(at right): 1 heavy duty felt + 3 butyl rubber caulk + 2 medium duty felt.

Effect of new reservoir method

The new method of bagging the WTG leads to a question: is the damping performance an outcome of the fluid alone, or do the fluid and WTG work in concert to damp the motion. We made 20.42 ml, silicone oil bags containing 5 kcps oil, and placed them in compression/compression. With felt3-1 added, the system has 29.12 N/mm stiffness and produces 0.23 tangent delta at 0.1Hz, which appears in the left plot in Figure 163. The bag combined with a felt4 insert reaches 34 N/mm stiffness and 0.25 of tangent delta, which shows the felt/rubber stacks affect stiffness, but do not affect damping.

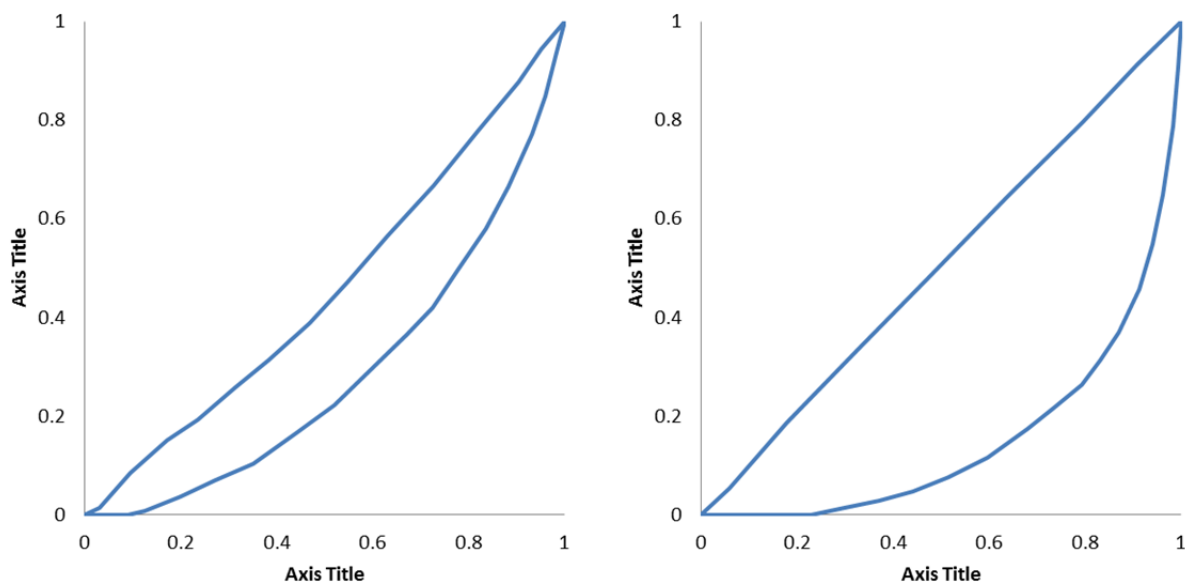


Figure 163. Cyclic test results of 5 kcps oil-filled bags(left) and bags containing 13WTGs in oil (right) shows that the new bagging method allows the WTGs to function.

So now the question is “do the WTGs have an effect beyond the fluid-filled bags acting alone?” Two 13WTGs bagged in 5 kcps silicone oil with felt3-1 dampers reach 43.74 N/mm stiffness. If this increase in stiffness is not accompanied with an increase in loss modulus the tan delta will drop as $\tan \delta = \text{loss modulus} / \text{storage modulus}$. The tan delta with WTGs in fluid-filled bags is 0.52,

which is double the tan delta measured without the machine. Therefore, loss modulus increased much faster than storage modulus and the WTGs are producing damping. Adding felt4 in 13WTG-5 kcps bags array shows 53.77 N/mm of stiffness, so TEES sent the specimen to Aerospace Corp. to request test with their rig.

Alternate fabrication with tubes and plates

While waiting for WTGs to arrive from Fineline rapid prototyping, TEES investigated an alternate method for building hourglass damping structures. When placed between skins that provide the geometric constraint structure, thin-wall thermoplastic tube sidewalls can act as hour glass and WTG shapes as shown in Figure 164. Six, 150mm long thermoplastic tubes are arrayed as a panel. At 1.5mm displacement (25% strain) the walls touch each other—we can eliminate this with wider spacing between the tubes.

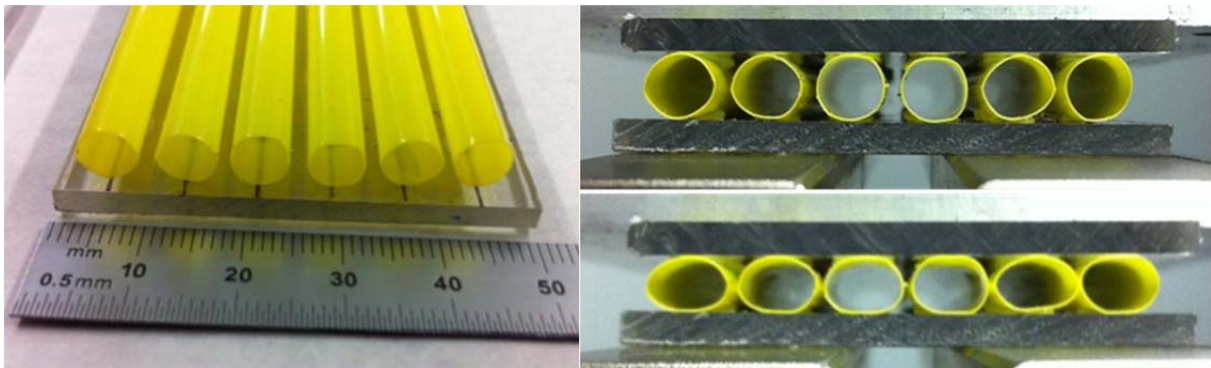


Figure 164. Arrayed six, 150mm long thermoplastic tube panel reached 25% strain when the walls touched each other.

Figure 165 shows a 25% strain cyclic test at 0.1Hz, giving a 72.48 N/mm spring constant. One tube, 50mm length, will show 4 N/mm. Four tubes, 50 mm length will be 16 N/mm and have 3 LHG channels

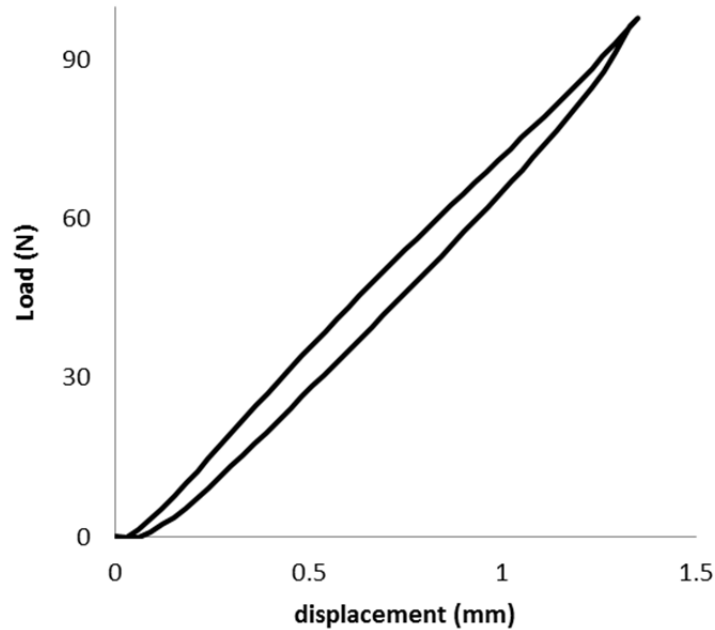


Figure 165. At 25% strain at 0.1Hz, six 150 mm-long thermoplastic tubes produce 72.48 N/mm spring constant with little damping without a fluid.

TEES built two damping specimens with tubes. Figure 166 shows 6 tubes that are 6mm tall with 4 fluid pumping channels in the left image. Grooves help align the tubes. The 4 tube panel in the right image has 4 mm tall elliptical tubes and provides 2 pumping channels. The six tubes panel has two more pumping capacity with higher spring constant. The 4 tubes elliptical tubes reduce stiffness. Figure 167 and Figure 168 show the 6 and 4 tube arrays with a constrained grip.

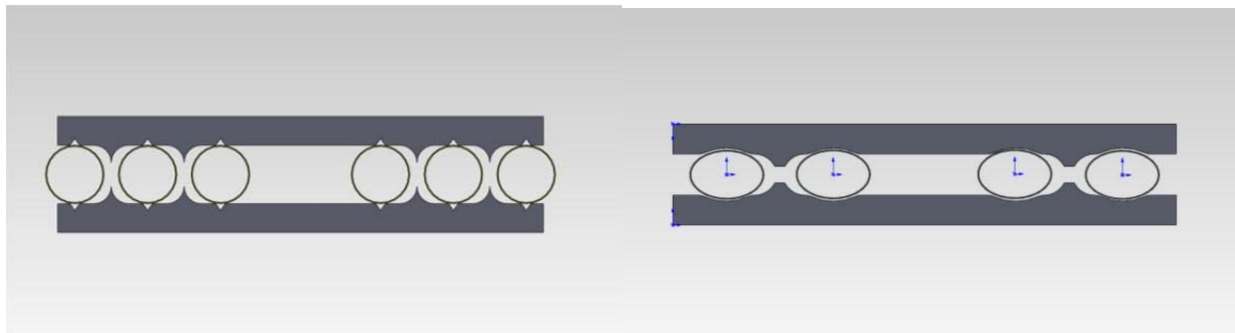


Figure 166. Tube-based dampers can have shapes like the LHG and WTG systems produced by rapid prototyping.

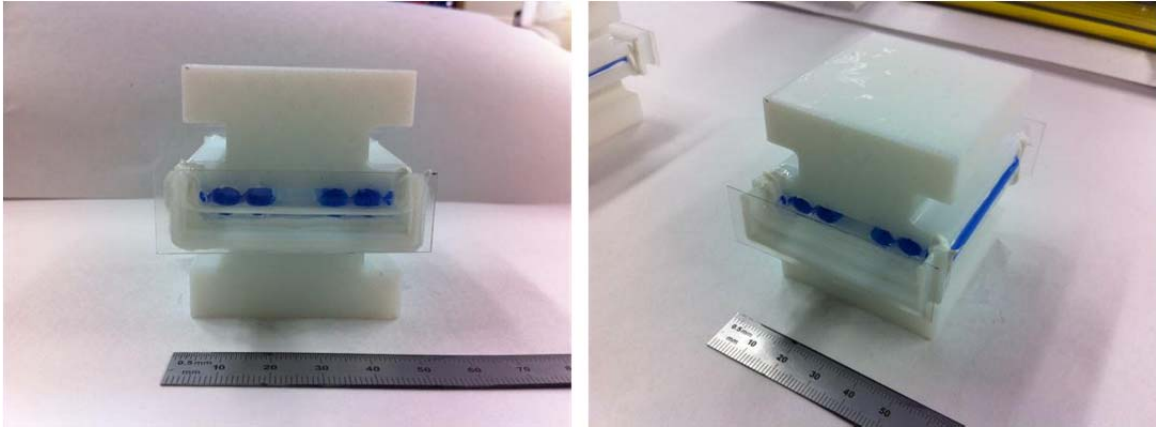


Figure 167. Six-tube array with the constraint grip will be tested with 5 kcps fluid.

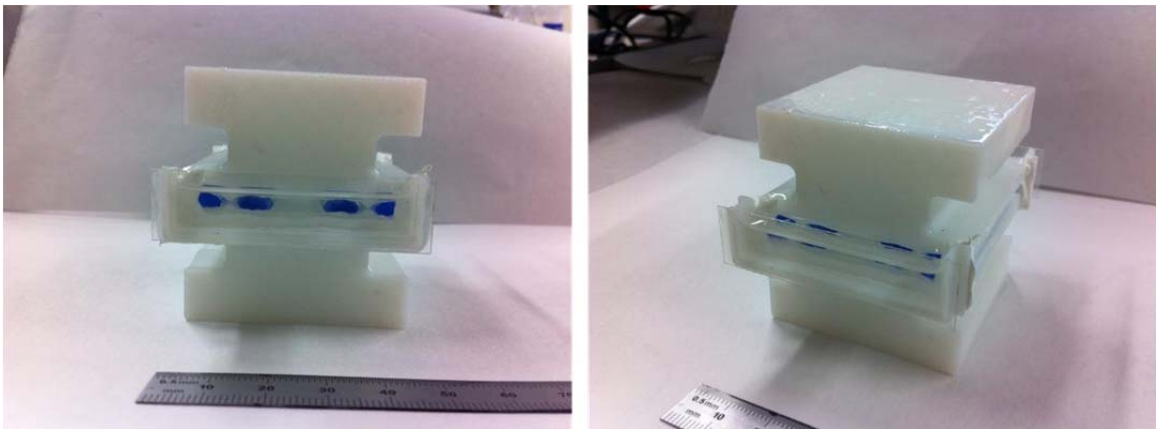


Figure 168. Four-tube array with the constraint grip will be tested with 5 kcps fluid.

Reducing spring constant in TEES damping panels

According to Amanda S. Lim(2010), 54, 52, and 50% volume fraction silica particles in the suspending medium(PEG) shows shear thickening effects as shown in Figure 169. By increasing strain rate, the fluid's viscosity decreases for shear thinning effect, and at some point above, increases for shear thickening effect.

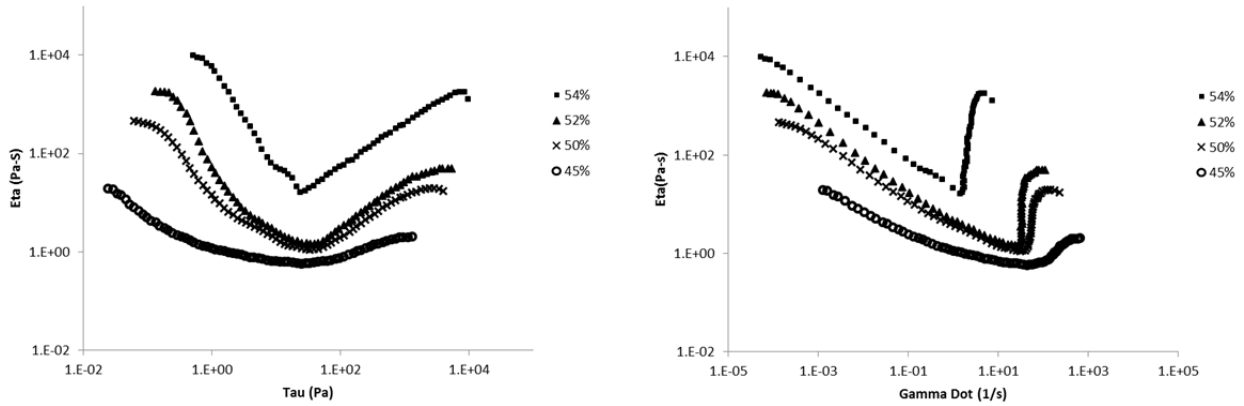


Figure 169. Amanda S. Lim(2010)'s SiO in PEG presents the shear thickening effect.

TEES injected the 54% SiO in PEG fluid in 64mm tall LHG as shown in Figure 170. The SiO particles took 2 hours of oven dry, and mixed with PEG by 72hours of rolling. We performed the cyclic test in compression/compression(C/C) from 0.1 to 1.25mm and half compression/tension ($\frac{1}{2}$ C/T) for ± 0.625 mm.

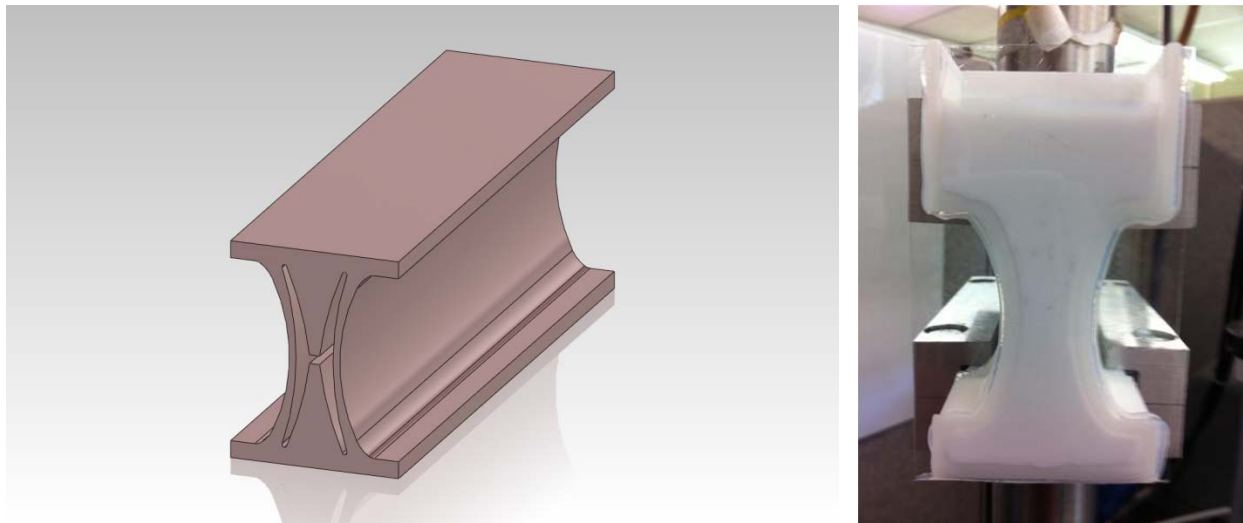


Figure 170. Left: shape of 64mm tall 170mm long LHG / Right: injected 54% of SiO in PEG into the LHG channel

Figure 171 shows the damping performance for 64 mm tall LHG with the shear thickening fluid. Both C/C and $\frac{1}{2}$ C/T tests produced low damping and potential adaptive behavior in low frequencies.

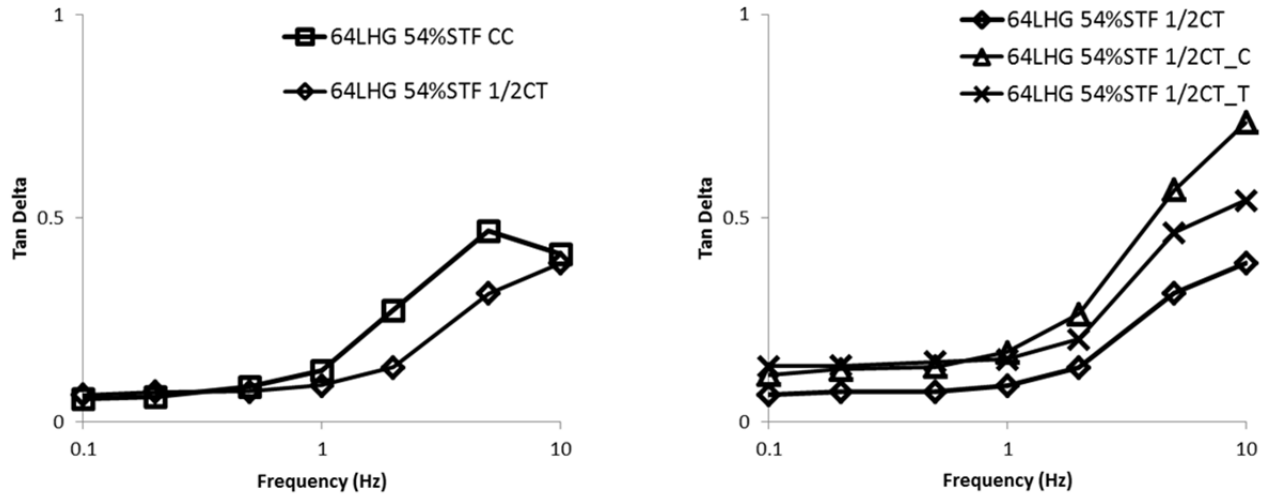


Figure 171. 64mm tall LHG with 54% SiO in PEG exhibits potential adaptive behaviors in low frequencies.

We can expect more damping in the WTG with the shear thickening fluid. Figure 172 presents the shape and test setting of WTG with the fluid. WTG has curved sidewalls and low stiffness compared with NTG. The specimen was tested in three conditions: C/C from 0.1 to 1.25mm, $\frac{1}{2}$ C/T for ± 0.625 mm, and C/T for ± 1.25 mm.

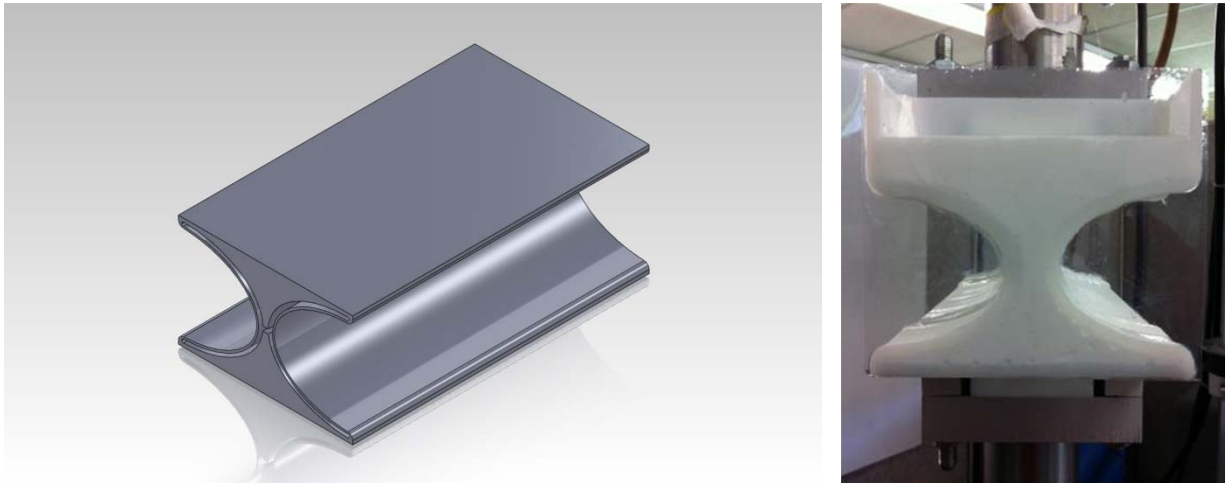


Figure 172. Left: shape of 64mm tall 170mm long WTG / Right: injected 54% of SiO in PEG into the WTG channel.

Compared with previous 60 kcps simple viscous silicone oil test, shear thickening fluid exhibits adaptive damping across the frequencies. Figure 173 exhibits C/C tests that the simple

viscous fluid's damping performance dropped with increasing frequencies while the shear thickening fluid presents a second peak near 5Hz.

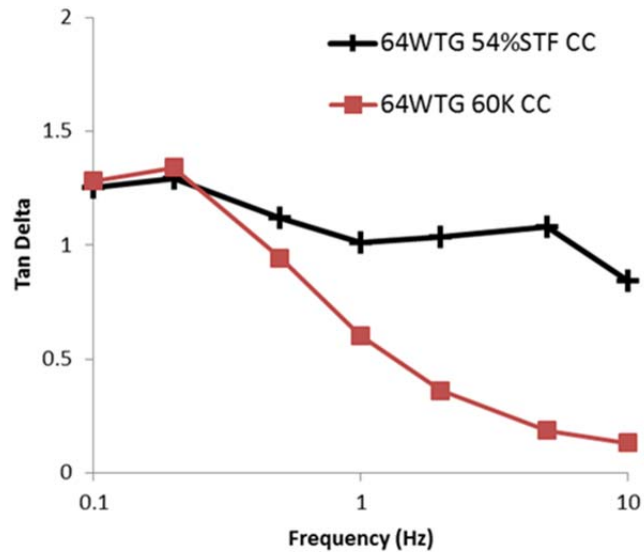


Figure 173. The WTG specimen with the shear thickening fluid presents a second peak near 5Hz exhibits in the C/C test. On the other hand, the simple viscous fluid's damping performance dropped with increasing frequencies.

The half C/T and full C/T test results show the similar damping performance as shown in Figure 174. All three C/C, $\frac{1}{2}$ C/T, and C/T cases exhibited the adaptive damping through the target frequencies.

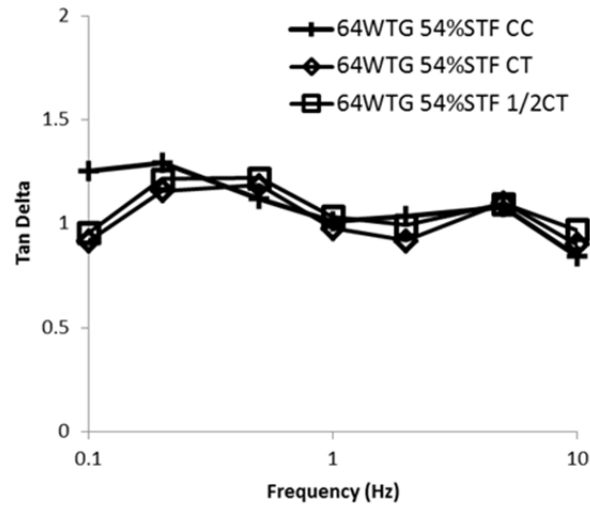


Figure 174. The half and full C/T tests also show the adaptive damping as well as the C/C test result.

When we calculate the damping regimes in compression and tension part separately, we can see this structure damps cyclic load on tension as well as compression as shown in Figure 175. It designates this system is a dual acting damper. Both full C/T and half C/T's compression and tension part exhibit two peaks, the first peaks near 0.1Hz and the second peaks near 0.5Hz.

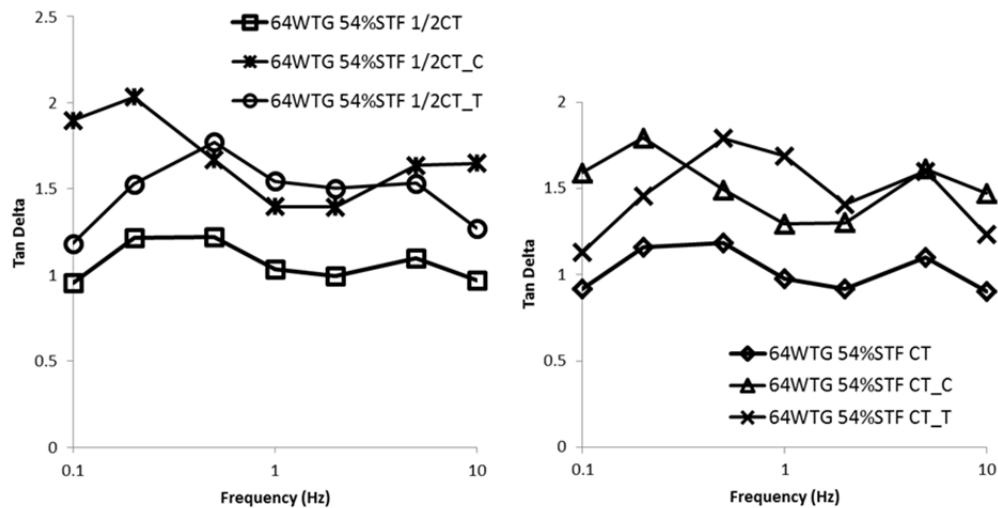


Figure 175. We split the loop at zero displacement point and calculate both compression and tension parts separately. As well as compression part, tension part also shows high damping performance. The compression part of 1/2 C/T (1/2 C/T_C) shows the highest peak near 0.2Hz and the second peak near 5Hz.

Figure 176, Figure 177, and Figure 178 present loop plots of 64mm tall WTG's C/C, $\frac{1}{2}$ C/T, and C/T with 54% SiO in PEG shear thickening fluid respectively.

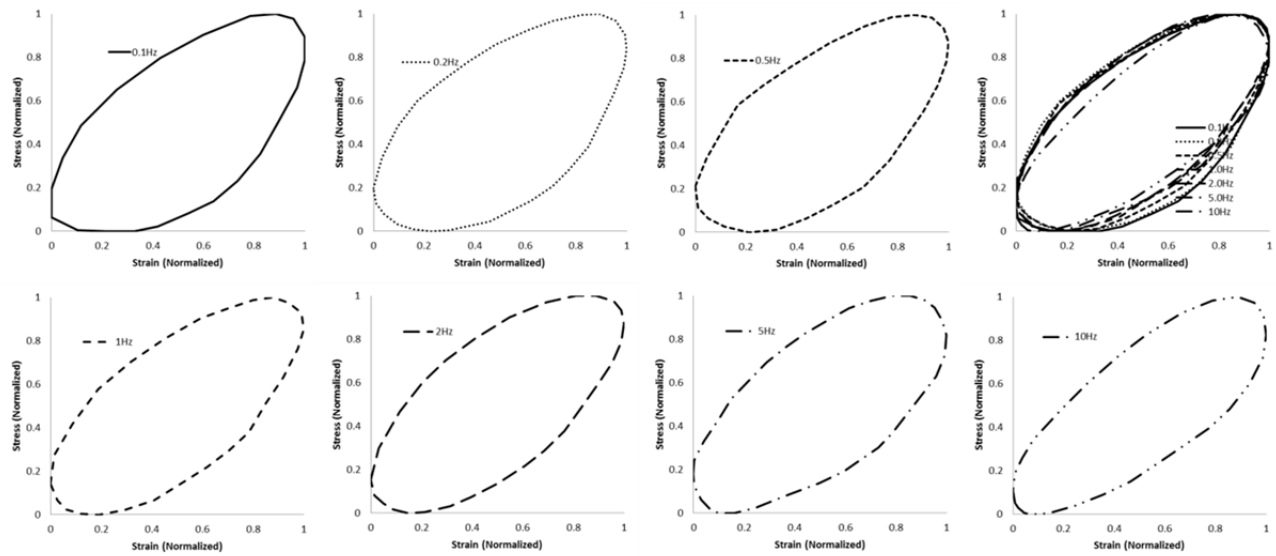


Figure 176. Loop plots for C/C test of 64mm tall WTG with the shear thickening fluid

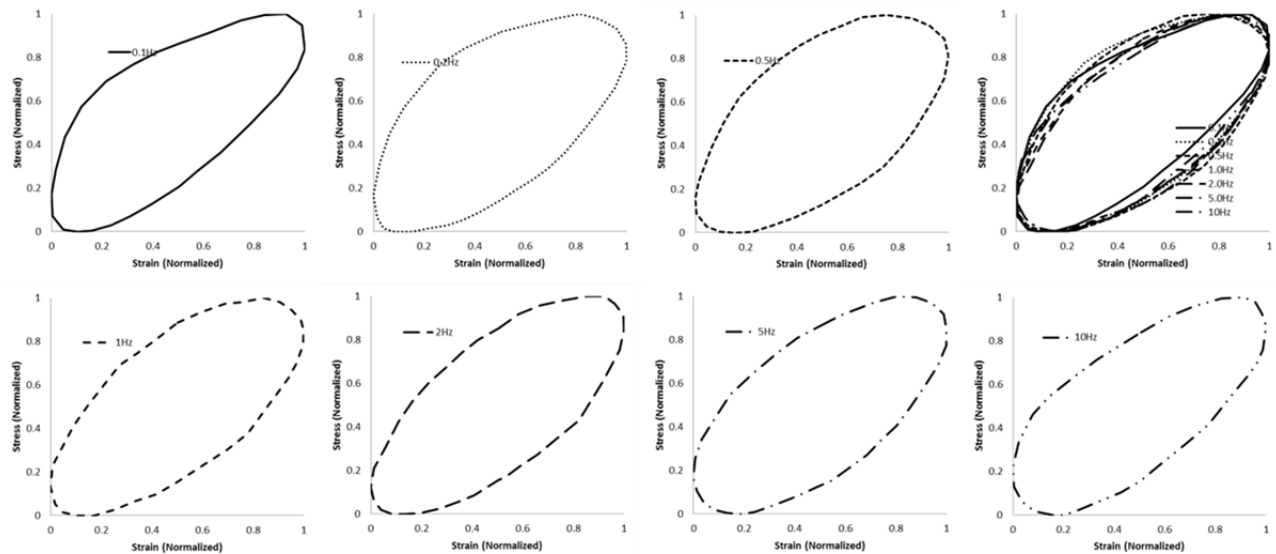


Figure 177. Loop plots for $\frac{1}{2}$ C/T test of 64mm tall WTG with the shear thickening fluid

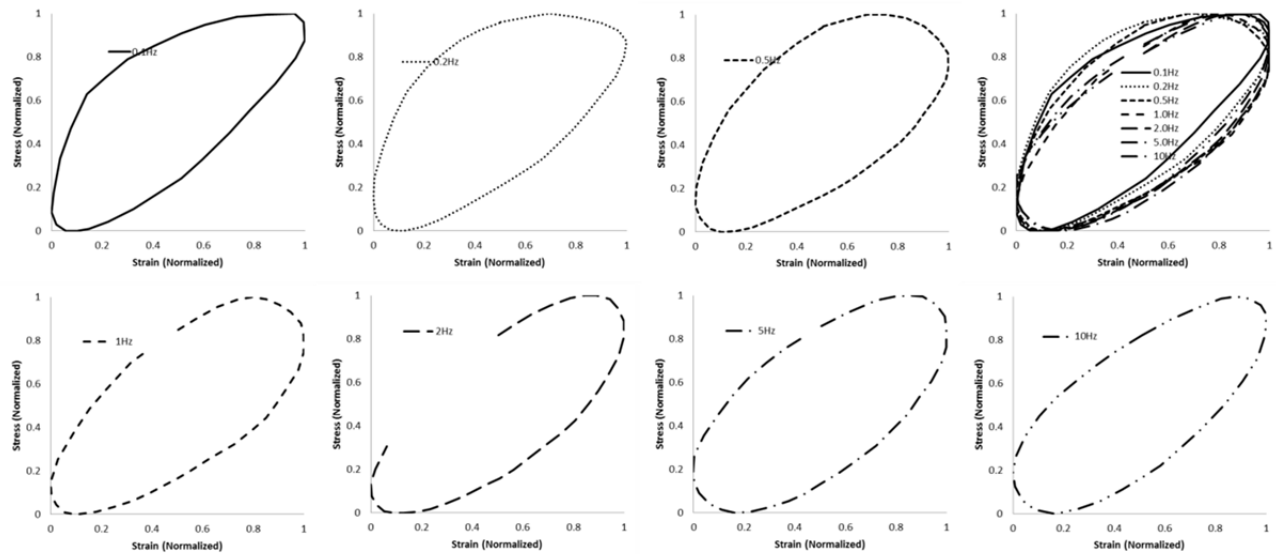


Figure 178. Loop plots for C/T test of 64mm tall WTG with the shear thickening fluid

Computational analysis for design and evaluate Machine augmented composite materials

Review Prior Work

Previous students' publications helps get concept of this study. Dr. Jonghyun Kim's dissertation designated the material properties, and Mr. Matthew Mccutcheon's thesis presented the detail procedure of this damping study using ABAQUS and ANSYS. That work is a basis for our future developments.

Explore Analysis Tools: Modal Response

An initial study determined that HGs do not have a natural response in the target frequency range; therefore they will not naturally assist fluid pumping. First, analysis was performed with Ansys workbench, which might be the best FEA tool for this research because it has powerful post processing functions for modal and harmonic response studies. Figure 179 presents the prototype design of HG machine. The additional material inside of the channel helps reduce hydraulic radius.

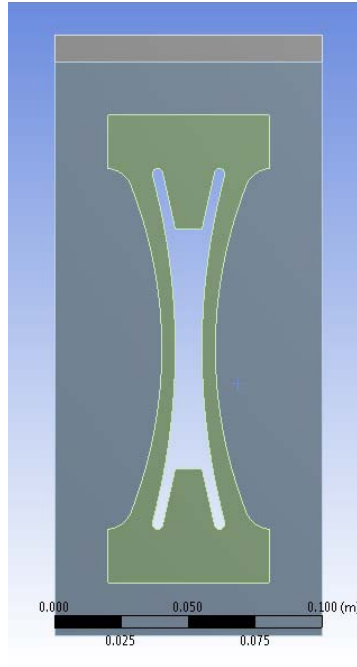


Figure 179. Ansys model of HG machine in matrix with rigid upper plate

The materials for HG and matrix are Repro 1075 rigid polyurethane and 1040 soft polyurethane respectively as shown in Table 13. Firstly, static structural analysis estimates how much pressure needs to be applied on the top of the rigid plate to close sidewalls. Pressure of 1.3MPa makes this structure deformed 6.70mm in y direction as shown in Figure 180.

Table 13. Ansys used these material properties for HG and matrix.

	Desity	Elastic modulus	Possion's ratio
HG	1140 kg/m ³	1.65 GPa	0.33
Matrix	1094 kg/m ³	4.24 MPa	0.49

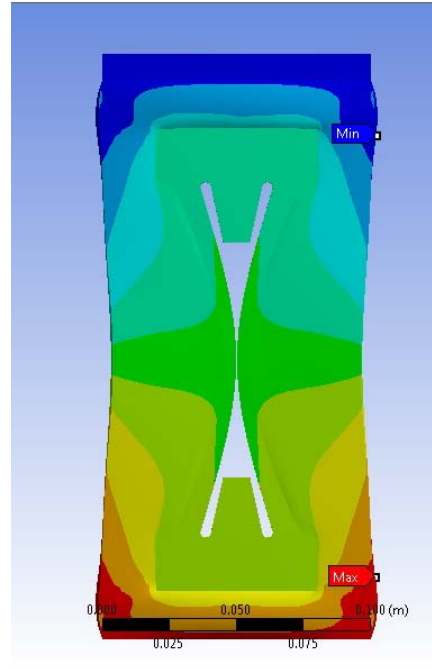


Figure 180. 1.3 MPa of pressure on the top of rigid plate makes close the sidewalls.

Modal study shows natural frequency results as shown in Table 14. These results indicate that the HG does not respond naturally in the 0.1 to 10 Hz frequency range; therefore the natural response of the HG will not assist in the pumping/damping action unless we change the materials or design to provide a natural response in the target frequency range.

Table 14. Modal response study shows below natural frequency.

Mode	Natrual Frequency
1	19.38 Hz
2	39.57 Hz
3	45.53 Hz
4	87.68 Hz
5	136.08 Hz
6	138.20 Hz

Explore Analysis Tools: Rayleigh Damping

We planned to use an initial Rayleigh damping analysis to drive the Task 1 experiments and rapid prototyping effort. However, the software was too simplistic and modeling took too long and our experiments outpaced analysis. Solidworks and Ansys require inputting Rayleigh damping constants to create damping phenomena. Definition of Rayleigh constant is shown in Equation 4

$$[C] = \alpha[M] + \beta[K]$$

Equation 4

The $n \times n$ symmetric damping matrix $[C]$ is formulated as a linear combination of the mass $[M]$ and stiffness $[K]$ matrices. In this case, displacement is so small that we can ignore Mass proportion but only consider beta, or we can consider damping ratio as shown in following equations.

$$\xi \text{ (damping ratio)} = C(\text{damping const}) / C_{cr}$$

$$C = \beta K$$

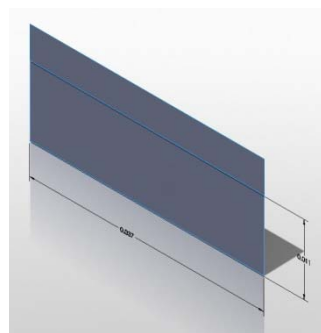
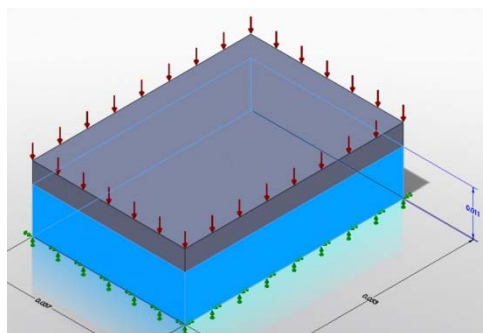
$$\xi = C / C_{cr} = \beta K / 2\omega m = \beta \omega / 2$$

We analyzed Repro 1040 Soft Polyurethane block, size of 53 x 37 x 11 mm and HG MAC block with the same outer shape and size. Cyclic load was applied and check phase lag at our target frequency to find matched damping const. with empirical phase angle data from a previous student as shown in Table 15.

Table 15. Previous student's experimental data of Repro 1040 Soft Polyurethane matrix block and HG MAC block

	Matrix			HG MAC		
Frequency	Tan δ	Time Lag (msec)	Phase Angle ($^\circ$)	Tan δ	Time Lag (msec)	Phase Angle ($^\circ$)
0.1 Hz	0.04	63.63	2.29	0.06	95.38	3.43
1.0 Hz	0.03	4.773	1.72	0.04	6.363	2.29
10 Hz	0.01	0.159	0.57	0.03	0.477	1.72
20 Hz	0.06	0.477	3.43	0.08	0.635	4.57
40 Hz	0.22	0.862	12.4	0.22	0.862	12.4

Solidworks requires inputting Rayleigh damping constants to create damping phenomena. TEES created both solid and shell model of the elastomer block as shown in Figure 181, and input the Rayleigh beta constant from 0 to meet the target phase angle.



Frequency (Hz)	Rayleigh Beta Const. in Shell Model
0.1	0.1382

1.0	0.0089
10	0.000697

The results designate that we cannot apply the Rayleigh constant value calibrated from the simple case into other complicated case like the HG MAC model. TEES decided to stop analysis this subject with Solidworks.

MODELING OF HOURGLASS DAMPING ELEMENTS WITH FLUID-SOLID INTERACTIONS

One of the keys to reaching high damping and high stiffness is the optimization of each component in the system. In order to maximize energy dissipation in the fluidic damper, a modeling effort was conducted. Due to the interaction between the solid deformation of the damper and the fluid pumping, the modeling was done using a two-way coupled computational fluid dynamics (CFD) and finite element analysis (FEA) code. This section describes the software implementation, the anchoring to experimental data, and the geometric study conducted with the modeling.

Software Implementation

When the fluidic damper is compressed, the sidewalls move towards each other and displace fluid. Of course, this pumping action is desired since the resultant pressure distribution is responsible for dissipating energy. However, the pressure distribution also affects the shape of the sidewalls. As shown in Figure 183, this creates a coupled fluid-solid system. In order to accurately model the damper, the method chosen was two-way coupled computational fluid dynamics and solid finite element analysis. The combined fluid-structural interaction (FSI) model provides coupling terms in each solver in order to represent the effect of the other phase. This section discusses the implementation of the software used to conduct FSI modeling of the fluidic damper.

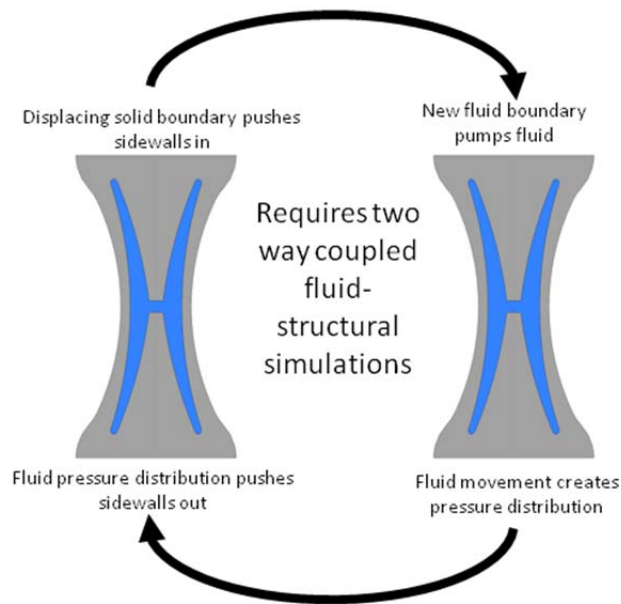


Figure 183. Schematic of two-way coupled fluid-structural interaction in the fluidic damper.

Given Aerospace's experience in CFD using the commercial code ANSYS-CFX, the fully coupled FSI simulations were conducted with ANSYS-CFX and ANSYS Mechanical. Aerospace obtained and installed an ANSYS Mechanical module. Together with the ANSYS-CFX module for computational fluid dynamics, the Mechanical module allows two-way fully coupled fluid structural interaction. The ANSYS framework simplifies the setup of coupled simulations and handles the information transfer between the FEA and CFD simulations. Preliminary geometry, shown in Figure 184, was constructed and used to demonstrate proper coupling between the two simulations. The geometry contains both a solid domain, shown as a wireframe, and a fluid domain, shown with the mesh faces.

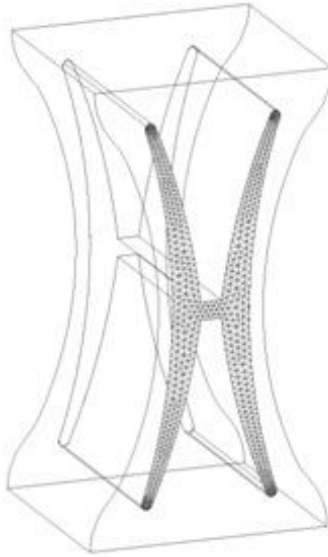


Figure 184. Geometry and mesh used for preliminary two-way coupled fluid structural simulations of the fluid damper.

The simulated displacement and fluid flow of the preliminary geometry simulations is shown in Figure 185. The trace representing fluid flow as a function of time shows that, as intended, displacement applied on the top of the hourglass element pushes the sidewalls inward. The displacement of the interior walls is transferred to the CFD simulation. The boundary nodes of the CFD mesh move inward, and the software calculates the resulting velocity profile as fluid is pumped in or out of the domain. The velocity profile creates pressure on the CFD boundary, and ANSYS transfers the pressure profile back to the FEA simulation.

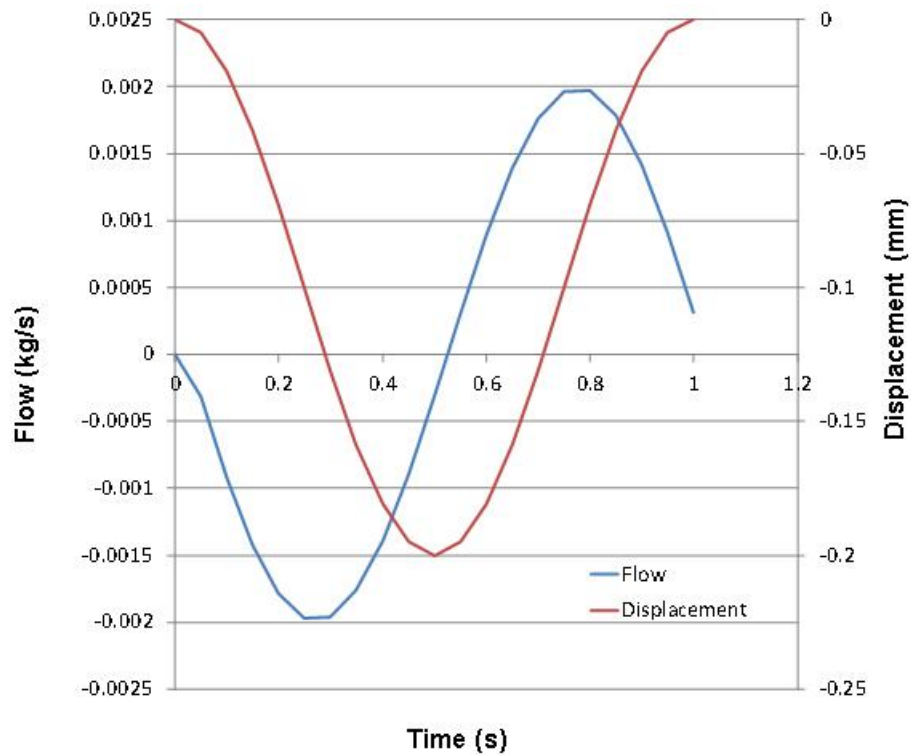


Figure 185. Flow and displacement for the preliminary hourglass damping element demonstrating solid motion creates flow in the fluid simulation.

Improving Modeling Implementation

Due to the strongly coupled nature of the fluidic damper calculations, there were a number of challenges to achieving good convergence and stability. During preliminary runs, it was apparent high viscosity or small timesteps caused convergence difficulty. The reason is due to the use of two separate solvers for a tightly coupled solution. When the solid boundary is displaced, the simulation prediction overshoots the correct displacement because the fluid pressure boundary condition in the FEA solver does not increase until the CFD module is allowed to iterate. When the CFD module does iterate with the overshoot boundary provided by FEA, the pressure field is higher than in reality. Thus, both the solid and fluid corrections to each other are higher than appropriate, and create instability in the computation. The viscosity of the fluid acts as a gain for this instability, creating higher fluid forces at a given solid deformation. In addition, for incompressible fluids, small displacements create very high pressure forces in the CFD solver. To overcome this instability, the default simulation parameters were modified by the addition of a source coefficient on the boundary. This term, which goes to zero at convergence, improves the solver coupling by simulating some of the terms that would exist in a completely coupled implicit solver.

However, the implementation of the boundary source term complicates determining whether the solution has achieved adequate convergence in a given timestep. To investigate this, several simulations were conducted that varied the boundary source term and the number of coupling substeps. The boundary source term controls the stability of the simulation and the speed of convergence. Larger values can almost guarantee convergence, but require more substeps, more

computational time, and make it harder to verify the solution has truly converged. The number of coupling substeps controls the convergence. A certain minimum, which is unknown for a given simulation set-up, is necessary for the solution at a specific timestep to settle at the correct total fluid force for that timestep. The behavior of the LHG problem is very sensitive to these parameters. Boundary source terms small enough to guarantee convergence with few substeps do not guarantee overall stability, leading to wasted runs that fail halfway through the computation. Setting a very high number of substeps that might be desirable for the use of large boundary source terms creates runs that produce no useful results in a realistic amount of time.

However, after several combinations were attempted, one pair of values showed improvement over the selection for previous simulations. Figure 1 shows the damping curve for the 64mm LHG for 60 kCp fluid. At 0.2 Hz, the preliminary simulation result of $\tan \delta = 0.26$ underpredicted the experimental data without any theoretical reason. The new choice of values for boundary source term and minimum coupling iterations results in a significantly higher computed damping value of $\tan \delta = 0.57$. In fact, that value overpredicts the experiments. However, that difference can be explained by the presence of bubbles or cavitation. Any vapor in the LHG allows compression without additional pumping, which reduces the total fluid force and decreases damping.

Figure 186 shows the effect of sub-iterations on the damping curve from 0.1 to 2 Hz. For the lower frequencies, the damping coefficient has been raised from approximately 0.1 to 0.4. While the peak damping value still occurs at 0.5 Hz, the damping with increased sub-iterations is quite large, rising to 0.93. Above the peak damping frequency, the damping ratio rapidly decreases. At 2 Hz, there is little change from the earlier simulations. It is expected that the greatest change due to increased sub-iterations would occur at peak damping. Increasing the sub-iterations allows the fluid force to develop to the correct steady state value. At higher frequencies, the fluid force is not as large due to the restriction of sidewall motion, and the earlier number of sub-iterations was adequate to achieve a steady state value. At lower frequencies, and especially at the peak damping frequency, it requires a larger number of iterations.

With the larger number of iterations comes an increase in run times. During the first runs with the new convergence parameters, run times were approximately 48-96 hrs. Several steps were taken to decrease the run time as additional data points were obtained. First, it was confirmed that the CFD simulations achieve steady state in 1.5 cycles. Earlier simulations used 2 full cycles, but the calculated damping coefficient changes very little when selecting the period between 0.5 and 1.5 cycles and the last cycle. Using a shorter overall time decreases the run time. In addition, the convergence parameters were changed to improve run time while still allowing for full convergence. For the 96 hour run, it was clear that the simulation ran for many sub-iterations after steady state was already achieved. Final run times were approximately 15 hrs, which is reasonable.

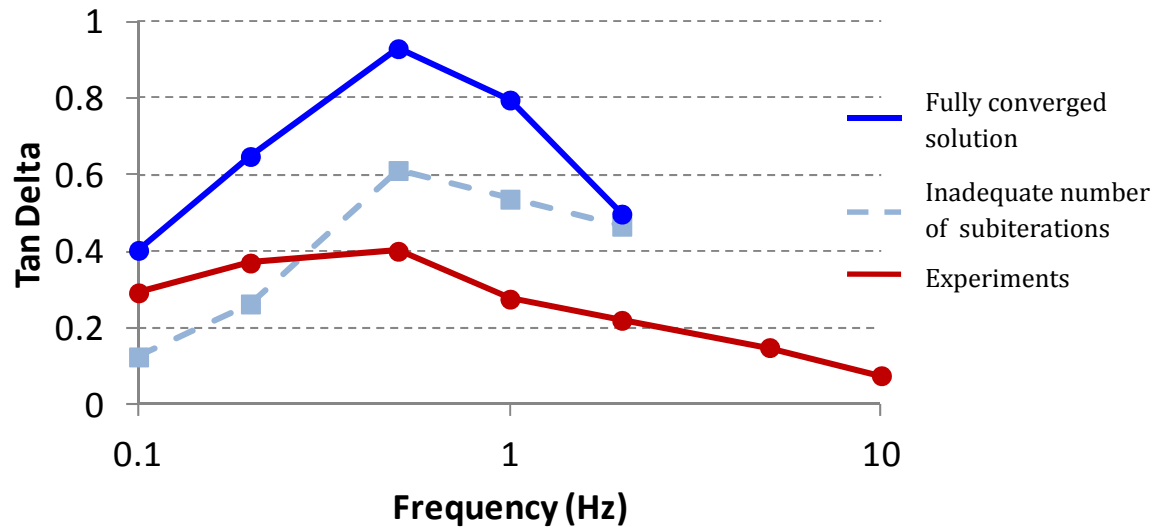


Figure 186. The damping curve for the 64mm LHG with 60 kCp fluid.

Another issue in modeling was that runs consisting of a large number of timesteps often crashed due to memory issues. Apparently the LHG scenario identified an issue in ANSYS's memory usage. The computational process continues to consume memory with each additional timestep and eventually outgrew the default allocation. It was recommended to upgrade to ANSYS version 14, which supposedly contained fixes to the issue. Unfortunately, upgrading did not fix the issue. After significant discussions with ANSYS, a workaround that increases the memory allocations was identified. The coupled fluid-structural problem is unique in that it requires the memory allocation to be increased for both the fluid and structural solver. After this solution was applied, longer simulations were conducted to insure steady-state behavior was reached for the fluidic damper. This was especially important in the case of the Wide Trial Geometry, discussed later.

Both run duration and timestep size were investigated to insure the calculated damping coefficient did not depend on these variables. For long duration runs that were conducted to verify that the simulations reach steady state, later cycles in the run produced identical values for damping as the earlier cycles. This validated the use of simulations consisting of only 2 cycles. Runs were conducted using a smaller timestep with a higher resolution mesh. At the expense of 2-3 times the computational time, these simulations produce about 5-10% difference in the final damping quantification.

To allow efficient processing for optimization runs, calculation of Tan Delta was automated. A tool was created to process displacement and force results from the computational runs. With minimal user involvement, the tool produces equivalent tan delta values for direct comparison with experiments.

Validation with Existing Experimental Data

Before using the simulations to optimize the hourglass damping-element, existing experimental trials were used to understand the accuracy of the model. The preliminary geometry was lengthened to match the prototypes built and tested by TEES. There is a small penalty in

computational time when the mesh size is increased. To counteract this, the simulations used a symmetric boundary condition in both the solid and CFD modules.

One of the key parameters in the simulation is the modulus of the polymer used to fabricate the damping machines. Unfortunately, it was not possible to use the elastic modulus obtained from a tensile test since the material properties of the dampers depend on the pattern used to produce the specimen. Thus, the elastic modulus was calibrated by conducting solid-only trials. The modulus needed to match experimental solid only runs was determined by trial and error to be 1333 Mpa.

Figure 187 shows the results for force versus time for two simulations compared to experimental data. The two computational trials were conducted for a viscosity of 75,000 cP. The viscosity of the experimental trial was 102,000 cP.

While not a comparison between identical operating conditions, the comparison between experiments and computations for reaction force shown in Figure 187 are encouraging. The computations show the correct trend, with force increasing as viscosity increases. For the higher viscosity, the total force is about 25% lower than the experiments, which scales well with the difference in viscosities. The simulations also predict that the fluid force is strong enough to create positive force. This is also present in the experimental trials, where the force is positive at the top of the cycle.

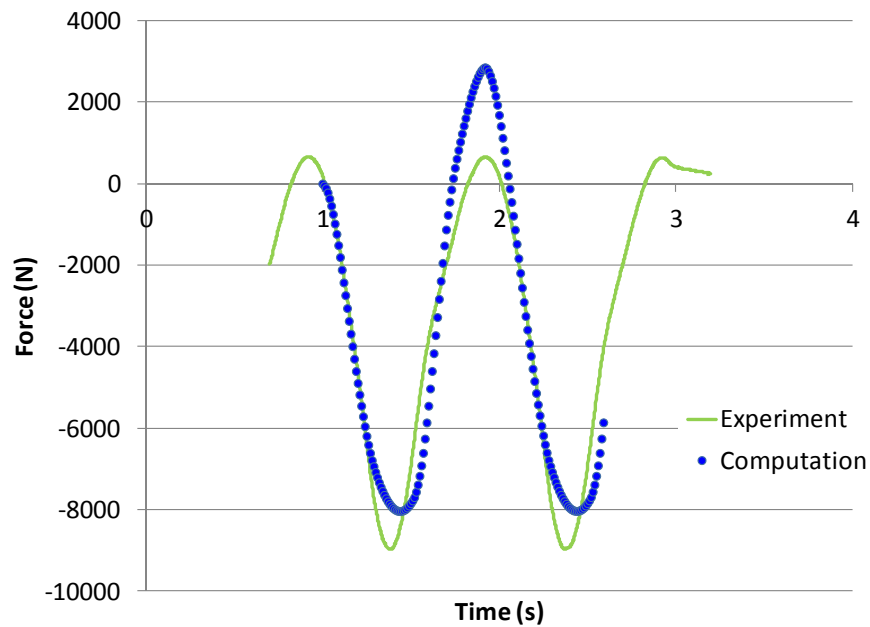


Figure 187. Total force for the 64 mm LHG filled with 60 kCps at 1 Hz

Geometric studies

One of the goals of the LHG modeling is to predict improvements in damping due to changes in geometry. This section will discuss geometric changes that use different pathways to increase the

damping coefficient. The first pathway is to increase fluid force. That was accomplished in the model by reducing the hydraulic diameter of the fluid channel. The second pathway to increasing damping is to reduce the stiffness of the damper. This decreases the energy stored during the damper's stroke and increases the damping coefficient.

Many of the possible geometric changes have the underlying effect of reducing the hydraulic diameter of the fluid cross-section and increasing the overall fluid force. Focusing on simplicity, a trial geometry was created to reduce the distance across the midsection of the LHG geometry and the fluid cross sectional area. Figure 188 shows the old geometry and the Narrow Trial Geometry (NTG). This design also decreased energy storage by creating more compliance in the vertical direction. In addition, the design should have increased stiffness in the transverse direction. Increasing stiffness in the transverse direction would extend the peak damping frequency. Results with this geometric change were very positive, showing a $\tan \delta = 0.96$ at 0.2 Hz for a 60 kCp fluid viscosity.

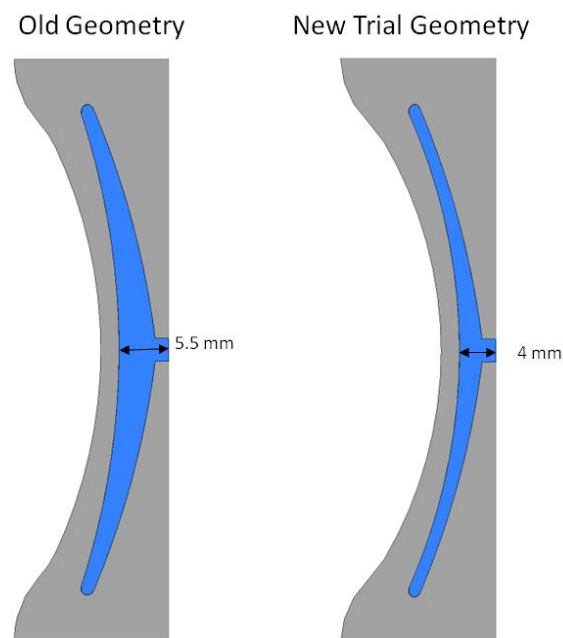


Figure 188. Geometry for a damper with a reduced transverse width

Figure 189 shows the calculated damping coefficient for the NTG geometry at 0.1 Hz, 0.2 Hz, and 0.5 Hz. Experimental data is also included. At 0.1 Hz, the comparison is quite good, showing the ability of the simulations to capture the behavior of the damping machines. At 0.2 Hz and above, the predicted damping is above the measurements. As will be discussed, at higher frequencies in the experiments the silicon oil in the damping machines cavitates and performance is dramatically reduced. The simulations do not include cavitation effects, and thus over predict the experimental results.

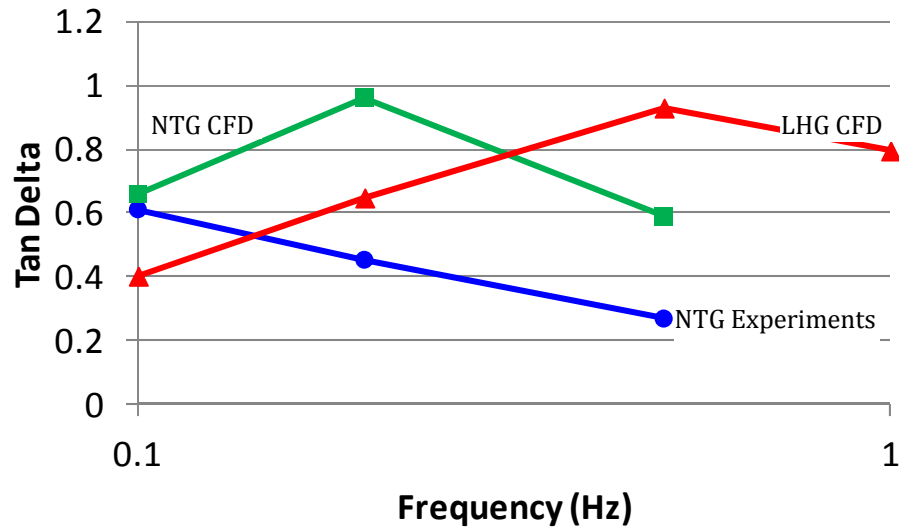


Figure 189. The damping curve for the 64mm NTG with 60 kCp fluid

An alternative to increasing damping by increasing fluid forces is to increase damping by decreasing energy storage. A third geometry was created that increases the width of the damper, which decreases stiffness and increases the area over which the fluid forces occur. Since the damping coefficient is the ratio of energy stored to energy dissipated, decreasing stiffness should increase the damping coefficient. Figure 190 shows a comparison between the original hourglass geometry (LHG), the Narrow Trial Geometry (NTG), and the Wide Trial Geometry (WTG). The results are encouraging. The WTG simulation for 0.2 Hz shows a damping coefficient of 1.76, compared to 0.96 for the NTG. The normalized force displacement curve for the WTG, shown in Figure 190, is approaching the ideal open circle. It is possible that with further optimization of the fluid passageway that the damping would further increase.

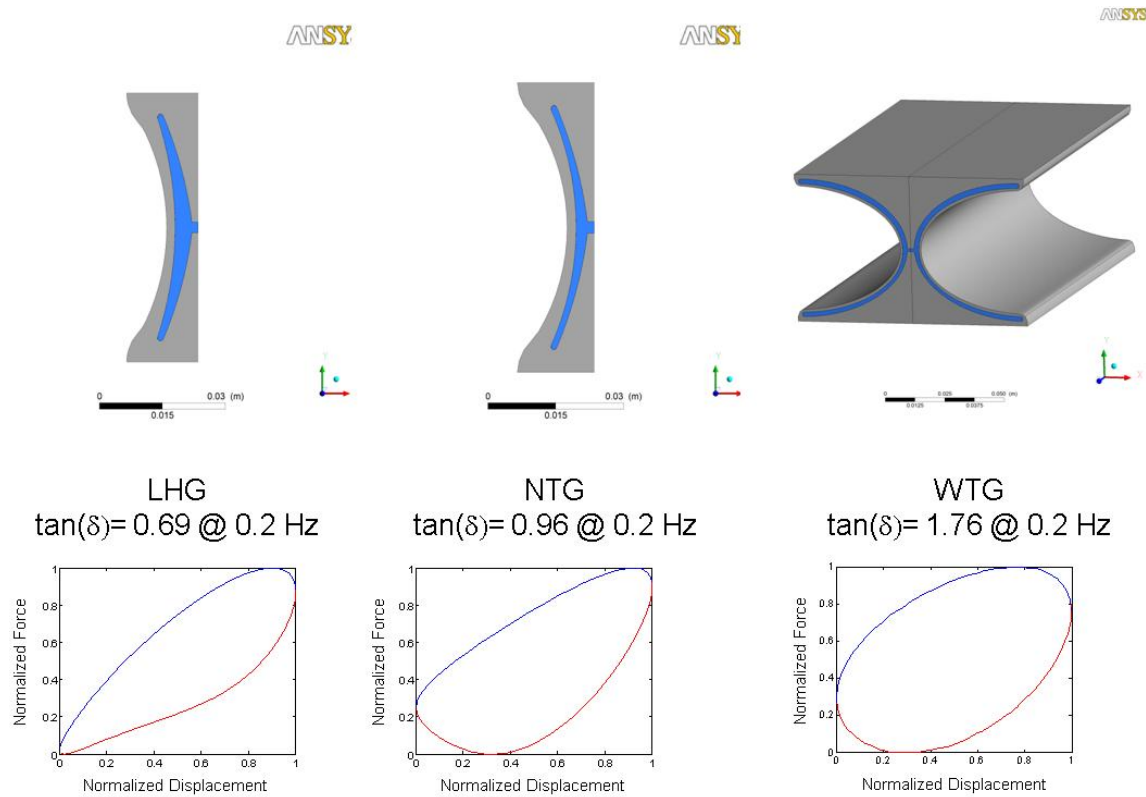


Figure 190. Damping machine geometry comparison

The WTG has another significant advantage over the LHG and NTG geometries. The wider overall area provides the same total force at lower fluid pressures when compared to the NTG or LHG. Figure 191 shows the pressure at the center of the fluid channel versus time for the three geometries. The amplitude for the LHG and the NTG is much higher than the WTG. The figure also shows a level below which the silicon oil in the machines would be expected to cavitate. The LHG and the NTG pressure falls well below this, showing that even at 0.2 Hz, those machines cavitate in the experiments. The WTG should not cavitate until higher frequencies, which will enable the experimental WTG to produce damping coefficients as high as the predictions from the simulations.

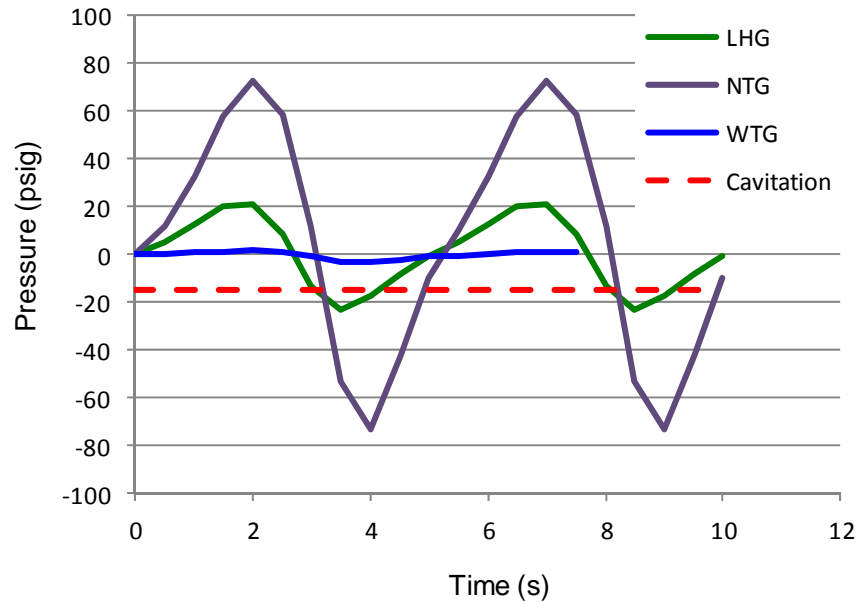


Figure 191. Fluid pressure in the damping machines at 0.2 Hz

WTG Simulations

Simulations were run to predict performance of the WTG at higher frequencies. Unfortunately, the WTG undergoes more overall deformation than the LHG. This makes the structural portion of the simulation more difficult to converge. This was solved by decreasing the under relaxation term and increasing the number of sub-iterations, at the expense of run time. In addition, the WTG takes more cycles to achieve steady state than either the LHG or the NTG. Previous calculations demonstrated those geometries achieve steady state in the simulations within 2 cycles. The WTG took 6 cycles to achieve steady state at 1 Hz. The combined effect of the increase in sub-iterations and the increase in overall simulation time is very long run times. The WTG simulation for 1 Hz took approximately 6 days to run.

Figure 192 shows the results for the WTG at higher frequencies. The figure also contains data for the WTG experiments and simulations for the LHG geometry. The comparison between the experiments and simulations for the WTG is encouraging. One of the design goals for the WTG was to lower the amplitude of the pressure fluctuations inside the damper to avoid cavitation. This appears to have been achieved, since the experimental data for the WTG is very close to the theoretical prediction at 1 Hz. However, the overall performance at higher frequencies is not as high as expected. The curved sidewalls that create low stiffness were also intended to form an arch that would continue to pump fluid even as fluid pressure increases at higher frequencies. Comparing the LHG to the WTG at 1 Hz, the LHG shows superior performance and appears to be more resistant to the effects of increasing fluid pressure. One possibility is that the pumping in the WTG comes from the entire area rather than the center of the damping machine. If that is the case, high fluid pressure along the length of the arch would quickly overcome the lack of stiffness in that area. One additional goal for future work could be to further optimize the geometry of the WTG.

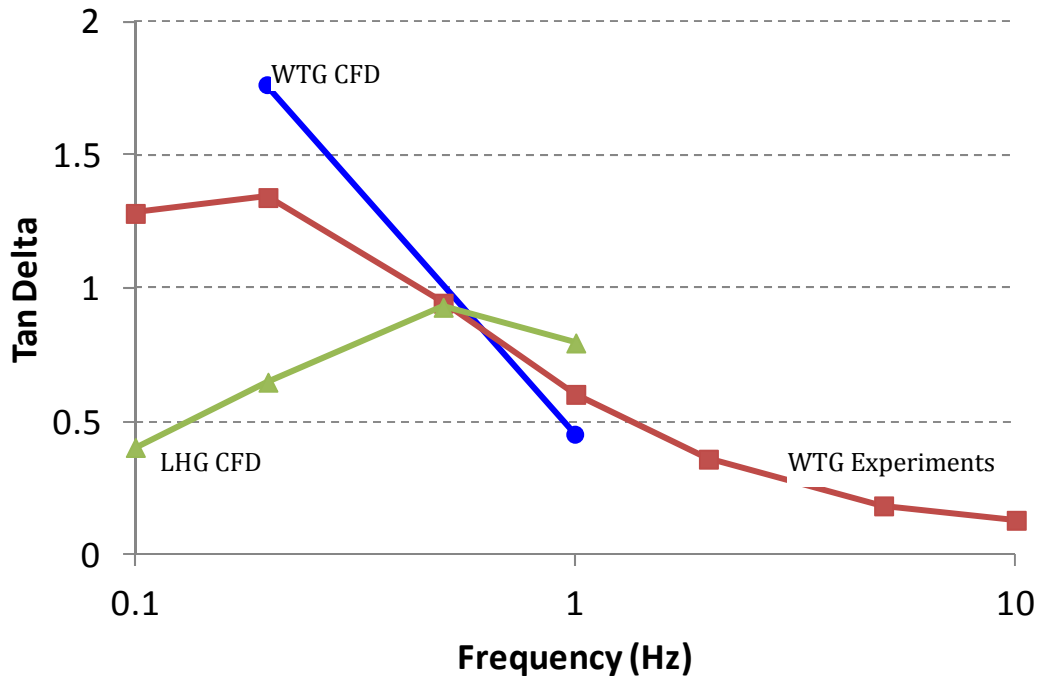


Figure 192. The damping curve for the 64mm WTG and 64mm LHG with 60 kCp fluid

Shear-Thinning Fluid

One of the design improvements has been to use shear thinning fluids in an effort to improve damping at higher frequencies. ANSYS-CFX contains several sub-models to simulate variable viscosity fluids, even in coupled fluid-structural problems. For this problem, the Bird-Carreau model was used. A variant of the typical power law model, this submodel limits viscosity at lower shear rates. This insures the CFD solver functions well at startup when the fluid experiences zero strain rates. Figure 193 shows the viscosity of the experimental fluid, 5% polyacrylamide, compared to the modeled viscosity. The modeled viscosity represents the real fluid's viscosity well in the range of shear rates experienced by the LHG. Simulations were run at three different frequencies using the 5% PAM solution. The results shown in Figure 194 show that the decrease in damping at higher frequencies is mitigated by using the shear thinning fluid. One advantage of simulations is the ability to investigate flow field variables. By examining the shear strain rate at various points in the simulation, it was determined that the maximum viscosity experienced by the LHG with 5% PAM is about 50 kCps. Much of the field experiences less than this. Thus, it is not surprising that the overall damping in both the experiments and the simulations for 5% PAM is lower compared to the experiments that use higher viscosity simple fluids.

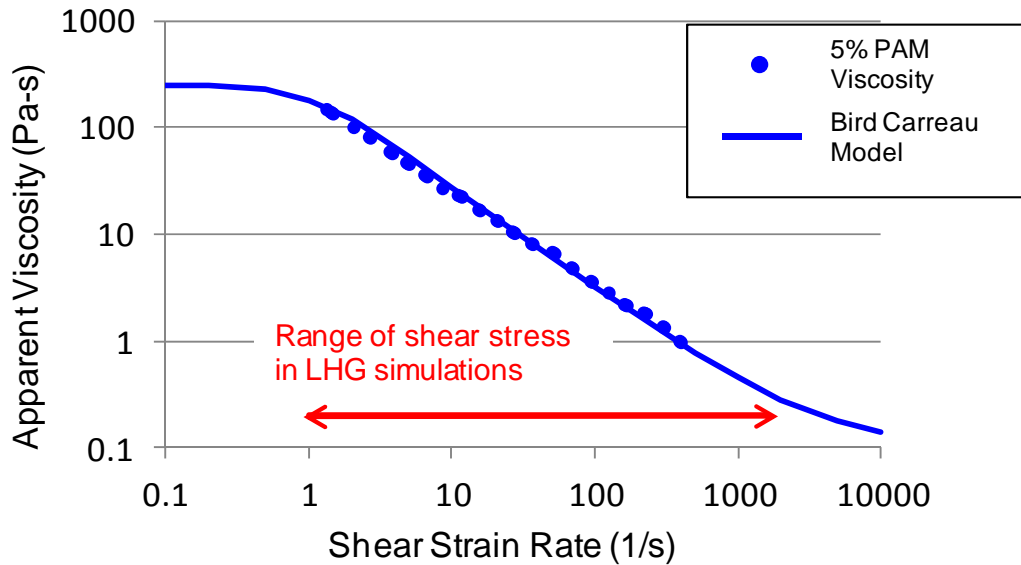


Figure 193. Experimental and simulated viscosity for 5% polyacrylamide

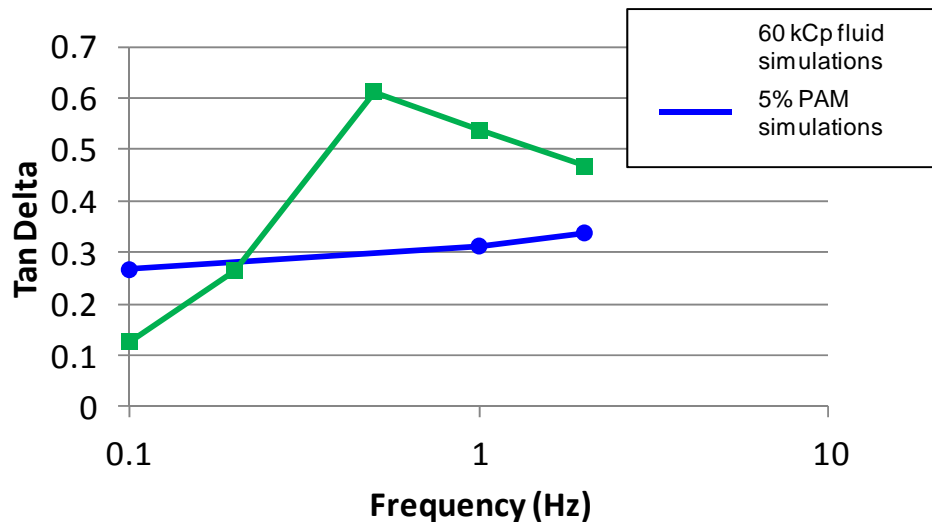


Figure 194. Comparison of damping between simple fluid (60 kCps) and shear-thinning fluid (5% PAM).

Shear Thickening

Additional simulations were conducted for shear-thickening fluids that increase in viscosity as the shear rate increases. Figure 195 shows the viscosity of a PEG/Silica solution compared to the CFD submodel calculations for viscosity as a function of shear rate. Similar to the methodology for the shear thinning simulations, the submodel used is a power law variant that limits viscosity at high and low shear rates. However, to simulate shear-thickening fluid, the exponent is greater than one. Another difference between the shear thinning and thickening fluid simulations is that the shear thinning fluid demonstrates consistent behavior with changes in shear rate. The shear thickening fluid shows a more complex behavior, with viscosity decreasing with increasing shear rate at low

shear rates (shear-thinning), then switching to shear-thickening behavior at higher shear rates. The CFD submodel for shear-thickening viscosity only captures the shear thickening behavior. The assumption is that the application of shear thickening fluids would be conducted in the region that demonstrates increasing viscosity.

Figure 196 shows the damping results as a function of frequency for the shear thickening fluid, along with the shear thinning and simple 60 kCp fluid for reference. As expected, the rate of increase in damping as frequency increases is much higher for shear thickening fluids than either the simple fluid or the shear thinning fluid. As frequency increases with a shear thickening fluid, the gain in damping due to the fluid velocity increase is added to the gain due to the increase in velocity.

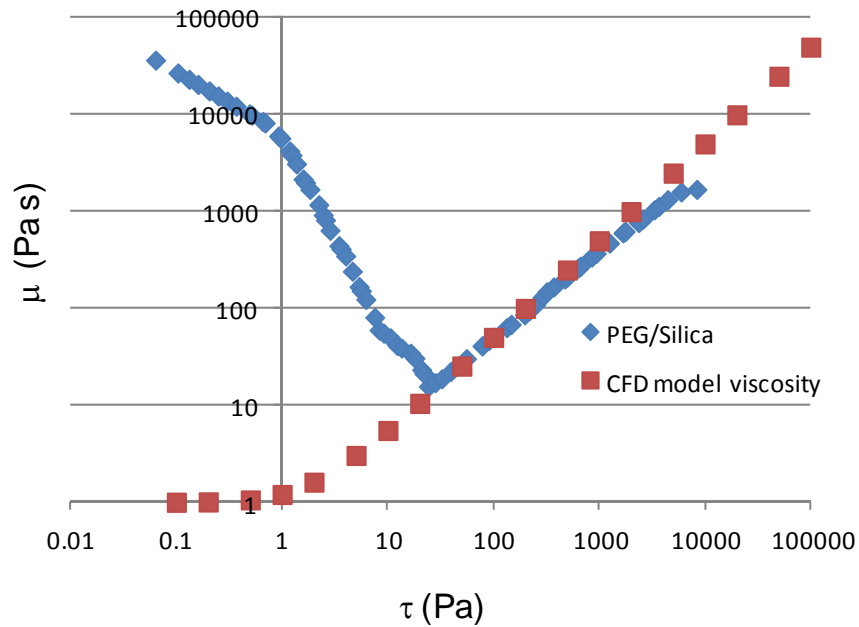


Figure 195. Viscosity submodel for shear-thickening fluid

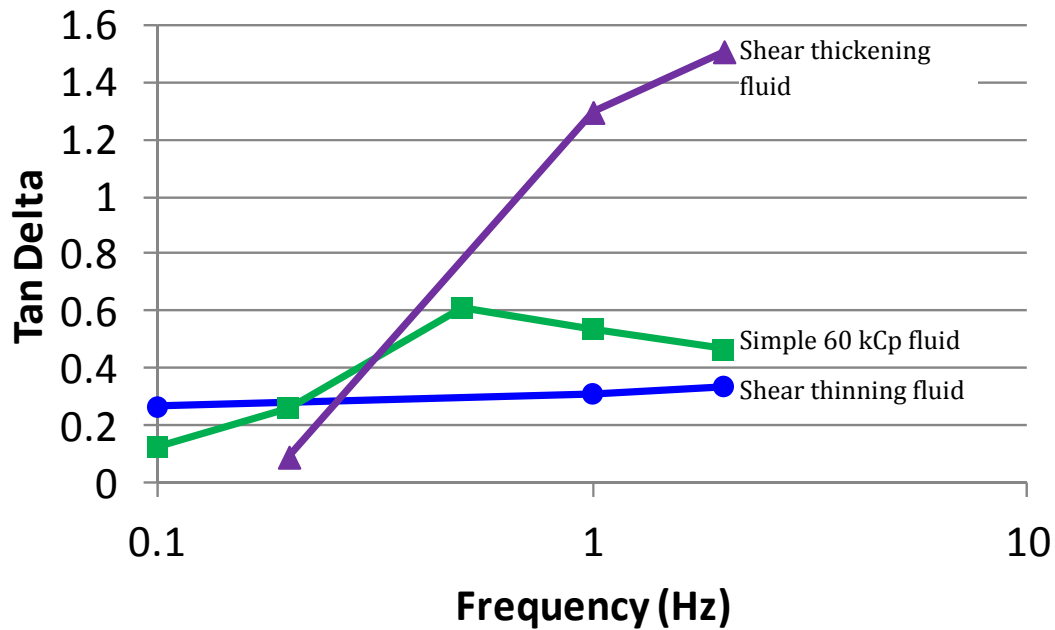


Figure 196. Damping curves for shear thickening, shear thinning and simple fluids

Modeling Conclusions and Future Work

It has been shown that using coupled fluid-structural modeling, implemented in ANSYS, is successful at calculating the response of the fluidic damper. One of the advantages of using a high fidelity model is the ability to observe fundamental measurements in spaces that are difficult to access experimentally. Thus, the model provided the insight that the machines were highly susceptible to cavitation. The resultant bubbles greatly diminish performance.

The model was also used to evaluate the effect of geometry, providing two shapes that have increased damping capabilities. The shape that focused on increasing fluid forces provided higher damping, but was vulnerable to cavitation. The other shape focused on decreasing energy storage. This shape proved to have very high damping and is much less likely to cavitate.

The model shows that there is still significant room for optimization of the damping shapes. The fluid forces in the WTG are low, and there is a large margin against cavitation. Examination of the WTG shape during deformation shows little change in the fluid cross-sectional area during the pumping cycle. The fluid passageway in the WTG could be modified to increase pumping and to increase fluid forces up to the cavitation limit. The WTG, while a big improvement over the LHG and NTG, has the potential for very high damping levels.

Task 2 Integration

Task 2-1 Modeling (AERO)

The goal of this program is to develop a new class of composite material that can adapt to varying environmental and tactical loads while simultaneously exhibit high stiffness and high damping. The proposed concept involves exploiting the unique properties when negative-stiffness, positive-stiffness, and damping elements are combined to form a novel material system.

Because negative springs are inherently unstable (material displaces in the direction of the applied force), the overall system stability must be carefully analyzed. In this section, the results of the stability analyses will be summarized, and the work leading up to the development of a stable, high stiffness and high damping system will be discussed.

SYSTEM STABILITY ANALYSES (LMS DADS)

Because negative springs are inherently unstable, it is necessary to utilize discrete elements to understand which configurations (initial conditions) would lead to a stable system that can be physically assembled and tested in the laboratory. Dynamic Analysis Design Systems (DADS) was used to perform the stability analyses. DADS is a multi-body simulation package that has the ability to assemble, simulate, and animate mechanical systems.

For simplicity, the model is comprised of a positive spring (k_1), a negative spring (k_2), a fixed base, and an upper body that is allowed to displace vertically. The first step is to study the stability of the interface because if the interface could not be kept stable, the whole system would not be stable.

In Case 1a and 1b shown in Figure 197, $|k_1|$ is larger than $|k_2|$. Both springs had equal lengths and were initially in their free length. The upper body is fixed. The interface was initially at 0.1 in. above the centerline, i.e., positive spring is compressed 0.1 in. Figure 197 shows the stable response of the interface as the positive and negative springs settle to equilibrium (small damping applied to allow faster solution convergence). This demonstrates that when $|k_1| > |k_2|$, the system is stable.

Other similar cases were studied where the $|k_1| = |k_2|$ and $|k_1| < |k_2|$. Both cases yielded *unstable* solutions (unstable interface), which resulted in springs being shot into outer space (when $|k_1| = |k_2|$) and springs slammed down to the fixed base (when $|k_1| < |k_2|$).

In Case 2 (Figure 198), the interface was intentionally placed at its equilibrium position (information gained from Case 1a and 1b). The upper body was given a sinusoidal displacement profile: moved down 0.01 in., moved up 0.02 in., and moved down 0.01 in. (returned to starting position). Not only was this system stable (as expected based on previous results), but the whole system exhibited much stiffer response (approximately 50 times stiffer than either the positive or the negative spring). The interface moved in-phase with the upper body, but the motion was amplified by a factor of 50, which also matches theory. This result showed promise in terms of creating an assembly that is stable and provides the necessary increase in stiffness to achieve the goals of this program.

In the next few sections, the process of building a system that would ultimately possess high stiffness and high damping is described.

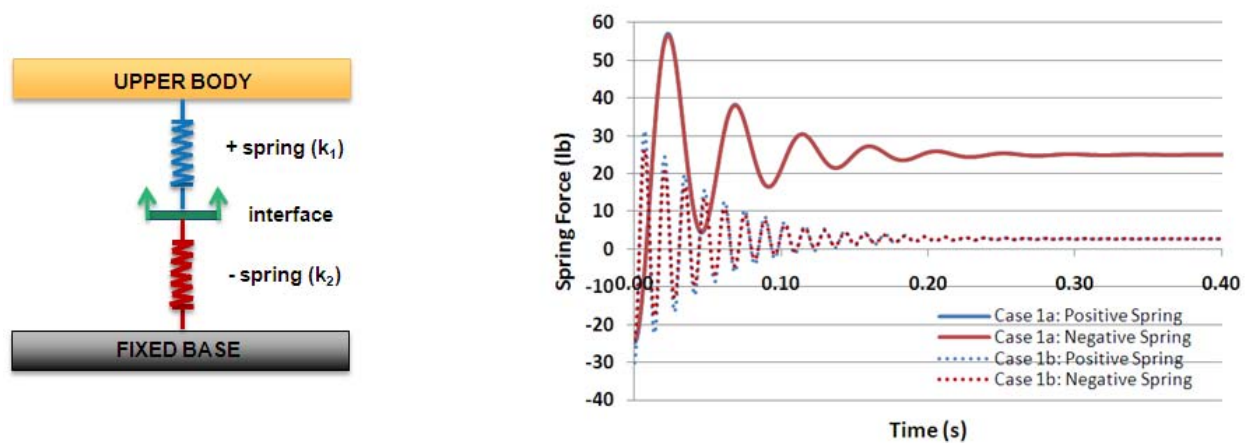


Figure 197. Case 1a: $k_1 = 250$ lb/in, $k_2 = -245$ lb/in. Case 1b: $k_1 = 300$ lb/in, $k_2 = -245$ lb/in. Stable interface.

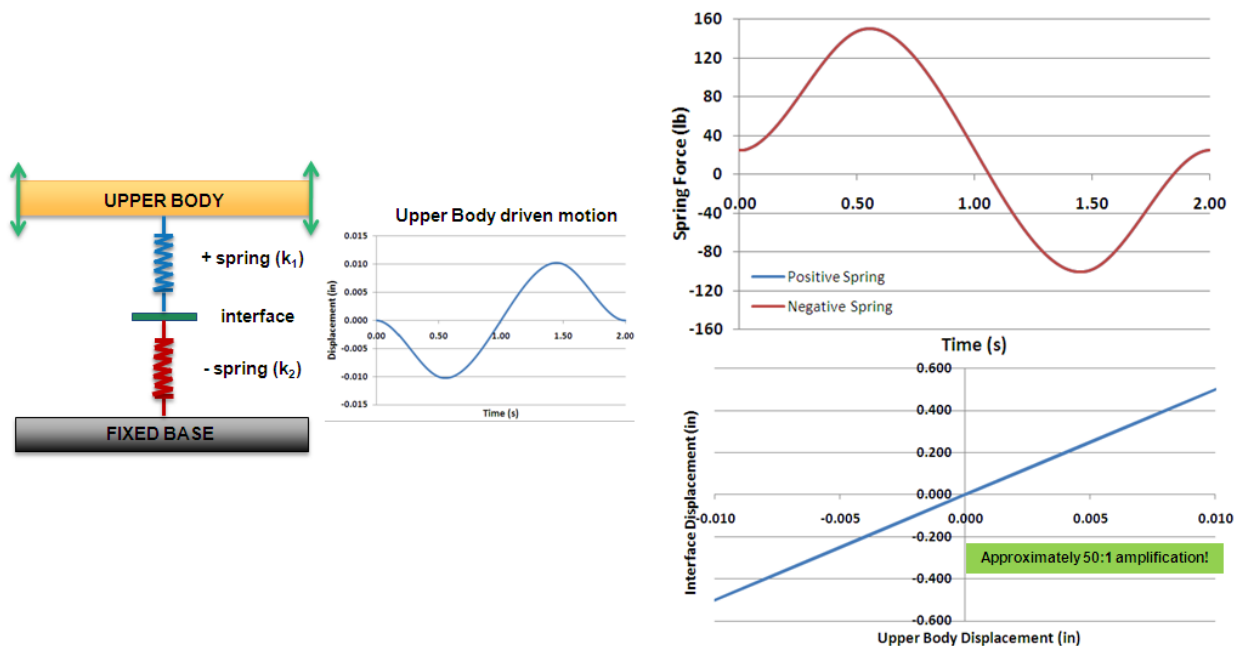


Figure 198. Case 2: $k_1 = 250$ lb/in, $k_2 = -245$ lb/in. Stable interface.

AN UNSTABLE SYSTEM DISPLAYING HIGH STIFFNESS AND HIGH DAMPING

In structural analysis, elastic material behavior can be modeled by linear springs. The idea of using springs to represent material behavior was used to simplify modeling of multi-body dynamic systems.

Solving this for two springs in series:

$$k_{eff} = \frac{k_1 k_2}{k_1 + k_2} \quad (2)$$

The idea was to have k_2 to have the same magnitude as k_1 , but with an opposite sign. The denominator would equal zero, which would result in an effective spring constant, k_{eff} , equal to infinity (theoretically). A damping element would then be added into the system of springs to provide an overall system with high stiffness and high damping.

When a positive spring connected in series with a negative spring shows amplified interface motion and system stiffness when $|k_1| > |k_2|$, i.e., $k_1 = 250$ lb/in and $k_2 = -245$ lb/in ($k_{eq} = -12250$ lb/in). The interface moved in phase with the upper body driven motion and the motion amplification was approximately 50 times. Because of the increased motion amplification, the force reacted on the upper body was also 50 times larger. This system showed great promise, which was the reason that we decided to pursue this further to see if we can obtain both high stiffness and high damping by taking advantage of the amplified interface stroke.

Figure 199 shows the result of adding a damper to the aforementioned system. Initially, when very little damping is in the system, the hysteresis loop was essentially non-existent (when $c=0.01$ lb·s/in). As the damping coefficient gradually increased, the hysteresis loop grew. At $c=1.00$ lb·s/in, a system displaying high stiffness and high damping was achieved. The reason that the maximum and minimum forces were lower for that case was because of the lag in the interface motion. As more damping is added to the system, the motion of the upper body (driver) and the interface go out of phase. The interface never had a chance to reach its full stroke before the motion was reversed. Even though stiffness suffered slightly (compared to the least-damped case), the increase in damping by 2 orders of magnitude was worth the expense. At the extreme, when the system is over-damped, the whole system became compliant (no stiffness), as shown by the horizontal hysteresis loop ($c=10.0$ lb·s/in).

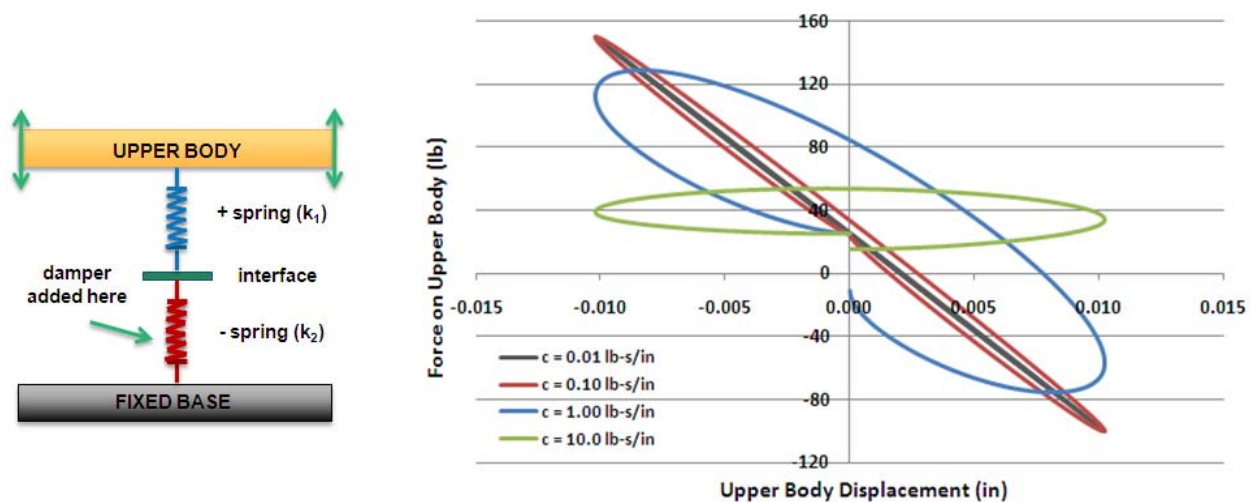


Figure 199.An unstable, but high (negative) stiffness and high damping system.

This system is inherently unstable, i.e., if the upper body was unconstrained, the upper body would not remain stable. The system is a negative spring. A material like this could be useful if it is inserted into a pre-existing gap, where the upper body resembles a part of the structure that required damping.

A STABLE SYSTEM DISPLAYING LOW STIFFNESS AND HIGH DAMPING

In order to create a stable system, a third spring was added in parallel to the two spring system and attached to the center of gravity of the base and the upper body (Figure 200). The addition of the third, positive spring allowed the overall stiffness of the three springs k_{123} to turn positive, where:

$$k_{123} = \frac{k_1 k_2}{k_1 + k_2} + k_3 \quad (3)$$

Furthermore, k_3 could provide the upper body stability when no constraint was applied to the upper body. Because k_1 was in tension initially to stabilize the Interface, the upper body had to be constrained and driven. By adding k_3 , and setting it in compression initially, it could counteract the force of k_1 on the upper body, and thus have a free standing, unconstrained, and stable system of two bodies. In addition, by varying the stiffness of k_3 , we can tailor the system to possess stiffness ranging from high negative stiffness to positive stiffness.

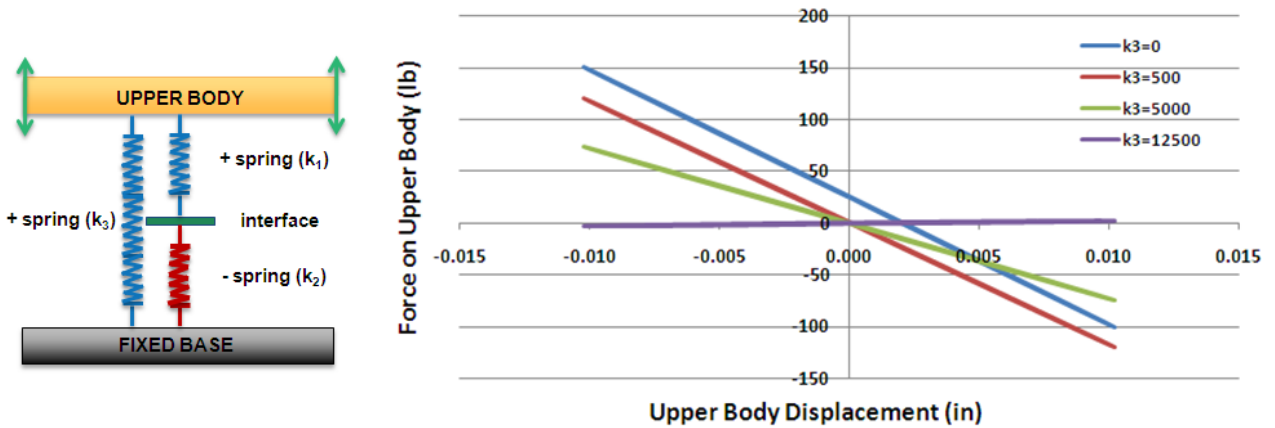


Figure 200. A stable, but low (positive) stiffness and high damping system.

In order to represent a damping element in DADS, an arbitrary damping coefficient was added to k_2 in DADS to observe its effect on the overall system. Figure 201 plots the force versus displacement of various coefficient of damping on k_2 . The slope of each curve represents the stiffness of the system, where the larger the slope, the stiffer the response of the overall system. The size of the hysteresis loops represent the damping of the entire system; the larger the loops the greater damping the system possesses. Figure 201 shows that in the three spring system, as the damping applied on k_2 increases, the overall system damping and the overall stiffness *both* increase. This is contrary to conventional materials where stiffness and damping move in different directions.

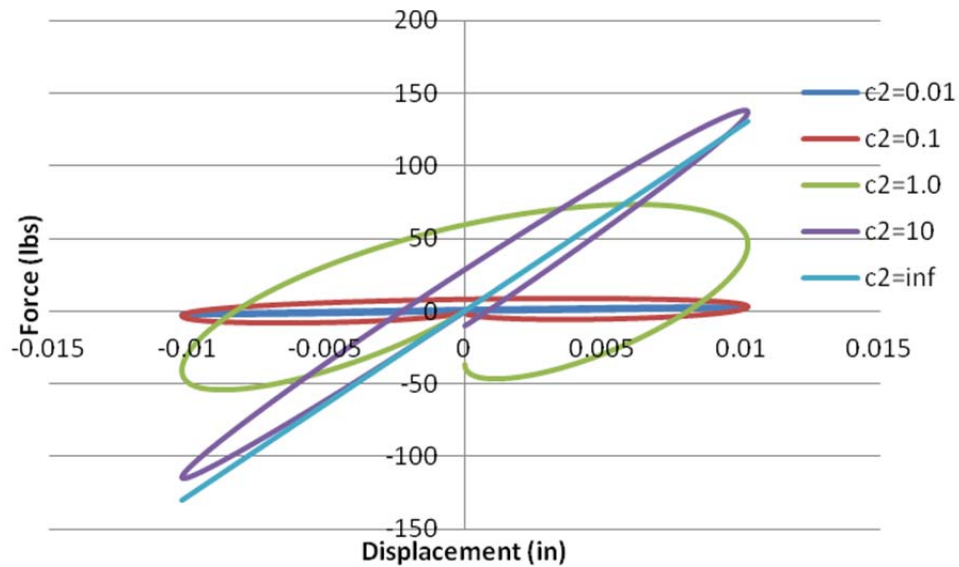


Figure 201. Overall system response with varying levels of damping (c_2) in k_2 .

INCREASED DAMPING DUE TO PRESENCE OF A NEGATIVE SPRING

From the results presented in Figure 201, the system is stable (a positive spring) when $k_3 = 12500$ lb/in, which is 250 lb/in greater than the effective stiffness of the system in Figure 199 ($k_{eq} = -12250$ lb/in). The overall stiffness of the system shown in Figure 201 is 250 lb/in. In order to ascertain the benefit of including a negative spring in the system in the first place, it is necessary to compare the response with another stable system that is comprised of only positive springs having the same overall stiffness (250 lb/in). This stable system consists of two positive springs connected in series, with each spring possessing stiffness of 500 lb/in. Figure 202 compares the load-displacement behavior of these two systems: one that is comprised of two positive springs and one that is shown in Fig. 4.

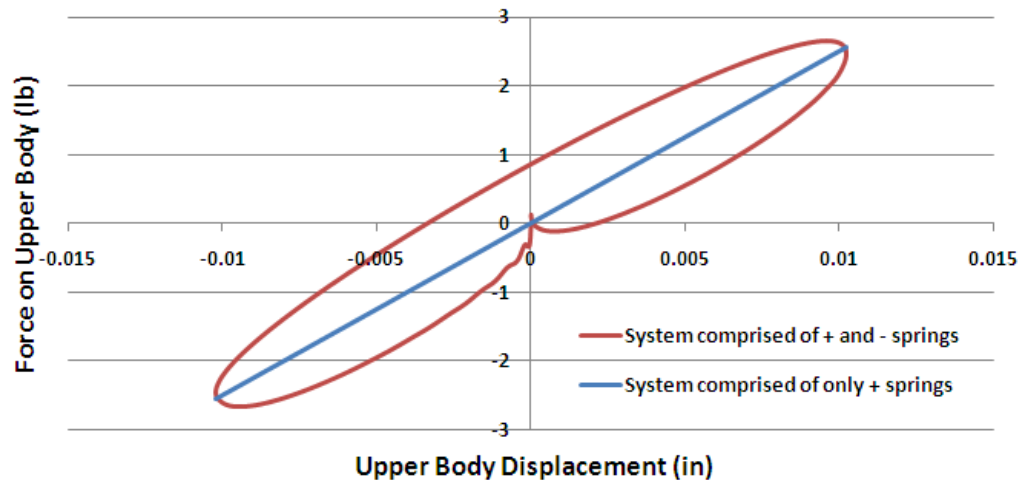


Figure 202. Presence of a negative spring in the system shows increased damping.

Minor damping ($c=0.01$ lb·s/in) was included in the bottom spring for both systems. For the system with the negative spring, the hysteresis loop was much larger because of the motion amplification

of the interface. For the system with only positive springs, the hysteresis was hardly noticeable, which meant that the system had minimal inherent damping. This analysis demonstrates that it is possible to create a system with the same stiffness as a conventional, stable material, but with much greater damping capability.

A STABLE SYSTEM DISPLAYING HIGH STIFFNESS AND HIGH DAMPING

When a positive spring connected in series with a negative spring showed amplified interface motion and system stiffness when $|k_1| > |k_2|$, i.e. $k_1 = 250$ lb/in and $k_2 = -245$ lb/in ($k_{eq} = -12250$ lb/in). The interface moved in phase with the upper body driven motion and the motion amplification was approximately 50 times. Because of the increased motion amplification, the force reacted on the upper body was also 50 times larger. However, the combination of the two springs resulted in a stiff *negative* spring.

A new concept for a stable system displaying high stiffness and high damping is shown in Figure 203. The motion amplification assembly (k_1 and k_2) was used for damping purpose only because a dashpot works best when the stroke can be maximized. In order to stabilize the negative-stiffness resulting from k_1 and k_2 , an additional positive spring, k_3 , whose stiffness magnitude exceeds $k_{eq} = -12250$ lb/in from k_1 and k_2 , was attached in parallel. The entire assembly consisting of k_1 , k_2 , and k_3 was inserted into a 4-bar linkage with hinges (pinned joints) that allow the links to move vertically. An additional positive spring, k_4 , provides additional rigidity to the system. In a practical material system, k_3 and k_4 are coupled, i.e., k_3 is the stiffness of the material in the transverse direction, and k_4 is the stiffness of the material in the axial direction (the direction of the applied force or displacement). The system in Figure 203 is fixed on the left side and driven with a sinusoidal displacement profile (amplitude of 0.001 in.) on the right side. The overall system exhibits high stiffness and high damping as a result of the combination of k_4 , motion amplifier assembly (k_1 , k_2 , and k_3), and the mechanical advantage from the rigid links.

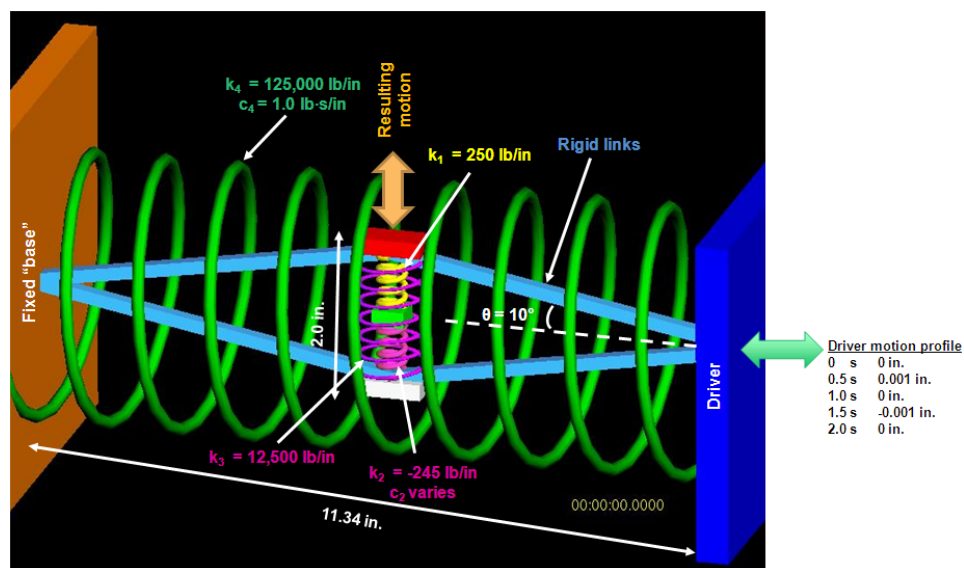


Figure 203. A stable material system that display high stiffness and high damping.

If the rigid links were replaced by a practical structural element, e.g., beams, the beams would be curved as shown in Figure 204. The curved beams are rotated 90 degrees from the assembly shown previously. To replicate more accurately the assembly in Figure 203, the curved beams were each given dimensions of 11.34" in height, 2.00" in width, and 0.25" in thickness. The material was stainless steel ($E = 210 \text{ GPa}$). The thickness was chosen because the transverse stiffness ($k_3 = 15,000 \text{ lb/in}$) of the dual beams (at 5-degree curvature angle, θ) closely matched the original k_3 (12,250 lb/in) that was assigned in the DADS model (Figure 203). Because of geometry, a beam with a lower curvature (larger radius) would have a higher mechanical advantage. The mechanical advantage is defined as the ratio of the displacement of the beam in the transverse direction to the displacement in the axial direction (direction of application). In the configuration shown in 35, the mechanical advantage was approximately 10.8, i.e., for every unit of displacement the beams were compressed, the combined transverse displacement (bulging out) of both beams was 10.8 units.

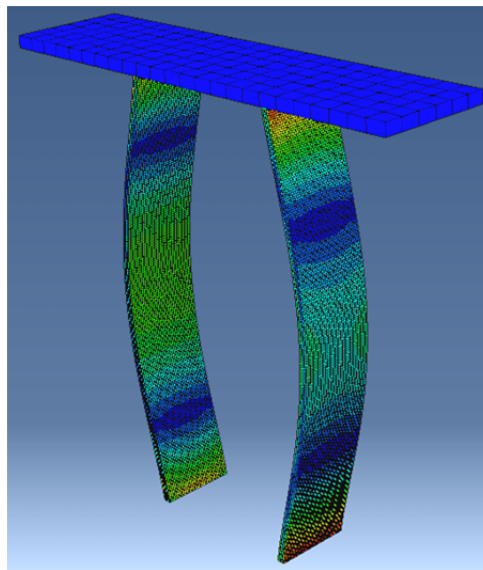


Figure 204. ABAQUS model of curved beams of 5-degrees to replicate the rigid links in Figure 203.

For the dual-beam configuration in 35, the axial stiffness (k_4) is 809,000 lb/in ($E = 63 \text{ GPa}$) according to the FEA result. This value was then used for the DADS model to provide a more realistic stiffness information and relationship between k_3 and k_4 . The DADS model was run again using the updated stiffness values, and the results are shown in Figure 205. The plots resemble the familiar force-displacement response of the system with varying damping coefficient for the damping element (c_2). For the case where c_2 is 1.0 lb·s/in, the resulting interface motion amplification was almost a factor of 500 (Figure 206). The stiffness of the system was approximately 1.6 million lb/in, which, given the geometries of the curved beams, $E = 124 \text{ GPa}$! The hysteresis loop was also large, which meant significant system dissipation. The modulus value needs to be validated with actual testing, but the modeling results clearly provided indication that reaching the stiffness metric of 100 GPa coupled with high damping is not impossible.

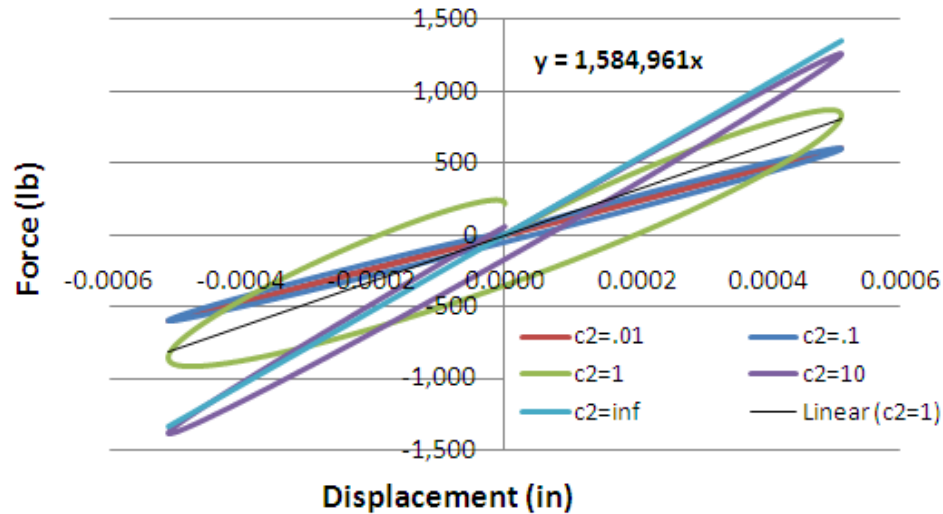


Figure 205. Response of a stable system displaying high stiffness and high damping.

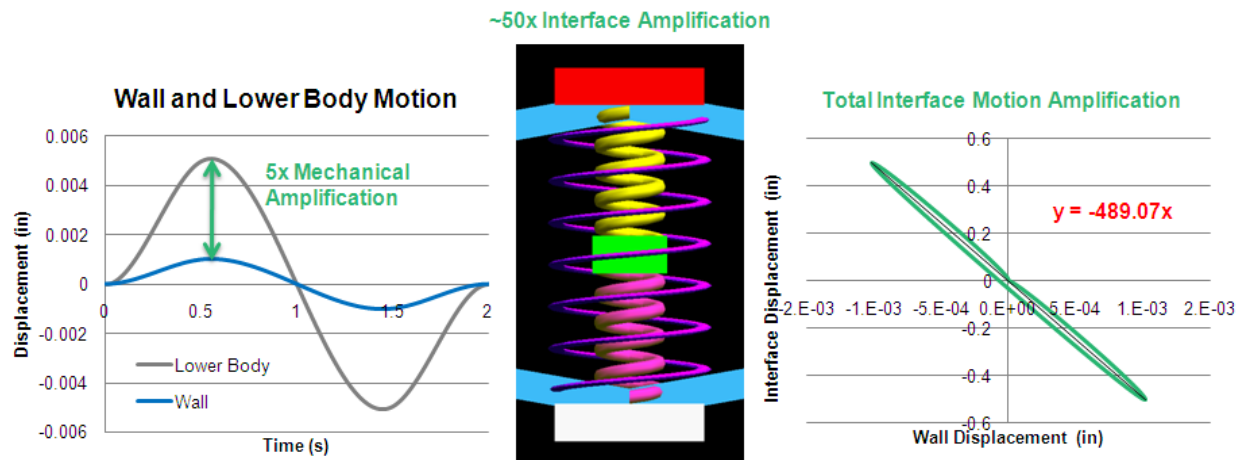


Figure 206. Total interface motion amplification of a stable, high stiffness and high damping system.

VERIFICATION OF MOTION AMPLIFICATION (PROVING THE CONCEPT OF COMBINING POSITIVE AND NEGATIVE SPRINGS)

Due to the inherent mechanical properties of a Clover Dome, the Clover Dome has limitations in terms of strain and stiffness. To verify and achieve measureable motion amplification as a result of combining a positive spring and a negative spring in series, it was necessary to match the stiffness of the positive and negative springs as closely as possible. The issue that arises in using the Clover Dome as the positive and the negative spring was the tendency for the Clover Dome to snap through when the stiffness magnitudes and forces converge due to slight mismatch in forces (inherent non-linear behavior of Clover Dome). In order to demonstrate the motion amplification concept and eliminate non-linearity and mismatch in forces, Aerospace fabricated a test fixture that uses a conventional spring as the positive-stiffness element. Even though the physical size of the compression spring was much larger than a Clover Dome, the stiffness was always constant and the snap-through phenomenon was eliminated. The fixture is shown in Figure 207.

The top half of the originally-designed fixture was replaced by a fixture that holds the compression spring. The compression spring was held firmly inside a top spring retainer and a bottom retainer via set screws at various axial locations around the circumference of the retainers. The top spring retainer had a tapped hole in the center that allows it to attach to the Instron crosshead. The bottom spring retainer also had a tapped hole in the center that attaches to the threaded rod (the “interface”). The bottom Clover Dome, which is the negative spring, was initially compressed until it reached its negative-stiffness regime. The force of the Clover Dome wanting to snap back was counteracted by the compression spring (which was being pulled in tension).

Figure 208 shows the actual set up of the fixture design. Spring retainers helped to hold the compression spring at the top (for mating with Instron) and at the bottom (for mating with the threaded rod that was attached to the Clover Dome). Compression was applied by the Instron and the total motion of the interface (which the bottom spring retainer also serves as) was visually captured. The total motion of the interface was actually known and finite and was limited by the negative stiffness range of the Clover Dome. By taking the ratio of the total displacement and the applied crosshead displacement, we determined the motion amplification of this system.

In the current set-up, the compression spring had a stiffness of 372 lb/in and the Clover Dome had a negative stiffness of approximately 285 lb/in. The theoretical motion amplification was calculated by taking the ratio of the stiffness of the positive spring and the sum (or difference in magnitude) of the stiffness of the positive and negative springs. In this case, the theoretical motion amplification was calculated to be 4.3.

Figure 209 shows the position of the interface at the start of the test and at the end of the test. A total crosshead compression of only 0.3 mm was needed for the interface to move 1.2 mm and exhaust the negative-stiffness range of the Clover Dome. This confirmed the theoretical amplification of 4 times the driving displacement. An additional verification was provided by the load-displacement response captured by the Instron (not shown). The peak and valley in load of the Clover Dome profile was traced out in a span of 0.3 mm instead of the usual 1.2 mm. This decrease in displacement translated into a stiffness increase of 4 times the Clover Dome’s usual negative stiffness.

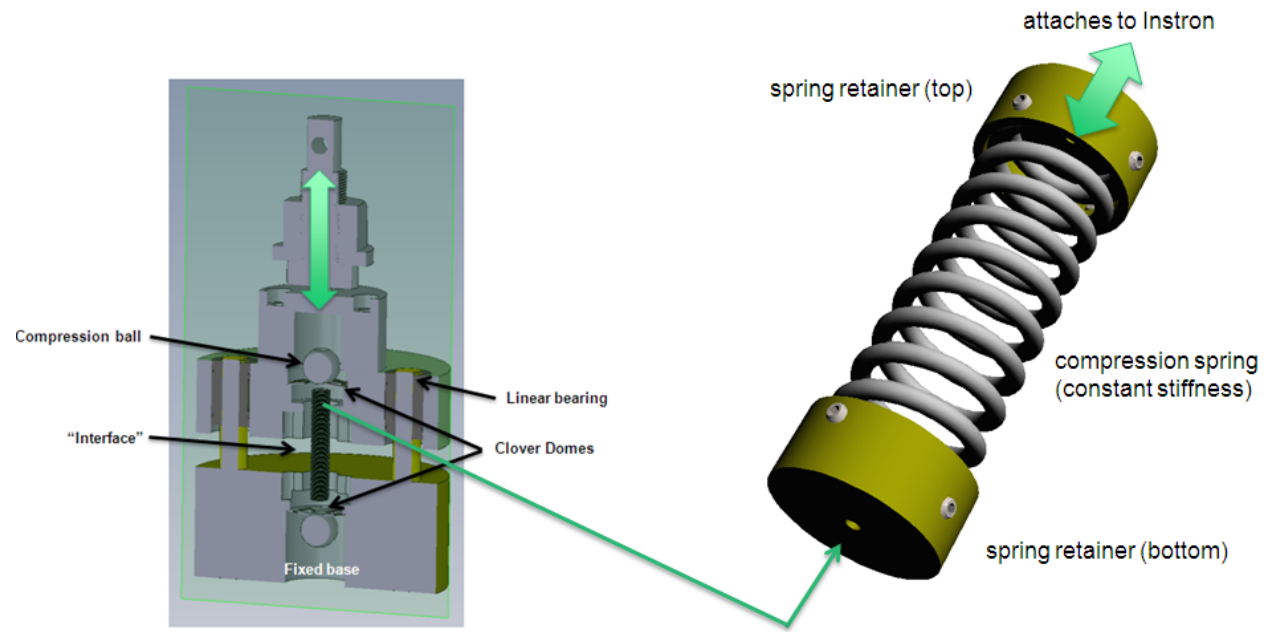


Figure 207. Increased displacement of the “interface” (threaded rod) demonstrated motion amplification.



Figure 208. A compression spring (positive spring) connected in series to a Clover Dome (hidden at bottom).



Figure 209. Demonstration of interface motion of 4x the driving displacement.



Figure 210. An example of a die spring (right) with stiffness of 300 lb/in.

There are very small die springs that come in various stiffness (Figure 210). A die spring with stiffness of 300 lb/in coupled with a Clover Dome with negative stiffness of -285 lb/in can theoretically provide 20x motion amplification. This 300 lb/in die spring would serve as the positive spring in the material assembly.

ASSEMBLY FABRICATION AND COMPONENT RESPONSE CHARACTERIZATION

Concept for a Material System Displaying High Stiffness and High Damping

Figure 211 shows the solid model of the material system that Aerospace fabricated. The two leaf-springs like beams are made out of composites (Figure 212). The adapter plates that are clamped to each side of the beam would hold the Clover Domes, with one being a positive spring and the other a negative spring. The threaded rod running through the beams was the interface. The system would be clamped on both sides by grips attached to the Instron in a vertical manner.

Compression/tension testing was performed to obtain the axial stiffness, lateral stiffness, and the mechanical advantage of the angled geometry in the beams. In addition, the threaded rod can be driven in a sinusoidal fashion with phase lag via an external device, such as a solenoid, to mimic the characteristics of damping materials. This would enable the understanding of damping requirements without the need to insert physical materials. A prototype is shown in Figure 213.

The fabricated composite beams are shown in Figure 212. The dimensions are approximately 13 inches in length, 2 inches in width, and 0.25 inches in thickness for each beam. The half angle between the beam and the horizontal was 5 degrees. The lateral stiffness of the beams, which was the k_3 in our multi-body dynamics model, was measured to be around 5000 lb/in.

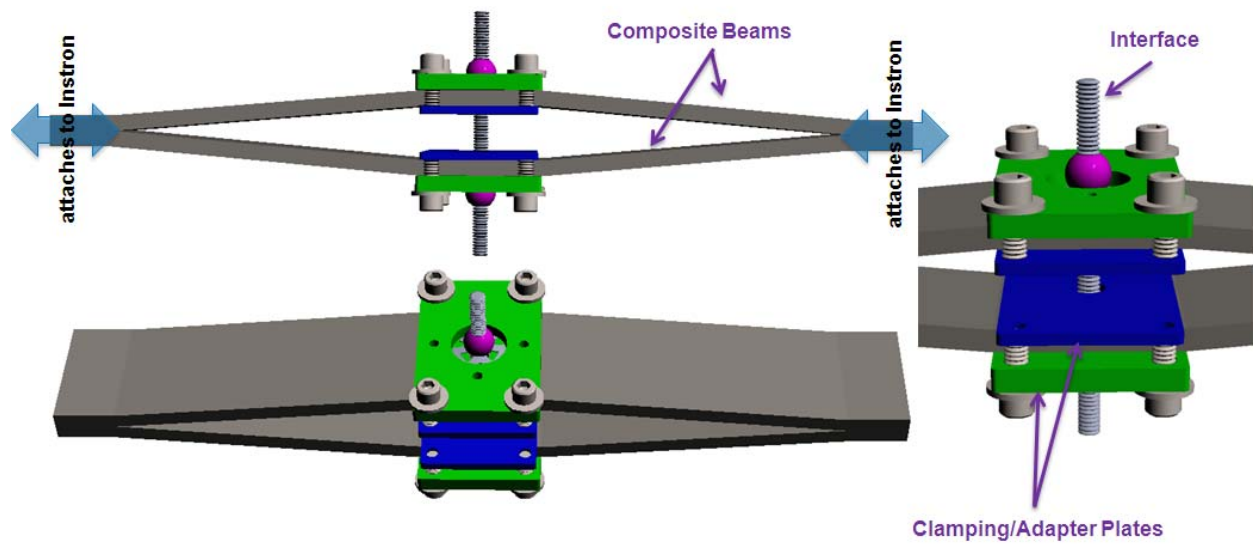


Figure 211. Aerospace prototype for a material system displaying high stiffness and high damping.

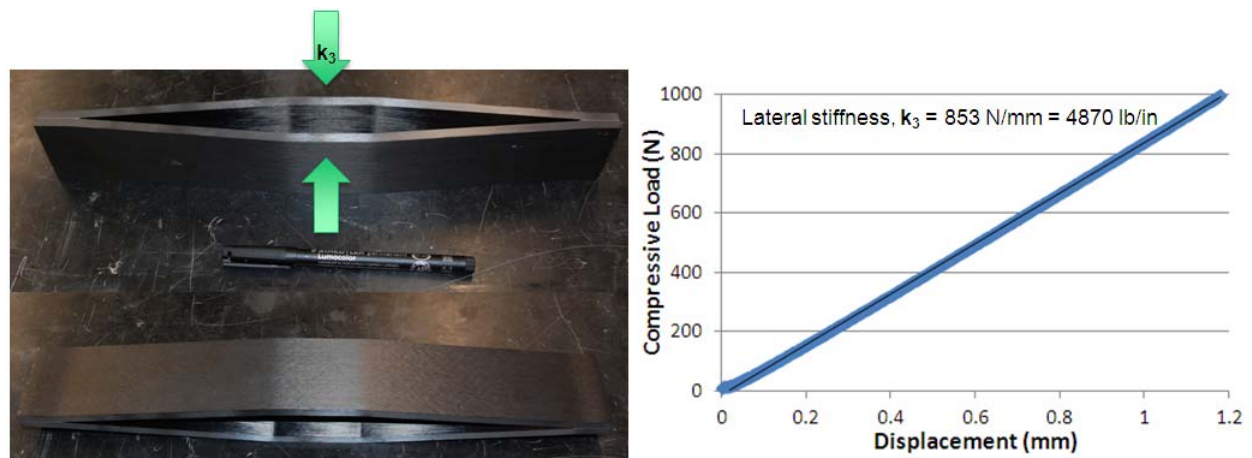


Figure 212. Dual-beam composite prototype system (left) and its lateral stiffness data (right).

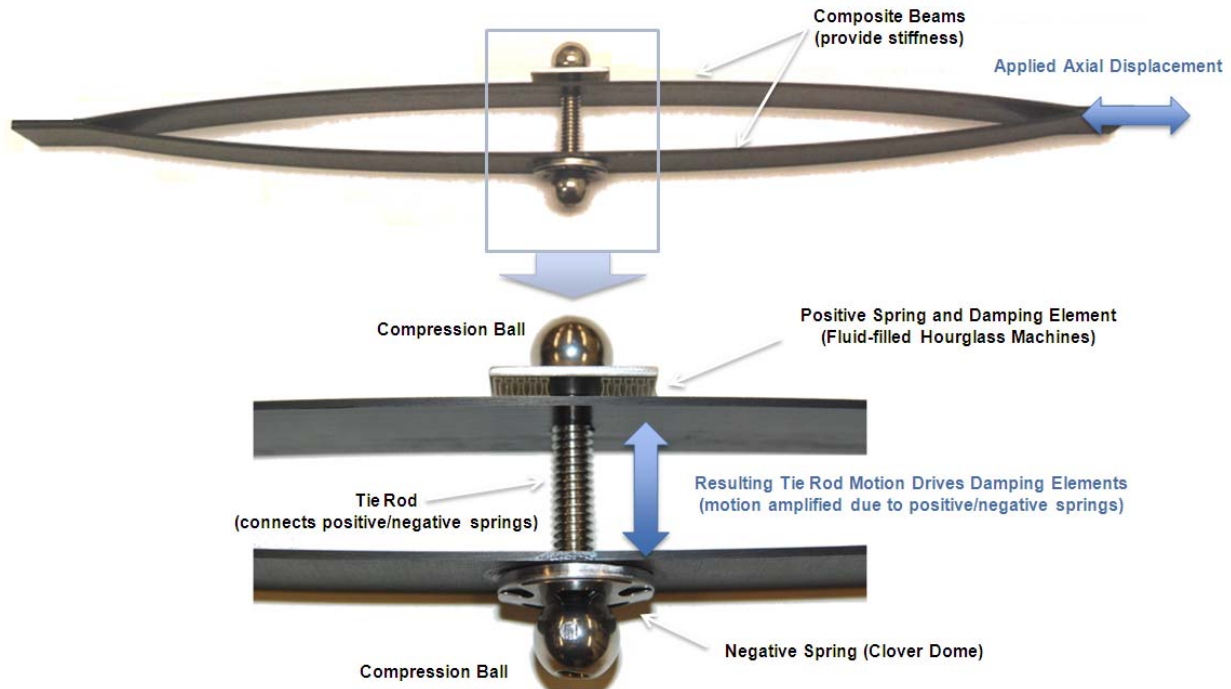


Figure 213. Prototype model of a high stiffness, high damping material.

Constitutive Properties and Mechanical Advantage of 5-Degree Composite Beams

Aerospace measured the mechanical properties of the composite beams of the material system. Figure 214 shows the experimental set-up and the results of the measurement. The beam was tested in compression via Instron to obtain its axial stiffness (lateral stiffness was measured and data shown last month). The axial stiffness was measured to be approximately 280,000 lb/in. The lateral stiffness was measured to be about $5,000 \pm 150$ lb/in.

To obtain the mechanical advantage of the beams, which is defined as the ratio between the lateral displacement and the driving axial displacement, an extensometer and a digital indicator were used. An extensometer was used to measure the axial displacement because it provides higher accuracy than the reading from the Instron crosshead, which did not take into account the compliance in the fixtures and the frame (specifically, the load cell). A preload of approximately 100 lbf was applied to eliminate slack in the system, and the beam was gradually compressed to 500 lbf at a rate of 2 mils (0.002 inches)/min. The lateral response of each beam was measured separately, i.e., the composite was rotated 180-degrees about the vertical axis when the measurement on one side was completed.

The table in Figure 214 summarizes the measured mechanical advantage of the beams. It can be seen that there was asymmetry in the beams because of the differences in the mechanical advantage of each beam. This asymmetry could be attributed to fabrication of the composite beams and the bond strength between the beams. The mean total mechanical advantage of 11.2 was expected based on previous modeling results.

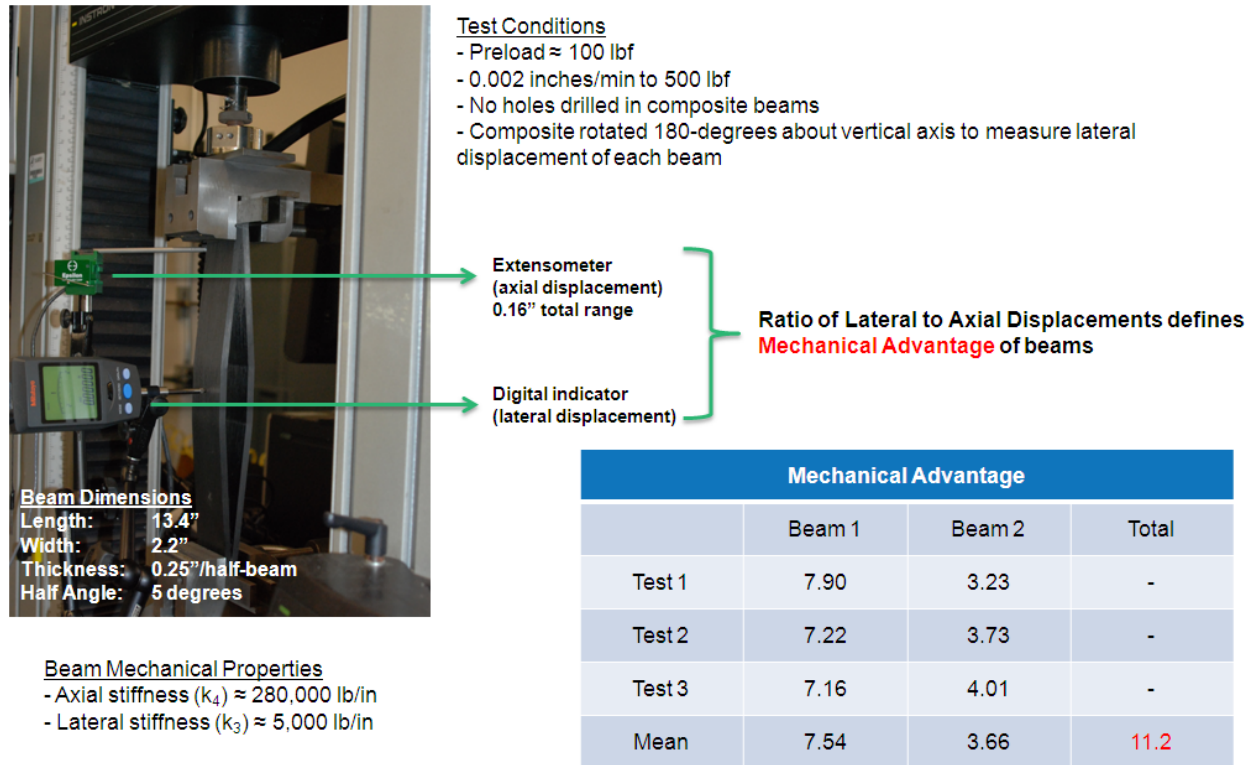


Figure 214. Mechanical properties (stiffness and mechanical advantage) of composite beam.

ASSEMBLY MODELING

Multi-body Dynamics Modeling (Updated Results)

Knowing the actual axial ($k_4 = 280,000$ lb/in) and lateral ($k_3 = 5,000$ lb/in) stiffness of the composite beams, Aerospace repeated the multi-body dynamics analyses that was done earlier by changing the k_3 and k_4 values in the model. The k_1 and k_2 values were also changed to obtain $k_{\text{eff}} = -5000$ lb/in. Please recall that the effective stiffness magnitude from the combination of k_1 and k_2 should be close to, but less than, the k_3 of the composite beam. In order to achieve motion amplifications of 3x (what had been obtained in the laboratory) and 10x (what we hoped was attainable in the laboratory) due to the combination of the positive and negative springs alone, the stiffness values used were $k_1 = 2500$ lb/in and $k_2 = -1667$ lb/in (for 3x amplification), and $k_1 = 556$ lb/in and $k_2 = -500$ lb/in (for 10x).

Figure 215 shows the overall system load-displacement response and the total interface motion amplification (from +/- springs and mechanical advantage of beam's geometry). For 3x amplification (top case), we expect to see an increase in damping because of the increased hysteresis loop in the data. If we can get the motion amplification to 10x (bottom case), then we should expect to see an increase in damping and in stiffness for the material system. The total interface motion amplification for both cases are also plotted and reported, with the 3x case being 27 and the 10x case being 80 when $c_2 = 10$ lb·s/in.

Please note that the k_1 and k_2 values are not the actual stiffness values of the Clover Domes, and were used only in the model to match the interface motion amplification. From what we have learned, the global trend (increase in damping and increase in stiffness) was the same as long as the total interface motion amplification matches, regardless of the stiffness values. The stiffness values

are less important during the proof-of-concept phase, but would come into play when we need to aim for specific stiffness and damping requirements.

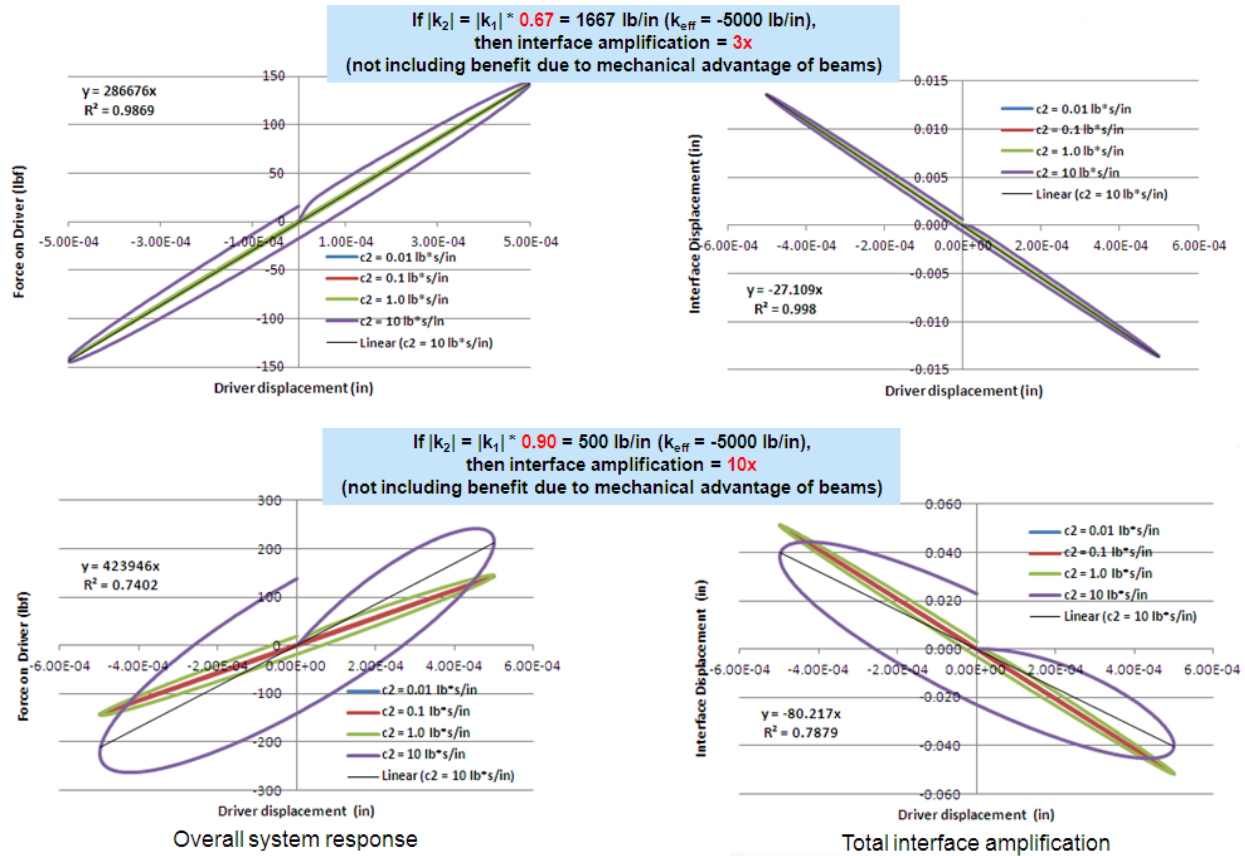


Figure 215. Overall system stiffness and damping assuming 3x (top) and 10x (bottom) interface motion amplification from +/- springs.

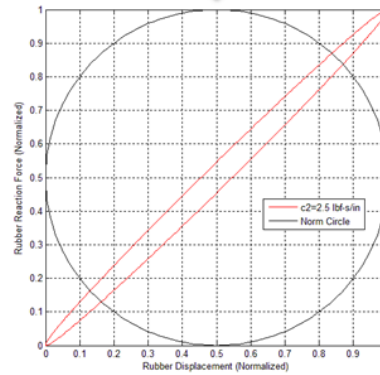
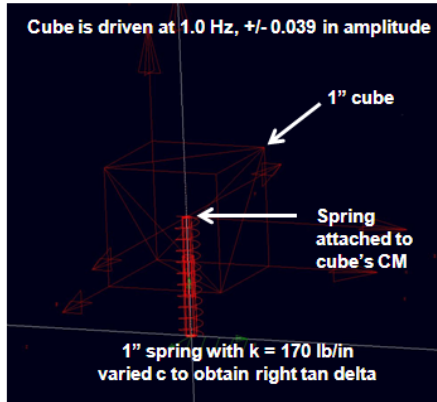
Correlating Damping Coefficient and $\tan \delta$

There had always been a lack of understanding in how the damping coefficient (units of force per velocity), c , values used in Aerospace's multi-body dynamics modeling relate with $\tan \delta$. Work had been done to uncover this mystery by using experimental values of stiffness and $\tan \delta$ of a polyurethane cube as measured by DMA. A separate model was created in our multi-body dynamics package (Figure 216) that consisted of a spring and a dashpot. The spring was given the same dimension (height) and stiffness of the polyurethane rubber sample, while the damping coefficient of the dashpot was given an arbitrary value. The result (load and displacement) of the simulation was exported to Matlab to calculate the corresponding $\tan \delta$. This iterative process was repeated until we obtained a damping coefficient value (2.5 lb*s/in) that provided the correct $\tan \delta$ of 0.07.

Frequency	Tan Delta	Stiffness
0.1 Hz	0.095	154 lb/in
1.0 Hz	0.070	170 lb/in
10.0 Hz	0.074	194 lb/in

DMA measurement of 1" cube polyurethane rubber (Smooth-On PMC 121/30)
dynamic amplitude = 0.04 inches

Multi-body dynamics modeling
1.0 Hz, 170 lb/in case



1.0 Hz, 170 lb/in	
c (lb-s/in)	Tan Delta
2.5	0.072
2.4	0.069
2.2	0.063
1.0	0.029
0.1	0.0029
0.01	0.00029

Figure 216. Relationship between damping coefficient, c , and $\tan \delta$.

Multi-Body Dynamics Analysis (10x Motion Amplification)

With the new understanding of how damping coefficient and $\tan \delta$ relate, we revisited the multi-body dynamics analysis by assuming an interface motion amplification of 10x (Figure 217). The stiffness magnitude of the positive spring and the negative spring must be within 10% of each other (the positive stiffness being the larger of the two) to obtain 10x amplification. The damping coefficient used were 0.01, 2.5, 14 lb-s/in, which corresponded to $\tan \delta$ values of 0, 0.07 (polyurethane rubber), and 0.4 (butyl rubber), respectively. A case where the interface was locked (to simulate infinite damping) was also included. As the damping coefficient increased, the overall stiffness of the material system also increased. On the other hand, overall damping reached a maximum when $c = 14$ lb-s/in (within these 4 cases). This demonstrated that if we were to embed the butyl rubber inside our material system and used the rubber as the positive spring and damper, we could potentially have a material that exhibits relatively high stiffness (close to that of aluminum) and relatively high damping ($\tan \delta \approx 0.3$).

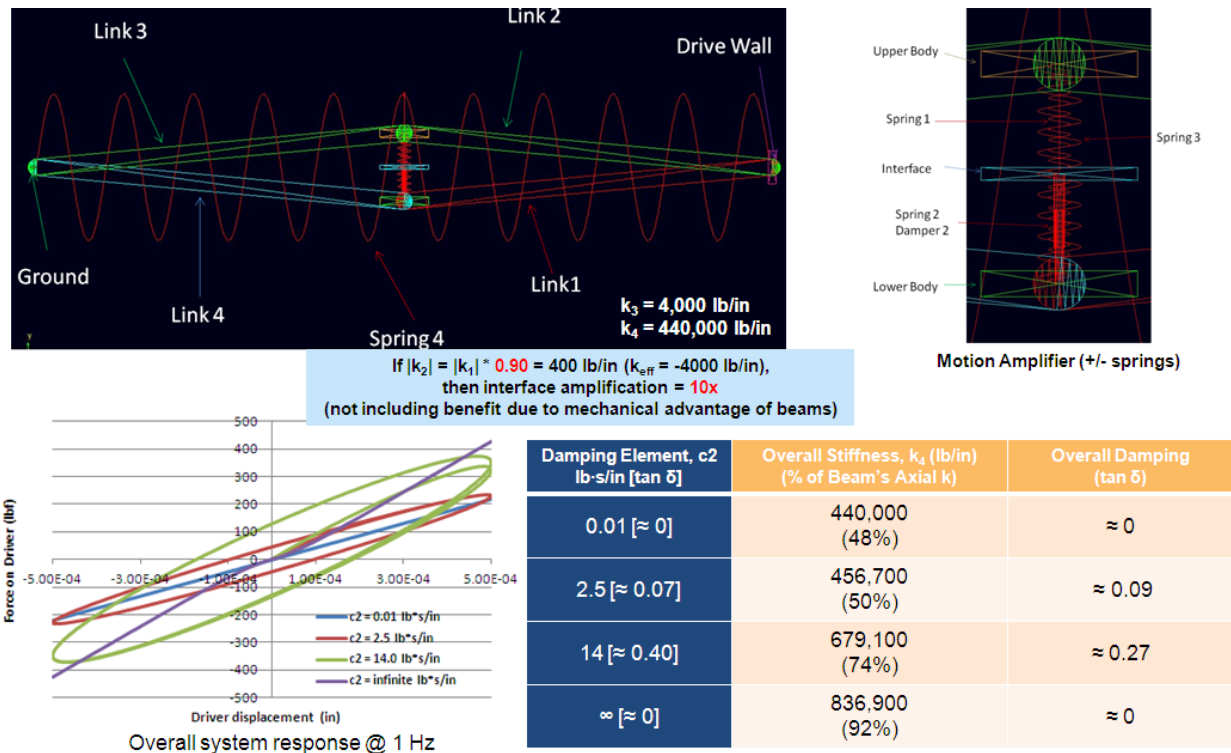


Figure 217. Overall system stiffness and damping assuming 10x interface motion amplification from +/- springs.

Parametric Study via Modeling

A series of modeling runs were conducted to understand performance and limitation of the material system. The variables in this study included the amount of interface motion amplification (3x, 5x, and 10x), half-angle of the beams (2, 5, and 8 degrees), tan delta of the damping element (0.4, 0.6, and 0.8), and the driving frequency (0.1, 1.0, and 10 Hz). This yielded $3^4 = 81$ permutations and the result of each trial is shown in Figure 218.

Many combinations yielded a material with modulus and tan delta that are orders of magnitude better than any engineering material used today. Each of those results was plotted on Ashby's stiffness-loss map as green diamonds and our earlier experimental data (butyl rubber as damping material) point is resembled by a purple star (Figure 219). Even without having performed any design optimization, the results show the potential for our material to be truly revolutionary.

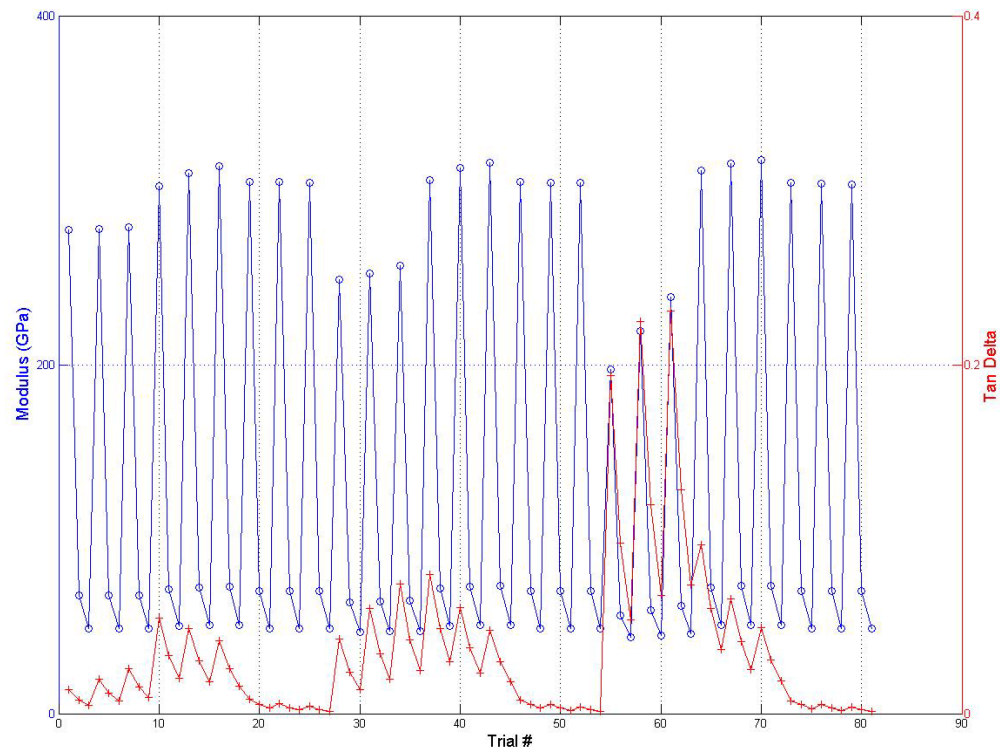


Figure 218. Parametric study through modeling shows potential for even greater combination of stiffness and damping.

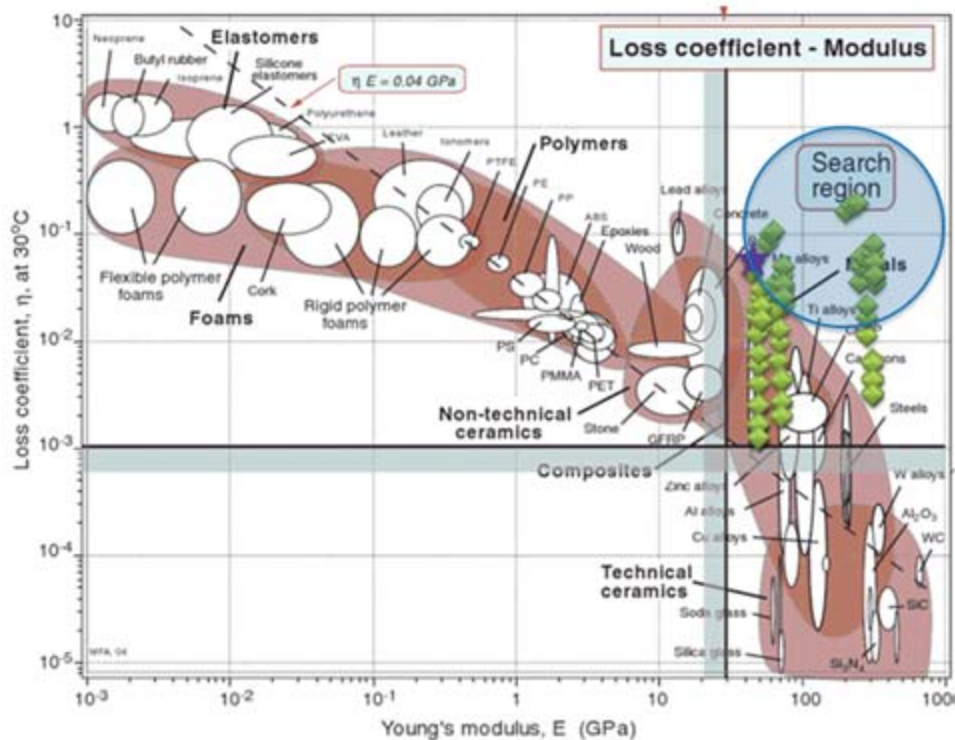


Figure 219. Ashby's stiffness-loss map with modeling results showing our material could exhibit performance not seen in engineering materials used today.

Influence of $k_{eff}/k_{lateral}$ on System Performance

We revisited the multi-body dynamics model to further understand how properties of constituents affect overall system performance. It was always known that the lateral stiffness of the composite beam was needed to provide stability (to prevent buckling) from the clamping effect of the positive and negative springs (k_{eff}), so the requirement was always to have the composite beams' lateral stiffness be greater than k_{eff} . We also knew that if the lateral stiffness of the composite beams was much greater than k_{eff} , then the effect of the springs becomes negligible. On the other hand, if the lateral stiffness was equal to k_{eff} , then the beams would exhibit high compliance (lower stiffness) when driven axially.

Figure 220 shows the system's response for a range of ratio of k_{eff} to the lateral stiffness ($k_{lateral}$) for the 5-degree beams. In this exercise, the k_1 and k_2 values, which are the stiffness of the positive and negative springs, respectively, were adjusted to maintain 10x amplification for each case. As expected, when k_{eff} becomes a smaller percentage of the beams' lateral stiffness, the overall system exhibits a non-linear combination of higher stiffness and lower damping.

The plot on the lower right in Figure 220 shows the desired ratio of k_{eff} to $k_{lateral}$ (shaded in green), which gives a good combination of overall stiffness and damping. The region in red is undesirable due to system instability.

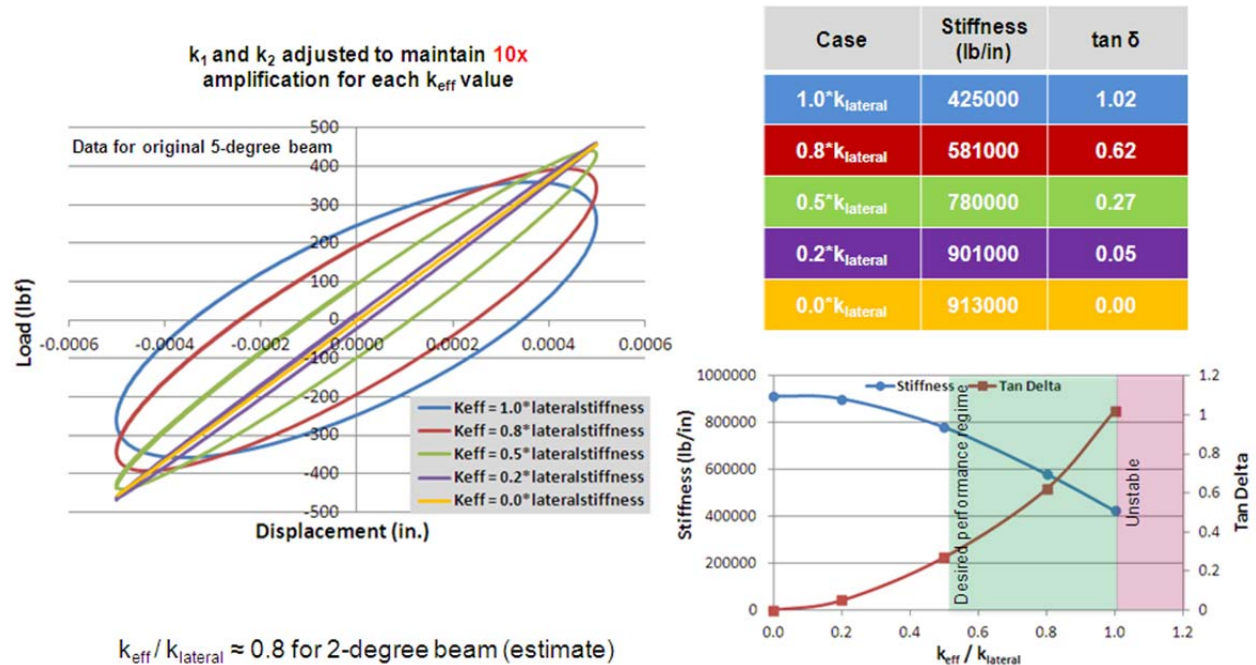


Figure 220. Multi-body dynamics modeling results showing the influence of $k_{eff}/k_{lateral}$ on overall system stiffness and damping.

EXPERIMENTS AND PERFORMANCE CHARACTERIZATION OF INTEGRATED MATERIAL SYSTEM

Integrated Material System (5-Degree Composite Beam)

Aerospace's concept for a high stiffness and high damping material was introduced previously and a demonstration unit is shown in Figure 221. The composite (graphite epoxy) beams provide rigidity to the system while the other components contribute to damping. The interface, which consists of a threaded rod, a steel ball, and an aluminum plate, moves as the beams are compressed and/or decompressed. As the gap between the beams opens and closes, the aluminum plate compresses and decompresses the positive spring while the ball decompresses and compresses the negative spring. To understand the mechanical responses (stiffness and damping) of the overall system, Aerospace conducted a series of tests by introducing components (springs and damping element) to the system one step at a time.

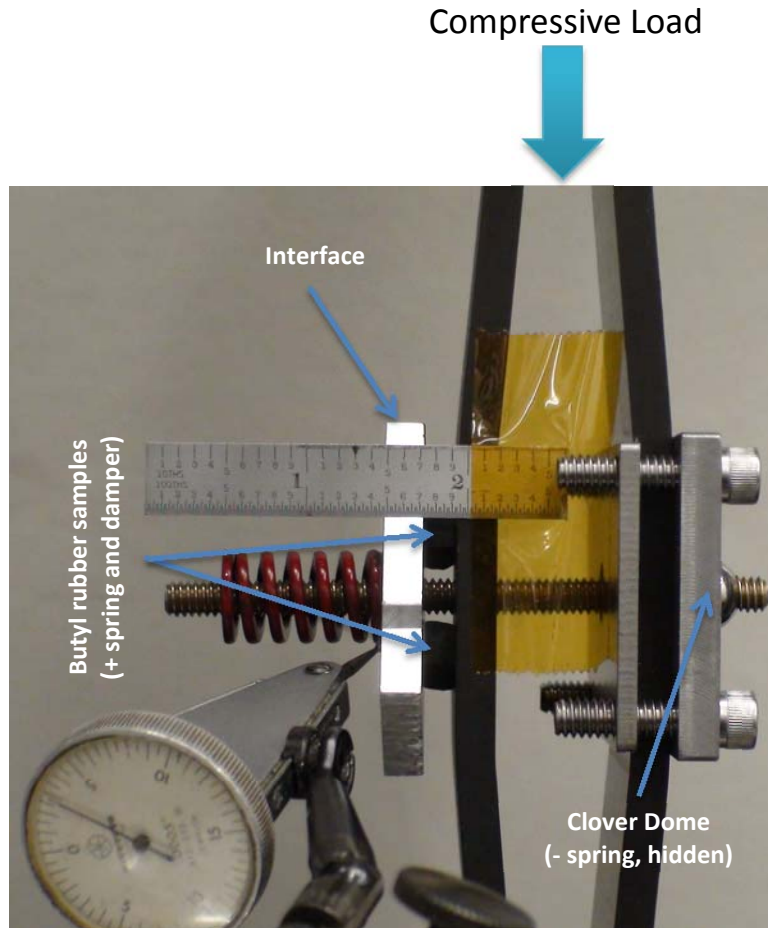


Figure 221. Components that comprise the integrated material system.

Three different configurations were tested. The first configuration consisted of a positive spring (die spring) and a negative spring (Clover Dome). The second and third configurations included a damping element (butyl rubber) in addition to the springs, but in the third case, the interface was locked in position.

During the test, compressive load was applied from the top by the Instron. The material system was always under compression: initial state of the beams was at the fully-compressed position (500 lb applied load) and the half-cycle position was at the fully-decompressed position (200 lb applied load). The frequency of loading ranged from 0.1 to 1.0 Hz, which was the mechanical limit for the screw-driven Instron.

Integrated Material System with Die Spring (5-Degree Composite Beam)

In this configuration (Figure 222), the die spring (shown in red) was the positive spring and was attached to the negative spring (Clover Dome) that was situated on the same face of the opposing beam. Due to motion amplification of the +/- spring assembly and the mechanical advantage of the beams, the interface moved laterally about 75x more than the applied axial displacement (lateral displacement of 30 mils, axial displacement of 0.4 mils). Because no damping element was incorporated in the system, the data showed negligible hysteresis. The stiffness of the system at 0.1 Hz was 710,000 lb/in, which corresponds to a material having an elastic modulus of 65 GPa.

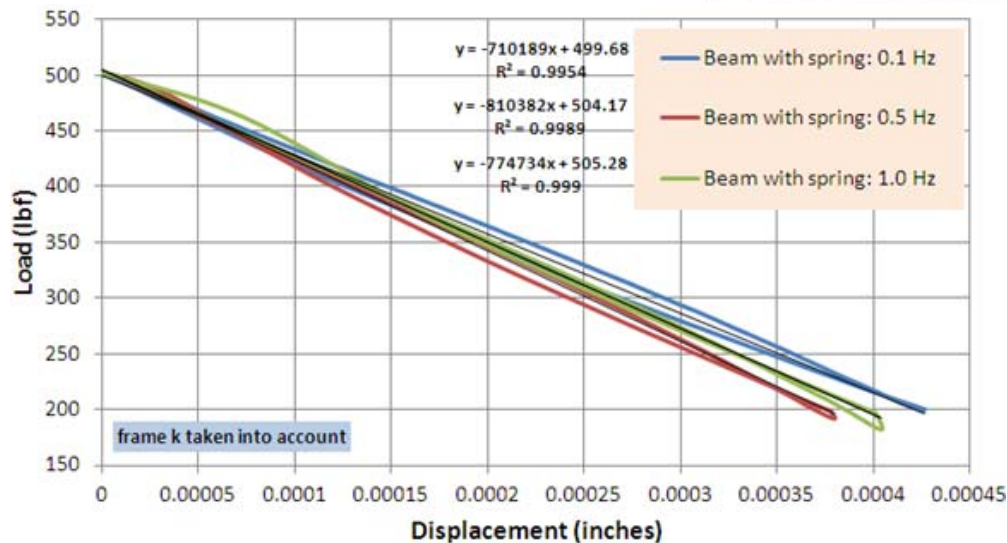
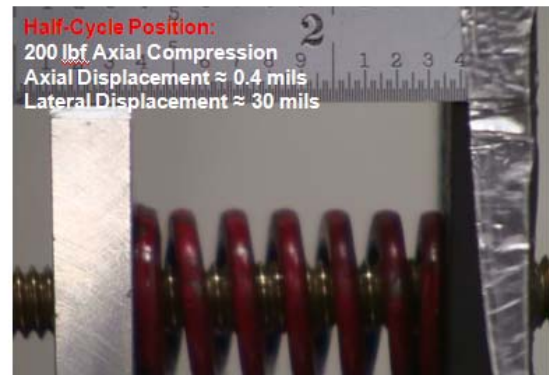
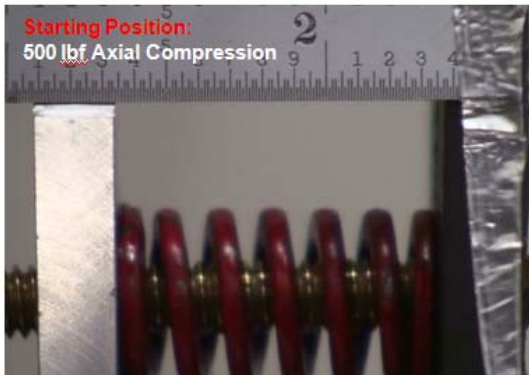


Figure 222. Load-displacement response of material system with die spring as positive spring.

Integrated Material System with Butyl Rubber (5-Degree Composite Beam)

In this configuration (Figure 223), butyl rubber served as the positive spring and the damping element. The butyl rubber pieces were cut to size so that the combined stiffness was close to, but larger than, the negative stiffness of the Clover Dome in order to maintain stability. For the case where interface motion occurs, the lateral displacement was approximately 30x the applied axial displacement. Because butyl rubber is inherently a good damper, the amplified motion of the interface drives up the overall damping response of the material system. This can be seen by the increase in hysteresis of the load-displacement data (data labeled “BR w/ motion”). For this case, the equivalent material had a modulus of 42 GPa and a tan delta of 0.04. The tan delta should actually be higher (potentially greater than 0.08) because Aerospace had observed that the motion of the interface was not fully irreversible, i.e., the interface did not revert to its starting position. This was most likely due to stiffness mismatch of the butyl rubber specimens (specimens were not made identical and the loading was asymmetric). To circumvent this issue, Aerospace repeated the test with a more uniform damping element, e.g., an O-ring made of high damping materials, such as neoprene or silicone.

For the third case, the aluminum plate was adjusted (by rotating along the threaded rod) so that the steel ball on the other side fully compressed the Clover Dome to a point beyond the negative stiffness range. At this saturated location, the Clover Dome no longer behaved like a negative spring, and the interface did not move when the beam was compressed. Because the interface was

essentially locked, the springs acted as clamps on the beams. Logically, this configuration should exhibit the highest stiffness, and the experimental data confirmed this response (data labeled “BR w/o motion”). For this configuration, the equivalent material would have a modulus of 78 GPa (stiffness of 865,000 lb/in) with very little damping.

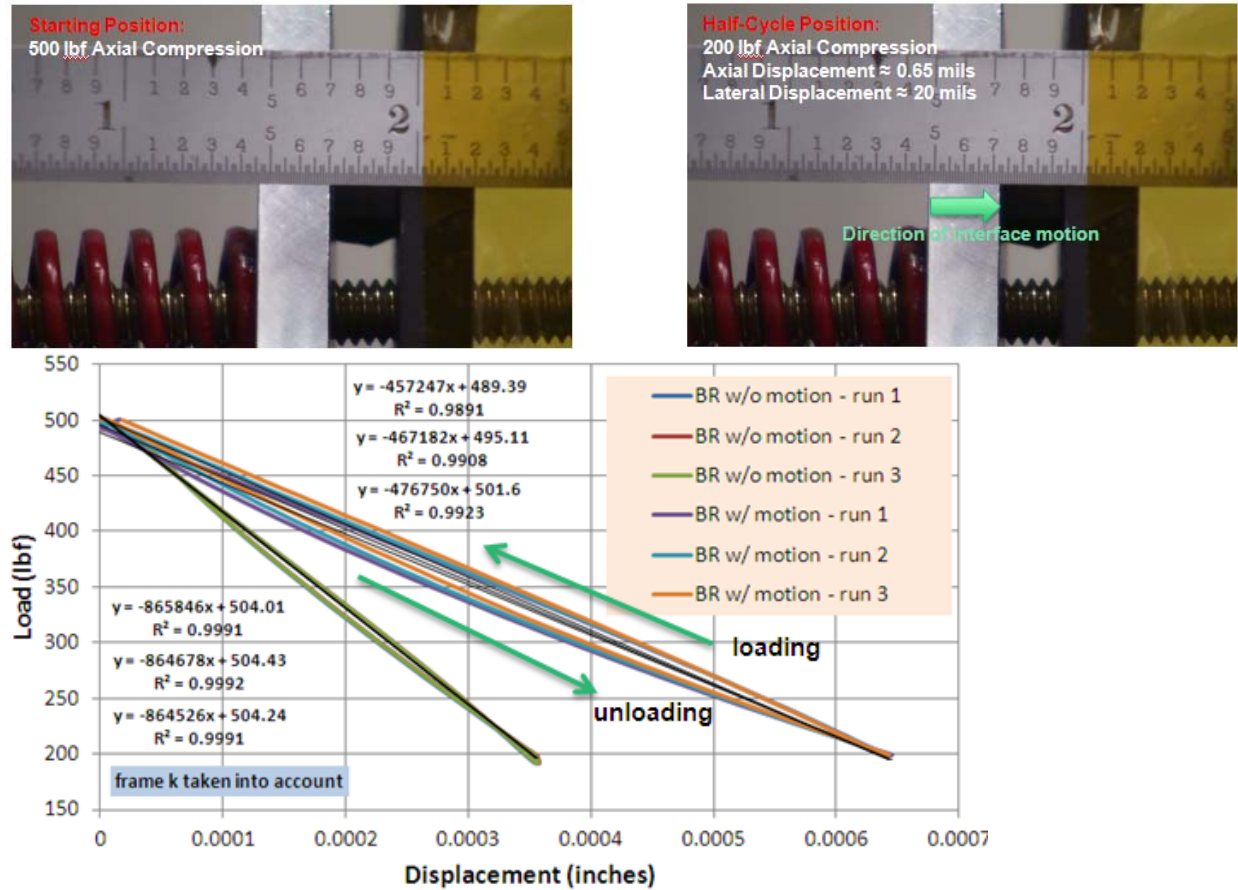


Figure 223. Constitutive response of the high stiffness, high damping material system with butyl rubber as positive spring and damping element (unlocked and locked cases).

Integrated Material System with Silicone O-Rings (5-Degree Composite Beam)

For this set of experiments, the configuration of the material system was similar to the one discussed in the previous month (composite beams with half-angle of 5 degrees, height of 13.4 inches, and a cross-section of 2.17" by 0.47"). Instead of using a die spring or butyl rubber as the positive spring, a stack of four, 1"-diameter silicone o-rings was used. Due to a greater stiffness mismatch between the o-rings and the Clover Dome (negative spring), the working range, in terms of interface motion, was diminished. The working range is defined as the total range in which the interface is able to move and return to its starting position, repeatedly. Instead of traveling the entire negative stiffness range (0.04") available in a Clover Dome, the interface traveled about 0.01". The load-displacement response of the material system is shown in Figure 224. The material exhibited an average stiffness of 1,345,000 lb/in, which corresponded to a modulus of 122 GPa. Unfortunately, because the full motion of the interface was not realized, the tan delta was only 0.025. For the case where there was no motion of the interface (locked), the equivalent material had a modulus of 164 GPa and a tan delta of 0.01.

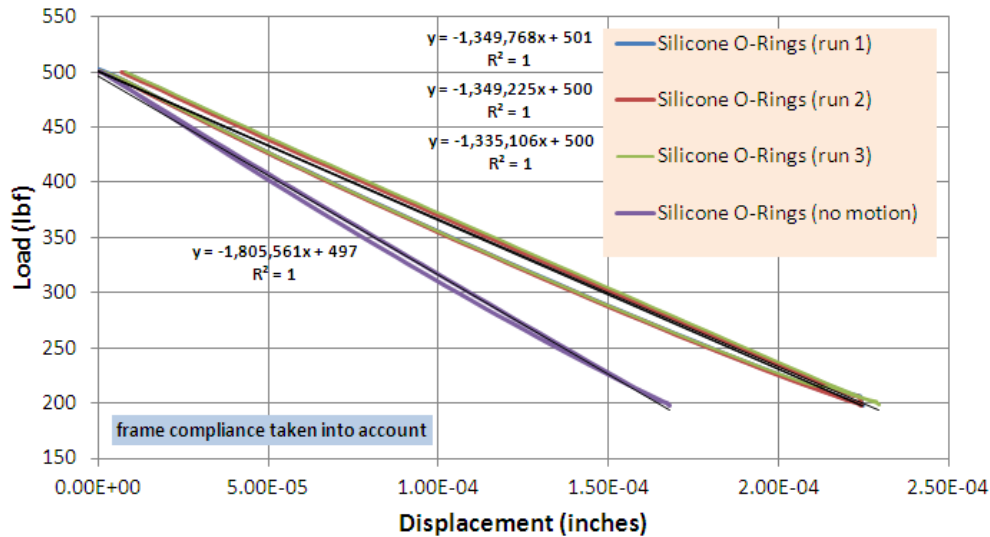


Figure 224. Constitutive response of the high stiffness, high damping material system using a stack of silicone o-rings as the positive spring and damping material.

Integrated Material System with Silicone Rubber (5-Degree Composite Beam)

To better match the stiffness between the positive and negative springs using the same material, silicone rubber with hardness of Shore 10A was used as the positive spring and as the damping material. Four 1" squares were cut from a ¼"-thick silicone rubber sheet. Each square was further cut in half to make two stacks measuring 1" (in length) by 0.5" (in width) by 1" (in height). The combined stiffness of the two stacks of silicone rubber had stiffness of approximately 70 lb/in. Each stack was placed on either side of a die spring whose stiffness was 260 lb/in. The total stiffness of the positive spring (die spring + silicone rubber) was approximately 330 lb/in. Because we know the magnitude of the negative stiffness of the Clover Dome (≈ 285 lb/in), we can calculate the expected motion amplification of the interface: 330 lb/in divided by (330 lb/in – 285 lb/in) or 7. The total motion amplification of the system when the mechanical advantage of the beams was included would be approximately 77.

According to images taken during the test (Figure 225), the interface displaced about 0.025". From the load-displacement data shown in Figure 225, the axial displacement was 0.0003". Taking the ratio of the interface displacement and the crosshead displacement, we got 83, which was close to the predicted value. The mean stiffness of the material system was 889,000 lb/in, and corresponded to a material with an elastic modulus of 81 GPa. The tan delta for this system was 0.07 (comparable to cork)! For comparison, aluminum has a modulus of 70 GPa with tan delta of only 0.0004. When the interface motion was disabled, the modulus (163 GPa), as expected, was comparable to the case with silicone o-rings (164 GPa).

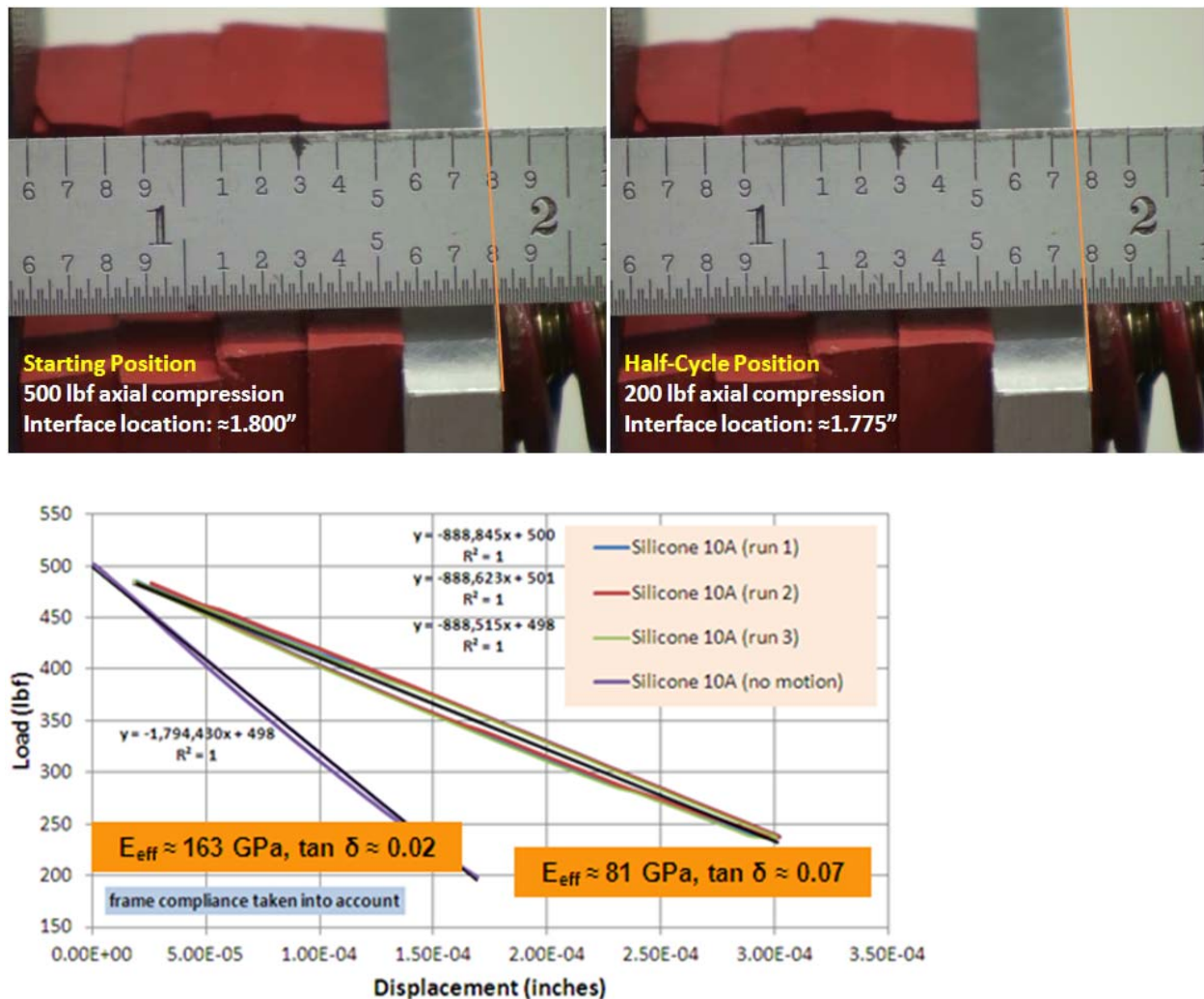


Figure 225. Constitutive response of the high stiffness, high damping material system using two stacks of silicone rubber (Shore 10A hardness) as the positive spring and damping material.

Integrated Material System with Die Spring (2-Degree Composite Beam)

Originally, the idea of fabricating the 2-degree beam (Figure 226) was to take advantage of the topology to increase mechanical advantage (ratio of lateral displacement to axial displacement). This fact was corroborated by simple trigonometry and multi-dynamics modeling (rigid links and hinged). To fully capture the response, a FEA model of the beam was used for the initial design. The material properties of the composite in the model were assigned so that the modeling results matched experimental data of the 5-degree beam. For the 2-degree beam, the dimensions and geometries of the model were adjusted accordingly to reflect the actual dimensions of the finished part. The results showed that the 2-degree beam should display higher mechanical advantage ($MA = 13$) than the 5-degree beam ($MA = 11$). Note: If the 2-degree beam were comprised of rigid links and hinges, the mechanical advantage would be 28. Unfortunately, due to composite compaction and subtle differences in the individual layer orientation, the fabricated beam turned out 0.014 inches thinner per side (accounted for by the model) and its mechanical properties departed greatly from model prediction. A minor difference in thickness has a significant impact on the stiffness ($k \propto t^3$).

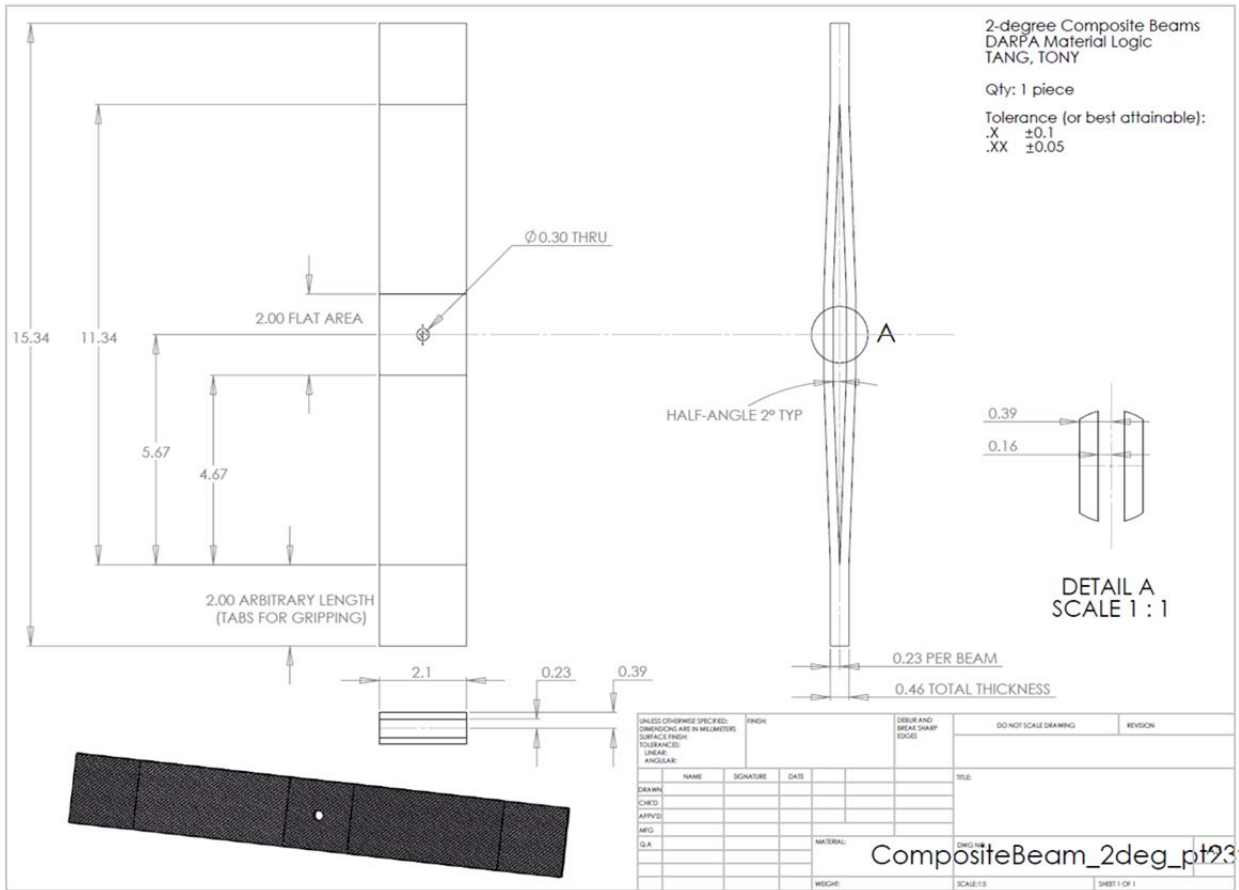


Figure 226. Mechanical drawing showing dimensions of the new composite beam with half-angle of 2 degrees.

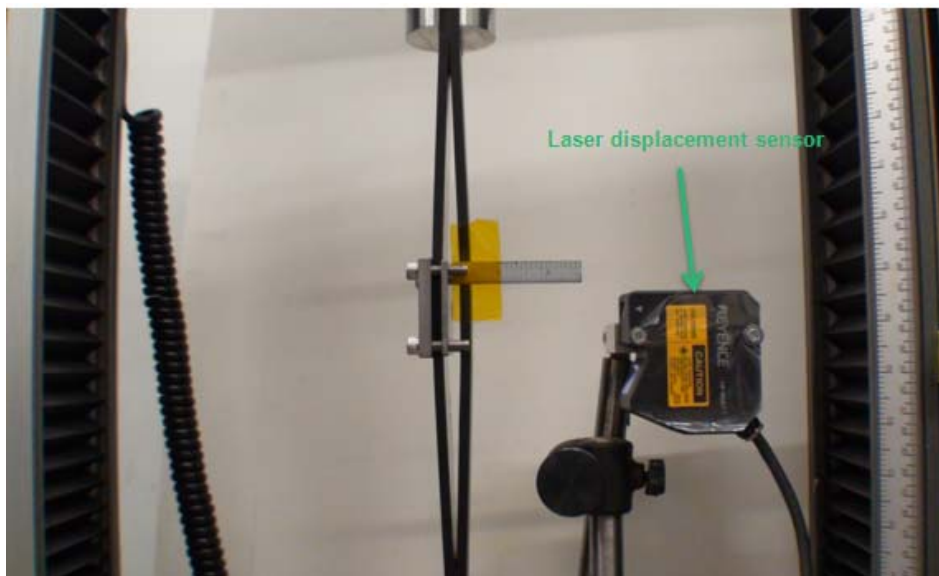


Figure 227. The 2-degree composite beam set up in a screw-driven Instron.

Figure 227 shows the set up used to accurately measure the mechanical response of the 2-degree beam. The response was taken by subjecting the beam to a tensile load of 300 lbf to match the change in load of the 5-degree beam. Lateral displacement was measured via a high-accuracy laser displacement sensor. The axial displacement was measured by the crosshead of the Instron, but with the load cell compliance (displacement) subtracted out to obtain only the true axial displacement of the beam. Figure 228 shows the mechanical behavior of the 2-degree beam with measured mechanical advantage of only 2.4 and a stiffness of 39,000 N/mm (about half of the 5-degree beam).

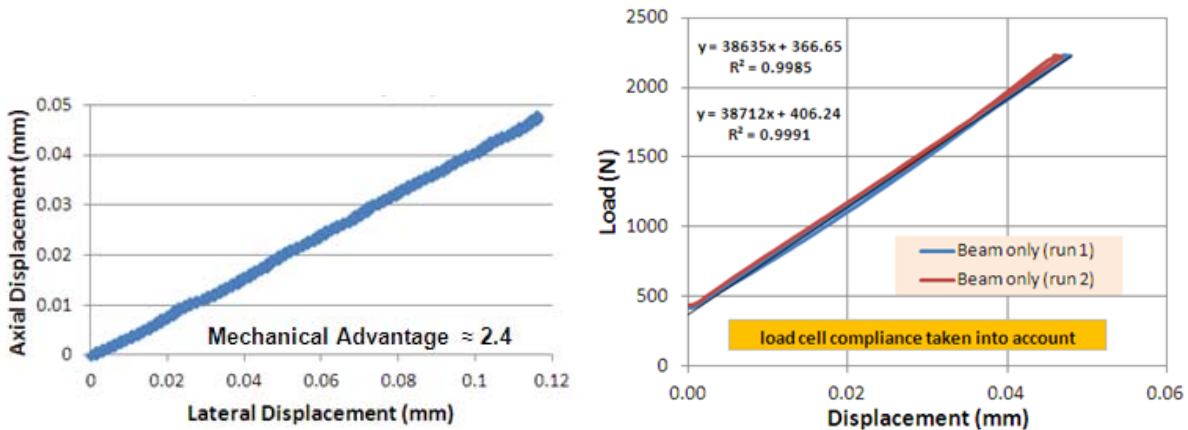


Figure 228. Mechanical response of 2-degree composite beam: mechanical advantage (left), constitutive response (right).

The same components used previously for the 5-degree beam were incorporated into the 2-degree assembly to get a feel for the total interface amplification. The first test combined the Clover Dome with a 300 lb/in die spring. The data obtained from the laser displacement sensor of the lateral displacement can be plotted against the axial displacement to quantify the non-linearity in the system during one cycle of motion (Figure 229). The result showed that the amplification varied as the tensile load was increased: started at 5x amplification, increased to 165x, and settled at 2x (at peak load). The latter 2x amplification portion was basically the response of the beam itself, i.e., the range of the Clover Dome had been exhausted. The total effective amplification was 22x, which was only the portion where the beam's mechanical advantage *and* the motion amplification of the positive/negative springs are active.

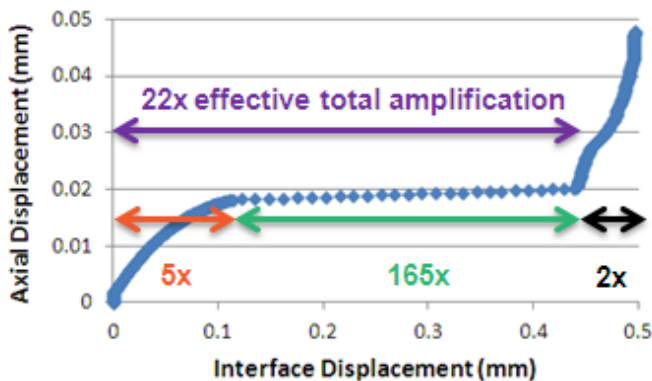


Figure 229. Total interface motion amplification of 2-degree beam with a Clover Dome and a 300 lb/in die spring.

Integrated Material System with Silicone Rubber (2-Degree Composite Beam)

The best performing system to-date for the 5-degree beam combined the stiffness of a 260 lb/in spring and the stiffness and damping of silicone rubber. The resulting equivalent modulus was 81 GPa and a tan delta of 0.07. The same combination of positive spring and damping element was incorporated inside the 2-degree beam for performance comparison.

The measured response is shown in Figure 230. The equivalent modulus of the system was 27 GPa, which was significantly lower than the 5-degree beam, and the tan delta was 0.03. Moving forward, the 5-degree beam, which displayed far better performance than the 2-degree beam, would be used.

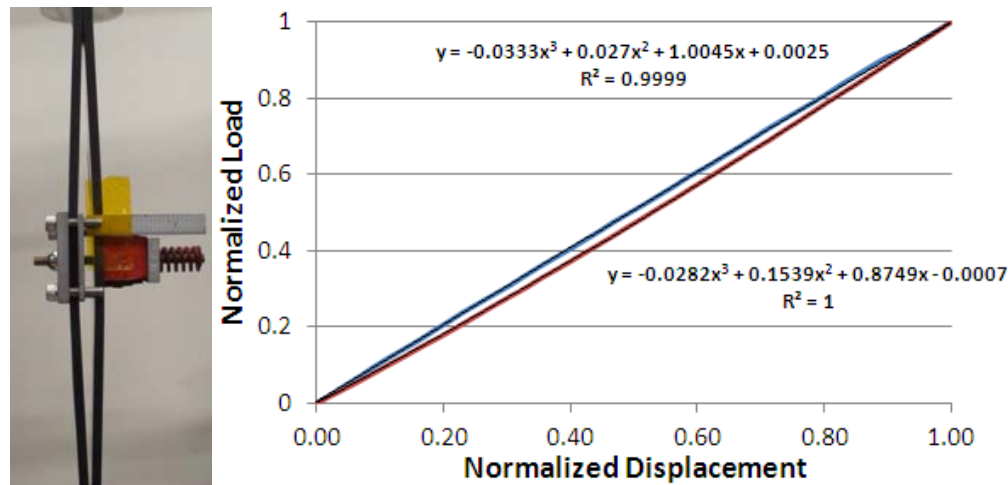


Figure 230. Mechanical response of 2-degree beam with 260 lb/in spring and silicone rubber.

Impact Testing of High Stiffness, High Damping Material

The high stiffness, high damping material assembly was subjected to impact loading with the goal of learning the material's response to a 0.01 s impulse per program requirements. Testing was conducted using an Instron drop tower. An instrumented tup was raised to a height that would result in a desired peak impact load and released to impact the material.

Three configurations of the composite beam was tested: 1) 5-degree composite beam only, 2) 5-degree composite beam with 260 lb/in spring and silicone rubber, and 3) 5-degree composite beam with 260 lb/in spring and silicone rubber, but interface locked.

The results of the test are shown in Figure 231. Unfortunately, there was no discernible difference between the standard 5-degree composite beam ("Beam only") and the material assembly that exhibited properties of high stiffness and high damping ("Interface unconstrained"). The characteristic time of the impact event was much shorter than the response time of the interface, hence by the interface responded, the instrumented tup had already rebounded from the material assembly's surface. There was slight narrowing of the impulse for the case where the interface was locked, which was an expected outcome due to the increased stiffness of the assembly from the clamping of the beam by the springs.

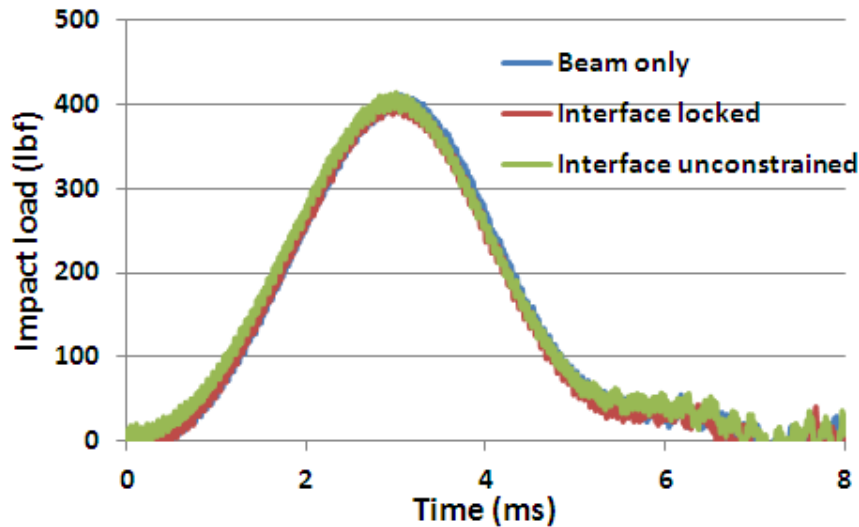


Figure 231. Response of material assembly subjected to peak impact load of 400 lbf (approximately 0.01 s impulse).

Fatigue Testing of High Stiffness, High Damping Material

The high stiffness, high damping material assembly (5-degree composite beam with 260 lb/in spring and silicone rubber) was subjected to long duration fatigue testing. This test was needed to ensure the performance would not decline or components fail prematurely.

The test was conducted using a servo-hydraulic Instron. The material assembly was subjected to 200-lbf tensile loading at frequencies of 1 Hz and 10 Hz. The material was well-behaved throughout the test and none of the components failed. No premature failure was expected for this material assembly, and testing was stopped after 88,000 applied cycles.

Best Performance To-Date of a High Stiffness, High Damping Material

The best performing material system to-date in terms of stiffness and damping is to utilize the 5-degree composite beam and to incorporate a die spring with stiffness of 260 lb/in as the positive spring and a stack of silicone rubber (Shore 10 A hardness) as the damping element. The rubber itself provided additional stiffness, which was needed to overcome the negative stiffness of the Clover Dome (-285 lb/in). With the interface clearly in motion as the composite beam was undergoing decompression and compression, the material system had an effective modulus of 81 GPa and a $\tan \delta$ of 0.07. According to Figure 232, this performance places the material at a location on the Ashby map well off the curve that contains most engineering materials available today.

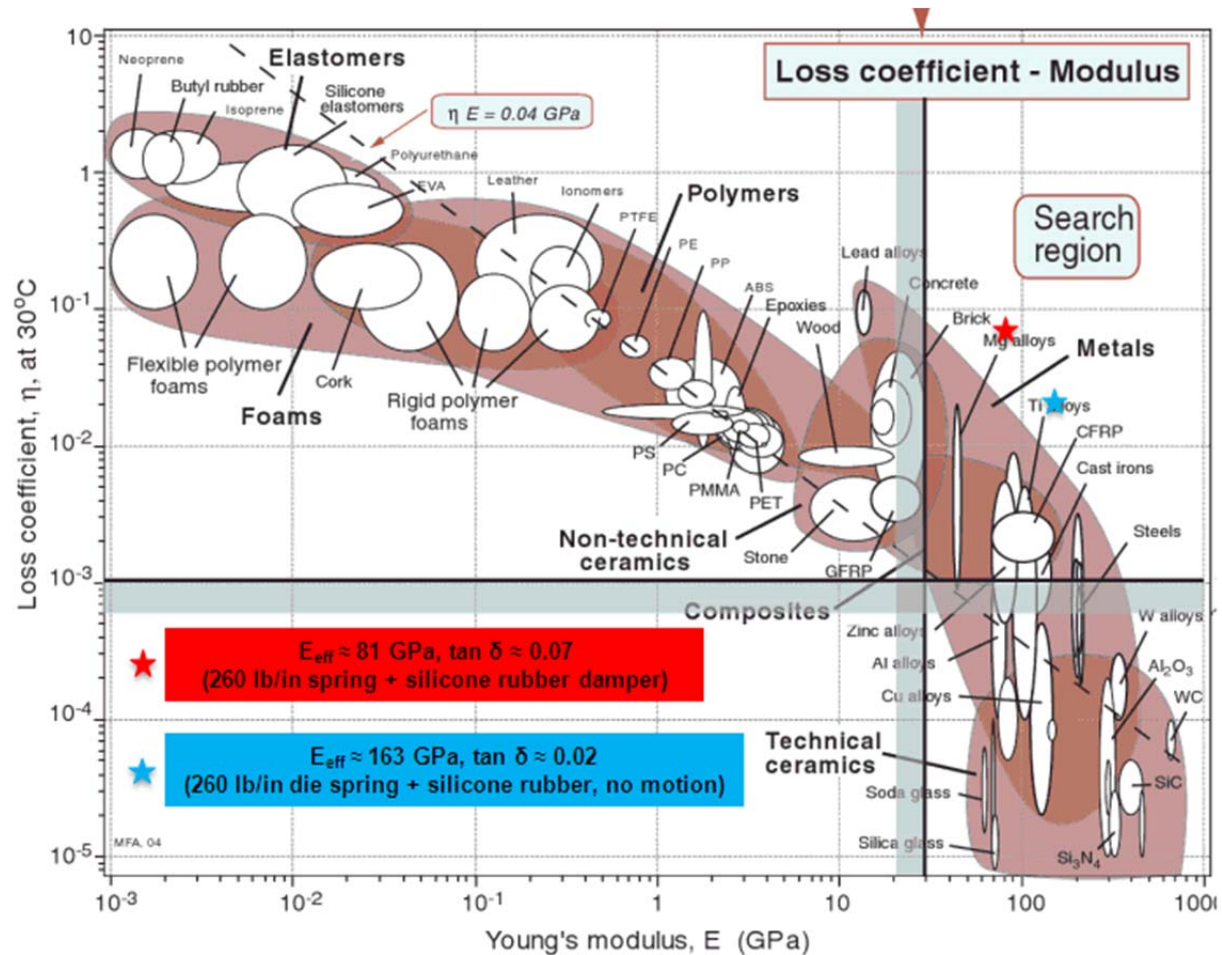


Figure 232. Ashby's stiffness-loss map showing measured performance of Aerospace's high stiffness, high damping material versus common engineering materials.

APPLICATIONS

Conventional Structures

The high stiffness, high damping material can be formed into various conventional structures, such as a structural plate (Figure 233) and tubes (Figure 234). Depending on how the material system is oriented, the tube can resist bending by having increased axial stiffness (if oriented longitudinally) or increased hoop stiffness (if oriented circumferentially).

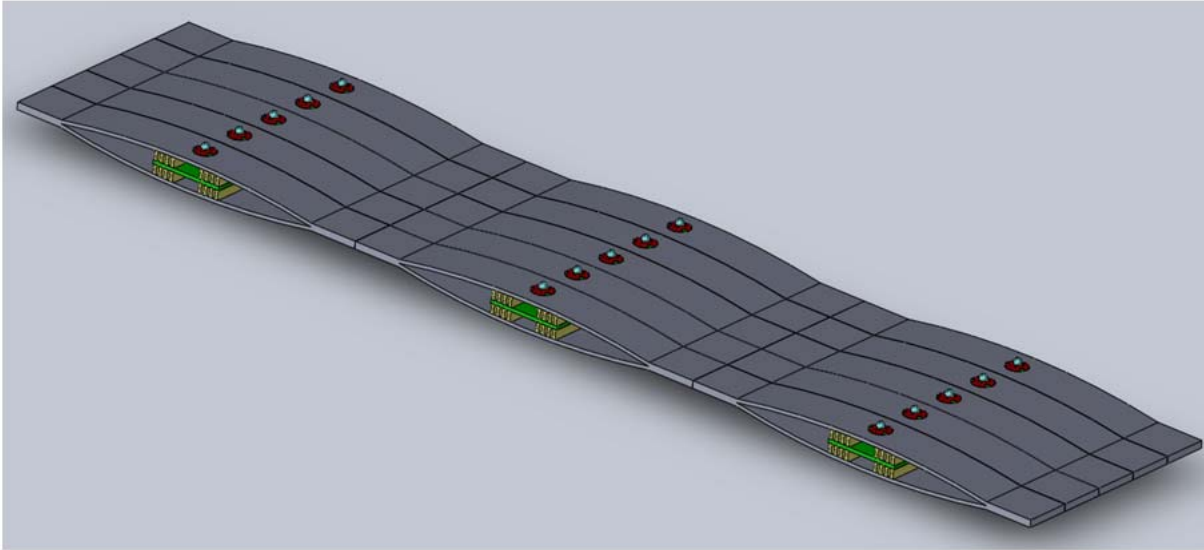
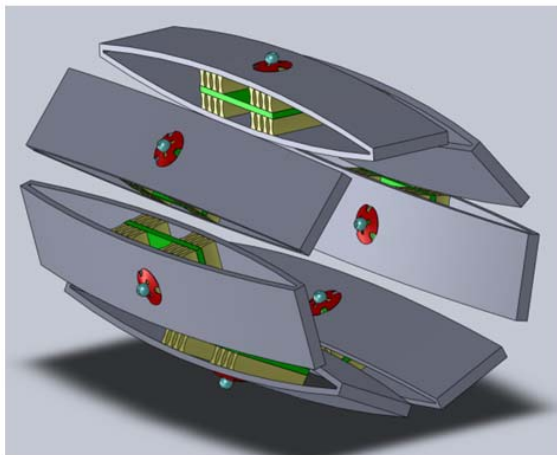
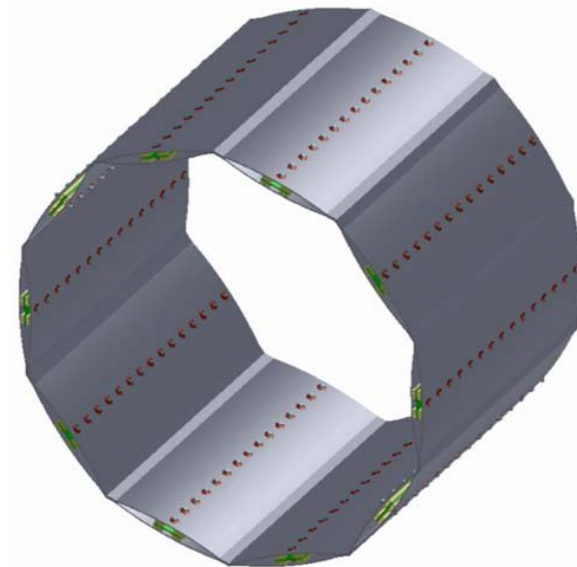


Figure 233. Model of a structural plate that can be formed from the high stiffness, high damping material.



Increase axial stiffness
Resists bending



Increase hoop stiffness
Resists bending

Figure 234. Models of structural tubes that can be formed from the high stiffness, high damping material.

Structural Skin or Shell (Applied Bending)

The material can be designed in such a way that it displays the high stiffness and high damping properties when subjected to bending. Figure 235 shows an application where the stiffeners and dampers are secondarily bonded to an existing exterior, e.g., airplane wing, boat hull, launch vehicle. When the material is under applied bending, the existing exterior would be under compression and the hourglass-shaped dampers (and spring) would provide some baseline

damping as the spacing between the exterior and interior faces diminish. If the applied bending is large enough such that the internal face is under tension, the spacing between the exterior and interior faces is further reduced, which would cause the interface (green plate) that is attaching the Clover Dome and the hourglass-shaped damper (and spring) to displace an amplified amount to provide augmented damping. The bending stress at which the interface becomes active can be tailored (and made adaptive) to the specific application.

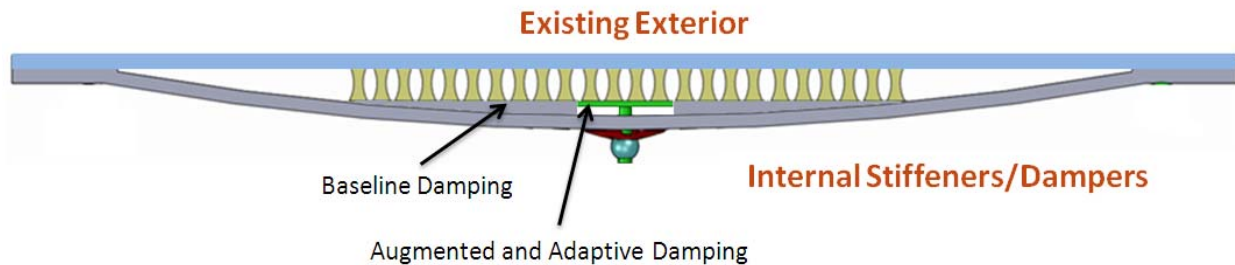


Figure 235. Material can be made as a skin/shell to function under applied bending.

Material System as Stiffening Ribs

Isogrid panels are plates with triangular-shaped stiffening ribs that are commonly used in spacecraft and launch vehicles as payload or booster shrouds (Figure 236). These panels have high strength, high stiffness, and are light weight (high strength-to-weight ratio). It is potentially possible to further increase the strength and stiffness of the isogrid panels by replacing some or all of the existing stiffening ribs with Aerospace's high stiffness and high damping material.

In the sample configuration (Figure 237), the high stiffness and high damping material would be a standalone element (has positive spring, damper, and negative spring embedded within the leaf-spring-like beams), and each element would be joined at the studs. Each element could be tuned to the desired stiffness, which would allow different parts of the panel to exhibit different properties.

Alternatively, the isogrid panel could be designed in such a way that the high stiffness and high damping material is secondarily attached to the exterior skin, as previously introduced in Figure 235. In this configuration, the damping elements would also serve as the positive springs are bonded or attached directly onto the skin. Performance wise, the two configurations of the stiffening ribs should be comparable, but the manufacturing cost and the ease of installation could differ drastically.

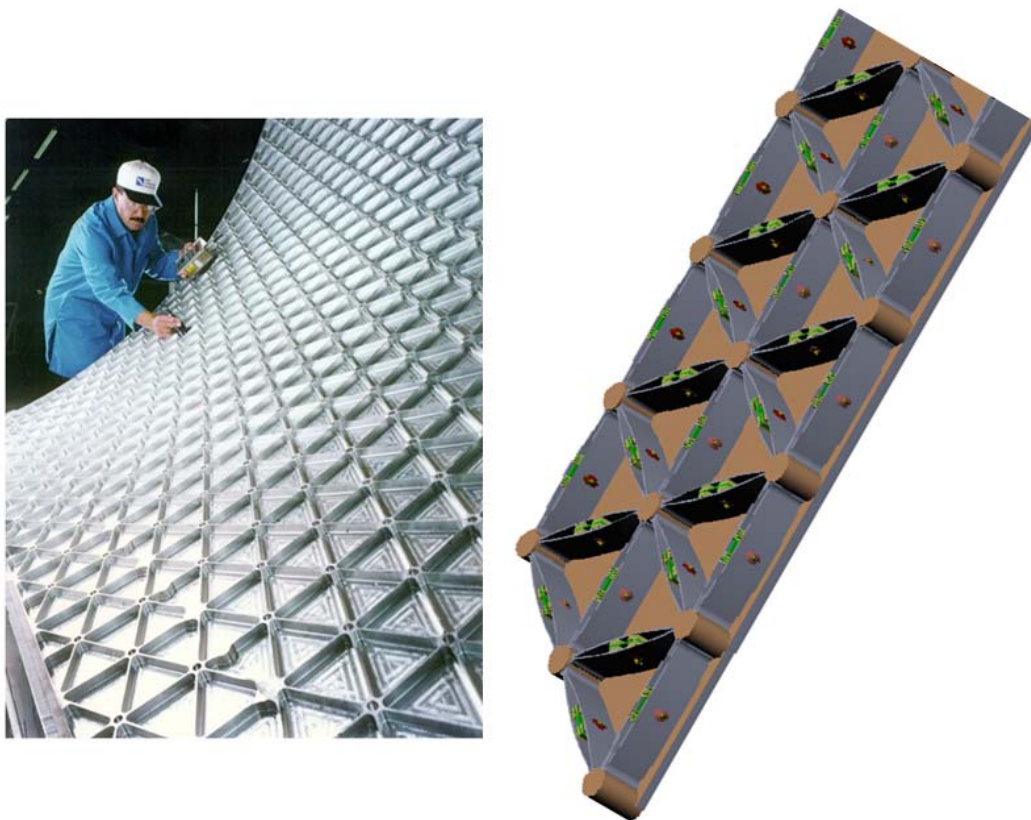
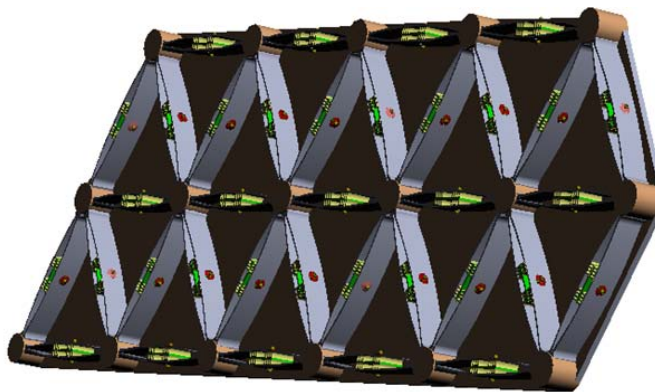


Figure 236. Isogrid panels commonly used in spacecraft and launch vehicles (left) and a concept to replace the stiffening ribs with high stiffness and high damping material (right).

Sample configuration



Alternate configuration

Rotate 90 degrees and utilize damping elements as positive springs

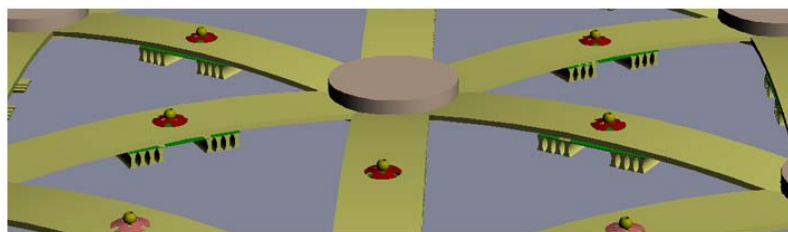


Figure 237. High stiffness and high damping material can be used as stiffening ribs in different configurations/orientations depending on application requirements and manufacturing feasibility.

Material System as Struts

One attractive feature of a material that exhibits high stiffness and high damping is its ability to provide stiffness (e.g., provides precise movement control), yet shield or mitigate vibration. Currently, struts used in launch vehicle payload attach fittings, as shown in Figure 238, are bulky and do not provide the payload much, if any, isolation from the external vibrations induced by the launch vehicle. If the struts were to be replaced by the high stiffness, high damping material, the payload would be well shielded from the vibrations and the attach fitting itself could be made less massive. Furthermore, if the material is connected in series, each individual element could be tuned so that the gross response is broadband and adaptive vibration isolation, i.e., each subsequent element would only be activated by increasing motion or load amplitudes.

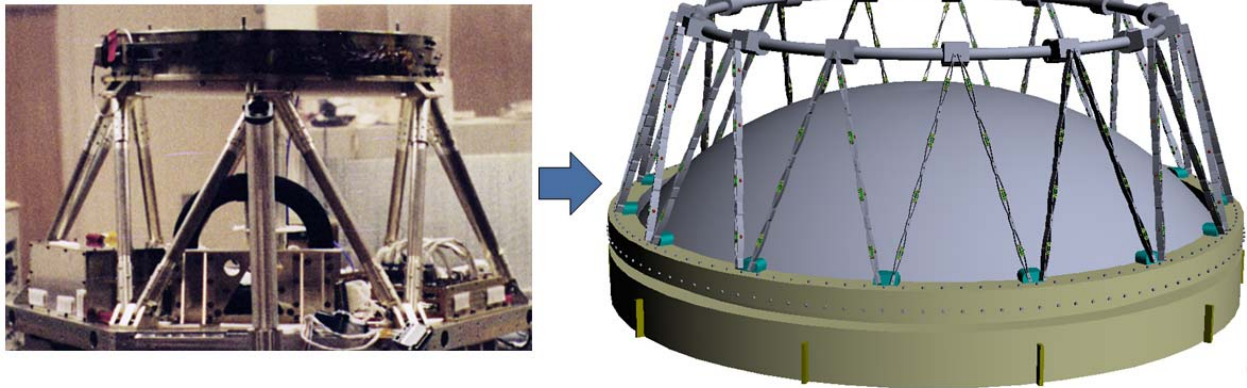


Figure 238. High stiffness, high damping material could be used as struts in payload attach fittings on launch vehicles.

Material System as Building Structural Systems

Buildings in earthquake-prone areas generally employ several methods to offer seismic protection and structural stability. One method is to install buckling resistant brace-frame systems (Figure 239) to provide support when the building undergoes shear. The high stiffness, high damping material could be added in series or parallel to the steel braces to dampen low-amplitude vibrations before the steel braces act on large amplitude motions.

The other technique commonly used for seismic protection is by adding concrete shear walls (Figure 240). Concrete is prone to cracking when shear or displacements reach a critical level. By reinforcing then concrete wall with the high stiffness and high damping material system, the material system would help to dissipate a significant fraction of the energy before the displacements reach a critical level that could damage the concrete walls. This method works because the high stiffness and high damping material would be stiffer than concrete, thus the material system would be able to attract and damp out the loads. This application has the potential to extend the life and reduce maintenance cost and inspection schedule of buildings.



Figure 239. High stiffness and high damping material could augment buckling resistant brace-frame systems in buildings for seismic protection.



Figure 240. Material system could supplement concrete shear walls.

CONCLUSIONS

Negative spring constant materials can produce a composite material with high damping at high stiffness if the negative spring can be stabilized to prevent snap-through. This work presents a method that keeps the negative spring from displacing to snap-through; therefore it provides an interface with high displacement that may be used to drive a damping system. From this combined action, the material maintains high stiffness while having higher damping than conventional materials.

The fluid-filled damping elements studied here can provide a range of stiffnesses—from quite stiff to soft—while moving fluids to dissipate energy in the structural material. The end-of-project results suggest that an optimized WTG with a custom formulated shear thickening fluid can provide passive, adaptive damping over two orders of magnitude in the driving frequency.

APPENDIX

One thing to note is that the CAD Solidworks file obtained from the manufacturer's website used different units. The outer diameter of the original Clover Domes is 0.896 inches, but the Solidworks file obtained from the manufacturer had dimensions of 0.035276 inches (or 0.896 mm). The Clover Dome dimensions in Solidworks were worked with the given dimensions from the manufacturer and later adjusted when imported into ABAQUS. When ABAQUS imported the STEP-file from Solidworks, it converted the units to the standard SI unit for length (meters). Thus when the Clover Dome STEP-file was imported to ABAQUS, a scaling factor of 0.64516 had to be used. This number came from the 25.4 scaling from inches to millimeters from the manufacturer and then multiplying that with the scaling of 0.0254, the conversion of inches in Solidworks to meters in ABAQUS. The metrics given in the following variation tables all have dimensions in inches with the standard outer diameter of 0.896 inches.

Parameter Values for Each Variation Model

Clover Dome – Web Thicknesses

	Outer Radius	Center Circle Radius (CCR)	Center Circle Angle (CCA)	Inner Circle Radius (ICR)	Stress Cutout Angle (SCA)
Original	0.448 in	0.304038 in	60°	0.163449 in	20°
50% Web Thickness	0.448 in	0.3759962 in	77.07°	0.2319528 in	20°
80% Web Thickness	0.448 in	0.3348228 in	62.91°	0.1907794 in	20°
90% Web Thickness	0.448 in	0.318389 in	58.1°	0.1743456 in	20°
110% Web Thickness	0.448 in	0.28956 in	48.14°	0.1455166 in	20°
120% Web Thickness	0.448 in	0.2751836 in	43°	0.1311402 in	20°

Clover Dome – Number of Cutouts

	Outer Radius	Center Circle Radius (CCR)	Center Circle Angle (CCA)	Inner Circle Radius (ICR)	Stress Cutout Angle (SCA)
Original (3 Cutouts)	0.448 in	0.304038 in	60°	0.163449 in	20°
4 Cutouts	0.448 in	0.304038 in	45°	0.163449 in	20°

5 Cutouts	0.448 in	0.304038 in	36°	0.163449 in	20°
-----------	----------	-------------	-----	-------------	-----

Clover Dome – Stress Cutout Angles

	Outer Radius	Center Circle Radius (CCR)	Center Circle Angle (CCA)	Inner Circle Radius (ICR)	Stress Cutout Angle (SCA)
Original	0.448 in	0.304038 in	60°	0.163449 in	20°
Reduced SCA	0.448 in	0.304038 in	60°	0.163449 in	14°
Increased SCA	0.448 in	0.304038 in	60°	0.163449 in	26°

Clover Dome – Height Angles

	Outer Radius	Center Circle Radius (CCR)	Center Circle Angle (CCA)	Inner Circle Radius (ICR)	Stress Cutout Angle (SCA)	Height Angle (HA)
Original	0.448 in	0.304038 in	60°	0.163449 in	20°	13.3°
-3° HA	0.448 in	0.304038 in	60°	0.163449 in	20°	10°
+3° HA	0.448 in	0.304038 in	60°	0.163449 in	20°	16°
+7° HA	0.448 in	0.304038 in	60°	0.163449 in	20°	20°

Finite-Element Model (ABAQUS)

The finite-element model was built in ABAQUS to resemble real life testing and application of the Clover Domes. To achieve this, a model consisting of a partial sphere, a cylindrical-hollow base, and a Clover Dome was used for all the ABAQUS runs. The sphere was used to compress the Clover Dome from the top while the base was used to support the Clover Dome from below. The base was hollowed out to allow the Clover Dome to deflect past the bottom of the Clover Dome. ABAQUS does not utilize units in its measurements, but all the input data is given in standard SI units. From ABAQUS, the reaction force on the bottom base and the displacement of the sphere were extracted and used to create the force-displacement profiles.

Figure 241 shows the Clover Dome before being compressed and at the end of the run.

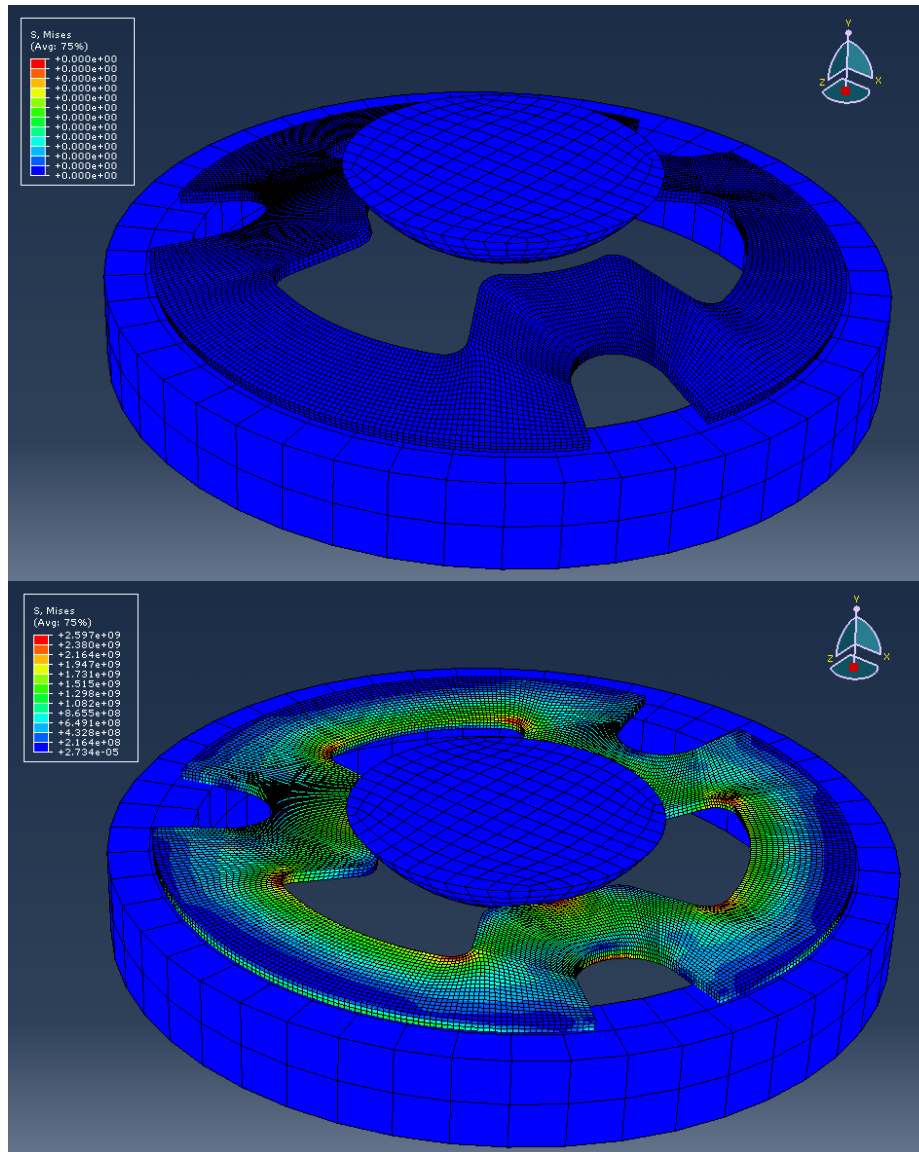


Figure 241. Clover Dome before compression (top) and after compression (bottom).

Mesh Refinement and Utilizing a Half Model

A part of the finite element analysis is to determine the density of elements needed in the model for an acceptably accurate result and whether the solution will converge with increasing mesh density. A mesh refinement study was done on the original Clover Dome model. The global seeding started with an approximate global size of 0.00015 which was called the “normal” mesh. A “coarse” mesh had a global seeding size of 0.0002, and the “fine” and “finest” meshes had global seeding size of 0.0001 and 0.00005, respectively.

In Fig. 6.2 each of the different mesh densities yielded a slightly different stiffness profile. Upon closer inspection, the curves appeared to converge as the mesh density increased. Looking at the maximum values of each plot, the results confirmed the observation. As the mesh density increased, the difference in maximum value from the previous mesh size decreased, and the results converged toward a load of 112 N (Table 6).

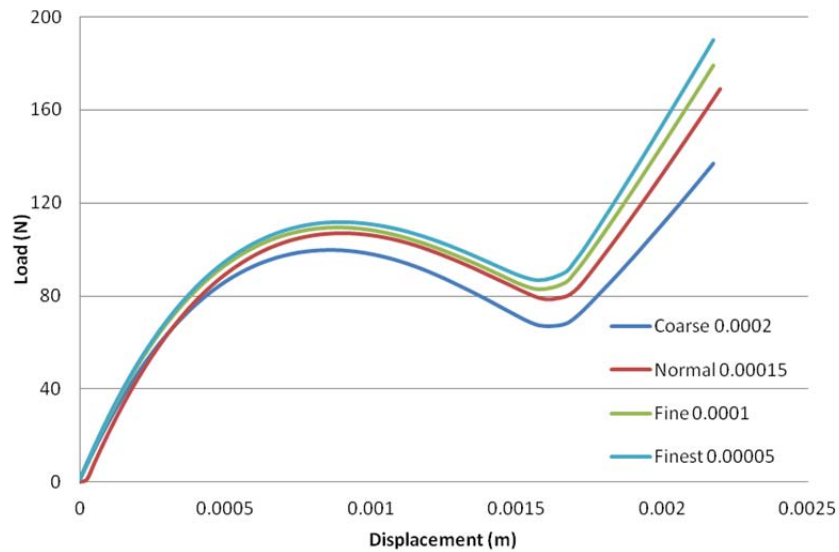


Figure 242. Influence of mesh density on the stiffness profile of a Clover Dome.

Table 18. Summary of results of the mesh sensitivity study.

Mesh	Peak Load (N)	Difference from previous mesh density	% Error from Finest mesh
Coarse	99.87	---	10.62%
Normal	106.86	6.99	4.37%
Fine	109.38	2.52	2.11%
Finest	111.74	2.36	0%

All the Clover Domes in the parametric study (prior to the improved models) were meshed at an approximate global size of 0.00015 using a full model. Starting with the improved models, the mesh density was increased such that the global size was 0.0001. This was done to improve accuracy, help with convergence, and decrease uncertainty to well below 5%.

Another change done to the ABAQUS runs was cutting the model in half, which lowered the computational time for each model. When doing this, the sphere, the Clover Dome and the supporting base were cut in half and a set of nodes along the face of the cut was created. The YZ plane was used as the plane of symmetry. The set of nodes was fixed in the x-direction, thus resembling the behavior of a whole Clover Dome. The node set is highlighted in red in Figure 243. The reaction forces taken on the support base had to be doubled to accurately represent the total force exerted on the Clover Dome.

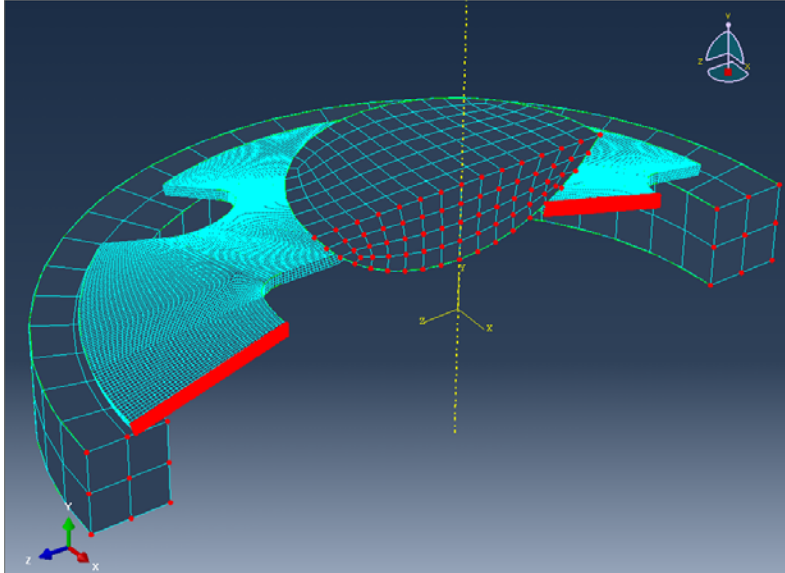


Figure 243. Half-model of a Clover Dome utilizing symmetry to decrease computation time. Symmetric boundary condition was imposed on the nodes highlighted in red.